# East European Journal of Physics

## No 4. 2019

# East European Journal of Physics

# East European Journal of Physics

## ORIGINAL PAPERS

HISTORY OF SCIENCE

# MODEL OF FORMING ISOTROPIC AND ANISOTROPIC GRAPHITE UNDER HIGH TEMPERATURES AND FLUENCES NEUTRON IRRADIATION

Mykola P. Odeychuk[1], Victor I. Tkachenko[1,2], Leonid A. Bulavin[3],
Boris V. Borts[1], Stella I. Skoromnaya[1]

*[1]National Science Center Kharkiv Institute of Physics and Technology*
*1, Academichna Str., 61108 Kharkiv, Ukraine*
*[2]V.N. Karazin Kharkiv National University*
*4, Svobody Sq., 61022 Kharkiv, Ukraine*
*[3]Taras Shevchenko National University of Kyiv*
*64/13, Volodymyrska Street, 01601 Kyiv, Ukraine*
*\*E-mail: odeychuk@kipt.kharkov.ua*

A model is proposed for describing the shape change of isotropic and anisotropic graphite under the influence of high temperatures and high neutron radiation fluences. The model is based on a new approach, which uses the following provisions: description of the near-pore neighborhood in graphite as a solid solution using the theory of phase transformations of the first kind; consideration of a new phase as a spheroidal pore of small eccentricity, flattened along the direction of greatest stress; taking into account the clustering of carbon atoms at fluences of more than $2 \times 10^{26}$ $n/\text{m}^2$. The graphite non-isotropy is characterized by different pore sizes, different diffusion coefficients, the lengths of the paths of graphite atoms along and across volume of the sample, which in turn depend on the temperature of the sample. It is proposed that the initial element on the basis of which a new phase will be formed is the spheroidal pore of small eccentricity, flattened along the direction of the highest tension. A kinetic equation that describes the diffusion of pores under the influence of high temperatures and intense neutron fluxes is obtained. Initially, the pores are in a field of predetermined stresses oriented along and across the sample. The contribution of diffusion processes is due to the term proportional to the pore distribution function in the sample, and the effect of the neutron flux is described by an additional term in the kinetic equation. The obtained kinetic equation for anisotropic graphite can be transformed for isotropic graphite. For isotropic and anisotropic graphite, model solutions have been obtained that characterize the change in its volume with time under the influence of a neutron flux and high temperature. It is shown that the magnitude of the change in the relative volume of reactor graphite for isotropic graphite exceeds a similar value for anisotropic graphite. Theoretical confirmation of the laws governing the swelling of anisotropic graphites under the influence of large neutron fluences and in the high-temperature field, previously obtained by other authors, is obtained: longitudinal compression of anisotropic graphite samples corresponds to a change in the linear dimensions of isotropic graphites; the transverse compression of anisotropic graphite samples is less than the change in the longitudinal linear dimensions of isotropic graphites.

**KEY WORDS:** theory, graphite, forming, neutron, fluence, high temperature

The radiation dimensional stability of graphite is its most important characteristic and it largely determines its performance as a material and construction as a whole [1-7]. The rate and nature of changes in the size of graphite products depend on irradiation temperature and are changing in the process of the set of neutron fluence at a fixed temperature. In the general case, the change in the dimensions of carbon materials under the influence of neutron irradiation is in a complicated dependence on the irradiation conditions: from the magnitude of the integral flow and temperature. As a rule, at the initial stage of irradiation the accelerated shrinkage of irradiated graphite is observed. With the growth of the neutron fluence the shrinkage rate is slowing, and then reverses the sign - shrinkage is replaced by secondary swelling.

The rate of secondary swelling of graphite is higher than the rate of shrinkage, and this is accompanied by a change in its physical properties. In graphite develops microcracks, which become larger and merge and form macrocracks [4].

The strength of the material decreases, which should limit the service life of the reactor, and, consequently, the entire masonry of the reactor.

The increasing of temperature reduces the dose corresponding to the transition from shrinkage to secondary swelling and increases the speed of the latter.

It is known that metals irradiated for a long time pass into a state of saturation with point defects. This state is unstable to the nucleation and formation of volumetric accumulations of vacancies in the form of vacancy pores. As a result of the formation of such cavities in the metal, an increase in its initial volume is observed, thus its swelling occurs. First vacancy swelling of metal about 10 nm in size associated with the cell was discovered experimentally in 1967. Moreover, as it turned out, swelling, such as steel, it may be 6 % or more of the initial volume

The most undesirable consequences of swelling include deformation, bends and an increase in the size of various structures that can lead to self-welding of individual parts, jamming, as well as to overheating inside the working units. Exposed radiation swelling phenomenon correlates not only for metals, but also for widely used as a neutron absorber reactor graphite.

In some types of nuclear reactors, graphite components are used inside the nuclear reactor as structural elements. Irradiation of neutron fluxes and high temperature carried to deformation (creep) graphite to disruption of its structural integrity. Therefore, the experimental and theoretical investigations of graphite forming under the influence of the above factors are important for the safe operation of nuclear reactors. In this direction, active research work is carried out, as a result of which theoretical models [8] are created that give a good correspondence with the experimental data on the graphites forming. However, it should be noted that the experimental database on the graphite forming under the influence of irradiation and high temperatures does not possess completeness and is fragmentary.

The purpose of this work is the development of the theory of graphite forming under the influence of high temperatures and high fluences of neutrons on the basis of the theory of phase transformations of the first kind, in which the near-porous neighborhood of graphite is considered as a solid solution [9,10], or similar to a liquid medium [11].

## FORMULATION OF THE PROBLEM
### Graphite forming under the influence of neutron fluxes of large fluences in a high-temperature field.
### Initial information about the graphite forming

The effect of neutron fluxes of large fluences and high temperatures on nuclear graphite, to some extent, is similar to the formation of pores in solid solutions under the influence of certain external factors. In the latter case, phase transformations of the first kind take place, accompanied by the formation of pores in a solid [9,10] or bubbles in a liquid [11].

The formation of pores in reactor graphite taking into account [9-11] can be described as follows.

In a simplified embodiment the reactor graphite is a mixture of petroleum coke and coal tar. Blocks are pressed from this mixture, usually about 500 mm in diameter and about 2000 mm in length, and then these blocks are processed at a high (up to 3000 °C) temperature. In the process of heat treatment, pores are formed in graphite, the amount of which (porosity) depends from the technology of production.

As practice shows, graphites under the influence of load and irradiation, as well as metals are subject to pore formation processes [2,12], as a result of which their dimensional changes take place.

However, these processes must occur in different scenarios due to the fact that for different graphite marks may vary not only the initial porosity, density and strength characteristics, but also internal stresses, which are caused by the method of graphite making. So, for example, there are isotropic graphites, in the manufacture of which isostatic pressing is used. For anisotropic graphites, which are produced with using traditional pressing methods with uniaxial compression, which determines the difference in properties of these graphites along the axes **a** and **c**.

The pressure in the pore is created by an inert gas, in which medium the production of reactor graphite takes place and at the initial instant of time always exceeds the pressure in the crystalline structure of graphite. During irradiation and temperature loading, graphite loses its elastic properties and passes into a state where the pressure in the pore tends to pressure in the crystal, slightly exceeding it.

The finished product is composed of compacted graphite fine grain size of about 500 Å [5] with different orientation of the graphite planes. The porosity of reactor graphite is usually about 26 %, and in modern grades of reactor graphite - (9-10) %.

The interaction of neutrons with the carbon atoms of the grain is accompanied by the formation of vacancies and the removal of atoms into the interstitial space. Moreover, along with the modification of the initially existing micropores, the formation of new pores is also observed in reactor graphite, i.e. the formation of a new phase.

In virtual space, the formation of a new phase can be viewed as the result of mutual transitions of carbon atoms from one phase (atoms at lattice sites or in internodes) to another phase (the pores formed by the accumulation of vacancies). It can be assumed that the crystal lattice of graphite in the immediate vicinity of the pore is strongly saturated with point defects (carbon atoms located in internodes).

Conditionally, we will consider a pore as such, which is not located in the crystal lattice, but in an amorphous, liquid-like medium located near the pore surface and consisting from irregularly arranged carbon atoms.

The phenomenon of amorphization of the reactor graphite is studied for a long time [13-16]. Graphite can be amorphized under the influence of high-energy ions, neutrons or electrons. Judging by the diffraction pattern of a transmission electron microscope (TEM), observed along the axis c, amorphization occurs when samples are irradiated to a dose of about 1 atomic displacement (sleep) at room temperature [13].

A schematic representation of the pore surrounded by an amorphous or liquid-like medium inside a graphite crystal is shown in Fig. 1.

With such an examination, the near-pore neighborhood can be considered as a solid solution, and the theory of phase transformations of the first kind can be applied to its description [9-11].

As follows from this theory, the equations describing the phase transformations contain coefficients that are expressed in terms of the coefficients: viscosity $\eta$, diffusion $D$, surface tension $\sigma$, as well as the mean free path of a point defect (carbon atom) in the crystal lattice $l$. These coefficients have a certain view [9-11] and can be used to construct a fundamental system of equations describing the time variation of the distribution pores function in a space of dimensions, which include the coordinates and velocities of the centers of spherical pores, as well as their size and the quantity of vacancies in them.
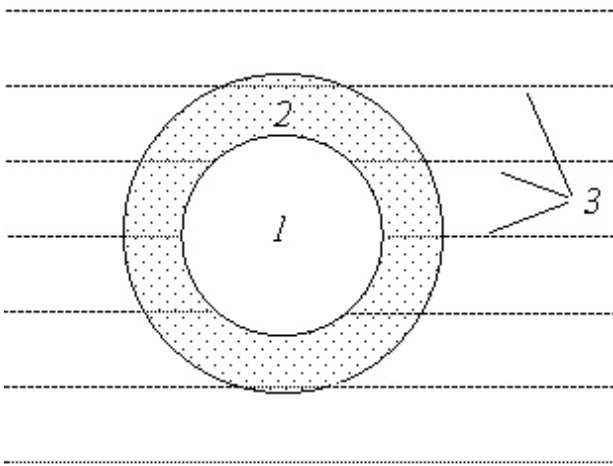
Fig.1. Location of the vacancy pore in a graphite crystal
1 - vacancy pore, 2 - liquid-like medium near the pore, 3 -
hexagonal planes of a graphite crystal.

For description of the phase transformations in reactor graphite, we will assume that the processes of pore formation during heat treatment of graphite at high temperatures and under the influence of neutron fluxes are similar. In the first case, the source of energy for the formation of a new phase is high temperature, in the second - a moderate temperature and neutron flux.

In isotropic graphite, the displacement of carbon atoms is isotropic due to the isotropy of internal stresses.

In anisotropic graphite, the knocked out carbon atoms will move in an inhomogeneous force field, which is characterized by various internal longitudinal $\sigma_P$ and transverse $\sigma_T$ mechanical stresses of the sample. Ultimately, the carbon atoms will preferably be displaced to the region of equal internal pressure from the medium, i.e., to the axis of the axisymmetric internal field of internal tension of the non-isotropic sample. In this connection, the formed pores will reflect the structure of internal stresses in the sample, and will apparently have the form of an ellipsoid of revolution. Such ellipsoidal form of pores is established as a result of computer analysis of plane optical images of reactor graphite samples [17]. Here, optical images obtained as a result of structural studies quantitatively revealed changes in the structure of pores and their cross-sectional area and the values of the eccentricity of the ellipses (0.908, 0.931, 0.929 and 0.922 for IG-110, PGX, NBG-18 and PCEA graphite samples respectively) and their preferential orientation was identified.

**Theoretical model of graphite forming under the influence of neutron fluxes
of large fluences in a high-temperature field**

On the basis of the foregoing, we obtain a kinetic equation for the pore distribution function having the form of an ellipsoid of revolution in anisotropic graphite under the influence of large neutron fluences and at high temperatures.

We assume that the distribution of pores in a viscous medium at a given time $t$ is determined by the distribution function $f(\vec{r}_T(t), \vec{r}_P(t), \vec{v}_T(t), \vec{v}_P(t), V_T(t), V_P(t), N_T(t), N_P(t), t)$, in which the variables are as follows: $V_T(t) = \dfrac{4\pi}{3} R_T^2 R_P$ - pore volume at constant radius along the anisotropy direction $R_P$ with coordinate $\vec{r}_T(t)$ and speed $\vec{v}_T(t)$ of its center; $N_T(t)$ – the number of vacancies in this pore (the number of carbon atoms, retired from the volume $V_T(t)$ ); $V_P(t) = \dfrac{4\pi}{3} R_T^2 R_P$ – pore volume, but at a constant transverse it radius $R_T$ with coordinate $\vec{r}_P(t)$ and speed $\vec{v}_P(t)$ of its center; $N_P(t)$ - number of vacancies in this pore.

When deriving an equation describing the dynamics of the pore distribution function in time $t$ and in the space of variables $\{\vec{r}_\beta(t), \vec{v}_\beta(t), V_\beta(t), N_\beta(t)\}$, where the index $\beta$ takes values $\beta = T, P$, it is convenient to introduce a dimensionless number $N_{\beta 1}(t) = V_\beta(t)/V_0$, where $V_0$ – change in pore volume over time $\delta t$, and we assume $\delta t$ so small, that when the volume changes on $V_0$ the number of vacancies changes on one. Over the same period of time $\delta t$ coordinate of the center of the pore $\vec{r}_\beta(t)$ is displaced on a small amount $\delta \vec{r}_0$ with the module $3 \cdot V_0^{1/3}/4\pi$ and the speed will change on a small amount $\delta \vec{v}_\beta(t) = \delta \vec{r}_0/\delta t$ with the module $3 \cdot V_0^{1/3}/(4\pi \cdot \delta t)$.

The introduction of a number $N_{\beta 1}(t)$ for the pore distribution function simplifies calculations because the similarity transformation is performed:

$$f(\vec{r}_T(t), \vec{r}_P(t), \vec{v}_T(t), \vec{v}_P(t), V_T(t), V_P(t), N_T(t), N_P(t), t) dV_T dV_P =$$
$$= \overline{f}(\vec{r}_T(t), \vec{r}_P(t), \vec{v}_T(t), \vec{v}_P(t), N_{1T}(t), N_{1P}(t), N_T(t), N_P(t), t) dN_{1T} dN_{1P}$$

Where

$$V_0^2 \cdot f(\vec{r}_T(t), \vec{r}_P(t), \vec{v}_T(t), \vec{v}_P(t), V_T(t), V_P(t), N_T(t), N_P(t), t) =$$
$$= \overline{f}(\vec{r}_T(t), \vec{r}_P(t), \vec{v}_T(t), \vec{v}_P(t), N_{1T}(t), N_{1P}(t), N_T(t), N_P(t), t)$$

In view of the foregoing, the time variation of the distribution function $\overline{f}(\vec{r}_T(t), \vec{r}_P(t), \vec{v}_T(t), \vec{v}_P(t), N_{1T}(t), N_{1P}(t), N_T(t), N_P(t), t)$, which we will write in abbreviated form in the form

$\overline{f}(\vec{r}_\beta, \vec{v}_\beta, N_{1\beta}, N_\beta, t)$, is described by the equation:

$$\frac{d\overline{f}}{dt} = -\left(I_{N_T} - I_{N_T-1}\right) - \left(I_{N_{T1}} - I_{N_{T1}-1}\right) - \left(I_{N_P} - I_{N_P-1}\right) - \left(I_{N_{P1}} - I_{N_{P1}-1}\right) = -\frac{\partial I_{N_T}}{\partial N_T} - \frac{\partial I_{N_{T1}}}{\partial N_{T1}} - \frac{\partial I_{N_P}}{\partial N_P} - \frac{\partial I_{N_{P1}}}{\partial N_{P1}} + \Phi(t), \tag{1}$$

where: $I_{N_\beta}$ - flow in space $N_\beta$; $I_{N_{\beta1}}$ - flow in space $N_{1\beta}$;

$I_{N_\beta} = v_{N_\beta, N_\beta+1} \overline{f}(\vec{r}_\beta, \vec{v}_\beta, N_{1\beta}, N_\beta, t) - v_{N_\beta+1, N_\beta} \overline{f}(\vec{r}_\beta, \vec{v}_\beta, N_{1\beta}, N_\beta+1, t)$;

$I_{N_{1\beta}} = v_{N_{1\beta}, N_{1\beta}+1} \overline{f}(\vec{r}_\beta, \vec{v}_\beta, N_{1\beta}, N_\beta, t) - v_{N_{1\beta}+1, N_{1\beta}} \overline{f}(\vec{r}_\beta, \vec{v}_\beta, N_{1\beta}+1, N_\beta, t)$; $v_{K,K+1}$ - frequency of transition from state $K$ to state $K+1$, where $K = \{N_\beta, N_{1\beta}\}$; $v_{K+1,K}$ - frequency of the reverse transition from state $K+1$ to state $K$; $\Phi(t) > 0$ - monotonic increasing function, describes the influx of neutrons into the volume of a graphite sample. The monotonous growth with time of the function $\Phi(t)$ is explained by the fact that the fast neutron in graphite slows from the mean fission energy to the thermal energy, after experiencing about 114 collisions [5]. It should be noted that the last term in equation (1) characterizes the amorphous action of the neutron flux, i.e. an action aimed at creating point defects in the crystal, which means an increase in the number of pores or their dimensions.

We simplify the record of the subsequent calculations, introducing the abbreviated notation for the distribution function $\overline{f} \to f$, and come back again to the designation of the pore volume $N_{1\beta} \to \tilde{V}_\beta$, where the sign "tilde" in subsequent calculations is omitted.

Using the results obtained for isotropic graphite, we can formally generalize them to anisotropic graphite. Allowance for anisotropy leads to an increase in the arguments of the pore distribution function in graphite. The generalization gives the following form of the initial equations:

$$\frac{df}{dt} = \sum_\beta \left( -\frac{\partial I_{N_\beta}}{\partial N_\beta} - \frac{\partial I_{N_{1\beta}}}{\partial V_\beta} \right) + \Phi(t), \tag{2}$$

where:

$I_{N_\beta} = \frac{dN_\beta}{dt} \cdot f(\vec{r}_\beta, \vec{v}_\beta, V_\beta+1, N_\beta, t) - D_{N_\beta} \cdot \frac{\partial f(\vec{r}_\beta, \vec{v}_\beta, V_\beta+1, N_\beta, t)}{\partial N_\beta}$; $I_{V_\beta} = \frac{dV_\beta}{dt} \cdot f(\vec{r}_\beta, \vec{v}_\beta, V_\beta+1, N_\beta, t) - D_{V_\beta} \cdot \frac{\partial f(\vec{r}_\beta, \vec{v}_\beta, V_\beta+1, N_\beta, t)}{\partial V_\beta}$;

$\frac{dN_\beta}{dt} = -D_{N_\beta} \cdot \frac{1}{T} \cdot \frac{\delta F(V_\beta, N_\beta)}{\delta N_\beta}$, $D_{N_\beta} = v_{N_\beta, N_\beta+1} = 4R_\beta^2 \pi \alpha \frac{D_\beta}{2l_\beta} n^L$; $\frac{\delta F(V_\beta, N_\beta)}{\delta N_\beta} = T \cdot \ln \frac{p^{V_\beta}}{p}$;

$\frac{dV_\beta}{dt} = -D_{V_\beta} \cdot \frac{1}{T} \cdot \frac{\delta F(V_\beta, N_\beta)}{\delta V_\beta}$, $D_{V_\beta} = v_{V_\beta, V_\beta+1} \cdot V_0^2 = \frac{3V_\beta T}{4\eta_\beta}$; $\frac{\delta F(V_\beta, N_\beta)}{\delta V_\beta} = p^{L_\beta} - p^{V_\beta} + \frac{2\sigma(R_\beta)}{R_\beta}$;

$F(V_\beta, N_\beta) = \sum_\beta \left( V_\beta \left( p^{L_\beta} - p^{V_\beta} \right) + N_\beta \left( \mu^{V_\beta} - \mu^{L_\beta} \right) + \int_0^{V_\beta} \frac{2\sigma(R')}{R'} dV' \right)$; $F(N_{\beta1}, N_\beta)$ - the difference between the free energy of the medium pore volume $V_\beta$ and the number of vacancies $N_\beta$ and the free energy of the medium without pores; $T$ - medium temperature; $n^L$ - density of atoms in a crystal; $\mu^{V_\beta}$ - chemical potential of vacancies in the pore; $\mu^{L_\beta}$ - chemical potential of a crystal atom; $p$ - saturation pressure by pores; $p^{V_\beta}$ - the pressure of vacancies in the pore; $p^{L_\beta}$ - pressure in the crystal along ($\beta = P$) or across ($\beta = T$) the axis; $\sigma(R)$ - the coefficient of surface tension at the boundary of the pore, which in general can depend of the pore radius $R_\beta(t)$; $\eta_\beta$ - dynamic viscosity of a crystal along ($\beta = P$) and across ($\beta = T$) the axis of the stress field of a crystal; $0 \le \alpha \le 1$ - a coefficient that takes into account the additional barrier that can exist for the last jump of the carbon atom from the pore; $D_\beta, l_\beta$ - the diffusion coefficients of the carbon atoms and the length of the elementary displacement of the vacancy in the crystal along ($\beta = P$) and across ($\beta = T$) axes of the stress field in the crystal.

Assuming that the medium is uniform in space and in pores no external mechanical forces other than an external radiation source, the equation (2) is simplified and takes the form:

$$\frac{\partial f}{\partial t} = -\Gamma_a(N, V) \cdot f + \sum_\beta \left[ \frac{\partial}{\partial N_\beta} \left( \frac{1}{2} D_{N_\beta} \frac{\partial f}{\partial N_\beta} \right) + \frac{\partial}{\partial V_\beta} \left( \frac{1}{2} D_{V_\beta} \frac{\partial f}{\partial V_\beta} \right) \right] + \Phi(t), \tag{3}$$

where: $\Gamma_a(N, V) = \frac{1}{2} \sum_\beta \left[ \frac{\partial}{\partial N_\beta} \left( \frac{dN_\beta}{dt} \right) + \frac{\partial}{\partial V_\beta} \left( \frac{dV_\beta}{dt} \right) \right] \equiv \frac{d}{dt} \ln \left( \prod_\beta \left| \frac{dV_\beta}{dt} \right| \left| \frac{dN_\beta}{dt} \right|^{sign(S_\beta)} \right)$, $S_\beta \equiv \frac{dN_\beta}{dt} \frac{dV_\beta}{dt}$

The writing of the term $\Gamma_a(N,V)$ in the form of a total time derivative corresponds to a search for the signs of the quantities $\dfrac{dN_\beta}{dt}$ and $\dfrac{dV_\beta}{dt}$, as well as their derivatives by $N_\beta$ and $V_\beta$ The coefficient 1/2 in equation (4) is necessary to ensure the passage to the kinetic equation describing the creep of isotropic graphite (when the index $\beta$ corresponds only to the value $P$) under the influence of large fluences of neutrons at high temperatures.

Thus, the kinetic equation pore diffusion has divergent form in the crystal pore size in the space with the addition of the right side of a term proportional to pore distribution function.

Equation (3) must be supplemented by an equation describing the conservation of the number of atoms in a unit volume, including vacancies in the pores and carbon atoms dispersed in the crystal:

$$n^L(0)\left(1-\int_0^\infty\int_0^\infty\int_0^\infty\int_0^\infty (V_T+V_P)f(V_\beta,N_\beta,0)dV_T dV_P dN_T dN_P\right)=$$
$$=n^L(t)\left(1-\int_0^\infty\int_0^\infty\int_0^\infty\int_0^\infty (V_T+V_P)f(V_\beta,N_\beta,t)dV_T dV_P dN_T dN_P\right)+ \tag{4}$$
$$+\int_0^\infty\int_0^\infty\int_0^\infty\int_0^\infty (N_T+N_P)f(V_\beta,N_\beta,t)dV_T dV_P dN_T dN_P$$

Equations (3) and (4) constitute a system that describes the change in time $f(V_\beta,N_\beta,t)$ and $n^L(t)$. For a complete description of the time dynamics of these parameters in a medium, the system of equations must be supplemented by initial and boundary conditions.

In order to compare the parameters of the forming of isotropic and anisotropic graphites under the influence of large neutron fluences and in a high-temperature field, we briefly describe the phenomenological theory of the isotropic graphite forming.

## QUALITATIVE ANALYSIS OF ISOTROPIC GRAPHITE FORMING UNDER THE INFLUENCE OF HIGH TEMPERATURES AND LARGE NEUTRON FLUENCES
### Analysis of the isotropic graphite forming under the influence of neutron fluences to $2\times10^{26}\ n/m^2$

Equation (3) describes the time variation of the pore distribution function in an isotropic graphite crystal in the case when the pore is spherically symmetric $R_P=R_T$, and the index $\beta$ takes only the value $T$.

This equation can be analyzed in the simplest case, when the pore distribution function depends only on the time $f=n(t)$, and does not depend on the variables $V$ and $N$. Then we can assume that all pores have the same volume $V_u$ and contain an equal number of vacancies $N_u$. In this case, the total volume occupied by the pores is:

$$V_\Sigma(t)=\frac{1}{N_u}\int_0^{N_u}\int_0^{V_u} f(t)dVdN = n(t)V_u. \tag{5}$$

It follows from expression (5) that the change in the volume of graphite in the case under consideration is proportional to the distribution function of the pores in the space of dimensions. Moreover, the distribution function is normalized in such a way that at the initial time it is equal to the total number of pores in a unit volume of graphite: $n_i(0)=N_\Sigma$. For describing of the change in pore volume per unit volume of graphite, it is necessary to find a solution of equation (3), which, taking into account the above assumptions about the form of the distribution function, takes the form:

$$\frac{dn_i(t)}{dt}=-\Gamma(N(t),V(t))\cdot n_i(t)+\Phi(t), \tag{6}$$

where the index $i$ denotes isotropic graphite.

Equation (6) is a linear differential equation, whose solution has a simple form:

$$n_i(t)=exp(-F(t))\left(n_i(0)+\int_0^t \Phi(x)\cdot exp(F(x))dx\right), \tag{7}$$

where $F(t)=\int_0^t \Gamma(N(x),V(x))dx$.

For the analysis of solutions (7) introduces the simplifying assumptions:
– we assume that $\Gamma(N(t),V(t))$ is a positive constant, i.e. $\Gamma(N(t),V(t))=C_1=const>0$;
– we assume that the contribution of the neutron term on the right-hand side of (7) is described by a linear function of time: $\Phi(t)=\Phi_0\cdot t$.

In this case, the solution of (7) takes the form:

$$n_i(\tau) = n_i(0)(1+X_i)\left(\exp(-\tau)-1+\frac{\tau X_i+1}{1+X_i}\right) \tag{8}$$

where $\tau = C_1 \cdot t$ - dimensionless time, $X_i = \Phi_0\left(C_1^2 n_i(0)\right)^{-1}$ - parameter describing the neutron flux and the properties of isotropic graphite.

When calculating the total volume occupied by the pores, it was introduced by the assumption of the constancy of the pore size. Therefore, the total volume of pores will change only as a result of a change in their number.

If we proceed from this model representation, we can determine from (8) the change in the relative pore volume of isotropic reactor graphite in a result of exposure to high temperature and intense neutron flux:

$$\left.\frac{\Delta V_\Sigma(\tau)}{V_\Sigma(0)}\right|_i = \frac{(n_i(\tau)-n_i(0))}{n_i(0)} = (1+X_i)\left(\exp(-\tau)-1+\tau\frac{X_i}{1+X_i}\right). \tag{9}$$

From the expression (9) follows that at the initial time the change of the pore volume is zero. The influence of the neutron flux and temperature leads to a change in the total pore volume. In Fig. 2 shows a qualitative curve described by expression (9), and displaying the change in the relative volume of pores in the graphite with the time $\tau$ when the parameter $X_i = 7$. As follows from Fig. 2, graphite under irradiation first shrinks and then swells. This behavior of graphite under irradiation corresponds with experimental results.

From (9) we can determine the time to reach the maximum compression of the sample $\tau_{max} = \ln\left(\frac{1+X_i}{X_i}\right)$ and the maximum relative compression of its volume:

$$\left(\left.\frac{\Delta V_\Sigma(\tau)}{V_\Sigma(0)}\right|_i\right)_{max} = X_i \ln\left(\frac{1+X_i}{X_i}\right) - 1. \tag{10}$$

Analyzing the behavior of the curve in Fig. 2, it can be concluded that the change in the relative volume of pores of reactor graphite is due to the flow of two mutually exclusive processes. The first process is due to the decrease in time (exponentially) of the number of pores as a result of diffusion of point defects (thermal diffusion of graphite atoms in the graphite crystal lattice). The second process is characterized by a time-linear increase in the number of pores and is associated with the amorphization of graphite under the influence of fast neutron flux.

It should be noted that the dimensionless time can be expressed through the fluence of fast neutrons, since its value is proportional to the integral dose of irradiation of graphite by neutrons.
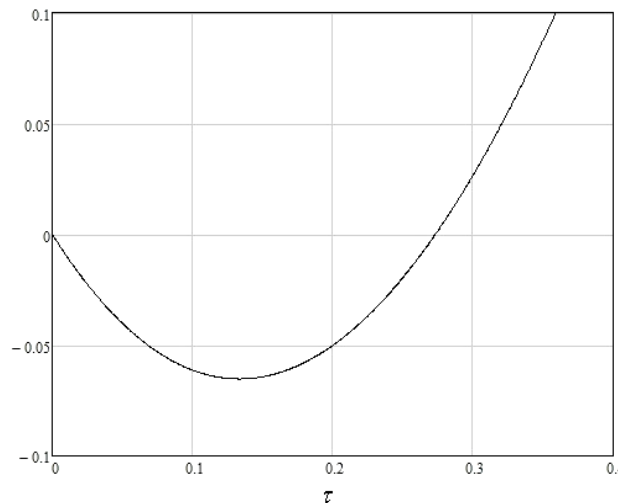


Fig.2. A qualitative curve for the change in the relative volume of pores in isotropic graphite with a dimensionless time $\tau$.

**Analysis of the isotropic graphite forming under the influence of neutron fluences is more $2\times10^{26}$ $n/m^2$**

With increasing neutron fluence to a value more $2\times10^{26}$ $n/m^2$ it's necessary, in our opinion, take into account the growing number of formation of lattice defects (vacancies) of reactor graphite. Displaced carbon atoms are clustered in small groups of 5-10 atoms [3]. At this stage, due to neutron scattering on such clusters, the effect of increasing (accumulating) neutron fluence should be observed. For process modeling of increasing the neutron fluence, we shall assume in the right-hand side of equation (3) that the function $\Phi(t)$ in the form:

$$\Phi(t) = \Phi_0 t + \Phi_1 t^2 \tag{11}$$

The solution of equation (7) in this case takes the form:

$$n_i^+(\tau) = n_i(0)(1+X_i)\left[(\exp(-\tau)-1)\left(1-\frac{2d\cdot X_i}{1+X_i}\right) + \frac{\tau X_i+1}{1+X_i} + \frac{d\cdot X_i}{1+X_i}\tau(\tau-2)\right],\tag{12}$$

where $d = \dfrac{\Phi_1}{\Phi_0 C_1}$ - constant, which is depending from the property of clustering of reactor graphite.

In order to determine the applicability of expression (12) for describing the change in the relative elongation of reactor graphite parallel to the direction of its formation, we use experimental data [3]. In Fig.3 shows the experimental points on which the analytical dependence (12) is imposed for the values $X_i = 1.3$, $d \cdot X_i = 177.87$. The dimensionless parameter $\tau$ is related with the neutron fluence by the relation: $\tau = \tau_0 \cdot 10^{-22}\Phi$, where $\tau_0 = 30.72$.
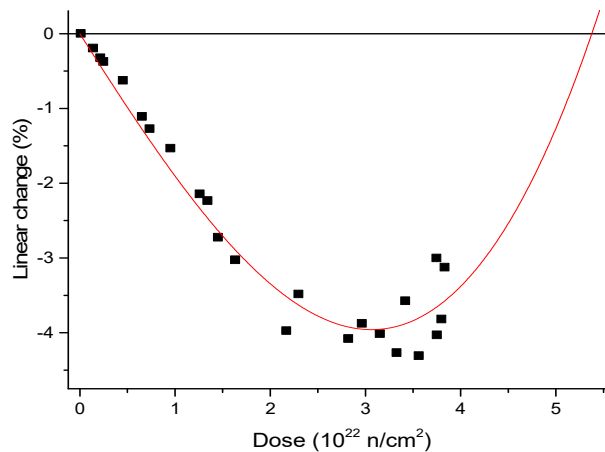


Fig.3. Changing the linear dimensions of the H451 reactor graphite sample parallel to the direction of its formation at 600 °C [3].

In Fig. 3 within the limits of permissible experimental errors seen a good quantitative correspondence of the proposed model to the experimental data.

Thus, this analytical representation of the effect of clustering of reactor graphites under the influence of increased levels of neutron fluxes is applicable to the description of the reactor graphite forming under the influence of high temperatures and increased neutron fluxes.

### The condition of applicability of the isotropic graphite forming model under the influence of neutron fluences and high temperatures

Consider the conditions for the applicability of the solution (8). It was obtained under the assumption of the validity of the relation:

$$\Gamma(N,V) = C_1 > 0.\tag{13}$$

The relation (13) can be detailed using the notation of symbols included in the expression $\Gamma(N,V)$. It can be rewritten in the form of an equation, using expressions (2,3):

$$\frac{d}{dt}\ln\left(\left|\frac{dV}{dt}\right|\left|\frac{dN}{dt}\right|^{sign(S)}\right) = C_1.\tag{14}$$

The solution of equation (14) gives the following relationship between the parameters of reactor graphite:

$$\left|\frac{dV}{dt}\right|\left|\frac{dN}{dt}\right|^{sign(S)} = C_4 e^{-C_1 t}.\tag{15}$$

From the condition $C_4 > 0$ that are chosen in the solution (15), it follows that the sign of the parameter $S = \dfrac{dN}{dt}\dfrac{dV}{dt}$ has a positive value. In this case, finally, taking into account (2), (3), equation (15) takes the following form:

$$\pi\alpha R^2 \frac{D}{l} n^L \frac{3V}{2\eta}\left(p^L - p^V + \frac{2\sigma_P}{R}\right)\ln\left(\frac{p^V}{p^L}\right) = C_4 e^{\tau},\tag{16}$$

where it is considered the assumption of the validity of the condition of equilibrium on the surface of the pore, $p(R,t) \approx p^L$, and also the fact was used, that the surface tension of pores of large dimensions does not depend on the size of the pores, i.e. $\sigma(R) = \sigma_P$. The constant $C_4$ is determined by the values of all the parameters specified in equation (17) at the initial moment of time ($\tau = 0$).

Equation (16) determines the temporal dynamics of the change in the ratio of pressures inside the pore $p^V$ and outside the pore $p^L$. From this equation it follows that the effect of high temperature and intense neutron flux indirectly affect the ratio of pressures inside and outside the pore through the coefficients of viscosity $\eta$, diffusion $D$, surface tension $\sigma_p$, and also through a point defect free path length $l$ (carbon atoms) in the crystal lattice.

Equation (16) has a solution expressed in terms of the ratio of pressures $p^V/p^L$:

$$\tau = -\ln\left(C_4'\right) + \ln\left(\left(1 - \frac{p^V}{p^L} + \frac{2\sigma_P}{Rp^L}\right)\ln\left(\frac{p^V}{p^L}\right)\right), \tag{17}$$

where $C_4' = \dfrac{C_4}{\pi\alpha R^2 p^L \dfrac{D}{l} n^L \dfrac{3V}{2\eta}}$.

It follows from equality (17) that for all pores of the same volume $V_u$ and an equal number of vacancies in them $N_u$, the ratio of pressures $p^V/p^L$ should depend on time. This means that the value $p^L$ is constant, and $p^V$ - function of time.

Thus, expression (17) determines the dependence of the relative pressure in the pore $p^V/p^L$ on time.

In Fig.4 shows graphs of the dependence of the dimensionless time $\tau$ from the ratio of pressures $p^V/p^L$ for different values of the constants: $\dfrac{2\sigma_P}{Rp^L}$ and $C_4'$.

Starting from the family of curves in Fig. 4, we can conclude that these curves for the same values of the constant $C_4'$ and different values $\dfrac{2\sigma_P}{Rp^L}$ do not intersect. However, the appropriate choice of these constants can be ensured, at least, by the intersection of two of these curves. Such an intersection can lead to a change in the time dynamics of the relative pressure in the pore: with increasing time, the decrease in the relative pressure in the pore can be replaced by its growth. For example, the intersection of curves 1 and 5, shown in Fig. 5, may lead to the following change in the pressure in the pore: point a in Fig. 5 is to the left of the maximum of curve 5. Therefore, with increasing time the pressure in the pore must decrease in accordance with the direction of travel along the arrow from point a to point b. When reaching the point b, corresponding to the intersection of curves 1 and 5, the pressure reduction in the pore is changed to its increase, which corresponds to moving along the curve 5 from point b to point c.
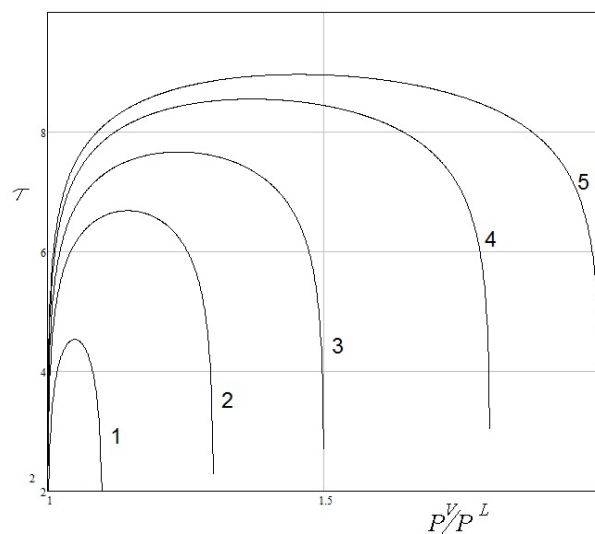


Fig. 4. Curves of the dependence of the dimensionless time $\tau$ from the ratio of pressures $p^V\left(p^L\right)^{-1}$ at a value $C_4' = 10.55$:

$$1 - \frac{2\sigma_P}{Rp^L} = 0.1\,; 2 - \frac{2\sigma_P}{Rp^L} = 0.3\,; 3 - \frac{2\sigma_P}{Rp^L} = 0.5\,; 4 - \frac{2\sigma_P}{Rp^L} = 0.8\,; 5 - \frac{2\sigma_P}{Rp^L} = 1.0$$

Thus, the presented numerical estimates demonstrate the validity of the condition (13). This condition can be fulfilled with a corresponding change in the relative pressure in the pore without changing its relative volume. The relative pore volume of isotropic reactor graphite, as noted in (5), will vary due to a change in the total number of pores.
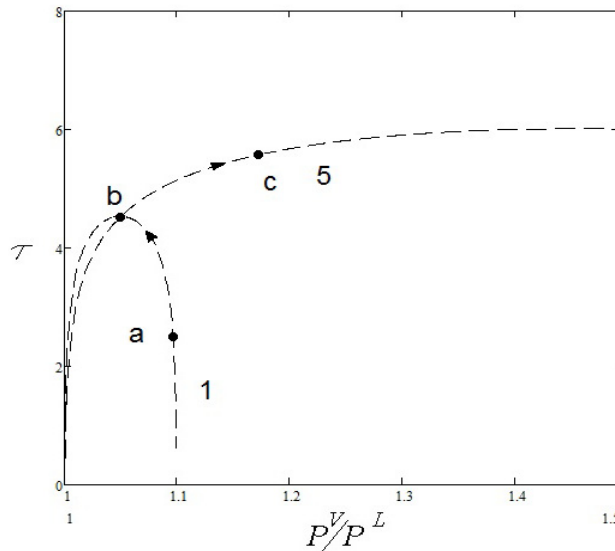


Fig.5. Intersection of curves 1 and 5 at values: $C_4'\big|_1 = 10.55$ and $C_4'\big|_5 = 7.6$.

## QUALITATIVE ANALYSIS OF ANISOTROPIC GRAPHITE FORMING UNDER THE INFLUENCE OF HIGH TEMPERATURES AND LARGE NEUTRON FLUENCES

**Analysis of the anisotropic graphite forming under the influence of neutron fluences to $2 \times 10^{26}\ n/m^2$**

For anisotropic graphite equation (3) can be analyzed for homogeneous in the variables $V$ и $N$ of pore distribution function, but depends only on the time $f = n_a(t)$. Then we can assume that all the pores have the same volume $V_{\beta u}$ but different shape (compressed or elongated ellipsoid of revolution), and contain an equal number of vacancies $N_{\beta u}$. In this case, the total volume occupied by the pores is:

$$V_\Sigma^2(t) = \frac{1}{N_{Tu}N_{Pu}} \int\limits_0^{N_{Tu}} \int\limits_0^{V_{Tu}} \int\limits_0^{N_{Pu}} \int\limits_0^{V_{Pu}} f(t)\,dV_T\,dN_T\,dV_P\,dN_P = n_a(t)V_{Tu}V_{Pu}\,. \tag{18}$$

It follows from expression (18) that the pore volume in anisotropic graphite is proportional to the pore distribution function in the size space. The distribution function is normalized in such a way that at the initial time it is equal to the total number of pores in a unit volume of graphite: $n_a(0) = N_{T\Sigma}N_{P\Sigma}$. For describing of the change in pore volume per unit volume of graphite, it is necessary to find a solution of equation (3), which, taking into account the above assumptions about the form of the distribution function, has the form:

$$\frac{dn_a(t)}{dt} = -\Gamma_a(N(t),V(t))\cdot n_a(t) + \Phi(t)\,, \tag{19}$$

where $N_P(t) = N_T(t) = N(t)$, $N_P(t) = N_T(t) = N(t)$ - by definition, all pores are the same in volume and have an equal number of vacancies.

Equation (19) is a linear differential equation whose solution has a simple form:

$$n_a(t) = exp(-F(t))\left( n_a(0) + \int\limits_0^t \Phi(x)\cdot exp(F(x))\,dx \right), \tag{20}$$

where $F(t) = \int\limits_0^t \Gamma_a(N(x),V(x))\,dx$.

As before, for the analysis of solutions (20) we introduce the simplifying assumptions:

– we consider that $\Gamma_a(N(t),V(t))$ is a positive constant, i.e. $\Gamma_a(N(t),V(t)) = C_1' = const > 0$;

– we assume that the contribution of the neutron term on the right-hand side (20) is described by a linear function of time: $\Phi(t) = \Phi_0 \cdot t$.

In this case, the solution (20) takes the form:

$$n_a(t) = n_a(0)(1+X_a)\left( \exp(-\tau) - 1 + \frac{\tau X_a + 1}{1+X_a} \right), \tag{21}$$

where $\tau = C_1' \cdot t$ - dimensionless time, $X_a = \Phi_0 \left( C_1'^2 n_a(0) \right)^{-1}$ - parameter which describing the neutron flux and properties of anisotropic graphite.

Under the condition of constancy of the pore size of the anisotropic reactor graphite relative change of their volume due to the high temperature and intense neutron flux can be determined by the following expression:

$$\left. \frac{\Delta V_\Sigma(\tau)}{V_\Sigma(0)} \right|_a \equiv \frac{V_\Sigma(\tau) - V_\Sigma(0)}{V_\Sigma(0)} = \frac{\sqrt{n_a(\tau)} - \sqrt{n_a(0)}}{\sqrt{n_a(0)}} = (1 + X_a) \frac{\left( \exp(-\tau) - 1 + \tau \dfrac{X_a}{1 + X_a} \right)}{1 + \sqrt{(\exp(-\tau)(1 + X_a) + \tau X_a - X_a)}} . \tag{22}$$

From the expression (22) it follows that:

– at the initial time, the change in pore volume is zero;

– the change in the pore volume in the case of anisotropic graphite is less than for an isotropic graphite.

In Fig. 6, curve 2 corresponds to expression (22), and displays the change in the relative pore volume in anisotropic graphite with time $\tau$ at a parameter value $X_a = 10$. In Fig.6 for comparison curve for the change in the volume of isotropic graphite is shown (curve 1).
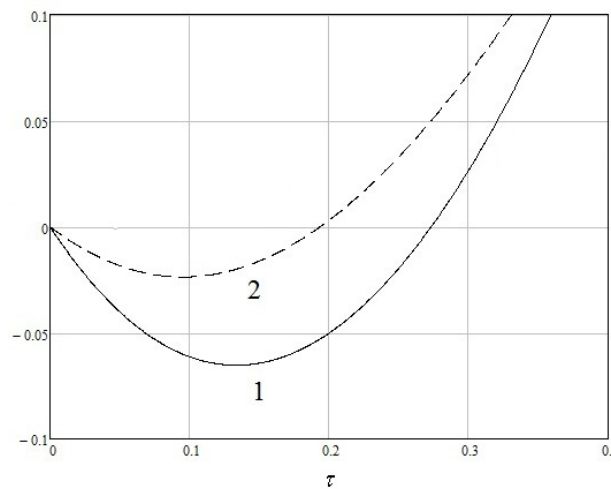


Fig.6. Model curves of the change in the relative volume of pores with dimensionless time $\tau$ in graphites
1 – isotropic graphite; 2 – anisotropic graphite

Analyzing the curves in Fig. 6, we can conclude that the magnitude of the change in the relative volume of reactor isotropic graphite exceeds the analogous value for anisotropic graphite. At the same time, both in one case and in the other, a decrease in the volume of samples is observed first, and then an increase in the volume. Based on the experimental results on the swelling of reactor graphites given in [3], we can formulate the following patterns of swelling of anisotropic graphites under the influence of large fluences of neutrons in a high-temperature field:

– the longitudinal compression of anisotropic graphite samples corresponds to a change in the linear dimensions of isotropic graphites;

– the transverse compression of anisotropic graphite samples is less than the change in the longitudinal linear dimensions of isotropic graphites.

**Analysis of the anisotropic graphite forming under the influence of neutron fluences is more $2 \times 10^{26}$ $n/m^2$.**

Taking into account the clusterization of reactor graphite with increased fluences of neutrons of the form (11) gives an expression for changing the number of pores in a unit volume in the direction perpendicular to the molding direction of reactor graphite depending on the dimensionless irradiation time:

$$n_a^+(\tau) = n_a(0)(1 + X_a) \left( (\exp(-\tau) - 1) \left( 1 - \frac{2d_1 X_a}{1 + X_a} \right) + \frac{\tau X_a + 1}{1 + X_a} + \frac{d_1 X_a}{1 + X_a} \tau(\tau - 2) \right), \tag{23}$$

where $d_1 = \dfrac{\Phi_1}{\Phi_0 C_1'}$ - constant, depending on the property of clustering of reactor graphite.

For determination of the applicability of expression (23), we use the experimental data from work [3]. In Fig.7 shows experimental point on which the analytic dependence (23) is imposed for the values of the parameters $X_a = 4.0$, $d \cdot X_a = 30.2$. The dimensionless parameter $\tau$ is related with the neutron fluence $\Phi$ by the relation $\tau = \tau_0 \cdot 10^{-22} \Phi$, where $\tau_0 = 30.72$.
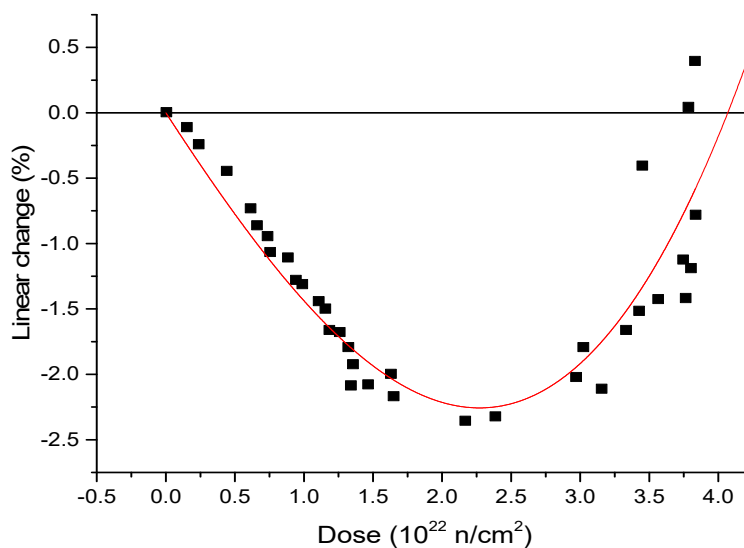
Fig. 7. Changing the linear dimensions of the H451 reactor graphite sample perpendicularly
to the direction of its formation at 600 °C [3].

Comparison of the experimental data and the theoretical dependence shown in Fig.7 show their good qualitative and quantitative correspondence.

Thus, the analytical dependence (23), which takes into account the clusterization of reactor graphites under the influence of elevated levels of neutron fluxes and high temperatures, is applicable to the description of the forming of anisotropic reactor graphites.

## CONCLUSION

The model to describe the forming of the isotropic and anisotropic graphite under high temperatures and high fluence neutron radiation was proposed. The non-isotropy of graphite is characterized by different pore sizes, different values of the diffusion coefficients, the mean free paths of the graphite atoms along and the volume of the sample, which in turn depend on the temperature of the sample. It is suggested that the initial element on the basis of which a new phase will be formed is the spheroidal pore of the small eccentricity flattened along the direction of the greatest stress. A kinetic equation is obtained that describes the diffusion of pores under the influence of high temperatures and intense neutron fluxes. Initially, the pores are in a field oriented along and across the sample, given stresses. Contribution of diffusion processes which driven by terms proportional to pore distribution function in a sample, and the effect of the neutron flux is described by an additional term in the kinetic equation. The resulting kinetic equation for anisotropic graphite can be converted for isotropic graphite. Model solutions are obtained for isotropic and anisotropic graphite, which characterize the change in its volume over time under the influence of the neutron flux and high temperature.

It is shown that the change in the relative volume of reactor graphite for isotropic graphite exceeds the analogous value for anisotropic graphite.

Theoretical confirmation of the regularities of the swelling of anisotropic graphites under the influence of large neutron fluences and in the field of high temperatures obtained by other authors was obtained:

– the longitudinal compression of anisotropic graphite samples corresponds to a change in the linear dimensions of isotropic graphites;

– the transverse compression of anisotropic graphite samples is less than the change in the longitudinal linear dimensions of isotropic graphites.

### ORCID IDs

**Mykola P. Odeychuk** https://orcid.org/0000-0002-6507-2588, **Victor I. Tkachenko** http://orcid.org/0000-0002-1108-5842,
**Leonid A. Bulavin** http://orcid.org/0000-0002-8063-6441, **Boris V. Borts** https://orcid.org/0000-0002-1492-4066,
**Stella I. Skoromnaya** https://orcid.org/0000-0002-9293-5932

## REFERENCES

[1]   M.I. Heggie, I. Suarez-Martinez, C. Davidson and G.H. Buckle, Journal of Nuclear Materials. **413**, 150–155 (2011), https://doi.org/10.1016/j.jnucmat.2011.04.015

[2]   S.V. Panyukov, A.V. Subbotin and M.V. Arzhakov, Journal of Nuclear Materials. **439**, 72–83 (2013), https://doi.org/10.1016/j.jnucmat.2013.03.070

[3]   Tim Burchell, (2012), e-print in: http://citeseerx.ist.psu.edu/viewdoc/download?doi=10.1.1.565.2836&rep=rep1&type=pdf

[4]   Irradiation Damage in Graphite due to Fast Neutrons in Fission and Fusion Systems, IAEA-TECDOC-1154, (IAEA, Vienna, 2000), pp. 184, retrieved from: http://www-pub.iaea.org/MTCD/Publications/PDF/te_1154_prn.pdf

[5]   Gerd Haag, http://juser.fz-juelich.de/record/49235/files/Juel_4183_Haag.pdf

[6]   T.D. Burchell and L.L. Snead, Journal of Nuclear Materials. **371**, 18–27 (2007), https://doi.org/10.1016/j.jnucmat.2007.05.021

[7]   B.J. Marsden, http://www.iaea.org/inis/collection/NCLCollectionStore/ Public/28/008/28008803.pdf

[8]   T.D. Burchell, K.I. Murty and J. Eapen, JOM, **62**, 93-99 (2010), https://doi.org/10.1007/s11837-010-0145-0.

[9]   I.M. Lifshitz and V.V. Slyozov, The kinetics of precipitation from supersaturated solid solutions, J. Phys. Chem. Solids, **19**(1-2), 35 (1961), https://doi.org/10.1016/0022-3697(61)90054-3.

[10]  V.V. Slezov, Journal of colloid and interface science, **255**, 274-292 (2002), https://doi.org/10.1006/jcis.2002.8610.

[11]  B.V. Borts, S.F. Skoromnaya and V.I. Tkachenko, The Journal of Kharkiv National University, physical series "Nuclei, Particles, Fields", **946**, 81-89 (2011), http://nuclear.univer.kharkov.ua/lib/946_1(49)_11_p81-89.pdf. (in Russian).

[12]  W.J. Gray, Carbon, **11**, 383-386 (1973), https://doi.org/10.1016/0008-6223(73)90078-X.

[13]  K. Niwase, Philosophical Magazine Letters, **82**, 401-408 (2002), https://doi.org/10.1080/09500830210137416.

[14]  K. Niwase, Phys. Rev. B, **52**, 15785 (1995), https://doi.org/10.1103/PhysRevB.52.15785.

[15]  K. Niwase, K. Nakamura, T. Shikama and T. Tanabe, Journal of Nuclear Materials, **170**, 106-108 (1990), https://doi.org/ 10.1016/0022-3115(90)90332-H.

[16]  B.A. Gurovich, K.E. Prihod'ko, Problems of atomic science and technology, ser.: Physics of Radiation Effect and Radiation Materials Science, **1**(65)-**2**(66), 156-164 (1997). (in Russian)

[17]  B. Rand, P. Bowen, J.F. Knott and B.J. Marsden, in: GTAC Report R39 (2010).

### МОДЕЛЬ ФОРМОЗМІНИ ІЗОТРОПНОГО І АНІЗОТРОПНОГО ГРАФІТУ ПІД ДІЄЮ ВИСОКИХ ТЕМПЕРАТУР І ФЛЮЕНСІВ НЕЙТРОННОГО ОПРОМІНЕННЯ

**М.П. Одейчук[1], В.І. Ткаченко[1,2], Л.А. Булавін[3], Б.В. Борц[1], С.І. Скоромная[1]**
*[1]Національний науковий центр «Харківський фізико-технічний інститут»*
*вул. Академічна, 1, 61108, Харків, Україна*
*[2]Харківський національний університет імені В.Н. Каразіна*
*майдан Свободи, 4, 61022, Харків, Україна*
*[3]Київський національний університет імені Тараса Шевченка*
*вул. Володимирська, 60, 01033, Київ, Україна*

Запропоновано модель для опису формозміни ізотропного і анізотропного графіту під дією високих температур і високих флюенсів нейтронного опромінювання. Модель заснована на новому підході, який використовує такі положення: опис навколопорової околиці в графіті як твердого розчину із застосуванням теорії фазових перетворень першого роду; розгляд нової фази, як сфероїдальної пори малого ексцентриситету, сплюсненої вздовж напрямку найбільшої напруги; облік кластерізації атомів вуглецю при флюенсах більше $2 \times 10^{26}\ n/m^2$. Неізотропність графіту характеризується різними розмірами пор, відмінними значеннями коефіцієнтів дифузії, довжинами пробігів, атомів графіту уздовж і поперек об'єму зразка, які в свою чергу залежать від температури зразка. Запропоновано, що початковим елементом, на основі якого буде формуватися нова фаза, є сфероїдальна пора малого ексцентриситету, сплюснута вздовж напрямку найбільшої напруги. Отримано кінетичне рівняння, що описує дифузію пір під впливом високих температур і інтенсивних потоків нейтронів. Спочатку пори знаходяться в полі орієнтованих уздовж і поперек зразка заданих напружень. Внесок дифузійних процесів, обумовлений складовою, пропорційною функції розподілу пор у зразку, а дія нейтронного потоку описується додатковою складовою в кінетичному рівнянні. Отримане кінетичне рівняння для анізотропного графіту може бути перетворено для ізотропного графіту. Для ізотропного і анізотропного графіту отримані модельні рішення, які характеризують зміну його об'єму з часом при впливі потоку нейтронів і високої температури. Показано, що величина зміни відносного об'єму реакторного графіту для ізотропного графіту перевищує аналогічну величину для анізотропного графіту. Отримано теоретичне підтвердження закономірності розпухання анізотропних графітів під впливом великих флюенсів нейтронів і в полі високих температур, раніше отримані іншими авторами: поздовжнє стиснення зразків анізотропних графітів відповідає зміні лінійних розмірів ізотропних графітів; поперечне стиснення зразків анізотропних графітів виявляється менше змінення поздовжніх лінійних розмірів ізотропних графітів.
**КЛЮЧОВІ СЛОВА:** Теорія, графіт, формозмінення, нейтрон, флюєнс, висока температура

### МОДЕЛЬ ФОРМОИЗМЕНЕНИЯ ИЗОТРОПНОГО И АНИЗОТРОПНОГО ГРАФИТА ПОД ДЕЙСТВИЕМ ВЫСОКИХ ТЕМПЕРАТУР И ФЛЮЕНСОВ НЕЙТРОННОГО ОБЛУЧЕНИЯ

**М.П. Одейчук[1], В.И. Ткаченко[1,2], Л.А. Булавин[3], Б.В. Борц[1], С.И. Скоромная[1]**
*[1]Национальный научный центр «Харьковский физико-технический институт»*
*ул. Академическая, 1, 61108, Харьков, Украина*
*[2]Харьковский национальный университет имени В.Н. Каразина*
*пл. Свободы, 4, 61022, Харьков, Украина*
*[3]Киевский национальный университет имени Тараса Шевченко*
*ул. Владимирская, 60, 01033, Киев, Украина*

Предложена модель для описания формоизменения изотропного и анизотропного графита под действием высоких температур и высоких флюенсов нейтронного излучения. Модель основана на новом подходе, который использует

следующие положения: описание околопоровой окрестности в графите как твердого раствора с применением теории фазовых превращений первого рода; рассмотрение новой фазы, как сфероидальной поры малого эксцентриситета, сплюснутой вдоль направления наибольшего напряжения; учет кластеризации атомов углерода при флюенсах более $2 \times 10^{26}\, n\,/\,\mathrm{m}^2$. Неизотропность графита характеризуется разными размерами пор, отличными значениями коэффициентов диффузии, длинами пробегов, атомов графита вдоль и попрек объема образца, которые в свою очередь зависят от температуры образца. Предложено, что первоначальным элементом, на основе которого будет формироваться новая фаза, является сфероидальная пора малого эксцентриситета, сплюснутая вдоль направления наибольшего напряжения. Получено кинетическое уравнение, описывающее диффузию пор под воздействием высоких температур и интенсивных потоков нейтронов. Первоначально поры находятся в поле ориентированных вдоль и попрек образца заданных напряжений. Вклад диффузионных процессов обусловлен слагаемым, пропорциональным функции распределения пор в образце, а воздействие нейтронного потока описывается дополнительным слагаемым в кинетическом уравнении. Полученное кинетическое уравнение для анизотропного графита может быть преобразовано для изотропного графита. Для изотропного и анизотропного графита получены модельные решения, которые характеризуют изменение его объема со временем при воздействии потока нейтронов и высокой температуры. Показано, что величина изменения относительного объема реакторного графита для изотропного графита превышает аналогичную величину для анизотропного графита. Получено теоретическое подтверждение закономерности распухания анизотропных графитов под воздействием больших флюенсов нейтронов и в поле высоких температур, ранее полученные другими авторами: продольное сжатие образцов анизотропных графитов соответствует изменению линейных размеров изотропных графитов; поперечное сжатие образцов анизотропных графитов оказывается меньше изменения продольных линейных размеров изотропных графитов.

**КЛЮЧЕВЫЕ СЛОВА:** Теория, графит, формоизменение, нейтрон, флюенс, высокая температура

# THE STABILITY OF A ROTATING AND HEATED FROM BELOW HORIZONTAL CYLINDRICAL LAYER OF A VISCOUS, INCOMPRESSIBLE LIQUID WITH FREE BOUNDARIES

Oksana L. Andreeva[1,2]*, Leonid A. Bulavin[3], Viktor I. Tkachenko[1,2]

*[1]National Science Center Kharkiv Institute of Physics and Technology*
*1, Academichna Str., 61108 Kharkiv, Ukraine*
*[2]V.N. Karazin Kharkiv National University*
*4, Svobody Sq., 61022 Kharkiv, Ukraine*
*[3]Taras Shevchenko National University of Kyiv*
*64/13, Volodymyrska Street, 01601 Kyiv, Ukraine*
*\*E-mail: andreeva@kipt.kharkov.ua*

The stability of a rotating and heated from below horizontal cylindrical layer of a viscous, incompressible liquid with free boundaries was theoretically investigated. Neglecting the centrifugal forces, the equations of motion, thermal conductivity and incompressibility of the liquid were written, from which the well-known dispersion equation was derived in the linear approximation. The stability of a rotating cylindrical volume of a liquid with no heating from below was considered, provided that the temperature difference between the horizontal boundaries of the liquid was fixed and equal to zero. It was demonstrated, that with no heating from below the temperature difference between the horizontal boundaries of the rotating liquid was not fixed and not maintained from the outside, the perturbed liquid temperature would increase, but its final value did not exceed the phase transition temperature. The obtained result was used to explain the heating of water in Ranque – Hilsch vortex tubes. It was concluded that the water heating in Ranque - Hilsch tubes should be considered as the inverse Rayleigh problem, in which the temperature gradient can be determined from the known distribution of velocities inside the volume. The stability of a rotating cylindrical volume of a liquid when heated from below was analyzed. It was demonstrated, that the value of the specified temperature difference at cylinder boundaries, as well as the initial rate of its variation, determine the final heating temperature of the liquid. A comparison of the proposed theory and experimental data for water heating shows their good qualitative and quantitative agreement.
**KEY WORDS:** theory, stability, viscous, incompressible, liquid, horizontal cylindrical layer, rotating, heated, free boundaries

It is known that a periodic structure in the form of Benard cells [1] is formed in a horizontal layer of a viscous, incompressible, below-heated liquid. Rayleigh described in [2] the physical nature of the convection onset in such layers. He obtained analytical expressions for perturbed velocity and temperature in the Cartesian coordinate system. On the basis of this theory, it was possible to explain the threshold nature of the convective instability development, when the convection occurs only at a certain temperature difference. The obtained solutions describe the occurrence of convective rolls in a horizontal liquid layer, on the vertical common boundaries of which the velocity was directed periodically up / down and vice versa. However, these solutions did not describe the experimental fact of the availability of polygonal structures, the number of angles of which varied from four to seven, but with a predominance of six [1]. Therefore, to explain the appearance of hexagonal convective cells, geometric transformations of the found solutions were used. The description of cells with a different number of angles also means involving geometric manipulations. And if we continue the work and try to describe the entire set of polygonal convective cells, then this task turns out to be practically impossible.

In contrast to the method of geometric transformations described above, the energy principle of the formation of Benard cells was proposed in the work [3]. The principle is based on the fact that cells in the nucleation phase are few in number and have a cylindrical form [3]. As the temperature of the lower boundary of the layer increases, their number increases. Ideally, all cells are tightly packed in a liquid layer, and create a polygonal (hexagonal or other) structure, i.e. Benard cells.

As we see, initially the main element of Benard cells is an elementary cylindrical convective cell, whose perturbed parameters under free boundary conditions are described in the work [3]. At a uniform rotation of the liquid in the cell relative to the vertical axis, new possibilities of controlling the thermal convection described in [1 - 3] emerge. The control parameters under the new conditions will be Coriolis and centrifugal forces [4, 5].

In this work the onset of convection in a uniformly rotating and below-heated cylindrical tank with a viscous, incompressible liquid with free boundaries was investigated.

## THE INITIAL EQUATIONS OF CONVECTION IN A ROTATING VISCOUS, INCOMPRESSIBLE LIQUID OF A CYLINDRICAL FORM WITH FREE BOUNDARIES

Let us consider a cylindrical volume of radius $R_0$ filled with a viscous, incompressible liquid, the lower and upper boundaries of which coincide with the planes $z = 0$ and $z = h$. The liquid rotates uniformly as a whole with an angular velocity $\vec{\Omega} = \Omega \cdot \vec{e}_z$, where $\vec{e}_z$ - the unit vector directed along the vertical, which coincides in direction with the

axis $z$ and is in the gravitational field, the direction of acceleration of which is $\vec{g} = -g \cdot \vec{e}_z$ opposite to the direction of the axis $z$. In Fig. 1 vector $\vec{g}$ - gravitational acceleration, $\vec{r}$ - radial coordinate.

The temperature distribution inside the cylinder $T_0(z)$ is set so, that the temperature of the lower boundary is higher than the temperature of the upper one: $T_0(0) = T_{0,2}$, $T_0(h) = T_{0,1}$, $(T_{0,2} > T_{0,1})$. We suppose, that in equilibrium the temperature distribution is described by a linear function in the coordinate $z$:

$$\vec{\nabla} T_0(z) = -\frac{\Theta}{h} \vec{e}_z$$

were, $\Theta = T_{0,2} - T_{0,1}$ - the temperature difference between lower and upper plains.
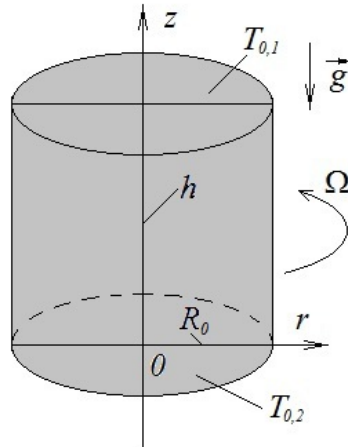


Fig. 1. Schematic representation of a cylindrical volume with a viscous incompressible
liquid rotating at an angular velocity $\Omega$ in a gravitational field $\vec{g}$.

Let us write the equations describing convection in a cylindrical volume heated from below and rotating as a whole. These equations consist of the Navier – Stokes equation, with regard to inertial forces in a rotating coordinate system – Coriolis and centrifugal [4], the heat conduction equation and the continuity equation:

$$\frac{\partial \vec{v}}{\partial t} + \left( \vec{v} \vec{\nabla} \right) \vec{v} = -\frac{1}{\rho} \vec{\nabla} p + \nu \Delta \vec{v} + \vec{g} - 2\vec{\Omega} \times \vec{v} - \vec{\Omega} \times \left( \vec{\Omega} \times \vec{r} \right), \tag{1}$$

$$\frac{\partial T}{\partial t} + \left( \vec{v} \vec{\nabla} \right) T = \Delta T, \tag{2}$$

$$\mathrm{div}\left( \vec{v} \right) = 0, \tag{3}$$

where $\vec{v}$ - small perturbations of the liquid velocity in a rotating coordinate system, $\vec{r}$ - radius-vector of the liquid element, $\rho$, $p$, $T$ density, pressure and temperature of the liquid, $\vec{\nabla}$ - gradient operator, $\Delta$ - Laplace operator.

From system (1-3) it is possible to obtain equations that describe the spatial-temporal dynamics of small perturbations of pressure $\tilde{p}$ and temperature $\tilde{T}$ with respect to their equilibrium values $p_0(r, z)$ and $T_0(z) = T_{0,2} - \frac{\Theta}{h} z$:

$$p = p_0 + \tilde{p}, \; T = T_0(z) + \tilde{T}. \tag{4}$$

Small values of pressure and temperature perturbations meet the requirement: $\left| \tilde{f} \right| << \left| f_0 \right|$.

When analyzing the Navier – Stokes equation we assume that Boussinesq's assumptions regarding the being determind influence of the temperature compressibility of a liquid are met, i.e. we assume $\rho = \rho_0 \left( 1 - \beta \tilde{T} \right)$ [4], where $\beta$ - the coefficient of a liquid temperature compressibility.

We assume, that the velocity perturbations are small, which allows us to neglect the quadratic in velocity summands in (1). Taking into account the assumptions made, and after substitution (4) into equation (1) we have:

$$\left( 1 - \beta \tilde{T} \right) \frac{\partial \vec{v}}{\partial t} = -\frac{1}{\rho_0} \vec{\nabla} \left( p_0 + \tilde{p} \right) + \nu \Delta \vec{v} - \left( 1 - \beta \tilde{T} \right) g \vec{e}_z - 2\vec{\Omega} \times \vec{v} - \left( 1 - \beta \tilde{T} \right) \vec{\Omega} \times \left( \vec{\Omega} \times \vec{r} \right). \tag{5}$$

We suppose the diameter of the cylindrical tank is small: $D << g\Omega^{-2}$. This condition allows neglecting the centrifugal convective force, as a result of which the last summand in (5) can be neglected [4].

Let us eliminate the unperturbed summands in the equation (5), setting:

$$\vec{\nabla}p_0 = -\rho_0 g \vec{e}_z. \tag{6}$$

The remaining summands give the force balance equation for perturbed values:

$$\frac{\partial \vec{v}}{\partial t} = -\frac{1}{\rho_0}\vec{\nabla}\tilde{p} + \nu\Delta\vec{v} + \beta\tilde{T}g\vec{e}_z - 2\vec{\Omega}\times\vec{v}. \tag{7}$$

In units of layer thickness $h$, time $\tau = h^2\nu^{-1}$ and temperature $\Theta$ the equation (7) is converted to a dimensionless form:

$$\frac{\partial\vec{v}'}{\partial t'} = -\vec{\nabla}\tilde{p}' + \Delta\vec{v}' + R\tilde{T}'\vec{e}_z - E^{-1}\vec{e}_z\times\vec{v}', \tag{8}$$

where the "prime mark" denotes the corresponding dimensionless value, $R = g\beta h^3\Theta/(\nu\chi)$ - the Rayleigh number, $\nu$ and $\chi$ - the coefficients of liquid kinematic viscosity and thermometric conductivity, correspondingly, $E = \nu/(2\Omega h^2)$ - the Ekman number, which is very small in most experiments with rotating liquid [6].

In further calculations to simplify writing process the "prime mark" notation is omitted.

Equation (8) should be supplemented by the equation of heat conduction (2), which, taking into account the linear dependence of temperature on height, takes the dimensionless form:

$$P\frac{\partial\tilde{T}}{\partial t} - \vec{v}\vec{e}_z = \Delta\tilde{T}, \tag{9}$$

where $P = \nu/\chi$ - the Prandtl number.

The continuity equation (3) in dimensionless variables has the same form. For a rotating viscous, incompressible liquid of a cylindrical form we will assume that the boundary conditions are free [2, 4, 5]. These conditions mean that vertical projections of the velocity perturbations are equal to zero at the boundaries of the liquid:

$$\left.v_z\right|_{\substack{z=0,\\z=1}} = 0, \tag{10}$$

and tangential stresses:

$$\sigma_{rz} = \rho_0\nu\left(\frac{\partial v_r}{\partial z} + \frac{\partial v_z}{\partial r}\right)\Bigg|_{\substack{z=0,\\z=1}} = 0. \tag{11}$$

The boundary conditions (11) taking into account the continuity equation (3) can be transformed to the form:

$$\frac{\partial^2 v_z}{\partial z^2}\Bigg|_{\substack{z=0,\\z=1}} = 0. \tag{12}$$

We assume that the temperature at horizontal boundaries of the cylinder is fixed. It follows that the temperature perturbations at the boundaries $z=0, z=1$ are equal to zero:

$$\left.\tilde{T}\right|_{\substack{z=0,\\z=1}} = 0. \tag{13}$$

To the boundary conditions (10), (12), (13), we should add the condition for the perturbed velocity at the external boundary: $v_r(r,z,t) = v_\varphi(r,z,t) = 0$ at $r = R_0$.

As an initial condition we assume, that at the time point $t = 0$ all the perturbations are either missing:

$$\left.\vec{v},\tilde{T},\tilde{p}\right|_{t=0} = 0 \tag{14}$$

or specified as:

$$\left.\vec{v},\tilde{T},\tilde{p}\right|_{t=0} = \vec{v}(\vec{r},0),\tilde{T}(\vec{r},0),\tilde{p}(\vec{r},0). \tag{15}$$

Thus, the problem of studying the stability of a rotating, heated from below, viscous, incompressible liquid of a cylindrical form with free boundaries is reduced to solving the eigen value problem for the system of equations (3), (8), (9) with boundary conditions (10), (12), (13) [4] and with initial conditions (14), (15).

## SOLUTIONS OF THE ORIGINAL SYSTEM OF EQUATIONS

We write equations (3), (8), (9) in a cylindrical coordinate system $r, \varphi, z$. We assume the perturbations are axisymmetric, i.e. such that the perturbations do not depend on the angular coordinate $\varphi$. This means that all the perturbed values meet the condition $\partial .../\partial \varphi = 0$. Rotation of the cylindrical volume of a liquid is a flow with an equilibrium azimuthal velocity $V_\varphi(r) = \Omega \cdot r$ [7, 8], which is obtained from the Couette flow, if we set the radius and angular velocity of rotation of the inner cylinder to zero. Based on this we write the projections of the velocity vector in the cylinder: $\vec{v} = \left( v_r, V_\varphi(r) + v_\varphi, v_z \right)$.

The equations for the perturbed velocity projections follow from (8):

$$\frac{\partial v_r}{\partial t} = -\frac{\partial}{\partial r} \tilde{p} + \Delta v_r - \frac{v_r}{r^2} + E^{-1} v_\varphi, \tag{16}$$

$$\frac{\partial v_\varphi}{\partial t} = \Delta v_\varphi - \frac{v_\varphi}{r^2} - E^{-1} v_r, \tag{17}$$

$$\frac{\partial v_z}{\partial t} = -\frac{\partial}{\partial z} \tilde{p} + \Delta v_z + R\tilde{T}, \tag{18}$$

where $\Delta = \frac{1}{r} \frac{\partial}{\partial r} \left( r \frac{\partial}{\partial r} \right) + \frac{\partial^2}{\partial z^2}$.

In cylindrical coordinates the continuity equation (3) is converted to the form:

$$\frac{1}{r} \frac{\partial}{\partial r} (r v_r) + \frac{\partial}{\partial z} v_z = 0 \tag{19}$$

Equations (16) (19) should be supplemented by the equation of heat balance (9).
We will seek solutions of the original task in the form:

$$v_r(r, z, t) = -A \cdot \exp(-\lambda t) \cdot n\pi k_r^{-1} \cos(n\pi z) J_1(k_r r), \qquad \text{a)}$$

$$v_\varphi(r, z, t) = D \cdot \exp(-\lambda t) \cdot \cos(n\pi z) J_1(k_r r), \qquad \text{b)}$$

$$v_z(r, z, t) = A \cdot \exp(-\lambda t) \cdot \sin(n\pi z) J_0(k_r r), \qquad \text{c)} \quad (20)$$

$$\tilde{p}(r, z, t) = C \cdot \exp(-\lambda t) \cdot \cos(n\pi z) J_0(k_r r). \qquad \text{d)}$$

$$\tilde{T}(r, z, t) = B \cdot \exp(-\lambda t) \cdot \sin(n\pi z) J_0(k_r r) = B(t) \cdot \sin(n\pi z) J_0(k_r r), \qquad \text{e)}$$

where $\lambda$ - eigen values characterizing attenuation ($\lambda > 0$), increase ($\lambda < 0$) or stationary state ($\lambda = 0$) of perturbations (18); $A, B, C, D = \dfrac{An\pi}{k_r E \left( k_r^2 + (n\pi)^2 - \lambda \right)}$ - perturbation amplitudes; $J_0(x), J_1(x)$ - Bessel functions of the first kind of zero and first order of the argument $x$ respectively; $k_r$ - radial wave number characterizing the dependence of the perturbations on the transverse coordinate $r$, $n = 1, 2, 3...$ - the mode number.

It is easy to see, that the boundary conditions on the external boundary are automatically satisfied, if we set $k_r = \sigma_{1,i}/R_0$, where $\sigma_{1,i}$ - $i$ - th zero of Bessel functions of the first kind of the first order ($J_1(\sigma_{1,i}) = 0$), $i = 1, 2, 3, .....$.

From (20) a), c), and e) it follows that the spatial distribution of perturbations of horizontal and vertical velocities and temperature are similar to those implemented for a layer of heated from below, viscous, incompressible liquid without rotation in a cylindrical coordinate system [3].

## THE STABILITY ANALYSIS OF A ROTATING, VISCOUS, INCOMPRESSIBLE, HEATED FROM BELOW LIQUID OF A CYLINDRICAL FORM

Substitution of solutions (20) into equations (9), (16) (18) gives a cubic characteristic equation for determining eigen values $\lambda$:

$$\lambda^3 + a\lambda^2 + b\lambda + c = 0, \tag{21}$$

where, $a = -k_\perp^2 \dfrac{(2P+1)}{P}, b = k_\perp^4 \dfrac{(P+2)}{P} + \dfrac{P(n\pi)^2 Te - k_r^2 R}{k_\perp^2 P}, c = \dfrac{k_r^2 R - k_\perp^6 - (n\pi)^2 Te}{P}, \quad k_\perp^2 = k_r^2 + (n\pi)^2,$

$Te = E^{-2} = 4\Omega^2 h^4 / \nu^2$ - Taylor number.

Let us consider the solutions of the characteristic equation (21), which describe a stable rotation of a viscous, incompressible and heated from below liquid of a cylindrical form.

We determine the condition of a monotone instability of a rotating, viscous, incompressible and below-heated liquid of a cylindrical form from (21), similarly to [5].

$$k_r^2 R_c = \left( (k_\perp^2)^3 + (n\pi)^2 Te \right), \tag{22}$$

where $R_c$ - critical Rayleigh number of monotone instability.

It should be noted, that the expression (22) goes into the expression obtained in the Cartesian coordinate system by Rayleigh, if we replace $k_r^2$ by $k^2 = k_x^2 + k_y^2$ [4, 5].

The condition of monotone instability (22) in graphic form is shown in Fig. 2. Here the dependence of the lines of the logarithm levels of the critical Rayleigh number $ln(R_c)$ upon the wave number $k_r$ and the Taylor number $Te$ is presented.

The level lines show, that the wave number $k_{r,m}$ (the abscissa of the maximum of the level line) corresponding to the minimum critical Rayleigh number increases with increasing Taylor number, starting from the value of $k_{r,m} = \pi/\sqrt{2} \approx 2.221$ [5]. In this case, the critical Rayleigh number increases also from value $R_c^* = 27(n\pi)^4/4 \approx 657.11$ that corresponds to the case of no rotation, i.e. $\Omega = 0$.
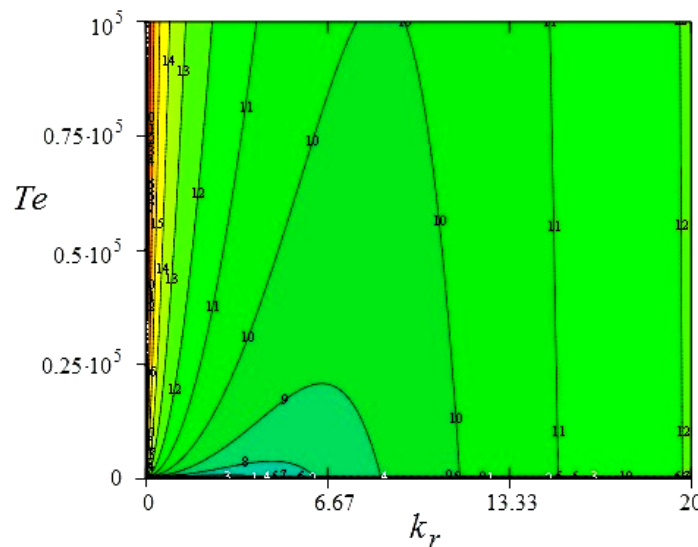


Fig. 2. Lines of the logarithm level of the critical Rayleigh number
$ln(R_c)$ versus the wave number $k_r$ and the Taylor number $Te$.

Let us define the conditions for the equation fulfillment (22).

We rewrite the equation (22) relatively the unknown $k_\perp^2$, and get an incomplete cubic equation:

$$(k_\perp^2)^3 + pk_\perp^2 + q = 0, \tag{23}$$

where $p = -R_c; q = (n\pi)^2 (Te + R_c)$.

Since $k_\perp^2 = k_r^2 + (n\pi)^2 > 0$, then we will look only for real positive solutions of the equation (23).

It is known that the type of solutions (23) depends on the sign of the discriminant $Q$:

$$Q = \left( \frac{p}{3} \right)^3 + \left( \frac{q}{2} \right)^2 = \left( \frac{(n\pi)^2 R_c^*}{2} \right)^2 \left[ \frac{Te}{R_c^*} + \frac{R_c}{R_c^*} \left( \sqrt{\frac{R_c}{R_c^*}} + 1 \right) \right] \left[ \frac{Te}{R_c^*} - \frac{R_c}{R_c^*} \left( \sqrt{\frac{R_c}{R_c^*}} - 1 \right) \right]. \tag{24}$$

The discriminant $Q$ is positive for $Te/R_c^* > R_c/R_c^* \left( \sqrt{R_c/R_c^*} - 1 \right) > 0$. The equation (23) in this case has one negative real and two complex conjugate roots. Therefore, by the requirement of $k_\perp^2 > 0$ the solutions (23) are not considered for the case $Q > 0$.

The discriminant $Q$ is equal to zero for $Te/R_c^* = R_c/R_c^* \left( \sqrt{R_c/R_c^*} - 1 \right)$. The equation (23) has one negative and two coincident positive roots. The negative root is equal to $\left( k_\perp^2 \right)_1 = -2 \sqrt[3]{\left( (n\pi)^2 (Te + R_c) \right)/2}$ and positive roots -

$\left( k_\perp^2 \right)_{2,3} = -\frac{1}{2}\sqrt[3]{-\frac{q}{2}+\sqrt{Q}} - \frac{1}{2}\sqrt[3]{-\frac{q}{2}-\sqrt{Q}} = \sqrt[3]{q/2} = \sqrt[3]{\left( (n\pi)^2 (Te + R_c) \right)/2}$. Therefore, $k_\perp^2$ can only take the value $k_\perp^2 = \sqrt[3]{\left( (n\pi)^2 (Te + R_c) \right)/2}$.

The discriminant $Q$ is negative for Taylor numbers $0 < Te/R_c^* < R_c/R_c^* \left( \sqrt{R_c/R_c^*} - 1 \right)$. This condition is true for Rayleigh numbers $R_c/R_c^* > 1$. Within these ranges of variation of the Rayleigh and Taylor numbers the equation (23) has three different real roots. From them, by virtue of the requirement, we select positive root within the whole range of variation $Te$ and $R_c$:

$$\left( k_\perp^2 \right)_3 = -\left( \frac{(n\pi)^2 R_c^*}{2} \right)^{\frac{1}{3}} \left[ \sqrt[3]{i\sqrt{\left[ X^3 - (Y+X)^2 \right]} - (Y+X)} \right] \frac{1 + i\sqrt{3}}{2} + c.c., \tag{25}$$

where $Y = Te/R_c^*$, $X = R_c/R_c^*$, c.c. - denotes a complex conjugate value.

The lines of the logarithm level of the radial wave number $ln(k_r)$ versus the Rayleigh number ($1 \le R_c/R_c^* \le 10$) and the Taylor number ($0 \le Te \le 100$) for the case $n = 1$ are presented in Fig. 3.
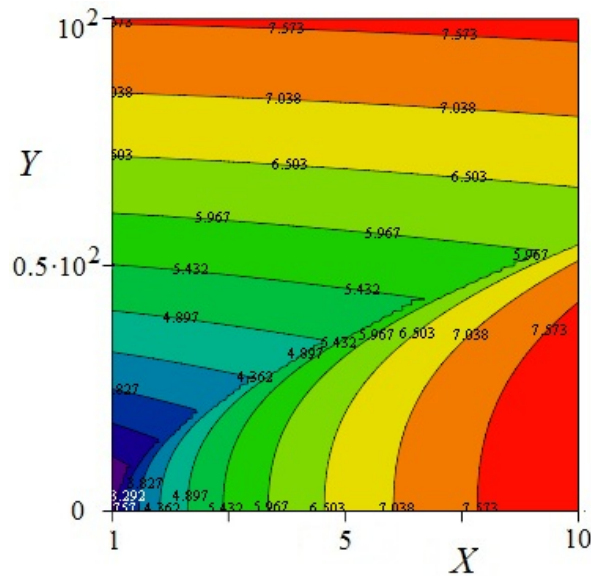


Fig. 3. Lines of the logarithm level of the radial wave number $ln(k_r)$ versus
the Rayleigh number $X = R_c/R_c^*$ and the Taylor number $Y = Te/R_c^*$

According to the level lines for the radial wave number, $(k_r)_{min}$ differs in exponent from that given in [5] by a factor of two

Thus, from the Fig. 3 it is seen that the minimum radial wave number (the inflection points of level lines) increases nonlinearly with increasing the Taylor number and the Rayleigh number.

At large Taylor numbers $Y \gg 1$ the minimum critical Rayleigh number varies according to the law $(R_c)_{min} \sim \left( R_c^* \right)^{1/3} Te^{2/3} = \left( 27\pi^4/4 \right)^{1/3} Te^{2/3} = 3\left( \pi^2/2 \right)^{2/3} Te^{2/3}$ [5, 9] and the corresponding radial wave number - $(k_r)_{min} \sim \left( \pi^2/2 \right)^{1/3} Te^{1/3}$ (Fig. 2).

It should be noted that the expression of monotone instability (22) is observed for the values of radial wave numbers:

$$k_\perp^2 = \sqrt[3]{\left((n\pi)^2 (Te + R_c)\right)/2} \, , \quad k_\perp^2 = -\left(\frac{(n\pi)^2 R_c^*}{2}\right)^{\frac{1}{3}} \sqrt[3]{i\sqrt{\left[X^3 - (Y+X)^2\right]} - (Y+X)} \, \frac{1+i\sqrt{3}}{2} + \text{c.c.} \tag{26}$$

To analyze the stability of perturbations of the boundary-value problem we turn to expressions (21), (22).

Further, when describing the stability of perturbations in a medium, we will consider only the perturbed temperature, noting that the transition to other perturbed quantities is carried out in accordance with expressions (20), a) - e).

The fulfillment of the monotone instability condition (22) gives the following eigen values of the problem:

$$\lambda_1^c = 0, \quad \lambda_{2,3}^c = k_\perp^2 \frac{(2P+1)}{2P} \pm \sqrt{k_\perp^4 \frac{(1-4P)}{4P^2} - \frac{P(n\pi)^2 Te - k_r^2 R_c}{k_\perp^2 P}}. \tag{27}$$

The perturbed temperature (20), e) depends on time as a general solution of the characteristic equation (21), consisting of the sum of partial perturbations:

$$B(t) = \sum_{m=1}^{3} C_m' \exp(-\lambda_m t), \tag{28}$$

where $C_m'$ - arbitrary constants determined by initial conditions, $m = 1;2;3$ .

For the case of the development of monotonous instability, the eigen value $\lambda_1 = \lambda_1^c$ equal to zero corresponds to the time-invariant amplitude of the partial perturbation and the eigen values $\lambda_{2,3} = \lambda_{2,3}^c$ describe the temporal dynamics of the partial perturbations depended on the radicand value.

Below, we consider the solution (21) for the case with lack of external temperature effect (the lower boundary of the layer is not heated), as well as for the case when this temperature effect occurs.

### THE STABILITY ANALYSIS OF A ROTATING LIQUID CYLINDRICAL VOLUME WITHOUT HEATING FROM BELOW

Let us determine the characteristic numbers of the equation (21) without heating the liquid from below. Despite the fact that there is no heating of the liquid, the Rayleigh number is not equal to zero, but it is determined by the temperature difference between the lower $T_{2,fl}$ and upper $T_{1,fl}$ boundaries at the fluctuation level: $\Theta_{fl} = T_{2,fl} - T_{1,fl}$ .

The temperature fluctuation value of the upper boundary of the liquid cylindrical volume with radius $R_V$ and thickness of several molecular layers $h_V$ is determined by a number of water molecules in it and the average temperature of the medium $T^*$ [10]: $T_{1,fl} \sim N^{-\frac{1}{2}} T^*$, where $N$ is the number of particles in the volume $V \sim \pi R_V^2 h_V$ . For water the fluctuation level of temperatures is sufficiently small and is of the order of $\Theta_{fl} \approx 10^{-8} \div 10^{-7}$ C.

Therefore, if the liquid is not heated from below, we assume that the Rayleigh number is equal to $R = R_{fl}$ , where $R_{fl} = g\beta h^3 \Theta_{fl}/(\nu\chi)$ - the Rayleigh number for the fluctuation temperature difference between the lower and upper boundaries of the tank. Here it should also be noted that the temperature unit in (8) is no longer $\Theta$ as well $\Theta_{fl}$ . However, this value is clearly not included in the characteristic equation (21), and thus does not affect its solutions.

At the above fluctuation level of temperature difference, the Taylor number is a fairly large value: $Te \gg R_{fl}, k_\perp^2 \gg 1$

In this case, the discriminant of the equation (21) takes the value $Q_0 \approx \left(\pi^2 Te/3k_\perp^2\right)^3 + \left(\pi^2 Te(P-1)/3P\right)^2 > 0$ , that

corresponds to one real root and two complex conjugate roots $\lambda_{2,3} = k_\perp^2 \pm i\left(\frac{\pi^2 Te}{k_\perp^2}\right)^{\frac{1}{2}}$

Substituting the roots of the characteristic equation in (28) and assuming $C_2'' = -(C_2' + C_3')$, $C_3'' = i(C_3' - C_2')$ we get:

$$B(t) = C_1' \exp\left(-\frac{\alpha_1}{P} t\right) - \left(C_2'' \cos(\alpha_2 t) - C_3'' \sin(\alpha_2 t)\right) \exp(-\alpha_1 t) \tag{29}$$

where $\alpha_1 = k_\perp^2$, $\alpha_2 = \left(\pi^2 Te/k_\perp^2\right)^{\frac{1}{2}}, \alpha_2 \gg \alpha_1$ .

If we set in (29), for example, $C_2'' = C_1'$ and, $C_3'' = 0$ then the amplitude $B(t)$ will have the form:

$$B(t) = C_1' \exp\left(-\frac{\alpha_1}{P}t\right)\left(1 - \exp\left(-\left(\frac{P-1}{P}\right)\alpha_1 t\right)\cos(\alpha_2 t)\right). \tag{30}$$

Further everywhere, without loss of generality, we can set $C_1' = 1$ in (30).

### The temperature difference between the horizontal boundaries of the liquid is fixed and equal to zero

As noted above, in case with no heating from below the temperature difference between the horizontal boundaries of the liquid is not equal to zero, but it is determined by the fluctuation level $\Theta_{fl} = T_{2,fl} - T_{1,fl}$.

From (30) it follows, that the amplitude of the perturbed temperature as a result of action of viscous forces increases from zero at $t = 0$ to a maximum value at $t = t_{max}$. After reaching a maximum it decreases to zero, oscillating with exponentially decreasing amplitude of oscillations. The law of decreasing the average amplitude value $B(t)$ is determined by the expression (30) averaged over the period of fast oscillations.

The temperature variation rate of the liquid (30) at the initial time (zero time) is equal to $\left.\dfrac{dB_T}{dt}\right|_{t=0} = \Theta_{fl} \cdot \left(\dfrac{P-1}{P}\right)\alpha_1$,

where $B_T$ - the liquid temperature in °C.

The temperature dependence upon the time for different values $\alpha_2$ is presented in Fig. 4.
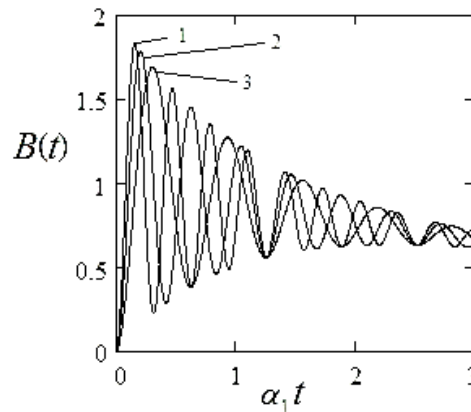


Fig. 4. Temperature $B(t)$ versus time without water heating from below

for different values $\alpha_2$ : 1 - $\alpha_2 = 10 \cdot \alpha_1$ ; 2 - $\alpha_2 = 15 \cdot \alpha_1$ ; 3 - $\alpha_2 = 20 \cdot \alpha_1$ .

From Fig. 4 it follows that with increasing $\alpha_2$ and, consequently, the Taylor number, the amplitude of the first temperature maximum increases and the time of the maximum reaching decreases.

Thus, in rotating liquid cylindrical volume with free horizontal boundaries at a temperature difference between the lower and upper boundaries at the fluctuation level, increasing the perturbed temperature from zero is observed. Then it reaches a maximum $B(t) \approx 1.5,...,2.0 = \kappa$, and after it again decreases to zero with exponentially decreasing amplitude of oscillations. In the final state at large times the water will rotate as a whole without perturbation of velocity, pressure and temperature.

However, it should be noted, that the value of the first maximum of the liquid temperature exceeds the fluctuation level by a factor of $\kappa \approx 1.5,...,2.0$. This indicates that the liquid is being heated within the time interval $0 \le t \le t_{max}$.

### The temperature difference between the horizontal boundaries of the liquid is not fixed and not supported from the outside

If the temperature difference between the horizontal boundaries of the liquid cylindrical volume $\Theta$ is specified at the fluctuation level and is not supported from the outside, then the system can be considered as isolated. In such a system according to (30) the temperature $B(t)$ will increase from zero to the maximum value $\kappa$ within the time interval $0 \le t \le t_{max}$ (refer to Fig. 4)

According to (30) a point in time $t = t_{max}$, when the temperature should decrease with time increasing, comes in the system. However, this cannot be realized, since the entropy of an isolated system $S_{fl}(t)$ is a non-decreasing function of time [11], i.e. the condition $dS_{fl}/dt \ge 0$ should be met.

Based on the principle of entropy increasing we will describe the dynamics of temperature variation in the system within the time interval $t > t_{max}$.

The law of variation of the system entropy can be written using (30) in the form:

$$\frac{dS_{fl}}{dt} = \frac{\Theta_{fl}}{\kappa T_{2,fl} T_{1,fl}}\left(\kappa - \exp\left(-\frac{\alpha_1}{P}t\right)\left(1 - \exp\left(-\left(\frac{P-1}{P}\right)\alpha_1 t\right)\cos(\alpha_2 t)\right)\right)\frac{dS_{1,fl}}{dt} > 0 \tag{31}$$

where, $S_{fl} = S_{2,fl} + S_{1,fl} = const$ - the sum of entropies of microvolumes on the lower and upper boundaries of the liquid, $dS_{1,fl}/dt > 0$ - the entropy of the upper boundary increased with time.

From (31) it follows that the entropy increases for the time interval $0 \le t < t_{max}$. At times $t > t_{max}$ the inequation (31) is violated, i.e. the entropy decreases. Therefore, the system has one way out: at the point of time $t = t_{max}$ it passes from the first stage of instability to the second. At this stage of instability the cylindrical volume of a liquid is described by the original system of equations (9), (16) - (19), but with the temperature difference at the boundaries of the volume increased by a factor $\kappa$ compared with the first stage: $\Theta_{fl} \to \kappa\Theta_{fl}$. Increasing the temperature difference at the liquid boundaries by a factor $\kappa$ leads to the same increase of the Rayleigh number: $R_{fl} \to \kappa R_{fl}$.

The overall increase of the liquid temperature at the second stage will be equal to $(1+\kappa)$. Increasing the Rayleigh number does not violate the applicability of the characteristic equation (21) and the expression (30), since the condition $Te >> \kappa R_{fl}$ is still met.

At the third stage, the process of increasing the temperature will repeat, and the maximum temperature will now be equal to $\kappa^2$. The overall increase of the temperature will be equal to $(1+\kappa+\kappa^2)$.

With multiple repeating of temperature rise stages, the liquid temperature will increase in increasing geometric progression to the value $\sum_{i=1}^{n}\kappa^{i-1}$, where $n >> 1$ - the number of stages of the temperature rise.

However, with a certain number of rise stages $n = N >> 1$, the Rayleigh number $R = R_{fl}\sum_{i=1}^{N}\kappa^{i-1}$ may increase to a value $R = R_c$. In this case the characteristic equation (21) will have another eigen values and, consequently, another expression for the temperature $B(t)$ [1]. At that, the liquid temperature will increase, but its final value should not exceed the temperature of the phase transition. Otherwise, the original system of equations is not applicable.

As an example of heating a uniformly rotating cylindrical volume of a viscous, incompressible liquid can be used the heating of water in the Ranque – Hilsch vortex tubes [12, 13].

For a pure water with an initial fluctuation level of the temperature difference $\Theta_{fl} \approx 10^{-7}$ °C [10] and $\kappa \approx 1.8$, heating to a temperature difference of the order of (8-9)·$10^{-2}$°C (temperature difference at which the Rayleigh number increases to a value $R = R_c$) corresponds to the number of temperature rise stages $n \approx 23$.

Further increase of the difference in the water temperature from (8-9)·$10^{-2}$ C to a given temperature is a continuation of the previous multistage rise and will be described in the next Section (Stationary temperature perturbations at large Rayleigh numbers ($R = R_c$)).

As follows from the above analysis, heating of the rotating volume of water in Ranque – Hilsch tubes is due to the action of viscous forces. The spatial distribution of the vertical and horizontal velocity of water coincides with a similar distribution in the Rayleigh problem on convection in a layer of a viscous, incompressible liquid heated from below. Therefore, the problem of occurrence of a temperature gradient in a rotating volume of water, as well as the problem of heating water in Ranque -Hilsch tubes should be considered as the inverse Rayleigh problem.

Rayleigh's inverse problem involves searching the temperature difference between the boundaries of a viscous, incompressible liquid of a cylindrical form according to a given distribution of its vertical and horizontal velocities.

### Analysis of the stability of a rotating cylindrical volume of liquid when heated from below

The expression for the perturbed temperature (30) will change if the rotating cylindrical volume of the liquid is heated from below with a certain rate. To show this, let us set a dependence of the perturbed temperature amplitude upon the time at heating in the form:

$$B_h(t) = B(t)\alpha_T \exp(\lambda_T t) \tag{32}$$

---

[1] The solution of the characteristic equation (21) and the expression for the perturbed temperature for large Rayleigh numbers are given in Section 5.

where $\alpha_T, \lambda_T$ - constants determining the parameters of water heating.

Such a representation is similar to introduction to the characteristic equation (22) a number with a shift $\lambda - \lambda_T$ instead of an eigen value $\lambda$, where the shift value $\lambda_T$ is selected so that to reduce the free term $c$ to zero.

From (32) it follows, that there is no heating for the parameter values $\alpha_T = 1$ and $\lambda_T = 0$.

If we set $\lambda_T = \alpha_1/P$, we will get the expression for the temperature of the rotating liquid with heating:

$$B_h(t) = C_1'' \left[ 1 - \exp\left( -\left( \frac{P-1}{P} \right) \alpha_1 t \right) \cos(\alpha_2 t) \right], \tag{33}$$

where $B_h(t) = B_{T,h}/\Theta_{ex}$ is measured in units $\Theta_{ex} = T_{2,ex} - T_{1,ex}$, $B_{T,h}$ - liquid temperature - in °C, $T_{2,ex}, T_{1,ex}$ - temperatures of the lower and upper boundaries of the liquid layer, respectively.

We will assume $C_1'' = 1$ in (33), as before.

The dependence of the perturbed temperature amplitude upon the time (33) for different values $\alpha_2$ is presented in Fig.4.
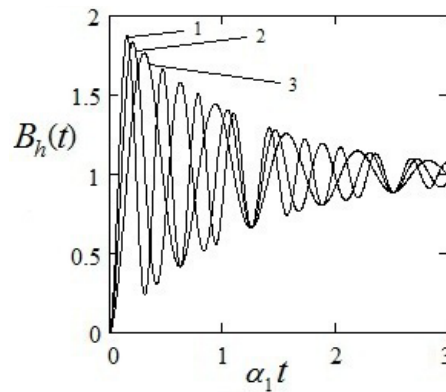


Fig. 5. Temperature $B_h(t)$ versus time at heating from below for different values $\alpha_2$: 1 - $\alpha_2 = 10 \cdot \alpha_1$; 2 - $\alpha_2 = 15 \cdot \alpha_1$; 3 - $\alpha_2 = 20 \cdot \alpha_1$.

From Fig. 5 it follows, that the liquid temperature increases from zero with time at $t = 0$, reaches the first maximum $B_h(t) \approx \kappa$ and oscillating with an exponentially decreasing amplitude tends to unity.

From this we can conclude, that in experiments with heating a rotating cylindrical volume of liquid, the value $\Theta_{ex}$ determines the final temperature of the liquid heating, as well as the initial rate of temperature variation, i.e. $\left. \frac{dB_{T,h}}{dt} \right|_{t=0} = \Theta_{ex} \cdot \left( \frac{P-1}{P} \right) \alpha_1$. It follows that the rate of variation in the temperature of a heated liquid is greater than that of a non-heated one.

### STATIONARY TEMPERATURE PERTURBATIONS AT LARGE RAYLEIGH NUMBERS ( $R = R_c$ )

As follows from the previous presentation, the temperature difference between the horizontal boundaries of the rotating cylindrical volume of a liquid increases. This leads to an increase in the Rayleigh number, which may possess eventually a value $R = R_c$. In this case, the characteristic equation (22) has solutions in the form of stationary perturbations, which differ from solutions (33).

Let us consider these stationary perturbations.

The eigen values of the characteristic equation at $R = R_c$ are as follows:

$$\lambda_1 = 0; \lambda_{2,3} = k_\perp^2 \frac{(2P+1)}{2P} \pm i\omega, \tag{34}$$

where $n = 1$, $R_w = \frac{k_\perp^6 (2P-1)^2}{4k_r^2 (P-1)P}$, $\omega^2 = \frac{(P-1)}{P} \frac{k_r^2}{k_\perp^2} (R_c - R_w)$.

We will set the dependence of temperature on time in (20), e) for eigen values (34) in the form $D(t) = B \exp(-\lambda t)$. Then the overall solution can be represented as:

$$D(t) = \sum_{m=1}^{3} D_m \exp(-\lambda_m t) = D_1 - (D_2 \cos(\omega t) - D_3 \sin(\omega t)) \exp(-\delta t), \tag{35}$$

where $D_m$ - arbitrary constants determined by initial conditions.

From (35) it follows, that in a stationary state the general solution for the liquid perturbed temperature consists of the sum of three particular solutions. One summand with an eigen value $\lambda_1 = 0$ is a constant number. The other two summands with eigen values $\lambda_{2,3}$ describe either exponentially damped temperature variation with a damping decrement $\mathrm{Re}(\lambda_{2,3}) = \alpha_1^{R_c > R_w} = k_\perp^2 \dfrac{(2P+1)}{2P}$ and oscillation frequency $\mathrm{Im}(\lambda_{2,3}) = \alpha_2^{R_c > R_w} = \pm \sqrt{\dfrac{(P-1)}{P}\dfrac{k_r^2}{k_\perp^2}(R_c - R_w)}$ at $R_c > R_w$, or damped variation without oscillations with decrements $\mathrm{Re}(\lambda_{2,3}) = \alpha_{1,2}^{R_c < R_w} = k_\perp^2 \dfrac{(2P+1)}{2P} \pm \sqrt{\dfrac{k_r^2}{k_\perp^2}\dfrac{(P-1)}{P}(R_w - R_c)}$ at $R_c < R_w$. Moreover, in the latter case $\alpha_1^{R_c < R_w} > \delta_2^{R_c < R_w} > 0$ .

We use the expressions (33), (35) to describe the experimental data on the stability of a rotating cylindrical volume of water heated from below [5, 9].

In some experiments (let's designate them as experiments I) the water was placed in glass cylinders with an outer diameter of 29.4 cm. An electric heating element was attached to the horizontal bottom of the cylinder, which provided controllable temperature variation. Heating was carried out at a low rate (heater power - 1 W), medium rate (heater power - 3 W) and high rate (heater power - 10 W). The cylinder with water rotated around its axis using special tools. The layer of water with a depth of 3 cm and the rotation velocity of 10 rpm was studied in the experiments.

For experiments I) in (34), the relation $R_c \gg R_w$ is satisfied and, thus, the instability with the parameters $\alpha_{1,2}^{R_c > R_w}$ is realized.

In other experiments (experiments II) [4, 9] in water layers of 18 cm depth at a temperature difference of lower and upper boundaries - 0.7 ° C and a rotation velocity of 5 rpm we have found by visual observations using a rotoscope, that for a heating rate of more definite value in a cylindrical volume of water rotating as a whole the convective cells with a diameter of 4.6 cm arose. The motion inside the cells becomes visible as a result of dispersing a small amount of aluminum powder over the surface of the water.

We will analyze the described experiments on the basis of the performed analytical calculations below.

### Stationary temperature perturbation at a low rate of liquid heating

At a low rate of heating the bottom of the tank, the process of water heating will take place in two stages. These stages, due to the low rate of liquid heating and the low level of saturation temperature, will not go into one another, but overlap, i.e. to the first stage of temperature variation, valid within the entire time interval, one should add the second stage of its variation, valid after the temperature is established of the order of $(8 - 9) \cdot 10^{-2}$°C (when the equality $R = R_c$ is satisfied).

At the first stage the water temperature increases as a result of multi-stage rise, reaches values of the order of $8\text{-}9 \cdot 10^{-2}$°C and the Rayleigh number increases to a value $R = R_c$. This stage of the multistage temperature rise will be approximated by the expression:

$$B_h(t) = A_s(1 - \exp(-B_s t))\theta(t_{tr} - t), \tag{36}$$

where $A_s, B_s$ - constants describing the first stage of water heating, $t_{tr}$ - the time of transition of water temperature rise from the first stage to the second.

At the second stage, when $R \simeq R_c$, the temperature variation is described by the sum of two temperatures, where the first temperature from this sum $B_h'(t)$ is set by the sum of the summands of the solution (36) with arbitrary coefficients

$$B_h'(t) = A_s' - D_s' \exp(-B_s t), \tag{37}$$

and the second $D(t)$ is the sum of particular solutions of the characteristic equation at $R = R_c$ :

$$D(t) = \theta(t - t_{tr})\left\{ D_1 - (D_2 \cos(\alpha_2^{R_c > R_w} t) - D_3 \sin(\alpha_2^{R_c > R_w} t)) \exp(-\alpha_1^{R_c > R_w} t) \right\} =$$
$$= \theta(t - t_{tr})(A_e + B_e \cos(C_e(t - t_e)) \exp(-D_e(t - t_e))), \tag{38}$$

where $A'_s, D'_s, A_e, B_e, C_e, D_e, t_e$ - constants describing the second stage of water heating.

After summing up the solutions (37), (38) we obtain an expression for water temperature variation at the second stage of instability:

$$D_{\Sigma}(t) = (A'_s + A_e)\theta(t - t_{tr})\left(1 - \frac{D'_s e^{-B_s t_e}}{A'_s + A_e}\left(1 - \frac{B_e}{D_s}e^{B_s t_e}\cos(C_e(t - t_e))\right)e^{-B_s(t - t_e)}\right), \tag{39}$$

where $\theta(x)$ - Heaviside unit function.

Constants in (39) can be determined by combining the theoretical dependencies (36), (39) with experimental data [4, 9].

Graphs of temperature versus time for the rotating cylindrical volume of water heated from below, obtained experimentally, and calculated by formulas (36), (39) are presented in Fig. 6. The experimental dependence of temperature upon time (solid line) was obtained as a result of digitization and graphic transformation to the Cartesian coordinate system. The beginning of the obtained experimental curve was brought into coincidence with the beginning of the Cartesian coordinate system.

As a result of approximation of formulas (36), (39) with experimental data the following values of the constants were obtained: $A_s = 36.4, B_s = 0.055$, $A'_s = D'_s = 8.86, A_e = 0, B_e = 1.92, C_e = 0.5, D_e = B_s = 0.08$, $t_e = -1, t_{tr} = 15.8$.



Fig. 6. Temperature versus time of a rotating cylindrical volume of water with a low

heating rate: solid line - experiment [4, 9]; ○ - formula (36), ◇ - formula (39)

In Fig. 6 the water heating rate at the initial time is determined by the quantity: $\left.\dfrac{dB_h}{dt}\right|_{t=0} = 0.676$, it is a fairly small

quantity.

From Fig. 6 it follows, that the experimental data and theoretical dependences are quantitatively consistent. The data show, that in a rotating cylindrical volume of water with a low heating rate, a monotonic rise in temperature to a certain level and its stabilization at a slightly higher level are observed. Lack of convective vortices in the experiment indicates that temperature stabilization in a cylindrical volume of water occurs, apparently, due to mechanical heat and mass transfer, which occurs as a result of the liquid rotation.

The radial and vertical spatial distribution of the velocity of mechanical heat and mass transfer of a rotating liquid, as follows from (20), is determined by the same expressions as for convective heat and mass transfer in the below heated water layer with free boundaries [3].

### Stationary temperature perturbation at high heating rate

At the tank heating rate of more than a definite value the process of water heating can be divided also into two stages. However, the second stage of temperature variation, due to the high rate of water heating and rapid establishment of the equality $R = R_c$, will be described only by the sum of particular solutions of the characteristic equation.

Thus, at the first stage in the time interval $0 \le t < t_{max}$ the water will be heated to the value $(1.5 \div 2)T_{ex}$ according to the law (36).

At the second stage, when $t \ge t_{max}$, the temperature variation is described by the expression:

$$D'(t) = \theta(t - t_{tr})\left\{D'_1 - \left(D'_2\cos(\alpha_2^{R_c>R_w}t) - D'_3\sin(\alpha_2^{R_c>R_w}t)\right)\exp(-\alpha_1^{R_c>R_w}t)\right\} =$$
$$= \theta(t - t_{tr})\left(A'_e + B'_e\sin(C'_e(t - t'_e))\exp(-D'_e(t - t'_e))\right). \tag{40}$$

The constants in (36), (40) can be determined by combining theoretical dependences with experimental data.

Graphs of temperature versus time of a rotating cylindrical volume of water heated from below, obtained experimentally and calculated by formulas (36), (40) are presented in Fig. 7. The experimental temperature dependence on time was taken from [4, 9], digitized, and graphically transformed to the Cartesian coordinate system. The beginning of the experimental curve thus obtained was brought into coincidence with the beginning of the Cartesian coordinate system.

As a result of approximation of the experimental data using formulas (36), (40) the following values of the constants were obtained: $A_s = 36.4, B_s = 0.055$, $A'_e = 15.45, B'_e = 27.245, C'_e = 0.557, D'_e = 0.197$, $t'_e = 8.3411, t_{tr} = 15.57$ .



Fig. 7. Temperature versus time of a rotating cylindrical volume of water heated from below

with a high heating rate: solid line - experiment [4, 9]; ○ - formula (36), ◇ - formula (40).

In Fig. 7 the water heating rate at the initial time is determined by the value: $\left. \dfrac{dB_h}{dt} \right|_{t=0} = 2.0$ . It can be seen that in

the case under consideration the water heating rate at the initial time is higher than the heating rate in the experiment described above.

From Fig. 7 it follows, that at the first stage within the time interval $0 \le t < t_{max}$ the temperature increases according to the exponential law (36) to a certain level. Then, at $t \approx t_{max}$ the first stage goes into the second, where the perturbed temperature variation is described by the expression (40). At that, the perturbed temperature experiences oscillations damped in time with respect to temperature $T \approx 15.45$ .

It should be noted, that in Fig. 6, 7 and below, the part of the experimental curve, not marked with markers, describes the water temperature variation after the heater is turned off.

Let us consider another experiment in which the water heating rate was higher than the heating rate used in the experiment in Fig. 7.

Fig. 8 shows experimentally obtained and calculated by formulas (36), (40) graphs of dependence of the disturbed temperature upon the time of a cylindrical volume of water heated from below at rate exceeding the heating rate in the experiment in Fig. 7.

As before, the experimental dependence of temperature difference on time [4, 9] is digitized, and graphically transformed to the Cartesian coordinate system. The beginning of the experimental curve thus obtained was brought into coincidence with the beginning of the Cartesian coordinate system.

As a result of approximation of the experimental data using formulas (36), (40) the following values of the constants were obtained: $A_s = 52.5, B_s = 0.055$, $A'_e = 14.817, B'_e = 3.592, C'_e = 0.772, D'_e = 0.2$, $t'_e = 11.451, t_{tr} = 8.44$ .

In Fig. 8 the water heating rate at the initial time is higher than the heating rate in two previous experiments $\left. \dfrac{dB_h}{dt} \right|_{t=0} = 2.9$ .

From Fig. 8 it follows that increasing the water heating rate compared with the data in Fig. 7 changes the temporal dynamics of the perturbed temperature: the first stage of heating exists for a shorter period of time, and the damped vibrations at the second stage have a shorter period and larger amplitude of oscillations. As to the rest, the amplitude dynamics of the perturbed temperature in Fig. 8 corresponds to the dynamics in Fig. 7: the amplitude of the first maximum and the saturation level are almost the same.

The discrepancy between the experimental data and the theoretical curve in Fig. 8 at $t > t_{max}$ is, apparently, due to the fact that with a high heating rate it is necessary to take into account the contribution of nonlinear summands in the initial equations (9), (16) - (19).
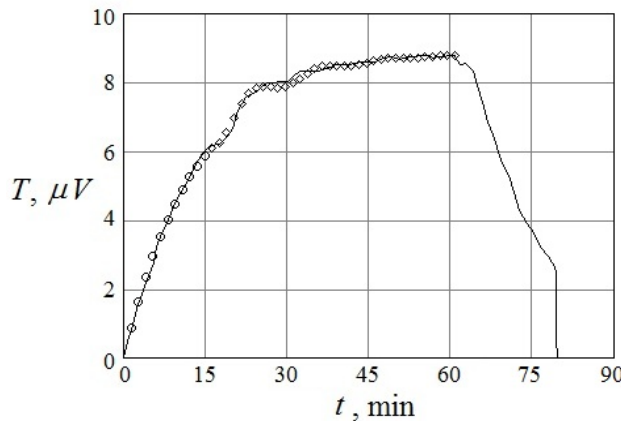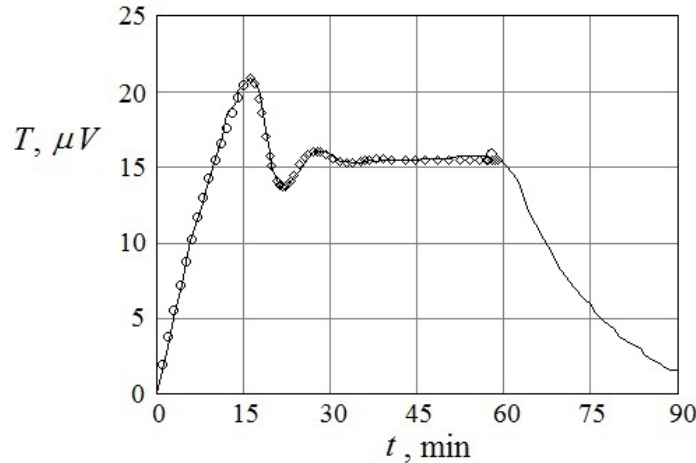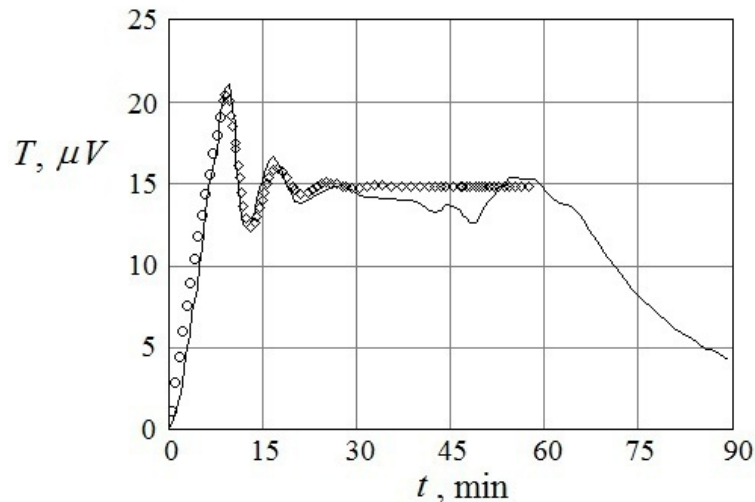
Fig. 8. Temperature versus time of a rotating cylindrical volume of water with a

high heating rate: solid line - experiment [4, 9]; ○ - curve (36), ◇ - curve (40).

## CONCLUSION

In this work, in neglect of the centrifugal convective force, the equations of heat and mass transfer in a rotating, viscous, incompressible liquid of a cylindrical form with free boundaries are analyzed. Solutions of the linearized original system of equations in cylindrical geometry are obtained that satisfy the boundary conditions of the problem. The spatial distributions of the projections of the perturbed velocity and the perturbed temperature of the liquid are determined with the accuracy to constants.

It is shown, that the spatial distribution of horizontal and vertical velocities and the temperature of a rotating, viscous, incompressible liquid of a cylindrical form with free boundaries are similar to those implemented for a layer of a viscous, incompressible liquid heated from below without rotation, which correspond to solutions of the Rayleigh problem in the cylindrical coordinate system.

The analysis of stability of a rotating, viscous, incompressible liquid of a cylindrical form heated from below was carried out. A stability condition for the rotating, viscous, incompressible liquid of a cylindrical form heated from below in the cylindrical coordinate system was obtained. For the case of its stable rotation the graphs of dependence of the logarithm of the critical Rayleigh number $ln(R_c)$ on the wave number $k_r$ and the Taylor number $Te$, as well as the logarithm of the radial wave number $ln(k_r)$ on the Rayleigh number $X = R_c/R_c^*$ and the Taylor number $Y = Te/R_c^*$ were plotted. The obtained dependences, except for the minimum radial wave number $(k_r)_{min} \sim (\pi^2/2)^{1/3} Te^{1/3}$, fully match the previous studies by other authors.

The stability analysis of a rotating cylindrical volume of a liquid without heating from below was carried out. It has been shown that at a fixed, zero temperature difference between the horizontal boundaries of the cylindrical tank of a liquid, an increase in its temperature is observed starting from zero. Then it reaches a maximum value of the order $\kappa = 1.5,...,2.0$, and after, oscillating with exponentially decreasing amplitude of oscillations, again decreases to zero. In the final state at large times the liquid will rotate as a whole without perturbations of velocity, pressure and temperature.

If the temperature difference between the horizontal boundaries of the cylindrical volume of the liquid $\Theta$ is set at a fluctuation level and is not supported from the outside, then the system can be considered as isolated. In this case, according to the law of entropy increasing in isolated systems, the liquid will successively go through only the stages of temperature rise with the rise coefficient at each stage of the order $\kappa$ so, that its temperature eventually will increase in increasing geometric progression up to the value $\sum_{i=1}^{n} \kappa^{i-1}$, where $n >> 1$ - the number of stages of the temperature rise.

However, at a certain number of rise stages $n = N$, the Rayleigh number $R = R_{fl} \sum_{i=1}^{N} \kappa^{i-1}$ may increase to a value $R = R_c$. In this case, the characteristic equation will have another eigen values and, consequently, another expression for increasing the liquid temperature. The water temperature will increase, but its final value should not exceed the phase transition temperature, since in this case the original system of equations is not applicable.

Based on performed calculations an example of heating a rotating cylindrical volume of water without heating from below is considered. This example shows that the problem of the occurrence of a temperature gradient in the volume of water, as well as its heating in Ranque-Hilsch tubes, should be considered as an inverse Rayleigh problem. In

the Rayleigh inverse problem it is required to find the temperature difference between the horizontal boundaries of a viscous, incompressible liquid of a cylindrical form according to a given distribution of its horizontal and vertical velocities.

The stability analysis of a rotating cylindrical volume of a liquid at heating from below has shown, that over time the temperature difference of the liquid increases from zero at $t = 0$, reaches the first maximum value of the order $\kappa$ and tends to unity oscillating with exponentially decreasing oscillation amplitude. In experiments with heating the rotating cylindrical volume of a liquid, the value of the temperature difference set from outside determines the final heating temperature of the liquid, as well as the initial rate of its variation. It is shown that the rate of temperature variation of a heated liquid is greater than that of a similar one without heating.

Stationary temperature perturbations are considered for different rates of water heating.

In all cases it was proposed to consider two stages of the development of stationary perturbations.

At the first stage the water, as a result of a multistage heating at a rate set from outside, acquires a temperature at which the Rayleigh number is small, but increases from the value $R << R_c$ to $R \approx R_c$.

At the second stage of heating, when $R = R_c$, the eigen values of the characteristic equation and the type of particular solutions, of which the general solution for a temperature consists, change. The temperature of the system is described either by a superposition of general solutions for the first and second stages of the temperature rise (at a low heating rate), or only by a general solution for the case $R = R_c$ (at a high heating rate).

Comparison of theory and experimental data for heating water shows a qualitative and quantitative agreement.

### ORCID IDs
**Oksana L. Andreeva** https://orcid.org/0000-0001-9757-8519, **Leonid A. Bulavin** https://orcid.org/0000-0002-8063-6441
**Viktor I. Tkachenko** https://orcid.org/0000-0002-1108-5842

### REFERENCES
[1] H. Bernard, Revue generale des Sciences, pures et appliquées, **11**, 1261-1271 and 1309-1328 (1900), retrieved from: https://gallica.bnf.fr/ark:/12148/bpt6k17075r?rk=21459;2.
[2] J.W. Strutt (Lord Rayleigh), Phil. Mag. **32**, 529-546 (1916), https://doi.org/10.1080/14786441608635602.
[3] L.S. Bozbei, B.V. Borts, A.O. Kostikov and V.I. Tkachenko, East Eur. J. Phys. **1**(4), 49-56 2014, retrieved from: https://periodicals.karazin.ua/eejp/article/view/1442.
[4] S. Chandrasekhar, *Hydrodynamic and hydromagnetic stability,* (University Press, Oxford, 1970), pp. 657.
[5] G.Z. Gershuni and E.M. Zhukhovitskiy, *Конвективная устойчивость несжимаемой жидкости* [*Convective stability of an incompressible fluid*]*,* (Nauka, Moscow, 1972), pp. 393. (in Russian)
[6] Kh.P. Grinspen, *Теория вращающихся жидкостей* [*Theory of Rotating Fluids*], (Gidrometeoizdat, Leningrad, 1975), pp. 321. (in Russian)
[7] L.D. Landau and E.M. Lifshits, *Теоретическая физика, Т.6, Гидродинамика* [*Theoretical Physical, Vol.6, Hydrodynamics*], (Nauka, Moxcow, 1986), pp. 736. (in Russian)
[8] E.L. Koschmieder, *Bénard Cells and Taylor Vortices: monograph on mechanics,* (University Press, Cambridge, 1993), pp. 350.
[9] Y. Nakagawa and P. Frenzen, Tellus, **7**, 1-21 (1955), https://doi.org/10.1111/j.2153-3490.1955.tb01137.x.
[10] N.A. Smirnova, *Методы статистической термодинамики в физической химии* [*Methods of statistical thermodynamics in physical chemistry*], (Vysshaya shkola, Moscow, 1982), pp. 455. (in Russian)
[11] L.D. Landau and E.M. Lifshits, *Теоретическая физика, Т.5, Статистическая физика* [*Theoretical Physics Vol.5, Statistical Physics*], (Nauka, Moscow, 1976), pp. 584. (in Russian)
[12] A.P. Merkulov, *Вихревой эффект и его применение в технике* [*Vortex effect and its application in technology*], (Mashinostroeniye, Moscow, 1969), pp. 183. (in Russian)
[13] A.D. Suslov, S.V. Ivanov., A.V. Murashkin and Yu.V. Chizhikov, *Вихревые аппараты* [*Vortex devices*], (Mashinostroeniye, Moscow, 1985), pp. 256. (in Russian)

## СТІЙКІСТЬ ГОРИЗОНТАЛЬНОГО ЦИЛІНДРИЧНОГО ШАРУ В'ЯЗКОЇ, НЕСТИСЛИВОЇ РІДИНИ З ВІЛЬНИМИ МЕЖАМИ, ЩО ОБЕРТАЄТЬСЯ ТА ПІДГРІВАЄТЬСЯ ЗНИЗУ
**О.Л. Андрєєва[1,2], Л.А. Булавін[3], В.І. Ткаченко[1,2]**
*[1]Національний науковий центр «Харківський фізико-технічний інститут»*
*вул. Академічна, 1, 61108, Харків, Україна*
*[2]Харківський національний університет імені В.Н. Каразіна*
*майдан Свободи, 4, 61022, Харків, Україна*
*[3]Київський національний університет імені Тараса Шевченка*
*вул. Володимирська, 60, 01033, Київ, Україна*

Теоретично досліджено стійкість циліндричного горизонтального шару в'язкої, нестисливої рідини з вільними межами, що обертається і підгрівається знизу. У нехтуванні відцентровими силами записані рівняння руху, теплопровідності і нестисливості рідини, з яких в лінійному наближенні отримано відоме дисперсійне рівняння. Розглянуто стійкість обертового циліндричного об'єму рідини у відсутність підгріву знизу за умови, що різниця температур горизонтальних границь рідини фіксована, і дорівнює нулю. Показано, що у відсутність підгріву знизу і якщо різниця температур горизонтальних кордонів рідини, що обертається, не фіксована, і не підтримується ззовні, то збурена температура рідини буде збільшуватися, але її кінцеве значення не перевищуватиме температуру фазового переходу. Отриманий результат використаний для пояснення нагріву води у вихрових трубках Ранка-Хілша. Зроблено висновок про те, що нагрів води в

трубках типу Ранка-Хілша слід розглядати як зворотну задачу Релея, в якій за відомим розподілом швидкостей всередині об'єму рідини можна визначити градієнт температури, що виникає. Наведено аналіз стійкості обертового циліндричного об'єму рідини при підігріві знизу. Показано, що в експериментах величина різниці температур на кордонах циліндра, задається, а також початкова швидкість її зміни визначає кінцеву температуру нагрівання рідини. Порівняння запропонованої теорії та експериментальних даних для нагріву води показує їх гарну якісну і кількісну відповідність.
**КЛЮЧОВІ СЛОВА:** теорія, стійкість, в'язкий, нестисливий, рідина, горизонтальний циліндричний шар, обертається, нагрівається, вільні границі

## УСТОЙЧИВОСТЬ ВРАЩАЮЩЕГОСЯ И ПОДОГРЕВАЕМОГО СНИЗУ ГОРИЗОНТАЛЬНОГО ЦИЛИНДРИЧЕСКОГО СЛОЯ ВЯЗКОЙ, НЕСЖИМАЕМОЙ ЖИДКОСТИ СО СВОБОДНЫМИ ГРАНИЦАМИ

**О.Л. Андреева[1,2], Л.А. Булавин[3], В.И. Ткаченко[1,2]**
*[1]Национальный научный центр «Харьковский физико-технический институт»*
*ул. Академическая, 1, 61108, Харьков, Украина*
*[2]Харьковский национальный университет имени В.Н. Каразина*
*пл. Свободы, 4, 61022, Харьков, Украина*
*[3]Киевский национальный университет имени Тараса Шевченко*
*ул. Владимирская, 60, 01033, Киев, Украина*

Теоретически исследована устойчивость вращающегося и подогреваемого снизу горизонтального цилиндрического слоя вязкой, несжимаемой жидкости со свободными границами. В пренебрежении центробежными силами записаны уравнения движения, теплопроводности и несжимаемости жидкости, из которых в линейном приближении получено известное дисперсионное уравнение. Рассмотрена устойчивость вращающегося цилиндрического объема жидкости в отсутствие подогрева снизу при условии, что разность температур горизонтальных границ жидкости фиксирована, и равна нулю. Показано, что в отсутствие подогрева снизу и, если разность температур горизонтальных границ вращающейся жидкости не фиксирована, и не поддерживается извне, то возмущенная температура жидкости будет увеличиваться, но ее конечное значение не превышает температуру фазового перехода. Полученный результат использован для объяснения нагрева воды в вихревых трубках Ранка-Хилша. Сделан вывод о том, что нагрев воды в трубках типа Ранка-Хилша следует рассматривать как обратную задачу Рэлея, в которой по известному распределению скоростей внутри объема можно определить возникающий градиент температуры. Приведен анализ устойчивости вращающегося цилиндрического объема жидкости при подогреве снизу. Показано, что в экспериментах величина задаваемой разности температур на границах цилиндра, а также начальная скорость ее изменения определяет конечную температуру нагрева жидкости. Сравнение предложенной теории и экспериментальных данных для нагрева воды показывает их хорошее качественное и количественное соответствие.
**КЛЮЧЕВЫЕ СЛОВА:** теория, устойчивость, вязкий, несжимаемый, жидкость, горизонтальный цилиндрический слой, вращается, нагревается, свободные границы

# PHASE TRANSITIONS IN CONVECTION

**Ivan V. Gushchin, Volodymyr M. Kuklin\*, Eugen V. Poklonskiy**

*V.N. Karazin Kharkiv National University, Kharkiv, Ukraine*

*Svobody Sq. 4, Kharkiv, Ukraine, 61022*

*\*E-mail: kuklinvm1@gmail.com*

The paper presents the results of the study of the models of convective instability near its threshold of thin layers of liquid and gas bounded by poorly conducting walls. These models single out one spatial scale of interaction, leaving the possibility for the evolution of the system to choose the symmetry character. This is due to the fact that the conditions for the realization of the modes of convective instability near the threshold are chosen. All spatial perturbations of the same spatial scale, but of different orientations, interact with each other. It turned out that the presence of minima of the interaction potential of the Proctor-Sivashinsky equation modes, the absolute value of the wave number vectors of which is unchanged, determines the choice of symmetry and, accordingly, the characteristics of the spatial structure. In the case of a more realistic model of convection described by the Proctor-Sivashinsky equation, it was possible to observe both the first-order phase transition and the second-order phase transition and detect the form of the state function, which is responsible for the topology of the resulting convective structures: metastable rolls and stable square cells. In this paper, it is shown that the nature of the structural-phase transition in a liquid when taking into account the dependence of viscosity on temperature in the Proctor-Sivashinsky model is similar to the case of the absence of such a dependence. The transition time turns out to be the same, despite the fact that a different structure is formed - hexagonal convective cells. As in the Swift-Hohenberg model, a hard mode for the formation of hexagonal cells in a gas medium is possible only for a sufficiently noticeable dependence of its viscosity on temperature. The phase transition times are inversely proportional to the difference in the values of this function for two consecutive states. A similar description of phase transitions did not use phenomenological approaches and various speculative considerations, which allows for a closer look at the nature of transients.

**KEYWORDS:** first-order phase transition, the second-order phase transition, state function, convective structures, Swift-Hohenberg, Proctor-Sivashinsky models.

Below, we discuss the possibility of phase transitions in a thin layer of liquid or gas, between walls with poorly conducting heat. The layer is limited only from below and above, in other directions there are no borders.

We first consider the Proctor-Sivashinsky equation with allowance for the temperature dependence of viscosity [1, 2] in the case of the proximity of the Rayleigh number to the critical value of the occurrence of convection $Ra_c$, that is, $Ra = Ra_c(1+\varepsilon)$

$$\frac{\partial \phi}{\partial T} + \nabla^4 \phi + \nabla\left[\left(2 - \gamma\phi - (\nabla\phi)^2\right)\nabla\phi\right] + a\phi = 0, \qquad (1)$$

where $\varepsilon \ll 1$, $\nabla\phi = \vec{i}\cdot\frac{\partial\phi}{\partial\zeta} + \vec{j}\cdot\frac{\partial\phi}{\partial\vartheta}$ is a two-dimensional operator, and, $\vec{i}$, $\vec{j}$ are single unit orthogonal to each other unit vectors in the $(\zeta, \vartheta)$ plane of the media separation, and we will assume $k_0 \approx 1$, since we restrict ourselves to the case of a weak excess over the threshold of convective instability. Indeed, for any deviation of the wavenumber from unity, the perturbation amplitude rapidly decreases. Here $\phi$ is the relative temperature at the upper boundary of the layer. An increase in this value indicates an increase in the thermal conductivity of the layer as a whole.

Table 1.

Transition from used variables to real physical quantities

| Physical Value | | Representation |
|---|---|---|
| Temperature | $T(x\sqrt{\varepsilon}, y)$ | $T_d + (T_d - T_u)(-y + F(x\sqrt{\varepsilon}, y)$ |
| Horizontal speed | $\psi_y$ | $60\sqrt{\varepsilon}\cdot F_{x\sqrt{\varepsilon}}\cdot(2y^3 - 3y^2 + y)$ |
| Vertical speed | $-\psi_x$ | $-30\varepsilon\cdot(F_{x\sqrt{\varepsilon}})_{x\sqrt{\varepsilon}}\cdot(y^4 - 2y^3 + y^2)$ |

where $\xi = x\sqrt{\varepsilon}$, $\eta = y$, $F = \phi\cdot\sqrt{17/660}$.

Equation (1) contains vector quadratic nonlinearity (that is, dependent on the orientation of perturbations and derived quantities), and the cubic nonlinearity, which takes into account the influence of the temperature field at the upper boundary of the layer, responsible for the change in the topology of spatial structures of convection.

To describe such convection under the same conditions, the simplified Swift–Hohenberg equation is often used [3]

$$\frac{\partial \phi}{\partial T} = e\phi - (1+\nabla^2)^2\phi - 2\gamma\phi^2 + 3\phi^3 , \tag{2}$$

where the vector character of the nonlinear terms is replaced by the scalar one. Here $e = (1-a)$, where such dependences are chosen $\beta = a \cdot \sqrt{231/68}$, and the dimensionless heat transfer coefficient between the fluid and the boundary, here equals the number of Biot and is equal to $b = \varepsilon^2 \cdot \beta$.

The growth of disturbance amplitudes in case of instability $\phi \propto \exp\{\operatorname{Im}\omega \cdot T\}$ occurs with an increment $\operatorname{Im}\omega \approx e - (k^2-1)^2$. For $\gamma > 0$ gas flow (this corresponds to gas convection) it goes back to the center of the cell, with $\gamma < 0$ (which corresponds to the movement of the liquid) - vice versa.

The Swift-Hohenberg equation, as noted in the review [4], describes, after the formation of an amorphous state of disorderly convection, a system of distinct hexahedral cells as a result of a soft (for liquid) and hard (for gas) instability regime, observed in particular in [5]. Moreover, the nature of the instability demonstrates all the features of the first-order phase transition – the formation of a clear spatial structure of convection from an amorphous state.

The purpose of the work is the analysis of the soft and hard regimes of structural-phase transitions in the Proctor-Sivashinsky model in the conditions of temperature dependence of viscosity.

## DESCRIPTION OF PHASE TRANSITIONS IN THE MODEL OF THE PROCTOR-SIVASHINSKY IN THE ABSENCE OF TEMPERATURE DEPENDENCE OF VISCOSITY

In contrast to the traditionally used Swift-Hohenberg equations, we use the 3D Proctor-Sivashinsky equation that meets the real conditions. This task is obviously three-dimensional in space and non-stationary, which at first glance creates significant problems. However, the Proctor-Sivashinsky model makes it possible to reduce the dimension of the description and focus on topological aspects, that is, appearance, size and development time of spatial structures.

In the case of a more realistic model of convection, described by the Proctor-Sivashinsky equation (1), both the first-order phase transition and the second-order phase transition can be observed, and the state function, which is responsible for the topology of the resulting convective structure, was detected [6].

The equation that determines the dynamics of the temperature field of this process in the horizontal plane $(x, y)$ is:

$$\frac{\partial \Phi}{\partial T} = \varepsilon^2 \Phi - (1-\nabla^2)^2 \Phi + \frac{1}{3}\nabla\left(\nabla\Phi|\Phi|^2\right) + \varepsilon^2 f , \tag{3}$$

where $\Phi = \theta/\sqrt{3}$, $\varepsilon^2 = e$, $f -$ is a random function describing external noise, $\theta -$ the temperature deviation from the equilibrium one (varying according to a linear law), and the magnitude $\varepsilon$ determining the excess of the convection development threshold, we suppose, as before, to be quite small $(0 < \varepsilon < 1)$. We present the solution in the form of $\Phi = \varepsilon\sum_j A_j \exp(i\vec{k}_j\vec{r})$ with $|\vec{k}_j| = 1$.

For replacements $T \cdot \varepsilon^2 = t$, for slow amplitudes in the absence of noise, we obtain a mathematical expression for the Proctor-Sivashinsky model for describing convection.

$$\frac{\partial A_j}{\partial t} = A_j - \gamma A_{j+j_0} A_{j+2j_0} - \sum_{i=1}^{N} V_{ij} |A_i|^2 A_j , \tag{4}$$

where the interaction coefficients are defined by the relations $V_{jj} = 1$ and $V_{ij} = (2/3)\left(1 + 2\left(\vec{k}_i\vec{k}_j\right)^2\right) = (2/3)\left(1 + 2\cos^2\vartheta_{ij}\right)$, $\vartheta$ - the angle between the vectors $\vec{k}_i$ and $\vec{k}_j$ with the initial values of the amplitudes of the spectrum $A_j|_{t=0} = A_{j_0}$, $\vartheta_{j_0} = 2\pi/3$.

The analysis of the Proctor-Sivashinsky model in the absence of the dependence of viscosity on temperature $(\gamma = 0)$ was studied in detail by authors of this work earlier [7]. It was shown that after the first-order phase transition, a quasistable system of convective rolls (the form of which is shown in Fig. 1a) is formed from amorphous random convection of a state. Later, as a result of rolls modulation within the framework of a second-order phase transition, form a stable field of square convective cells (the form of which is shown in Fig. 1b).

The first-order structural-phase transition, noted earlier in [4], corresponds to the transition from an amorphous state of convection to a state that has the form of a pronounced spatial structure. It should be emphasized that such a spatial clarity of the structure is observed only in conditions of proximity to the instability threshold. If, as a result of instability, the topology of the structure changes, we can speak of a second-order structural-phase transition.

In this case, the phase transition times are inversely proportional to the difference in the values of the state function $\sum_i A_i^2$.

$$\tau_n \sim \left\{\left(\sum_i A_i^2\right)_n^{(+)} - \left(\sum_i A_i^2\right)_n^{(-)}\right\}^{-1} = \Delta I_n^{-1}. \tag{5}$$

It was the fulfillment of the last relation that allowed us to consider the value as a state function, since each spatial structure of convection uniquely corresponded to its value of this function, besides, the phase transition time was also related to the changes of the magnitudes of this function (these changes can be seen in Fig. 2). The fragments of the spatial structure of the temperature field distribution on the surface of layer are presented in Fig. 3.
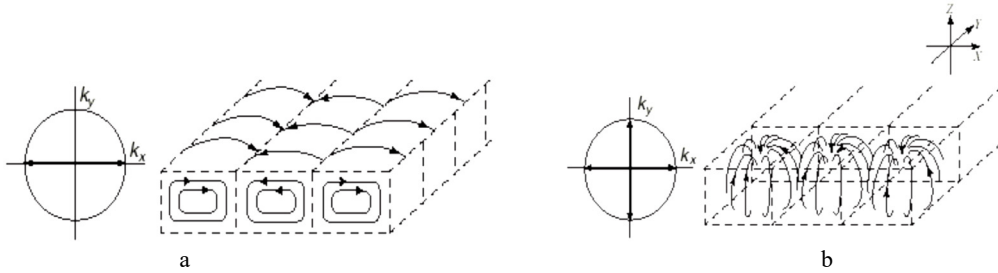


Fig. 1. Convective structures: rolls (a) and square cells (b)
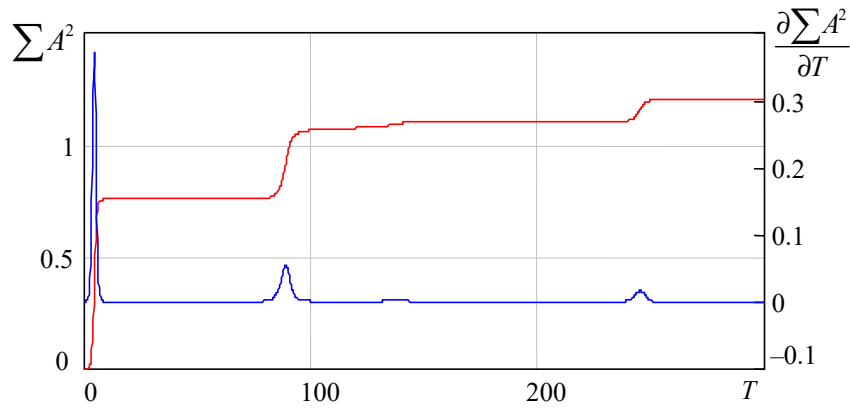


Fig. 2. Behavior of the quantity $\sum A^2$ (upper curve) and its derivative $\partial \sum A^2 / \partial T$ of time $T$
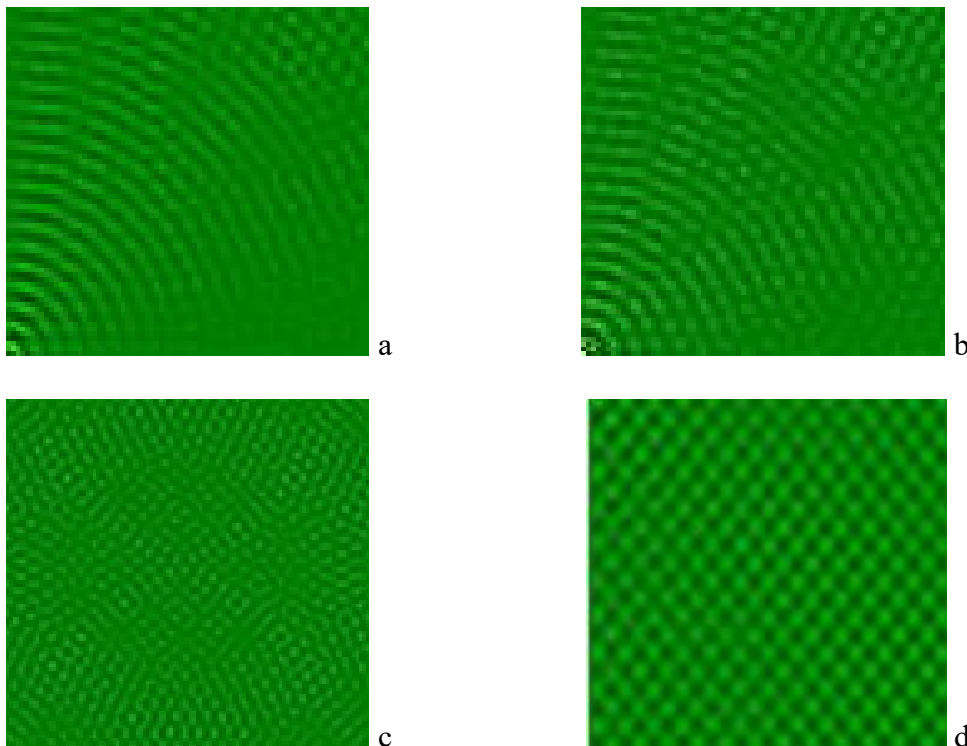


Fig. 3. The appearance of fragments of the spatial structure of the temperature field distribution on the surface of layer
a) – after the structural phase transition of the first kind with the formation of convective rolls,  b) – with the transverse modulation of the rolls, c) – with the formation of a metastable spatial structure, after the destruction of the system of rolls, d) – with the formation of a stable convective structure - square convective cells.

## PHASE TRANSITIONS IN THE PROJECT-SIVASHINSKY MODEL UNDER THE CONDITIONS OF VISCOSITY DEPENDENCE ON TEMPERATURE

**Soft mode of excitation of a six-sided convective structure.** Taking into account the temperature dependence of viscosity demonstrates the ability to implement soft (when $\gamma < 0$) and hard (that is, setting the initial perturbation already in the form of the desired structure 20% higher than the average values of the amorphous state upon $\gamma > 0$) excitation of six-sided convective cells, the state function of which is almost equal to the state function of the rolls system. The time of the first-order structural-phase transition from the amorphous state is almost the same. When negative $\gamma < 0$ is observed, as in the Swift-Hohenberg model, the mode of soft excitation of six-sided convective cells (Fig. 4).
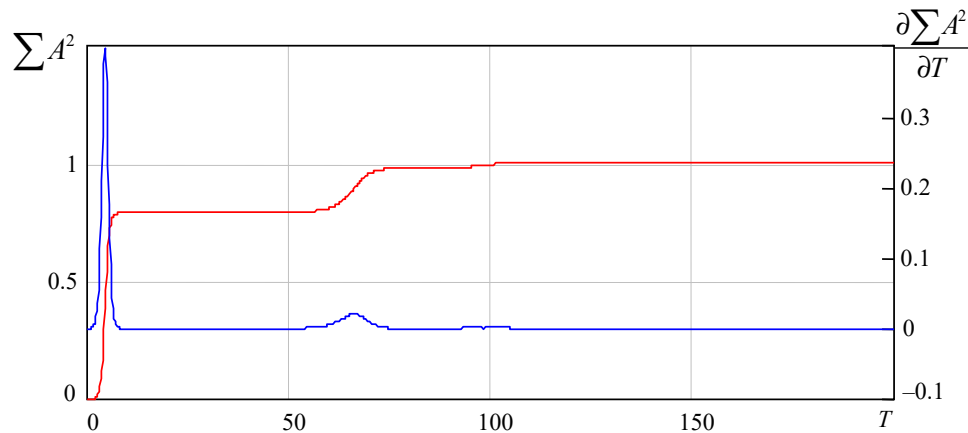


Fig.4. Behavior of the value $\sum A^2$ (upper curve) and its derivative of time $T$, $\partial \sum A^2 / \partial T$ in soft mode excitement at $\gamma = -0.25$

The time interval of the first-order phase transition is equal $\tau_2$, but despite the fact that the values of the state function are equal to unity, which in the former case of the absence of the temperature viscosity dependence ($\gamma = 0$), corresponded to a system of convective rolls. But in that case the system of six-sided cells is formed, as can be seen in Fig. 5, which depicts the dynamics of the instability spectrum.
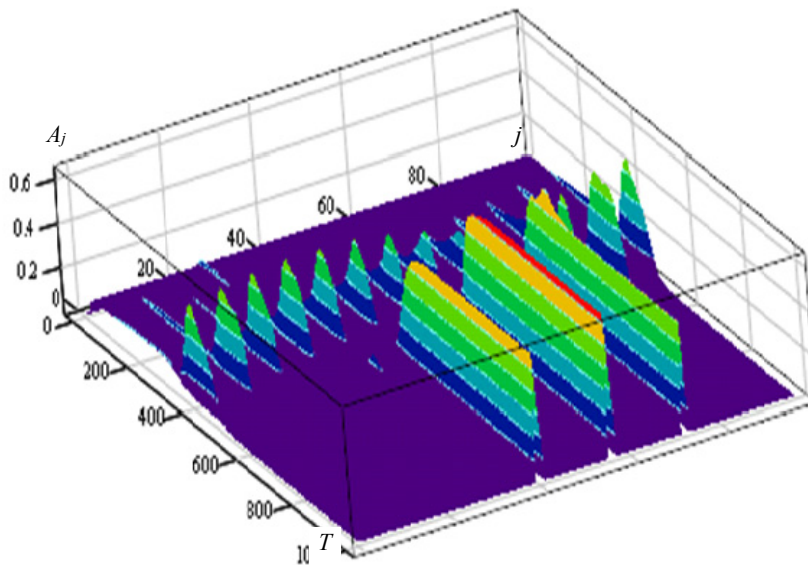


Fig. 5. Dynamics of the instability spectrum with soft imbalance mode ($\gamma = -0.25$)

**Hard mode convective hexagon structure.** In the case of $\gamma > 0$ mode only hard excitation possible, that is, the initial conditions must be specified in the form of hexagonal convective perturbations, clearly expressed against the background of fluctuations. Under these conditions, all characteristics of the process are similar to the case of mild excitation at the same values $|\gamma|$. Otherwise, the dynamics of the process even in the case of non-zero $\gamma > 0$ is similar to the case of the absence of dependence of viscosity on temperature, discussed above.

To implement a hard mode against the background of an amorphous state, a structure was formed whose amplitude was 20% higher than the average value of the amplitudes of the modes (Fig. 6).
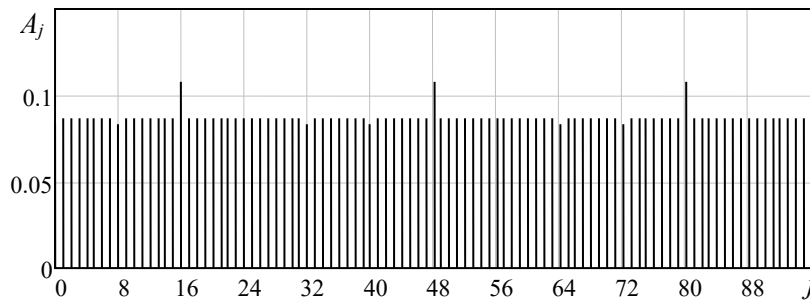
Fig. 6. The initial state of the spectrum of modes on the background of the amorphous state of the system before the phase transition in a gaseous medium ($\gamma > 0$)

The behavior of the state function $\sum A^2$ and the derivative of time $\partial \sum A^2 / \partial T$ is presented in Fig. 7 and Fig. 8 respectively.
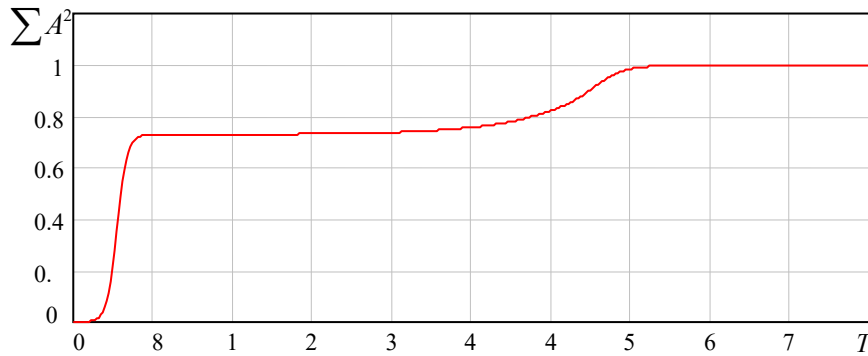


Fig. 7. Behavior of the value of time $T$ in hard excitation mode $\gamma = 0.2$
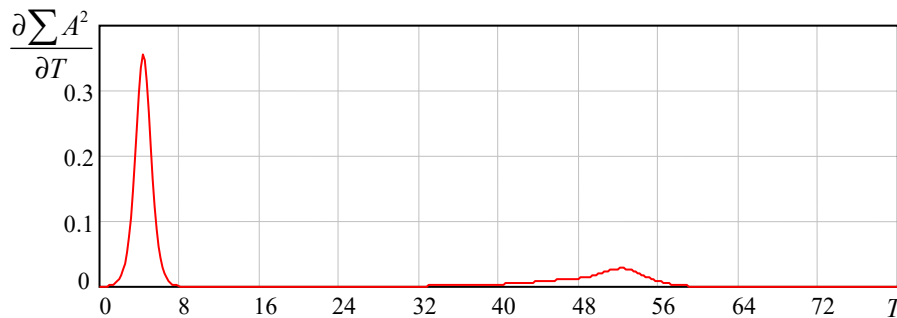


Fig. 8. Behavior of the value of time $T$ in hard excitation mode $\gamma = 0.2$

The dynamics of spectrum formation are shown in Fig. 9. The change $1 < j < 100$ corresponds to a change in angle $0 < \vartheta < 2\pi$. The appearance in the spectrum of three modes shifted by $2\pi / 3$ corresponds to the formation of hexagonal cells.
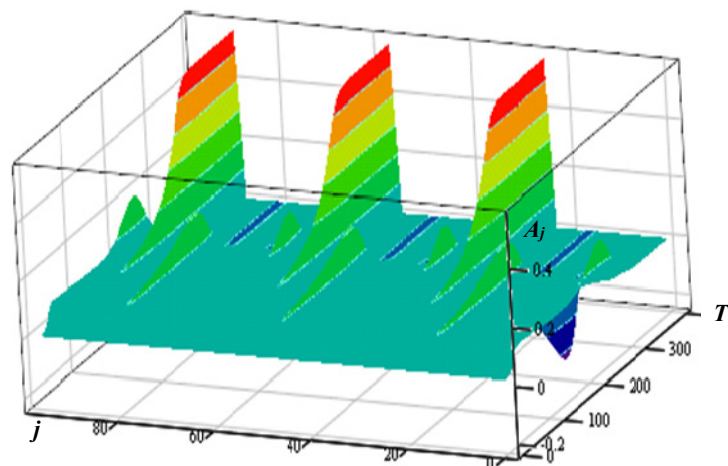


Fig. 9. Instability spectrum dynamics with hard imbalance mode ($\gamma = 0.2$)

## CONCLUSIONS

The peculiarity of the models describing convective instability of thin layers of liquid and gas, bounded by poorly conducting walls of Swift-Hohenberg and Proctor-Sivashinsky, is that they single out one spatial scale of interaction, leaving the possibility for the evolution of the system to choose the symmetry character. This is due to the fact that the conditions for the realization of the modes of convective instability near the threshold of convective instability are chosen. All spatial perturbations of the same spatial scale, but of different orientations, interact with each other. It turned out that the presence of minima of the interaction potential of the Proctor-Sivashinsky equation modes, the absolute value of the wave number vectors of which is unchanged, determines the choice of symmetry and, accordingly, the characteristics of the spatial structure. It was in the case of a more realistic model of convection, described by the Proctor-Sivashinsky equation (1), that we were able to observe both the first-order phase transition and the second-order phase transition and detect the form of the state function that is responsible for the topology of the resulting convective structures.

It should be noted that such a description of phase transitions did not use phenomenological approaches and various speculative considerations, which makes it possible to more closely examine the nature of the transient processes, which arouses the greatest interest of researchers. It is necessary to pay attention that presented on Fig. 3c. a metastable state in the vicinity of a second-order phase transition needs more careful analysis and will help clarify not only the particular nature of this transition, but it is possible to see some common features of such transitions.

### ORCID IDs
**Volodymyr M. Kuklin** http://orcid.org/0000-0002-0310-1582, **Eugen V. Poklonskiy** https://orcid.org/0000-0001-5682-6694

### REFERENCES
[1] J. Chapman and M.R.E. Proctor, J. Fluid Mech. **101,** 759–765 (1980), https://doi.org/10.1017/S0022112080001917.
[2] V. Gertsberg, and G.E. Sivashinsky, Prog. Theor. Phys. **66**, 1219–1229 (1981), https://doi.org/10.1143/PTP.66.1219.
[3] J.V. Swift and P.C. Hohenberg, Phys. Rev. A, **15**, 319 (1977), https://doi.org/10.1103/PhysRevA.15.319.
[4] M.I. Rabinovich, A.L. Fabricant and L.S. Zimring, Soviet Physics-Uspekhi, **162**(8), 1-42 (1992).
[5] E. Bodenschatz, J.R. de Bruyn, G. Ahlers and D. Connell, Preprint, (Santa Barbara, 1991).
[6] I.V. Gushchin, A.V. Kirichok and V.M. Kuklin, VANT series "Plasma Electronics and New Methods of Acceleration", **4**, 252-254, (2015).
[7] I.V. Gushchin, A.V. Kirichok and V.M. Kuklin, Journal of Kharkiv National University, physical series "Nuclei, Particles, Fields", **1040**(57), 4-27 (2013), https://periodicals.karazin.ua/eejp/article/view/13556.

### ФАЗОВЫЕ ПЕРЕХОДЫ В КОНВЕКЦИИ
**И.В. Гущин, В.М. Куклин, Е.В. Поклонский**
*Харьковский национальный университет имени В. Н. Каразина, Харьков, Украина*
*пл. Свободы 4, г. Харьков, Украина, 61022*

В работе представлены результаты изучения моделей описания конвективной неустойчивости вблизи ее порога тонких слоев жидкости и газа, ограниченных плохо проводящими стенками. Эти модели выделяют один пространственный масштаб взаимодействия, оставляя для эволюции системы возможность выбрать характер симметрии. Это связано с тем, что выбраны условия реализации режимов конвективной неустойчивости вблизи ее порога. Все пространственные возмущения одного пространственного масштаба, но разной ориентации взаимодействуют между собой. Оказалось, что наличие минимумов потенциала взаимодействия мод уравнений Проктора-Сивашинского, абсолютная величина векторов волновых чисел которых неизменна, и определяет выбор симметрии и соответственно характеристики пространственной структуры. В случае более реалистичной модели конвекции, описываемой уравнением Проктора-Сивашинского, удалось наблюдать процессы как структурно-фазового перехода первого рода, так и процесс фазового перехода второго рода и обнаружить вид функции состояния, которая отвечает за топологию образовавшихся конвективных структур: метастабильных валов и стабильных квадратных ячеек. В данной работе показано, что характер структурно-фазового перехода первого рода в жидкости при учете зависимости вязкости от температуры в модели Проктора-Сивашинского подобен случаю отсутствия такой зависимости. Время перехода оказывается тем же, несмотря на то, что формируется иная структура – шестигранные конвективные ячейки. Так же как в модели Свифта-Хоэнберга, возможен жесткий режим формирования шестигранных ячеек в газовой среде лишь для достаточно заметной зависимости ее вязкости от температуры. Времена фазовых переходов обратно пропорциональны разности значений этой функции для двух последовательных состояний. Подобное описание фазовых переходов не использовало феноменологические подходы и различные спекулятивные соображения, что позволяет более пристально рассмотреть характер переходных процессов.
**КЛЮЧЕВЫЕ СЛОВА:** фазовые переходы первого рода, фазовые переходы второго рода, конвективные структуры, функция состояния, модели Свифта -Хоэнберга и Проктора-Сивашинского.

### ФАЗОВІ ПЕРЕХОДИ В КОНВЕКЦІЇ
**І.В. Гущин, В.М. Куклін, Е.В. Поклонський**
*Харківський національний університет імені В. Н. Каразіна, Харків, Україна*
*пл. Свободи 4, м Харків, Україна, 61022*

У роботі представлено результати вивчення моделей опису конвективної нестійкості поблизу її порога тонких шарів рідини і газу, обмежених стінками, що слабко проводять тепло. Ці моделі виділяють один просторовий масштаб взаємодії, залишаючи для еволюції системи можливість вибрати характер симетрії. Це пов'язано з тим, що обрані умови реалізації режимів конвективної нестійкості поблизу її порогу. Всі просторові збурення одного просторового масштабу, але різної орієнтації взаємодіють між собою. Виявилося, що наявність мінімумів потенціалу взаємодії мод рівнянь Проктора-Сівашінського, абсолютна величина векторів хвильових чисел яких незмінна, і визначає вибір симетрії та характеристик

просторової структури. У випадку більш реалістичної моделі конвекції, описуваної рівнянням Проктора-Сівашінского, вдалося спостерігати процеси як структрно-фазового переходу першого роду, так і процес структурно-фазового переходу другого роду і виявити вид функції стану, яка відповідає за топологію конвективних структур: метастабільних валів і стабільних квадратних структур. У даній роботі показано, що характер структурно-фазового переходу першого роду в рідини при урахуванні залежності в'язкості від температури в моделі Проктора-Сівашінского подібний випадку при відсутності такої залежності. Час переходу виявляється тим же, не дивлячись на те, що формується інша структура - шестигранні конвективні структури. Так само як в моделі Свіфта-Хоенберга, можливий жорсткий режим формування шестигранних структур в газовому середовищі лише для досить помітною залежності її в'язкості від температури. Часи фазових переходів оберено пропорційні різниці значень цієї функції для двох послідовних станів. Подібний опис фазових переходів не використав феноменологічні підходи і різні спекулятивні міркування, що дозволяє більш пильно розглянути характер перехідних процесів.

**КЛЮЧОВІ СЛОВА**: фазові переходи першого роду, фазові переходи другого роду, конвективні структури, функція стану, моделі Свіфта -Хоенберга і Проктора-Сівашінского.

# ON FREQUENCY AND SPATIAL PERIODICITY OF THE WAVES OF THE ANOMALOUS AMPLITUDE IN THE OCEAN

Volodymyr M. Kuklin, Eugen V. Poklonskiy
*V.N. Karazin Kharkiv National University, Kharkiv, Ukraine*
*Svobody Sq. 4, Kharkiv, Ukraine, 61022*
*E-mail: kuklinvm1@gmail.com*
Received July 31, 2019, accepted October 15, 2019

The paper shows that the waves of anomalous amplitude are long-lived formations. They drift in the direction of the wave motion with the group velocity of the wave packet, which is half the phase velocity of the main wave. The swing of the wave (the distance from the hump to the trough) of the anomalous amplitude is more than three times the average value of the sweep of the wave motion. The modulation instability of this wave form a perturbation spectrum, the energy of which is twice the energy of the main wave in the developed process mode. The spatial size of the wave packet practically does not change, the amplitude of the swing in the maximum first increases, then gradually decreases. The number of such waves in areas of strong wind exposure is much larger than the statistics of random interference processes allow. This is due to the influence of the main wave (its amplitude remains noticeably greater than the amplitudes of each of the modes of the wave packet) on the behavior of each pair of modes from the wave packet of the perturbation. In the laboratory system, the duration of the anomalous wave coincides qualitatively with the time of existence of the Peregrin autowave. Although the Peregrin autowave corresponds to a different physical reality, where the dispersion of the wave is weak. Gravitational surface waves have a strong dispersion, and the NSE equation in this case is noticeably modified. However, in rest system of the wave packet (moving relative to the laboratory system) the abnormal amplitude wave lifetime is much longer. The distance that the wave packet travels with a persisting anomalous sweep is at least equal to several hundred wavelengths and can reach hundreds of kilometers. A simple calculation of such waves by means of space monitoring due to the small viewing area (frame) may be inaccurate. Once formed, such waves are able to drift over considerable distances. However, they may well get into the next frame of view. That is, estimates of the number of such waves can be overestimated.
**KEYWORDS**: long-lived wave of anomalous amplitude, ocean waves, modulation instability.

The actual problem of the safety of shipping and oil and gas production in the oceans and seas is to determine the conditions for the appearance of surface waves of abnormal amplitude that can lead to major disasters and accidents. Earlier, when the intensity of shipping and oil and gas production was not so intense, the occurrence of such waves was considered to be quite rare, and they simply did not consider it necessary to take into account their appearance and impact. However, with an increase in the number of vessels and their personnel, numerous evidences of the appearance of such anomalous waves appeared. However, people are not only worried about the detection of such waves of anomalous amplitude, it is necessary to find out the characteristics of the life cycle of such waves, how long they are able to exist and whether they can move. The purpose of this work is to try to find out the conditions for the existence of waves of anomalous amplitude, the nature of their appearance and the dynamics of propagation.

## DESCRIPTION OF SURFACE WAVES IN DEEP WATER
Large-amplitude surface waves in deep water that cause concern to ocean logistics have a frequency of [1]

$$\omega = \sqrt{g \cdot k} \cdot \left\{ 1 + |A|^2 \, k^2 / 2 \right\} \tag{1}$$

which approximately corresponds to the Lighthill-NSE equation [2] of the form

$$\frac{\partial}{\partial t} A = i\omega \cdot \left( 1 - \frac{1}{2} |A|^2 \, \frac{\partial^2 A}{\partial x^2} \right), \tag{2}$$

where $A = \sum_K |A_K| \cdot \exp\{-i\omega \cdot t + i(k_0 + K)x\}$ is the deviation of the surface, $g$ is the acceleration of free fall, with the maximum steepness for stable waves before they collapse $H / \lambda \approx 0.11 \div 0.13$, where $H = 2|A|$ is the steepness (span) of the wave, that is, the distance between the upper point of the wave crest and the lower point of the wave trough, $\lambda = 2\pi / k_0$ is the wavelength of large amplitude. The width of the spatial instability spectrum under these conditions is not so small; therefore, the equation for the complex slow varying (here the dependence $\propto \exp\{-i\omega \cdot t + i\phi_0\}$ is excluded) field amplitude is represented as [3, 4]

$$\frac{\partial A_K}{\partial t} = -\delta A_K - i \left( \sqrt{g(k_0 + K)} - \sqrt{gk_0} \right) A_K - i \sqrt{g(k_0 + K)} \frac{(k_0 + K)^2}{2} \left\{ |A|^2 \, A \right\}_K. \tag{3}$$

In the simplest case of a plane wave front, the field of perturbations is written in the form

$$A(\zeta,\tau) = (u_0 + \sum_{\substack{K \neq 0 \\ K > 0}} [u_K \cdot \exp\{+iK\zeta + i(\phi_K - \phi_0)\} + u_{-K} \cdot \exp\{-iK\zeta + i(\phi_{-K} - \phi_0)\}]), \tag{4}$$

where the following notation is used, $A_K / |A_0| = a_K = |a_K| \exp\{i\phi_K\} = u_K \exp\{i\phi_K\}$,

$$k_0\xi = \zeta, , \quad \alpha = k_0^2 |A_0|^2, \quad \tau = t \cdot \sqrt{gk_0}\frac{k_0^2 |A_0|^2}{2}, \quad K \to K / k_0, \quad 2\phi_0 - \phi_K - \phi_{-K} = \Phi_K = \Phi_{-K}.$$

Spectrum modes are located in the intervals $0 < K < 2K_{Max}$ and $-2K_{Max} < -K < 0$, $K = 0.3 \cdot \dfrac{i}{N}$, $i = \pm(1,2,... N)$, $\alpha = 0.05$, $N = 100$. The initial amplitudes $u_K(\tau = 0) = 10^{-3}$, and their phases $\phi_K(\tau = 0)$ are randomly distributed in the range of $(0 - 2\pi)$.

Finally, the system of equations describing the modulation instability of a wave of large amplitude takes the form for the main mode

$$\frac{\partial u_0}{\partial \tau} + \delta u_0 + 2u_0 \sum_{K>0} u_K u_{-K} sin\Phi_K = \delta, \tag{5}$$

$$\frac{\partial \phi_0}{\partial \tau} = -u_0^2 - 2\sum_{K>0}(u_K^2 + u_{-K}^2) - 2\sum_{K>0} u_K u_{-K} cos\Phi_K, \tag{6}$$

and for the modes of the spectrum of the modulation instability developing in this case [5]

$$\frac{\partial \phi_K}{\partial \tau} = -\frac{2[\sqrt{(1+K)}-1]}{\alpha} - (1+K)^{2.5} \cdot \{2\sum_{K' \neq K} u_{K'}^2 + u_K^2 + \frac{u_{-K}}{u_K} \sum_{K \neq K} u_K u_{-K} cos(\Phi_K - \Phi_K)\}, \tag{7}$$

$$\frac{\partial u_K}{\partial \tau} = -\delta u_K + (1+K)^{2.5} \cdot [u_{-K} \cdot u_0^2 sin\Phi_K + 2u_{-K}\sum_{K>0} u_K u_{-K} sin(\Phi_K - \Phi_K)], \tag{8}$$

where $\delta$ is the wave decrement, and to maintain the amplitude of the main wave, the same value is on the right-hand side of (5).

Here, the description is used within the framework of the so-called modified S-theory [6], and the interaction occurs only between the modes of the spectrum ($k_n + k_{-n} = 2k_0$, $k_S + k_{-S} = k_n + k_{-n}$) that are symmetrical with respect to pumping. In [5], it was shown that direct calculation of equation (2) and model (4) - (8) lead to qualitatively the same results.

In the presented model, the characteristic spatial scale correlates with the wavelength, that is $k_0\xi = \zeta$, the time scale is determined by the ratio, that is $\tau = t \cdot \dfrac{\alpha \cdot \omega}{2}$, the unit of measurement in space is the wavelength, and the unit of measurement in time is the oscillation period multiplied by $\alpha \cdot \pi$.

## MODELING OF THE PROCESS OF FORMATION OF WAVES OF THE ANOMALOUS AMPLITUDE

For each point in time, a relative maximum span is calculated: the ratio of the maximum span to the average over the entire space.
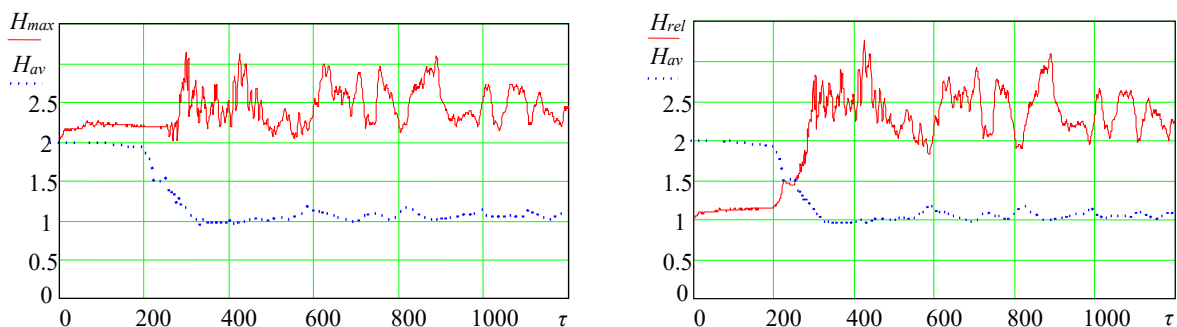


Fig. 1. Behavior of maximum wave span from time $H_{max}$ (left) and relative maximum wave span $H_{rel}$ (right) in the interval $-1047 < \zeta < 1047$ (about 333 wavelengths)

At the initial stage of instability development, an exit to a quasistationary regime occurs with an average swing of wave motion close to unity, which is approximately two times less than the initial value for the main wave. The largest sweep of the waves is reached at the moment of time $\tau = 425$ in the region near $\zeta = -482$ and also at the moment of

time $\tau = 888$ near $\zeta = 956$. For example, one can imagine phase diagrams and a field view in the vicinity of the swing peak (Fig. 2).
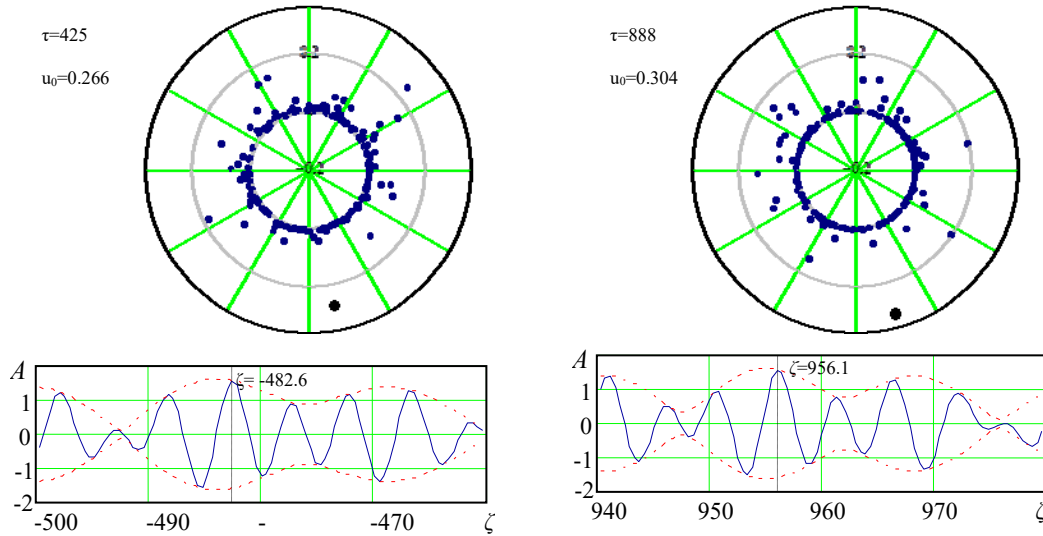


Fig. 2. Phase diagrams and field view near the maxima of the sweeps for the first maximum $H_{\max 1} = 3.118$ $H_{rel1} = 3.253$ (left) and $H_{\max 1} = 3.035$ $H_{rel1} = 3.094$ (right)

It should be noted that, although the amplitude of the main wave (the fat point) is not small, it already loses control of the instability. Indeed, in the developed mode, the energy of the main wave is half the energy of the spectrum (Fig. 3), which by the way is characteristic of developed modulation instability modes in other cases [7].
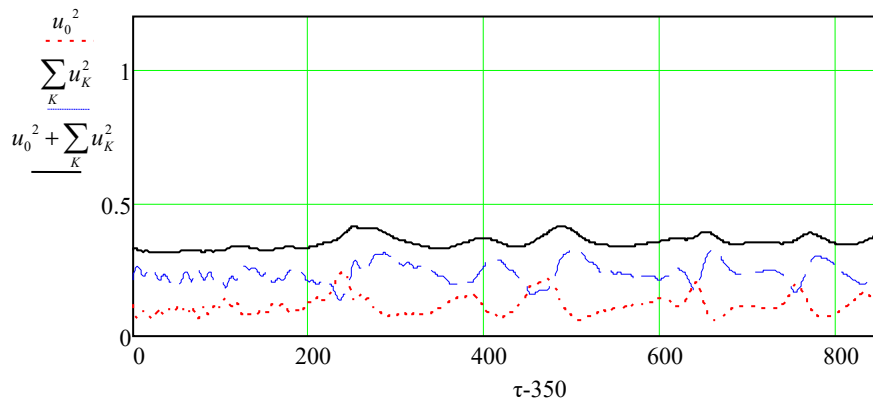


Fig. 3. Behavior in the developed mode of the energy of the main wave $u_0^{\,2}$ (lower curve), energy of the spectrum $\sum\limits_{K} u_K^2$ (middle curve) and total energy $u_0^{\,2} + \sum\limits_{K} u_K^2$ (upper curve)

It is of interest to consider the motion of wave packets with a maximum amplitude in space and in time (Fig.4.)
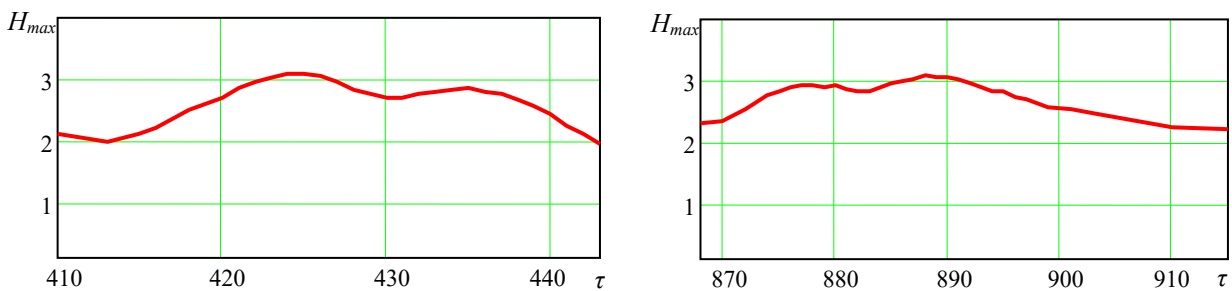


Fig. 4. The change with time of the maximum amplitude of the wave packets near the maximums of swing for the first maximum (left) and (right)

For the first package (left), the maximum speed in units of model 21.6, for the second package (right) the maximum swing speed is 21.7. That is, the movement of the crest of the anomalous wave occurs at the same speed. This speed is the group velocity of the packet, which is easy to see when considering the ratio from where.

$$\frac{\partial \zeta}{\partial \tau} = 21.6 = \frac{\partial x}{\partial t} \cdot \frac{k_0}{\omega \cdot (\alpha / 2)} = \frac{v_g}{v_{ph}} \cdot \frac{2}{\alpha}, \text{ and } \frac{v_g}{v_{ph}} \approx 0.54. \tag{9}$$

In the laboratory system, the change in the amplitude of the wave crest of the anomalous amplitude is more pronounced (Fig. 5). This qualitatively corresponds to the duration of the Peregrin autowave [9] in the laboratory reference frame. Although it should be noted that the Peregrin autowave corresponds to a different physical reality, where the dispersion of the wave is weak. It is easy to see that gravitational surface waves from expression (1) have a strong dispersion, and the NSE equation (3) in this case is strongly modified. However, in rest system of the wave packet (moving relative to the laboratory system) the abnormal amplitude wave lifetime is much longer.

From Fig. 4 it can be seen that the time of existence of an abnormal amplitude wave in the reference frame moving with the group velocity of the packet does not exceed 40 units in the model under consideration. Given its speed, a wave can go through hundreds of wavelengths (Fig. 6). It is worth noting that in the considered numerical experiment, at one time point, two waves of anomalous amplitude of 333 waves appeared in the observation area (Fig. 1) and during the time about 40 units of new waves did not occur, then people at sea may encounter this same wave more than once.
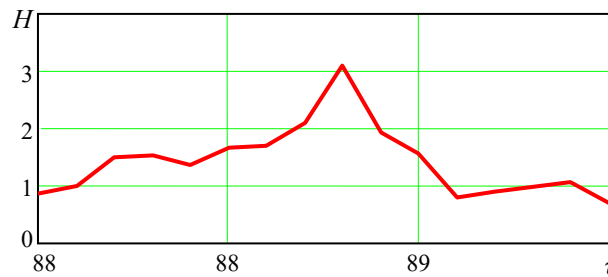


Fig. 5. Changing the amplitude of the wave of anomalous amplitude for the second packet, the maximum values of which were

In conclusion, it is possible to imagine the dynamics of the motion of the wave packet, the maximum range of which reached the highest value at the moment of time $\tau = 425$ in the region near $\zeta = -482$.
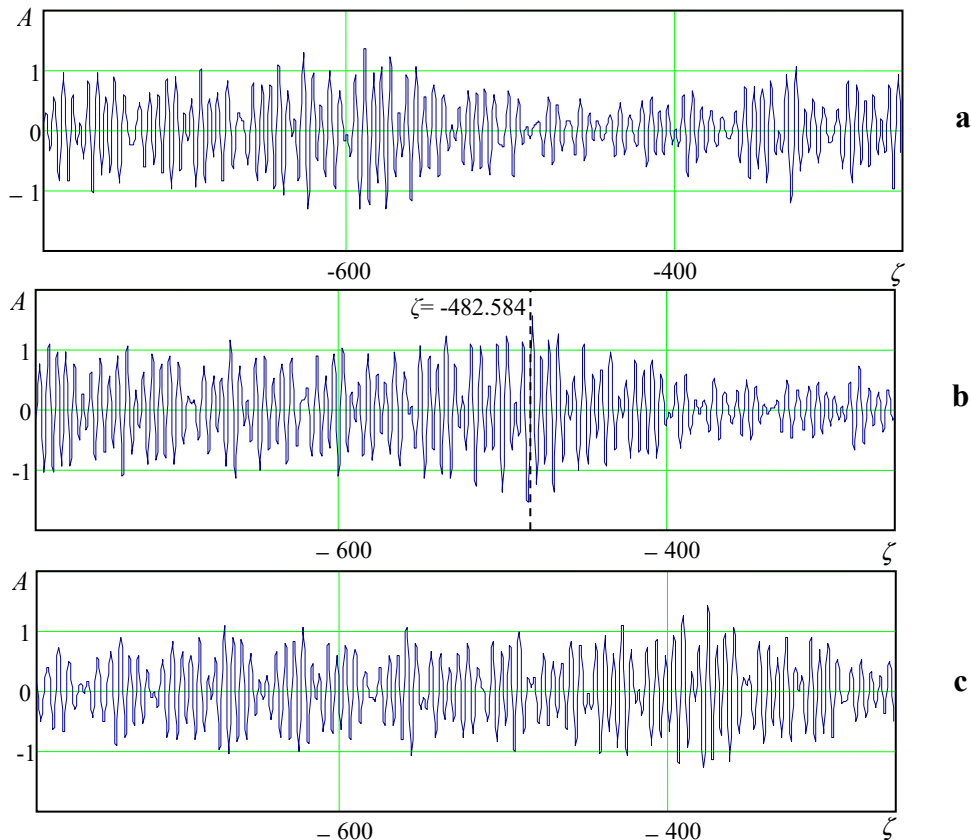


Fig.6. The dynamics of the wave packet, the maximum range of which reached its highest value at the time $\tau = 425$ instant in the area near $\zeta = -482$ for time points a) $\tau = 420$, b) $\tau = 425$, c) $\tau = 430$

## CONCLUSION

Waves of anomalous amplitude, as it turned out, are long-lived formations drifting in the direction of wave motion with the group velocity of the wave packet, which is half the phase velocity of the main wave. The longitudinal size of the wave packet practically does not change, the amplitude of the swing in the maximum first increases, then gradually decreases. The distance that the wave packet travels with a persisting anomalous sweep is at least equal to several hundred wavelengths and can reach hundreds of kilometers for 300 meter waves.

It is important to note that a wave excited as a result of wind exposure as a result of modulation instability forms a perturbation spectrum, whose energy is twice the energy of the main wave in the developed instability mode. It is the interference of the modes of this spectrum that forms a bizarre wave pattern, where from time to time anomalous amplitude waves appear.

On the one hand, the number of such waves in areas of strong wind exposure is much larger than the statistics of random interference processes allow. This is due to the influence of the main wave (its amplitude remains noticeably greater than the amplitudes of each of the modes of the wave packet) on the behavior of each pair of modes from the wave packet of the perturbation. This is the effect of forced interference imposed by the main wave. However, the simple calculation of such waves by means of space monitoring due to the small viewing area (frame) may also be inaccurate. Once formed, such waves are able to drift over considerable distances. Moreover, they may well fall into the next viewing frame, which will unreasonably increase the number of such waves in the entire observation zone. That is, estimates of the number of such modes can be overestimated.

As shown in [7, 8], the shape of the packet, which contains a wave of anomalous sweep, more than three times the average span of wave motion, is a train of three waves, similar to Peregrin's autowave [9]. V.E. Zakharov's remark that there are other types of anomalous waves of a given nature [10,11], based on observations [12,13], is explained by the results of [14], where it is shown that converging wave fronts can certainly generate more powerful abnormal perturbations of a different topology.

**ORCID IDs**
**Volodymyr M. Kuklin** http://orcid.org/0000-0002-0310-1582, **Eugen V. Poklonskiy** https://orcid.org/0000-0001-5682-6694

## REFERENCES

[1] V.I. Karpman, *Нелинейные волны в диспергирующих средах* [*Nonlinear waves in dispersing media*] (Nauka, Moscow, 1975), pp. 175. (in Russian)
[2] M.J. Lighthill, IMA Journal of Applied Mathematics, **1**(3), 269–306 (1965), https://doi.org/10.1093/imamat/1.3.269.
[3] E.V. Belkin. PhD-thesis (V.N. Karazin Kharkiv National University, Kharkiv, 2010), pp. 150. (in Russian)
[4] E.V. Belkin, A.V. Kirichok A.V. and V.M. Kuklin, VANT Ser. Plasma electronics and new acceleration methods, **68**(4), 291-295 (2010).
[5] E.V. Belkin, A.V. Kirichok, V.M. Kuklin and A.V. Priymak, East Eur. J. Phys. **1**(2), 4-39 (2014). (in Russian).
[6] V.M. Chernousenko, V.M. Kuklin, I.P. Panchenko and V.M. Vorob'ev, in *IV Int. Workshop on Nonlinear and Turbulent Proc. In Physics*. (Singapore, World Scientific, 1990), **2**, pp. 776-803.
[7] V.M. Kuklin. *Избранные главы. Теоретическая физика.* [*Selected Chapters. Theoretical Physics*] (V.N. Karazin Kharkiv National University, Kharkiv, 2018), pp. 224. (in Russian)
[8] A. Chabchoub, N. Hoffmann and N. Akhmediev, Physical Review Letters, **106**, 204502 (2011), https://doi.org/10.1103/PhysRevLett.106.204502.
[9] D. Peregrine. The ANZIAM Journal, **25**(1), 16–43 (1983), https://doi.org/10.1017/S0334270000003891.
[10] V.E. Zakharov, Eur. J. Mech. B Fluids. **18**(3), 327–344 (1999).
[11] A.I. Dyachenko and V.E. Zakharov, JETP Lett. **81**(6), 255–259 (2005), https://doi.org/10.1134/1.1931010.
[12] A.A. Kurkin and E.N. Pelinovsky, *Волны убийцы: Факты, теория и моделирование.* [*Killer waves: facts, theory and modeling*], (UNN, Nizhny Novgorod, 2004). (in Russian)
[13] P. Stansell, Ocean Engineering, **32**(8-9), 1015–1036 (2005), https://doi.org/10.1016/j.oceaneng.2004.10.016.
[14] A. Chabchoub, N. Hoffmann, M. Onorato, and N. Akhmediev, Physical Review X, **2**, 011015 (2012), https://doi.org/10.1103/PhysRevX.2.011015.

### ДО ПИТАННЯ ПРО ЧАСТОТУ І ПРОСТОРОВУ ПЕРІОДИЧНІСТЬ ПОЯВИ
### ХВИЛЬ АНОМАЛЬНОЇ АМПЛІТУДИ В ОКЕАНІ

**В.М. Куклін, Е.В. Поклонский**
*Харківський національний університет ім. В. Н. Каразіна, Харків, Україна*
*м. Свободи 4, м. Харків, Україна, 61022*

В роботі показано, що хвилі аномальної амплітуди є довгоживучими утвореннями. Вони дрейфують в напрямку хвильового руху з груповою швидкістю хвильового пакета, яка вдвічі менше фазової швидкості основної хвилі. Розмах хвилі (відстань від горба до западини) аномальної амплітуди більш ніж втричі перевершує середнє значення розмахів хвильового руху. В результаті модуляційної нестійкості цієї хвилі формується спектр збуджень, енергія якого вдвічі більше енергії основної хвилі в розвиненому режимі процесу. Просторовий розмір хвильового пакета практично не змінюється, амплітуда розмаху в максимумі спочатку наростає, потім поступово зменшується. Число таких хвиль в зонах сильного вітрового впливу значно більше, ніж це дозволяє статистика випадкових інтерференційних процесів. Це обумовлено впливом основної хвилі (її

амплітуда залишається помітно більше амплітуд кожної з мод хвильового пакета) на поведінку кожної пари мод з хвильового пакета обурення. У лабораторній системі тривалість виникнення аномальної хвилі якісно збігається з часом існування автоволни Перегрина. Хоча слід зазначити, що автохвиля Перегрина відповідає іншої фізичної реальності, де дисперсія хвилі слабка. Гравітаційні поверхневі хвилі мають сильну дисперсією і рівняння НУШ в цьому випадку помітно модифікується. Однак в системі спокою хвильового пакету, (яка рухається відносно лабораторної системи) час життя хвилі аномальної амплітуди істотно більше. Відстань, яку проходить хвильової пакет з аномальним розмахом, відповідає кільком сотням довжин хвиль і може досягати сотень кілометрів. Простий підрахунок таких хвиль засобами космічного моніторингу через невелику зону (кадр) перегляду може виявитися неточним. Одного разу з'явившись, такі хвилі здатні дрейфувати на значні відстані. При цьому вони цілком можуть потрапити в наступний кадр перегляду. Тобто оцінки числа таких мод можуть бути завищені.

**КЛЮЧОВІ СЛОВА**: довгоживуча хвиля аномально амплітуди, океанське хвилювання, модуляційна нестійкість

## К ВОПРОСУ О ЧАСТОТЕ И ПРОСТРАНСТВЕННОЙ ПЕРИОДИЧНОСТИ ПОЯВЛЕНИЯ ВОЛН АНОМАЛЬНОЙ АМПЛИТУДЫ В ОКЕАНЕ

**В.М. Куклин, Е.В. Поклонский**
*Харьковский национальный университет имени В. Н. Каразина, Харьков, Украина*
*пл. Свободы 4, г. Харьков, Украина, 61022*

В работе показано, что волны аномальной амплитуды являются долгоживущими образованиями. Они дрейфуют в направлении волнового движения с групповой скоростью волнового пакета, которая вдвое меньше фазовой скорости основной волны. Размах волны (расстояние от горба до впадины) аномальной амплитуды в результате модуляционной неустойчивости, более чем втрое превосходит среднее значение размахов волнового движения. В результате модуляционной неустойчивости этой волны формируется спектр возмущения, энергия которого вдвое больше энергии основной волны в развитом режиме процесса. Пространственный размер волнового пакета практически не меняется, амплитуда размаха в максимуме сначала нарастает, потом постепенно убывает. Число таких волн в зонах сильного ветрового воздействия значительно больше, чем это разрешает статистика случайных интерференционных процессов. Это обусловлено влиянием основной волны (ее амплитуда остается заметно больше амплитуд каждой из мод волнового пакета) на поведение каждой пары мод из волнового пакета возмущения. В лабораторной системе продолжительность возникновения аномальной волны качественно совпадает с временем существования автоволны Перегрина. Хотя следует отметить, что автоволна Перегрина отвечает иной физической реальности, где дисперсия волны слабая. Гравитационные поверхностные волны обладают сильной дисперсией и уравнение НУШ в этом случае заметно модифицируется. Однако в движущейся относительно лабораторной системе покоя волны время жизни волны существенно больше. Расстояние, которое проходит волновой пакет с сохраняющимся аномальным размахом, по крайней мере равно нескольким сотням длин волн и может достигать сотен километров. Простой подсчет таких волн средствами космического мониторинга из-за небольшой зоны (кадра) просмотра может оказаться неточным. Однажды образовавшись, такие волны способны дрейфовать на значительные расстояния. При этом они вполне могут попасть в следующий кадр просмотра. То есть оценки числа таких мод могут быть завышены.

**КЛЮЧЕВЫЕ СЛОВА:** долгоживущая волна аномально амплитуды, океанское волнение, модуляционная неустойчивость

# EFFECT OF THE OSCILLATING ELECTRIC FIELD DUE TO THE OSCILLATING ELECTRIC DIPOLE ON RAMAN LINES

Khanna M. Kapil[1]*, Murei K. Gilbert[2]

*[1]Department of Physics, University of Eldoret*
*P.O Box 1125-30100, Eldoret, Kenya*
*[2]Department of Physics, Laikipia University*
*P.O. Box 1100-20300, Nyahururu, Kenya*
*E-mail: [1]*khannak700@gmail.com, [2]gmurei@laikipia.ac.ke*
Received September 16, 2019; revised November 22, 2019; accepted November 22, 2019

Raman Effect is the measurement of the intensity and wavelength of the inelastically scattered radiation that falls on a molecule. The electric field of the incident radiation polarizes the molecule on which it falls and this leads to the creation of an oscillating dipole. The incident polarized laser light is inelastically scattered by the molecular sample. The scattered light contains modified wavelengths called the Stokes and anti-Stokes lines or wavelengths. The oscillating electric dipole, created by the incident radiation, creates an oscillating electric field around it. Since the oscillating electric field of the incident radiation creates an oscillating electric dipole that create an oscillating electric field around it, it was surmised that this oscillating electric field can affect the frequency of vibration or oscillation of the oscillating electric dipole that produces it. This novel effect will change the frequency (frequencies) of the scattered radiation resulting in Stokes and anti-Stokes lines with modified frequencies. This theoretical research and its importance can be understood like this. For instance, if there are two cells or molecules, side by side, in which one is a healthy cell and the other is cancerous, or two different types of molecules are sitting side by side, this types of scattering should be able to distinguish one from the other since the Stokes and anti-Stokes lines from the two molecules will not be identical. Thus, the incident radiation of angular frequency $\omega_1$ polarizes the charges of the molecule on which it falls and this leads to the creation of an oscillating dipole of frequency $\omega_2$. The oscillating dipole creates an oscillating electric field that can create additional frequency of the oscillating dipole that created it, and let this be $\omega_D$. Then the Raman lines can have frequencies $(\omega_1+\omega_2+\omega_D)$, $(\omega_1+\omega_2-\omega_D)$, $(\omega_1-\omega_2+\omega_D)$, and $(\omega_1-\omega_2-\omega_D)$. Depending on the relative magnitudes of $\omega_2$ and $\omega_D$, Raman lines will be designated as Stokes and Anti-Stokes lines. Due to the law of conservation of energy, $\omega_D$ will be less than $\omega_2$ since an oscillating dipole cannot create field of frequency more than its own frequency. Hence the frequencies $(\omega_1-\omega_2+\omega_D)$ and $(\omega_1-\omega_2-\omega_D)$ correspond to Stokes lines, and frequencies. $(\omega_1+\omega_2+\omega_D)$ and $(\omega_1+\omega_2-\omega_D)$ will correspond to Anti-Stokes lines. Calculations for Stokes and Anti-stokes lines have been done for some molecules, namely Ammonia compound ($NH_3$), Nitrousoxide compound ($N_2O$), Water ($H_2O$), Sulphur dioxide compound ($SO_2$), Ozone compound ($O_3$). Calculations have also been done for compounds containing carbon, such as Dichloromethane compound ($CH_4Cl_2$), Formic acid compound ($CH_2O_2$), Methanol compound ($CH_4O$), Benzene compound ($C_6H_6$), Propane compound ($C_3H_8$), and Carbonyl chloride compound ($Cl_2CO$). The theory developed predicts new phenomena of getting Stokes and anti-Stokes lines with modified wavelengths which have not been observed experimentally as of to-day.

**KEYWORDS:** electric dipole, Raman lines, Stokes lines, anti-Stokes lines, oscillating electric dipole

Inelastic scattering of light by a molecular sample was first predicted theoretically by Adolf Smekel [1] in 1923. The phenomenon was experimentally discovered in 1928 by an Indian Scientist C.V Raman [2,3]. He discovered the phenomena using filtered sunlight as a monochromatic source of photons, a colored filter as a monochromator, and a human eye as a detector. Originally Raman and Krishna observed the scattering of spectrally filtered sunlight from a liquid and observed that the scattered light contained very weak signals of light that had slightly different frequencies compared to the frequency of the incoming light. Some of the incident photons are elastically scattered (Rayleigh scattering), and it is found that hardly 1 in $10^7$ incident photons are elastically scattered. The number of inelastically scattered photons is much less. Quantum-mechanically, this process of scattering is interpreted as the shifted quantum states of the molecule. However, the intensity of the Raman signal is very low since hardly in 1 in $10^8$ incident photons are inelastically scattered. The shifted quantum states lead to shifted frequencies in the scattering process, and these appear symmetrically around the frequency of the exciting radiation. This leads to the conclusion that the molecule may be either excited or de-excited during the scattering process. If the molecule is excited before the scattering event, it leads to Stokes scattering i.e., if $\omega_{laser}$ is the frequency of the incident light and $\omega_s$ is the frequency of the scattered light, then the Raman shift in frequency (Stokes lines) is $\Delta\omega=\omega_{laser}-\omega_s$ which is positive. However, when the molecule is de-excited, the Raman shift in the frequency will be such that $\omega_s>\omega_{laser}$, and these Raman lines are called anti-Stokes lines. Hence, the frequencies of the Raman lines depend on the states of excitation of the molecule on which the incident radiation falls.

Now it is well known that when light falls on a molecule, the molecule is polarized by the electric field of the incident radiation (also called the incident field). Both linear and nonlinear optical effects can be understood as resulting from the interaction of the electric field component of the incident electromagnetic radiation with the charged particles of the molecule or material. In general, an applied electric field moves positive charges in the direction of the electric field, and negative charges in the opposite direction. The electric field associated with the visible and near-infrared range of the electromagnetic spectrum oscillates at frequencies in the range of the 103 THz. These driving frequencies are quite large such that light particles, like electrons in the molecules or material follow the rapid oscillations of the driving field. This

is not the case for nuclei that are heavy particles. As a result of the driving fields, the bound electrons are slightly displaced from their equilibrium position. This process creates induced oscillating dipole that creates oscillating electric field. This oscillating electric field can affect the state of polarization of the molecule that created it, and also the quantum states of the molecule. It is this phenomenon that motivated us to study its effect on the frequencies of the resulting Stokes and anti-Stokes lines. It needs to be emphasized that the spectroscopic technique based on Raman scattering has been widely used in chemical analysis, study of biomolecules, crystals and powders, food industry, medical and environmental applications. The greatest advantage of this technique is that it requires very little or no sample preparation. The theory developed in this manuscript and the experimental techniques that may be developed in future could be very useful in medical science since the technique could be used to locate the disease in hidden parts of the body without destroying or affecting any internal structure or organs of the body [4].

We will now describe the basic ideas that will lead to the development of the theory suggested in this paper. It is well known that a dipole creates an electric field, say $E_d$, that polarizes the solid [5-7]. If all the molecules of the system are at one place, they all get polarized (i.e. each molecule acquires an induced dipole moment) and each causes an electric field at some point $r_0$ where the local field is calculated. An oscillating molecule under the action of an electric field ($E_i$) from the incident radiation will develop an oscillating dipole resulting in the creation of an oscillating electric field ($E_L$). The magnitude of the molecular response is proportional to the sum of all the fields ($E_i+E_L$) acting at the same or some point $r_0$, and the sum of these fields is called primary field. More explicitly we write the fields at the position $r_0$ at the time $t$ as, $E_i(r_0, t)$ and $E_L(r_0,t)$, and the primary field say,

$$E_p(r_0,t)=E_i(r_0,t)+E_L(r_0,t). \tag{1}$$

Now if $\omega_1$ is the frequency of the incident radiation, $\omega_2$ is the frequency of vibration of the induced of the molecule receiving the incident radiation (the frequency of the induced dipole is not to be confused with the natural frequency of vibration of the molecule), and $\omega_D$ is the frequency of the oscillating electric field created by the oscillating molecular dipole, then the frequencies of the Raman scattering or Raman lines or Raman scattered radiation can be,

$$\omega_1+\omega_2+\omega_D, \tag{2}$$

$$\omega_1+\omega_2-\omega_D, \tag{3}$$

$$\omega_1-\omega_2+\omega_D, \tag{4}$$

$$\omega_1-\omega_2-\omega_D. \tag{5}$$

Depending on the relative magnitudes of $\omega_2$ and $\omega_D$ with respect to $\omega_1$, we can get Stokes and anti-Stokes lines. If $\omega_2>\omega_D$, then the following frequencies will correspond to anti-Stokes lines, i.e.

$$\omega_1+\omega_2+\omega_D \text{ and } \omega_1+\omega_2-\omega_D, \tag{6}$$

whereas the following will correspond to Stokes lines

$$\omega_1-\omega_2+\omega_D \text{ and } \omega_1-\omega_2-\omega_D. \tag{7}$$

Now $\omega_1$ is the frequency of the incident radiation and this will be known since the frequency of the selected incident light radiation for the experiment will be known. Then $\omega_2$ is the frequency of oscillation of the induced dipole and this will also be known for a given molecule. Now to calculate $\omega_D$, we have to first calculate the oscillating electric field ($E_L$) of the oscillating dipole of the molecule, and then calculate the energy due to this oscillating electric field. If this energy is denoted by $U$, then $U=\hbar\omega_D$ will give the value of $\omega_D$.

Some of the important objectives of this research are as follows:

(i) Since the incident radiation creates oscillating dipole, and the oscillating dipole creates oscillating electric field, it must therefore affect the oscillating dipole. This in turn leads us to $\omega_D$ that results in Stokes and anti-Stokes lines with new frequencies.

(ii) Electromagnetic field emitted or scattered by molecules located in close proximity can be used in areas such as chemical and material science art restorations, military, plasmonics nanoparticles, the existence of cancerous and healthy cells, infections and hereditary diseases [8-15].

(iii) It may motivate scientist to develop intense electric field lasers so that the value of $\omega_D$ can be increased such that the phenomena can be easily observed experimentally.

As usual there could be a larger or small gap between the proposed theory and the design of an experiment that can lead to the observation of the phenomena. For instance, Raman scattering was theoretically proposed in 1923, but discovered in 1928 [1,2]. The theory of simulated emission was proposed by Albert Einstein in 1917, but laser was discovered in 1960. Quite a few examples such, assuperconductivity, can be worth mentioning.

**FORMULATION**

We have to calculate the oscillating electric field ($\mathbf{E_L}$) of a dipole (oscillating dipole) when the charge at its two ends is alternating with the angular frequency $\boldsymbol{\omega}$ ($\boldsymbol{\omega=2\pi f}$). Thus we have alternating charges $^+\mathbf{q}$ and $^-\mathbf{q}$ such that,

$$q = Q\cos\omega t, \tag{8}$$

where Q – Is the maximum value of the charge on either sides.

Now to calculate the value of the oscillating electric field ($\mathbf{E_L}$) at the point of observation P, we have to know the value of the electric field at point P due to both charges, $^+\mathbf{q}$ and $^-\mathbf{q}$. Thus to know the value of $E_L$ at P due to the charges, we must consider that the apparent value of the charge is not $\mathbf{q}$ given as by Eqn. (8), but the value of q at some earlier moment. This is the moment at which a disturbance would have had to be emitted by the charge, and travelling at the speed of light $\mathbf{c}$, to reach at the point P. The time of delay is $\frac{r_1}{c}$, and hence the apparent value of the charge will be

$$q_1 = Q\cos\omega\left(t - \frac{r_1}{c}\right), \tag{9}$$

where $r_1$- distance between the center of the dipole and the point of observation P.

Similarly, for the charge $q_2$, we write

$$q_2 = -Q\cos\omega\left(t - \frac{r_2}{c}\right). \tag{10}$$

It should be noted that the apparent charge is a function of its distance from the observer (point P), and this is clear from Eqn. (9) and Eqn. (10). Secondly, with the oscillating dipole, the amount of this time delay is different for the two charges since they are at different distances ($r_1 \neq r_2$) from P(only when $\Theta = 90^0 = \frac{\pi}{2}$,that $r_1=r_2$). Thus viewed in this way, the apparent total charge on the dipole is not zero ($q_1 \neq q_2$) but fluctuates between positive and negative values. The apparent charge $q_{app}$ can be written as,

$$q_{app} = q_1 + q_2 = Q\left[\cos\omega\left(t - \frac{r_1}{c}\right) - \cos\omega\left(t - \frac{r_2}{c}\right)\right]$$
$$= -2Q\sin\omega\left(t - \frac{r}{c}\right)\sin\left(\frac{\omega l}{2c}\cos\theta\right), \tag{11}$$

where it is assumed that $r \gg l$, and

$$r = \frac{1}{2}(r_1 + r_2) \text{and} r_1 - r_2 \cong -l\cos\theta, \tag{12}$$

where $l$ is the distance between the charges $^+$q and $^-$q.

We should note that when $\boldsymbol{\omega} = 0$ (static dipole), $q_{app} = 0$, the field is localized and no oscillations. Now since $\boldsymbol{\omega}$ is finite and the apparent value of the total charge is not zero, the field has a longer range, and falls off less rapidly with the distance. Assuming that the length of the dipole is very short compared to the wavelength, λ, of the disturbance it sends out, we can write,

$$\frac{l}{\lambda} = \frac{\omega l}{2\pi c} \ll 1 \quad \left(\lambda = \frac{c}{f} = \frac{2\pi c}{\omega}\right). \tag{13}$$

Using Eqn. (13) in Eqn. (11), we can write $\sin\theta \cong \theta$ when $\theta$ is very small, and hence Eqn. (11) can be written as,

$$q_{app} \cong -\frac{\omega l}{c}Q\cos\theta . \sin\omega\left(t - \frac{r}{c}\right). \tag{14}$$

Here $Ql$ is the maximum value of the dipole moment $p_0$ of the dipole, such that we can write,

$$p_0 = Ql, \tag{15}$$

and

$$q_{app} = -\frac{\omega p_0}{c}\cos\theta . \sin\omega\left(t - \frac{r}{c}\right). \tag{16}$$

We have now to evaluate the potential, $v$, which the dipole produces at the point P. If $v_1$ is the potential at P due to the upper charge, and $v_2$ is the potential at P due to the lower charge, then,

$$v = v_1 + v_2, \tag{17}$$

where

$$v_1 = \frac{q_1}{4\pi\varepsilon_0 r_1}, \tag{18}$$

$$v_2 = \frac{q_2}{4\pi\varepsilon_0 r_2}. \tag{19}$$

Combining Eqns. (9), (10), (17), (18) and (19), we can write,

$$v = v_1 + v_2 = \frac{Q}{4\pi\varepsilon_0}\left[\frac{\cos\omega\left(t-\frac{r_1}{c}\right)}{r_1} - \frac{\cos\omega\left(t-\frac{r_2}{c}\right)}{r_2}\right]. \tag{20}$$

Assuming that the size of the dipole, $l$ is very small compared to $r_1$ and $r_2$ then $r_1$ and $r_2$ may be almost equal to each other. Using the approximations, we get,

$$v = -\frac{Ql}{4\pi\varepsilon_0}\frac{\partial}{\partial z}\left[\frac{\cos\omega\left(t-\frac{r}{c}\right)}{r}\right]. \tag{21}$$

Eqn. (21) gives the basic formula for the potential due to the oscillating dipole. By putting $\boldsymbol{\omega} = 0$, we get the potential for a stationary dipole. Eqn. (21) can be rewritten as,

$$v = -\frac{Ql}{4\pi\varepsilon_0}\frac{\partial}{\partial r}\left[\frac{\cos\omega\left(t-\frac{r}{c}\right)}{r}\right]\frac{\partial r}{\partial z}.$$

$$= -\frac{Ql}{4\pi\varepsilon_0}.\cos\theta.\frac{\partial}{\partial r}\left[\frac{\cos\omega\left(t-\frac{r}{c}\right)}{r}\right]$$

$$= \frac{Ql}{4\pi\varepsilon_0}\cos\theta.\left[\frac{\cos\omega\left(t-\frac{r}{c}\right)}{r^2} - \frac{\omega}{c}\frac{\sin\omega\left(t-\frac{r}{c}\right)}{r}\right]. \tag{22}$$

Here in Eqn. (22), the first term refers to the static potential ($\boldsymbol{\omega} = 0$), and the second term gives the electrostatic potential that would be produced by the apparent charge $q_{app}$ given by Eqn. (16). In order to get the limiting form of $v$ for large distances, r. It is evident that the second term in Eqn. (22) becomes quite large compared to the first term (since the second term has r in the denominator, and the first term has $r^2$ in the denominator). Thus the asymptotic value of $v$ can be written as,

$$v \cong -\frac{Ql\omega}{4\pi\varepsilon_0 c}\cos\theta.\frac{\sin\omega\left(t-\frac{r}{c}\right)}{r}. \tag{23}$$

From Eqn. (23) we can calculate the electric field strength E in polar coordinates $r, \theta, \emptyset$. It can be shown that at large distance $r$, the components of E that are denoted by $E_r$ (in the direction of increasing r), $E_\theta$, (in the direction of increasing $\theta$), and $E_\emptyset$ (in the direction of increasing $\emptyset$) have different values. In fact,

$$E_r \cong 0 \ \ and \ E_\emptyset = 0, \tag{24}$$

whereas,

$$E_\theta \cong \frac{Ql\omega^2}{4\pi\varepsilon_0 c^2}\sin\theta\frac{\cos\omega\left(t-\frac{r}{c}\right)}{r}. \tag{25}$$

Eqn. (25) shows that at large distances from the dipole the electric field E ($\cong E_\theta$) becomes entirely transverse, at whatever direction relative to the dipole it is measured, and transversality is a necessary condition for the plane electromagnetic radiation. (At large distances from the source, any wave become a plane wave).

It is important to understand that Raman Effect is a result of inelastic interaction between light and matter. This interaction can in turn, generate linear and nonlinear optical phenomena,depending on the strength of the applied electric field and the nature of the sample on which light falls. For instance, the electric field intensities must be higher than typically $10^9$ V/m to make the contributions of the induced dipole moment large enough to create a nonlinear effect in the medium [16]. Such high electric field intensities can be obtained by using giant- pulse lasers. In fact, linear scattering can be obtained when the frequency of the incident light (stream of photons) $\boldsymbol{\omega}_0$ is far away from the molecular electronic absorption frequency $\boldsymbol{\omega}_1$ such that $\omega_v \ll \omega_0 \ll \omega_1$, where $\omega_v$ is the vibrational frequency of the molecule. This is in line with the restriction of photon wavelength (energy) which lies in between the visible and near-visible regions and corresponds to vibrational and electronic molecular excitation energies. In this case, the photon transfers its energy ($\hbar\omega_0$) to the whole molecule in order to displace the electron and produce an induced dipole moment. However, the electron remains bound since the large mass of the molecule does not allow such a transition. Hence, most of the incident light (photon) is transmitted without change of frequency and this type of scattering is called Rayleigh scattering, and is also known as elastic scattering.

It is necessary to understand that the origin of the Stokes and anti-Stokes scattering can be explained in terms of energy transfer between the incident light (photons) and the scattering system. When the molecule is initially excited to a level above the ground state, the scattered photon will gain energy and this scattering is termed as anti-Stokes scattering when the energy of the scattered radiation is $\hbar(\omega_0 + \omega_v)$. However, if the molecule is initially at the lowest level (the ground state), the scattered photon will lose energy and is called Stokes scattering whose energy is $\hbar(\omega_0 - \omega_v)$ [17].

The magnetic field associated with the radiation emitted by the oscillating dipole is, B, i.e.

$$B = \frac{Ql\omega^2}{4\pi\varepsilon_0 c^3}\sin\theta.\frac{\cos\omega\left(t-\frac{r}{c}\right)}{r}. \tag{26}$$

Now $E_\theta$ and B are at right angles to **r**, and at right angles to each other. The power radiated by the oscillating dipole will begiven by the Pointing vector 'S' [18] which is,

$$S = \frac{1}{\mu_0}(ExB), \tag{27}$$

where

$$\mu_0 = \frac{1}{\varepsilon_0 c^2}. \tag{28}$$

The average total power radiated is the surface integral of S over a sphere of radius r, and hence we get [6],

$$S = \frac{\mu_0\omega^4 p_0^2}{12\pi c} \quad where \ p_0 = Ql \tag{29}$$

$$= \frac{\omega^4 p_0^2}{12\pi\varepsilon_0 c^3} \tag{30}$$

If $\omega_D$ is the angular frequency ($\omega_D = 2\pi f_D$) associated with this field, then we can write,

$$S = \hbar\omega_D. \tag{31}$$

Between Eqns. (30) and (31), we get,

$$\omega_D = \frac{\omega^4 p_0^2}{12\pi\varepsilon_0 c^3\hbar}. \tag{32}$$

Another method of calculating the energy, U, associated with the electric field $E_\theta$ will be to calculate the work done by the electricfield $E_\theta$ in the displacement of the charge say Q, i.e.,

$$U = E_\theta.q.r \tag{33}$$

$$= \frac{Qql\omega^2\sin\theta}{4\pi\varepsilon_0 c^2}\left[\cos\omega\left(t-\frac{r}{c}\right)\right] \tag{34}$$

Now

$$\cos x = 1 - \frac{x^2}{2!} + \frac{x^4}{4!} +, \tag{35}$$

and for small $x$, we can approximate,

$$\cos x = \left(1 - \frac{x^2}{2!}\right), \tag{36}$$

and hence U becomes,

$$U = \frac{Qql\omega^2\sin\theta}{4\pi\varepsilon_0 c^2} - \frac{Qql\omega^2\sin\theta}{4\pi\varepsilon_0 c^2}.\omega^2\left(t-\frac{r}{c}\right)^2. \tag{37}$$

Under initial conditions at just t = 0, the second term will have $c^4$ in the denominator, and this term will be very small compared to the first term that will have $c^2$ in the denominator. Thus Eqn. (37) gives U as,

$$U = \frac{Qql\omega^2\sin\theta}{4\pi\varepsilon_0 c^2} \tag{38}$$

Generally, the observations are made perpendicular to the z-axis, $\theta = 90^0$, $\sin\theta = 1$, and hence,

$$U = \frac{Qql\omega^2}{4\pi\varepsilon_0 c^2} \tag{39}$$

$$= \frac{qp_0\omega^2}{4\pi\varepsilon_0 c^2}\ (p_0 = Ql) \tag{40}$$

here Q=charge of one end of the electric dipole, q=electron charge.

Now if $\omega_D$ is the angular frequency associated with this energy, then,

$$U = \hbar\omega_D \ or \ \omega_D = \frac{U}{\hbar} = \frac{p_0\omega^2 q}{4\pi\varepsilon_0 c^2\hbar} \tag{41}$$

Now energy S given by Eqn. (30) is the energy radiated by the oscillating dipole, whereas the energy U given by Eqn. (40) is the energy fed into the oscillating dipole that was responsible for the creation of the oscillating electric field. It is this energy that can contribute to the Raman-shifted-frequencies or Raman scattering. Hence $\omega_D$ given by Eqn. (41) will affect the Stokes and anti-Stokes frequencies or lines.

## RESULTS

Equations (41) have been used to determine angular frequency $\omega_D$ for some compounds whose Electric dipole moments and their angular frequency of vibration of the molecule were obtained from literature [19].

We considered krypton laser of the following wavelength (in nm):799.3, 752.5, 728.7, 676.4, 647.1, 632.8, 568.2, 530.9, 514.5, 488.0, 454.6, and 416.0, as incident radiation. The results of each compound considered are given in their respective tables below:

**Ammonia compound (NH₃)**

Electric dipole moment ($p_o$) = 1.4718 Debye

Angular frequency of vibration of the molecule ($\omega_2$) = $6.2907\times10^{14}s^{-1}$.

Angular frequency due to the electric dipole created by the vibrating molecule ($\omega_D$) = $1.9405\times10^{14}s^{-1}$

| $\omega_1\times10^{14}s^{-1}$ | $\omega_1+\omega_2+\omega_D$ | $\omega_1+\omega_2-\omega_D$ | $\omega_1-\omega_2-\omega_D$ | $\omega_1-\omega_2+\omega_D$ |
|---|---|---|---|---|
| 45.3173 | 53.5485 | 49.6675 | 37.0861 | 40.9671 |
| 41.4694 | 49.7006 | 45.8196 | 33.2382 | 37.1192 |
| 38.6311 | 46.8623 | 42.9813 | 30.3999 | 34.2809 |
| 36.6414 | 44.8726 | 40.9916 | 28.4102 | 32.2912 |
| 35.5095 | 43.7407 | 39.8597 | 27.2783 | 31.1593 |
| 33.1785 | 41.4097 | 37.5287 | 24.9473 | 28.8283 |
| 29.7914 | 38.0226 | 34.1416 | 21.5602 | 25.4412 |
| 29.1331 | 37.3643 | 33.4833 | 20.9019 | 24.7829 |
| 27.8711 | 36.1023 | 32.2213 | 19.6399 | 23.5209 |
| 25.8707 | 34.1019 | 30.2209 | 17.6395 | 21.5205 |
| 25.0525 | 33.2837 | 29.4027 | 16.8213 | 20.7023 |
| 23.8564 | 32.0876 | 28.2066 | 15.6252 | 19.5062 |

**Nitrous Oxide (N₂O) compound**

Electric dipole moment ($p_o$) = 0.16083 Debye

Angular frequency of vibration of the molecule ($\omega_2$) = $4.1927\times10^{14}s^{-1}$.

Angular frequency due to the electric dipole created by the vibrating molecule ($\omega_D$) = $1.4217\times10^{13}s^{-1}$.

| $\omega_1\times10^{14}s^{-1}$ | $\omega_1+\omega_2+\omega_D$ | $\omega_1+\omega_2-\omega_D$ | $\omega_1-\omega_2-\omega_D$ | $\omega_1-\omega_2+\omega_D$ |
|---|---|---|---|---|
| 45.3173 | 49.6522 | 49.3678 | 40.9824 | 41.2668 |
| 41.4694 | 45.8043 | 45.5199 | 37.1345 | 37.4189 |
| 38.6311 | 42.9660 | 42.6816 | 34.2962 | 34.5806 |
| 36.6414 | 40.9763 | 40.6919 | 32.3065 | 32.5909 |
| 35.5095 | 39.8444 | 39.5600 | 31.1746 | 31.4590 |
| 33.1785 | 37.5134 | 37.2290 | 28.8436 | 29.1280 |
| 29.7914 | 34.1263 | 33.8419 | 25.4565 | 25.7409 |
| 29.1331 | 33.4680 | 33.1836 | 24.7982 | 25.0826 |
| 27.8711 | 32.2060 | 31.9216 | 23.5362 | 23.8206 |
| 25.8707 | 30.2056 | 29.9212 | 21.5358 | 21.8202 |
| 25.0525 | 29.3874 | 29.3874 | 20.7176 | 21.0020 |
| 23.8564 | 28.1919 | 27.9069 | 19.2515 | 19.8059 |

**Water (H₂O) compound**

Electric dipole moment ($p_o$) = 1.8546 Debye

Angular frequency of vibration of the molecule ($\omega_2$) = $6.8941\times10^{14}s^{-1}$.

Angular frequency due to the electric dipole created by the vibrating molecule ($\omega_D$) = $4.4327\times10^{14}s^{-1}$.

| $\omega_1\times10^{14}s^{-1}$ | $\omega_1+\omega_2+\omega_D$ | $\omega_1+\omega_2-\omega_D$ | $\omega_1-\omega_2-\omega_D$ | $\omega_1-\omega_2+\omega_D$ |
|---|---|---|---|---|
| 45.3173 | 56.6441 | 47.7787 | 33.9905 | 42.8559 |
| 41.4694 | 52.7962 | 43.9308 | 30.1426 | 39.0080 |
| 38.6311 | 49.9579 | 41.0925 | 27.3043 | 36.1697 |
| 36.6414 | 47.9682 | 39.1028 | 25.3146 | 34.1800 |
| 35.5095 | 46.8363 | 37.9709 | 24.1827 | 33.0481 |
| 33.1785 | 44.5053 | 35.6399 | 21.8517 | 30.7171 |
| 29.7914 | 41.1182 | 32.2528 | 18.4646 | 27.3300 |
| 29.1331 | 40.4599 | 31.5945 | 17.8063 | 26.6717 |
| 27.8711 | 39.1979 | 30.3325 | 16.5443 | 25.4097 |
| 25.8707 | 37.1975 | 28.3321 | 14.5439 | 23.4093 |
| 25.0525 | 36.3793 | 27.5139 | 13.7257 | 22.5911 |
| 23.8564 | 35.1832 | 26.3178 | 12.5296 | 21.3950 |

**Sulphur dioxide (SO₂) compound**

Electric dipole moment $(p_o)$ = 1.63Debye

Angular frequency of vibration of the molecule $(\omega_2)$ = $2.1699 \times 10^{14} s^{-1}$.

Angular frequency due to the electric dipole created by the vibrating molecule $(\omega_D)$ = $3.859 \times 10^{13} s^{-1}$

| $\omega_1 \times 10^{14} s^{-1}$ | $\omega_1+\omega_2+\omega_D$ | $\omega_1+\omega_2-\omega_D$ | $\omega_1-\omega_2-\omega_D$ | $\omega_1-\omega_2+\omega_D$ |
|---|---|---|---|---|
| 45.3173 | 47.8731 | 47.1013 | 42.7615 | 43.5333 |
| 41.4694 | 44.0252 | 43.2534 | 38.9136 | 39.6854 |
| 38.6311 | 41.1869 | 40.4151 | 36.0753 | 36.8471 |
| 36.6414 | 39.1972 | 38.4254 | 34.0856 | 34.8574 |
| 35.5095 | 38.0675 | 37.2935 | 32.9537 | 33.7255 |
| 33.1785 | 35.7343 | 34.9625 | 30.6227 | 31.3945 |
| 29.7914 | 32.3472 | 31.5754 | 27.2356 | 28.0074 |
| 29.1331 | 31.6889 | 30.9171 | 26.5773 | 27.3491 |
| 27.8711 | 30.4269 | 29.6551 | 25.3153 | 26.0871 |
| 25.8707 | 28.4265 | 27.6547 | 23.3149 | 24.0867 |
| 25.0525 | 27.6083 | 26.8365 | 22.4967 | 23.2685 |
| 23.8564 | 26.4122 | 25.6404 | 21.3006 | 22.0724 |

**Ozone (O₃) compound**

Electric dipole moment $(p_o)$ = 0.5337 Debye

Angular frequency of vibration of the molecule $(\omega_2)$ = $2.0794 \times 10^{14} s^{-1}$.

Angular frequency due to the electric dipole created by the vibrating molecule $(\omega_D)$ = $1.161 \times 10^{13} s^{-1}$.

| $\omega_1 \times 10^{14} s^{-1}$ | $\omega_1+\omega_2+\omega_D$ | $\omega_1+\omega_2-\omega_D$ | $\omega_1-\omega_2-\omega_D$ | $\omega_1-\omega_2+\omega_D$ |
|---|---|---|---|---|
| 45.3173 | 47.5128 | 47.2806 | 43.1218 | 43.3540 |
| 41.4694 | 43.6649 | 43.4327 | 39.2739 | 39.5061 |
| 38.6311 | 40.8266 | 405944 | 36.4356 | 36.6678 |
| 36.6414 | 38.8369 | 38.6047 | 34.4459 | 34.6781 |
| 35.5095 | 37.7045 | 37.4725 | 33.3140 | 33.5462 |
| 33.1785 | 35.3740 | 35.1415 | 30.9830 | 31.2152 |
| 29.7914 | 31.9869 | 31.7547 | 27.5959 | 27.8281 |
| 29.1331 | 31.3286 | 31.0961 | 26.9376 | 27.1698 |
| 27.8711 | 30.0666 | 29.8344 | 25.6756 | 25.6756 |
| 25.8707 | 28.0662 | 27.8340 | 23.6752 | 23.9074 |
| 25.0525 | 27.2480 | 27.0158 | 22.8570 | 23.0892 |
| 23.8564 | 26.0519 | 25.8197 | 21.6609 | 21.8931 |

**Compounds with Carbon**

**Dichloromethane (CH₄CL₂) compound**

Electric dipole moment $(p_o)$ = 1.60 Debye

Angular frequency of vibration of the molecule $(\omega_2)$ = $5.6537 \times 10^{14} s^{-1}$.

Angular frequency due to the electric dipole created by the vibrating molecule $(\omega_D)$ = $2.5719 \times 10^{14} s^{-1}$.

| $\omega_1 \times 10^{14} s^{-1}$ | $\omega_1+\omega_2+\omega_D$ | $\omega_1+\omega_2-\omega_D$ | $\omega_1-\omega_2-\omega_D$ | $\omega_1-\omega_2+\omega_D$ |
|---|---|---|---|---|
| 45.3173 | 53.5429 | 48.3991 | 37.0917 | 42.2355 |
| 41.4694 | 49.6950 | 44.5512 | 33.2438 | 38.3876 |
| 38.6311 | 46.8567 | 41.8129 | 30.4055 | 35.5493 |
| 36.6414 | 44.8670 | 39.7232 | 28.4158 | 33.5596 |
| 35.5095 | 43.7351 | 38.5913 | 27.2839 | 32.4277 |
| 33.1785 | 41.4041 | 36.2605 | 24.9529 | 30.0967 |
| 29.7914 | 38.0170 | 32.8732 | 21.5658 | 26.7096 |
| 29.1331 | 37.3587 | 32.2149 | 20.9075 | 26.0513 |
| 27.8711 | 36.0967 | 30.9529 | 19.6455 | 24.7893 |
| 25.8707 | 34.0963 | 28.9525 | 17.6451 | 22.7889 |
| 25.0525 | 33.2781 | 28.1343 | 16.8269 | 21.9707 |
| 23.8564 | 32.0820 | 26.9382 | 15.6308 | 20.7746 |

**Formic acid ($CH_2O_2$) compound**
Electric dipole moment ($p_o$) = 1.425 Debye
Angular frequency of vibration of the molecule ($\omega_2$) = $4.9618 \times 10^{14} s^{-1}$.
Angular frequency due to the electric dipole created by the vibrating molecule ($\omega_D$) = $1.7642 \times 10^{14} s^{-1}$.

| $\omega_1 \times 10^{14} s^{-1}$ | $\omega_1 + \omega_2 + \omega_D$ | $\omega_1 + \omega_2 - \omega_D$ | $\omega_1 - \omega_2 - \omega_D$ | $\omega_1 - \omega_2 + \omega_D$ |
|---|---|---|---|---|
| 45.3173 | 52.0433 | 48.5149 | 38.5913 | 42.1197 |
| 41.4694 | 48.1954 | 44.6670 | 34.7434 | 38.2718 |
| 38.6311 | 45.3571 | 41.8287 | 31.9051 | 35.4335 |
| 36.6414 | 43.3674 | 39.8390 | 29.9154 | 33.4438 |
| 35.5095 | 42.2355 | 38.7071 | 28.7835 | 32.3119 |
| 33.1785 | 39.9045 | 36.3761 | 26.4525 | 29.9809 |
| 29.7914 | 36.5174 | 32.9890 | 23.0654 | 26.5938 |
| 29.1331 | 35.8591 | 32.3307 | 22.4071 | 25.9355 |
| 27.8711 | 35.5971 | 31.0687 | 21.1451 | 24.6735 |
| 25.8707 | 32.5967 | 29.0683 | 19.1447 | 22.6731 |
| 25.0525 | 31.7785 | 28.2501 | 18.3265 | 21.8549 |
| 23.8564 | 30.5824 | 27.0540 | 17.1304 | 20.6588 |

**Methanol ($CH_4O$) compound**
Electric dipole moment ($p_o$) = 1.7 Debye
Angular frequency of vibration of the molecule ($\omega_2$) = $6.9394 \times 10^{14} s^{-1}$.
Angular frequency due to the electric dipole created by the vibrating molecule ($\omega_D$) = $4.1168 \times 10^{14} s^{-1}$.

| $\omega_1 \times 10^{14} s^{-1}$ | $\omega_1 + \omega_2 + \omega_D$ | $\omega_1 + \omega_2 - \omega_D$ | $\omega_1 - \omega_2 - \omega_D$ | $\omega_1 - \omega_2 + \omega_D$ |
|---|---|---|---|---|
| 45.3173 | 56.3735 | 48.1399 | 34.2611 | 42.4947 |
| 41.4694 | 52.5256 | 44.2920 | 30.4132 | 38.6468 |
| 38.6311 | 49.6873 | 41.4537 | 27.5785 | 35.8085 |
| 36.6414 | 37.6976 | 39.4640 | 25.5852 | 33.8188 |
| 35.5095 | 46.5657 | 38.3321 | 24.4533 | 32.6869 |
| 33.1785 | 44.2347 | 36.0011 | 22.1223 | 30.3559 |
| 29.7914 | 40.8476 | 32.6140 | 18.7352 | 26.9688 |
| 29.1331 | 40.1893 | 31.9557 | 18.0769 | 26.3105 |
| 27.8711 | 38.9273 | 30.6937 | 16.8149 | 25.0485 |
| 25.8707 | 36.9269 | 28.6933 | 14.8145 | 23.0481 |
| 25.0525 | 36.1087 | 27.8751 | 13.9963 | 22.2299 |
| 23.8564 | 34.9126 | 26.6790 | 12.8004 | 21.0338 |

**Benzene ($C_6H_6$) compound**
Electric dipole moment ($p_o$) = 0.4236 Debye
Angular frequency of vibration of the molecule ($\omega_2$) = $4.3228 \times 10^{14} s^{-1}$.
Angular frequency due to the electric dipole created by the vibrating molecule ($\omega_D$) = $3.9806 \times 10^{13} s^{-1}$.

| $\omega_1 \times 10^{14} s^{-1}$ | $\omega_1 + \omega_2 + \omega_D$ | $\omega_1 + \omega_2 - \omega_D$ | $\omega_1 - \omega_2 - \omega_D$ | $\omega_1 - \omega_2 + \omega_D$ |
|---|---|---|---|---|
| 45.3173 | 50.0382 | 49.2420 | 40.5964 | 41.3926 |
| 41.4694 | 46.1903 | 45.3941 | 36.7485 | 37.5447 |
| 38.6311 | 43.3520 | 42.5558 | 33.9102 | 34.7064 |
| 36.6414 | 41.3623 | 40.5661 | 31.9205 | 32.7167 |
| 35.5095 | 40.2304 | 39.4342 | 30.7886 | 31.5848 |
| 33.1785 | 37.8994 | 37.1032 | 28.4576 | 29.2538 |
| 29.7914 | 34.5123 | 33.7161 | 25.0705 | 25.8667 |
| 29.1331 | 33.8540 | 33.0578 | 24.4122 | 25.2084 |
| 27.8711 | 32.5920 | 31.7958 | 23.1502 | 23.9464 |
| 25.8707 | 30.5916 | 29.7954 | 21.1498 | 21.9460 |
| 25.0525 | 29.7734 | 28.9772 | 20.3316 | 21.1278 |
| 23.8564 | 28.5773 | 27.7811 | 19.1355 | 19.9317 |

## Propane (C₃H₈) compound

Propane ($C_3H_8$) compound

Electric dipole moment ($p_o$) = 0.084 Debye

Angular frequency of vibration of the molecule ($\omega_2$) = $5.6065 \times 10^{14} s^{-1}$.

Angular frequency due to the electric dipole created by the vibrating molecule ($\omega_D$) = $1.3278 \times 10^{13} s^{-1}$.

| $\omega_1 \times 10^{14} s^{-1}$ | $\omega_1 + \omega_2 + \omega_D$ | $\omega_1 + \omega_2 - \omega_D$ | $\omega_1 - \omega_2 - \omega_D$ | $\omega_1 - \omega_2 + \omega_D$ |
|---|---|---|---|---|
| 45.3173 | 51.0566 | 50.7910 | 39.5780 | 39.8436 |
| 41.4694 | 47.2087 | 46.9431 | 35.7301 | 35.9957 |
| 38.6311 | 44.3704 | 44.1048 | 32.8918 | 33.1574 |
| 36.6414 | 42.3807 | 42.1151 | 30.9021 | 31.1677 |
| 35.5095 | 41.2488 | 40.9832 | 29.7702 | 30.0358 |
| 33.1785 | 39.9178 | 38.6522 | 27.4392 | 27.7048 |
| 29.7914 | 35.5307 | 35.2651 | 24.0521 | 24.3177 |
| 29.1331 | 34.8724 | 34.6068 | 23.3938 | 23.6594 |
| 27.8711 | 33.6104 | 33.3448 | 22.1318 | 22.3974 |
| 25.8707 | 31.6100 | 31.3444 | 20.1314 | 20.3970 |
| 25.0525 | 30.7918 | 30.5262 | 19.3132 | 19.5788 |
| 23.8564 | 29.5957 | 29.3301 | 18.1171 | 18.3827 |

## Carbonyl chloride (Cl₂CO) compound

Carbonyl chloride ($Cl_2CO$) compound

Electric dipole moment ($p_o$) = 1.17 Debye.

Angular frequency of vibration of the molecule ($\omega_2$) = $1.0689 \times 10^{14} s^{-1}$.

Angular frequency due to the electric dipole created by the vibrating molecule ($\omega_D$) = $6.72 \times 10^{12} s^{-1}$.

| $\omega_1 \times 10^{14} s^{-1}$ | $\omega_1 + \omega_2 + \omega_D$ | $\omega_1 + \omega_2 - \omega_D$ | $\omega_1 - \omega_2 - \omega_D$ | $\omega_1 - \omega_2 + \omega_D$ |
|---|---|---|---|---|
| 45.3173 | 46.4534 | 46.3190 | 44.1812 | 44.3156 |
| 41.4694 | 42.6055 | 42.4711 | 40.3333 | 40.4677 |
| 38.6311 | 39.7672 | 39.6328 | 37.4950 | 37.6294 |
| 36.6414 | 37.7775 | 37.6431 | 35.5053 | 35.6397 |
| 35.5095 | 36.6456 | 36.5112 | 34.3734 | 34.5078 |
| 33.1785 | 34.3146 | 34.1802 | 32.0424 | 32.1768 |
| 29.7914 | 30.9275 | 30.7931 | 28.6553 | 28.7897 |
| 29.1331 | 30.2692 | 30.1348 | 27.9970 | 28.1314 |
| 27.8711 | 29.0072 | 28.8728 | 26.7350 | 26.8694 |
| 25.8707 | 27.0068 | 26.8724 | 24.7346 | 24.8690 |
| 25.0525 | 26.1886 | 26.0542 | 23.9164 | 24.0508 |
| 23.8564 | 24.9925 | 24.8581 | 22.7203 | 22.8547 |

## DISCUSSION AND SUMMARY

There are a number of important reasons as to why the development of Raman spectroscopy was very slow. An important reason is that the Raman Effect is very weak [20]. Hardly one part in a million of the total intensity of the incident light is elastically scattered (Rayleigh scattering), whereas for Raman scattering this value is one part in $10^8$ of the incident light intensity [21]. This is also the most important reason that the discovery of Raman Effect was delayed. Even the discovery of laser was delayed up to 1960, but once a large number of lasers with powerful beams were discovered, new laser techniques stimulated the field of molecular spectroscopy and Raman spectroscopy.

Raman Effect arises when a photon is incident on a molecule, and it interacts with the dipole created by the electric field of the incident light radiation. In fact, an oscillating dipole is created. Now an oscillating dipole creates an oscillating electric field, and in this manuscript it is assumed that the oscillating electric field, created by the oscillating dipole can affect the frequency scattered due to the Raman Effect. The modification in the frequency of the Stokes and anti-Stokes lines due to this effect is calculated and is denoted as $\omega_D$. The values of $\omega_D$ for different molecules have been calculated. These values are different for different molecules and are smaller than $\omega_1$ and $\omega_2$ by a factor of roughly 10. We emphatically believe that it should be possible to measure the value of $\omega_D$ by an appropriate experimental design and by using an intense electric field laser. One method could be that two laser beams are used. First a Q-switched laser beam (pulse of a beam) is projected on the molecule and then a continuous wave (CW) laser beam be projected on the same molecules. This process of getting Stokes and anti-Stokes lines may help in getting a specific value for $\omega_D$ for different molecules. This process can be called double beam Raman scattering. It is not easy to surmise how soon the exact value of $\omega_D$ can be measured since the gap between theoretical prediction and experimental observation has beengenerally large. Moreover, an intense electric field laser can lead to larger $\omega_D$ values that can be measured. Intense electric field

can affect $\omega_D$, but larger number of photons in the laser beam will affect the intensity of Raman lines. Typical electric field intensities of order of $10^{10}$V/m or more may be required to obtain values of $\omega_D$ that can be measured.

Raman spectroscopy provides a unique biochemical study capable of identifying and characterizing the structure of molecules, tissues, and cells. In identifying cervical cancer, it is established that it is a promising biochemical tool due to its ability to detect pre-malignancy and early malignancy stages [11-13, 22-25]. Raman lines differ between normal and malignant biopsy samples. In our case it is the value of $\omega_D$ that will differ between normal and malignant biopsy samples.

A greater body of experimental evidence may be needed in future to establish the validity of the theory developed in this manuscript. However, the fact remains that the type of Raman scattering proposed in this manuscript can be observed experimentally, and it can become a promising biomedical tool, especially by obtaining Raman lines after radiotherapy cycles and so on.

The concept in this manuscript is that the molecule may be excited not only by the incident laser radiation but also by the oscillating electric field created by the oscillating dipole. It is quite possible that our study can be used in the study of Four-Wave mixing microscopy of nanostructures [26], and Surface-Enhanced Raman Spectroscopy (SERS), and Coherent Raman Spectroscopy (CARS) [27-30,]. We are not competent to say how the experiments may be designed to observe these phenomena.

We must point out that we have not been able to find out any theoretical and or experimental observations on these lines in literature. From the above results, it shows that the theory developed predicts new phenomena of getting Stokes and anti-Stokes lines with modified wavelengths. It is proposed that such a phenomenon may be observed experimentally by using intense electric field laser.

**ORCID IDs**

**Khanna M. Kapil** https://orcid.org/0000-0003-4311-9987, **Murei K. Gilbert** https://orcid.org/0000-0002-7250-3454

**REFERENCES**

[1] A. Smekal, Naturwiss, **11**(43), 873-875(1923), https://doi.org/10.1007/BF01576902.

[2] C.V. Raman andK.S. Krishnan,Nature, **121**, 501-502 (1928), https://doi.org/10.1038/121501c0.

[3] K.F. Kohlrauch, *Der Smekal –Raman–Effect*, (Springer, Berlin, 1931); Ergänzungsband 1931-1937, (Springer,1938).

[4] E. Garcia-Rico, R.A. Alvarez-Puebla, L. Guerrini, Chem. Soc. Rev. **47**, 4909-4923 (2018), https://doi.org/10.1039/C7CS00809K.

[5] J.D. Jackson, *Classical Electrodynamics*, (Wiley, New York, 1975).

[6] L.D. Landau and E.M. Lifshitz, *Electrodynamics of Continuous Media*, (Pergamon, 1971).

[7] M. Born and E. Wolf, *Principles of Optics*, (Pergamon, 1970).

[8] A.N. Laurence, Journal of Raman spectroscopy, **41**, (2017), https://doi.org/10.1002/jrs.5310.

[9] P. Rostron, S. Gaber and D. Gaber, IJETR, **6**(1), 2454-4698 (2016), https://www.researchgate.net/profile/Paul_Rostron/publication/309179824_Raman_Spectroscopy_a_review/links/580329fe08ae23fd1b673f34/Raman-Spectroscopy-a-review.pdf.

[10] B. Hruška, A.A. Osipov, L.M. Osipova, M. Chromčíková, J. Macháček and M. Liškaac, Vibrational Spectroscopy, **105**, 102970 (2019), https://doi.org/10.1016/j.vibspec.2019.102970.

[11] R.R. Jones, D.C. Hooper, Liwu Zhang, D. Wolverson and V.K. Valev, Nanoscale Res Lett. **14**, 231 (2019), https://dx.doi.org/10.1186%2Fs11671-019-3039-2

[12] R. Ravanshad, A.K. Zadeh, and A.M. Amani, Nano Reviews & Experiments, **9**(1), 1373551 (2018), https://doi.org/10.1080/20022727.2017.1373551.

[13] K.E. Sundling and A.C. Lowe, Advance Anat. Pathology, **26**(1), 56-63 (2019), https://doi.org/10.1097/PAP.0000000000000217.

[14] S. Devpura, K.N. Barton, S.L. Brown, O. Palyvoda, S. Kalkanis, V.M. Naik, F. Siddiqui, R. Naik and I.J. Chetty, International Journal of Medical Physics Research and Practice, **41**(5), 050901 (2014), https://doi.org/10.1118/1.4870981

[15] L. Guerrini and R.A. Alvarez-Puebla, Cancers, **11**(6), 748 (2019), http://doi.org/10.3390/cancers11060748.

[16] *Non-Linear Raman spectroscopy and its chemical applications, Proceedings of the NATO Advanced Study Institute held at Bad Windsheim, Germany*, edited by W. Kiefer and D.A. Long (D. Reidel Publishing Company, London, 1982), pp. 643.

[17] A. Mohammed, H. Ågren and P. Norman, Chem. Phys. Lett. **468**, 119-123 (2009), https://doi.org/10.1016/j.cplett.2008.11.063.

[18] D.J. Griffiths, *Introduction to Electrodynamics*, 3$^{rd}$ edition,(Pearson Education, 2007).

[19] D.R. Lide, editor, *CRC Handbook of Chemistry and Physics, Internet Version 2005*, (CRC Press, Boca Raton, 2005), http://www.hbcpnetbase.com.

[20] H.J. Hibben, *The Raman Effect and its Chemical Applications*, (Reinhold Publishing Company, New York, 1939), https://doi.org/10.1002/ange.19400531511.

[21] D.A. Long, *The Raman Effect: A Unified Treatment of the Theory of Raman Scattering by Molecules*, (Willey, England, 2002), pp. 624.

[22] A. Mahadevan-Jansen, M.F. Mitchell, N. Ramanujamf, A. Malpica, S. Thomsen, U. Utzinger and R. Richards-Kortum, Photochemistry and Photobiology, **68**(1), 123–132 (1998), https://doi.org/10.1111/j.1751-1097.1998.tb03262.x.

[23] A. Mahadevan-Jansen, M.F. Mitchell, N. Ramanujam, U. Utzinger and R. Richards-Kortum, Photochemistry and Photobiology **68**(3), 427–431 (1998), https://doi.org/10.1111/j.1751-1097.1998.tb09703.x.

[24] P.R.T. Jess, D.D.W. Smith, M. Mazilu, K. Dholakia, A.C. Richesand and C.S. Herrington, International Journal of Cancer, **121**(12), 2723–2728 (2007), https://doi.org/10.1002/ijc.23046.

[25] J.L. González-Solís, C. Martínez-Espinosa, L.A. Torres-González, A. Aguilar-Lemarroy, L.F. Jave-Suárez and P. Palomares-Anda, Lasers in Medical Science, **29**(3), 979–985 (2014), https://doi.org/10.1007/s10103-013-1447-6.

[26] Yong Wang, Chia-Yu Lin, A. Nikolaenko, V. Raghunathan and E.O. Potma, Advances in Optics and Photonics, **3**(1), 1-52 (2011), https://doi.org/10.1364/AOP.3.000001.

[27] Ji-Xin Cheng and Xiaoliang Sunney Xie, *Coherent Raman scattering microscopy*, (CRCPress, Taylor&Francis group, 2013).

[28] N. Buzgar, A.I. Apopei and A. Buzatu, (2009), *Theory of Raman spectroscopy. Quantum and Classical Raman theory*, http://www.rdrs.ro/blog/quantum-classical-raman-theory/.

[29] Theory of Raman spectroscopy, (2019), https://chem.libretexts.org/Bookshelves/Analytical_Chemistry/ Map%3A_Principles_of_Instrumental_Analysis_(Skoog_et_al.)/18%3A_Raman_Spectroscopy/18.1%3A_Theory_of_Raman_ Spectroscopy.

[30] E.S. Winesett, C.H. Londergan and L.K. Charkoudian, Nat. Commun. **10**(1), 2227 (2019), https://doi.org/10.1038/s41467-019-10184-2.

## ВПЛИВ ОСЦИЛЮЮЧОГО ЕЛЕКТРИЧНОГО ПОЛЯ
## ЧЕРЕЗ ОСЦИЛЛЯЦІЇ ЕЛЕКТРИЧНОГО ДИПОЛЯ НА РАМАНІВСЬКІ ЛІНІЇ

**Ханна М. Капіл[1], Мурей К. Гілберт[2]**
*[1]Кафедра фізики, Університет Ельдорет, P.O. Box 1125-30100, Eldoret, Кенія*
*[2]Кафедра фізики, Університет Лайкіпія, P.O. Box 1100-20300, Ньяхуруру, Кенія*

Ефект Рамана полягає у вимірюванні інтенсивності та довжини хвиль непружно розсіяного випромінювання, яке падає на молекулу. Електричне поле випромінювання поляризує молекулу, на яку вона падає, і це призводить до створення коливань диполя. Поляризоване лазерне світло, що падає, непружно розсіюється молекулярним зразком. Розсіяне світло містить змінені довжини хвиль, які називаються Стоксівськими та анти-Стоксівськими довжинами хвиль. Електричний диполь, що коливається внаслідок падаючого випромінювання, створює навколо себе коливальне електричне поле. Оскільки коливальне електричне поле падаючого випромінювання створює коливальний електричний диполь, який створює навколо нього коливальне електричне поле, то вважається, що це коливальне електричне поле може впливати на частоту коливань або коливання електричного диполя, який його виробляє. Цей новий ефект змінить частоту (частоти) розсіяного випромінювання, що призведе до появи ліній Стокса та анти-Стокса зі зміненими частотами. Це теоретичне дослідження та його значення можна пояснити наступним чином. Наприклад, якщо є дві клітини або молекули поруч, у яких одна є здоровою клітиною, а інша – раковою, або два різних типів молекул що знаходяться поряд, цей тип розсіювання повинен бути в змозі розрізнити одну ситуацію від іншої, оскільки лінії Стокса і анти-Стокса від двох молекул не будуть ідентичними. Таким чином падаюче випромінювання кутової частоти $\omega 1$ поляризує молекулу, на яку вона падає, і це призводить до створення коливального диполя частоти $\omega 2$. Коливальний диполь створює коливальне електричне поле, яке може створити додаткову частоту коливального диполя, який його створив, і нехай це буде $\omega D$. Тоді лінії Рамана можуть мати частоти ($\omega 1+\omega 2+\omega D$), ($\omega 1+\omega 2-\omega D$), ($\omega 1-\omega 2+\omega D$) та ($\omega 1-\omega 2-\omega D$). Залежно від відносних величин $\omega 2$ і $\omega D$, лінії Рамана будуть позначатися як лінії Стокса і анти-Стокса. Через закон збереження енергії $\omega D$ буде менше ніж $\omega 2$, оскільки коливальний диполь не може створити поле частоти більше своєї власної частоти. Отже, частоти ($\omega 1-\omega 2+\omega D$) і ($\omega 1-\omega 2-\omega D$) відповідають лініям Стокса і частотам. ($\omega 1+\omega 2+\omega D$) і ($\omega 1+\omega 2-\omega D$) будуть відповідати лініям анти-Стокса. Розрахунки ліній Стокса та анти-Стокса були зроблені для деяких молекул: аміаку ($NH_3$), оксиду азоту ($N_2O$), води ($H_2O$), діоксиду сірки ($SO_2$), ($O_3$). Розрахунки також були проведені для сполук, що містять вуглець, таких як дихлорметан ($CH_4Cl_2$), мурашиної кислоти ($CH_2O_2$), метанолу ($CH_4O$), бензолу ($C_6H_6$), пропану ($C_3H_8$) та карбонілхлориду ($Cl_2CO$). Розроблена теорія передбачає нові явища для отримання ліній Стокса та анти-Стокса зі зміненою довжиною хвилі, які не спостерігалися експериментально на сьогоднішній день.
**КЛЮЧОВІ СЛОВА:** електричний диполь, лінії Рамана, лінії Стокса, анти-Стокса, коливальний електричний диполь

## ВЛИЯНИЕ ОСЦИЛЛИРУЮЩЕГО ЭЛЕКТРИЧЕСКОГО ПОЛЯ
## ЧЕРЕЗ ОСЦИЛЛЯЦИИ ЭЛЕКТРИЧЕСКОГО ДИПОЛЯ НА РАМАНОВСКИЕ ЛИНИИ

**Ханна М. Капил[1], Мурей К. Гилберт[2]**
*[1]Кафедра физики, Университет Елдорет, P.O. Box 1125-30100, Елдорет, Кения*
*[2]Кафедра физики, Университет Лайкипия, P.O. Box 1100-20300, Ньяхуруру, Кения*

Эффект Рамана состоит в измерении интенсивности и длины волн неупруго рассеянного излучения, которое падает на молекулу. Электрическое поле излучения поляризует молекулу, на которую она падает, и это приводит к созданию колебаний диполя. Поляризованный лазерный свет, падающий не упруго рассеивается молекулярным образцу. Рассеянный свет содержит изменены длины волн, которые называются Стоксовскими и анти-Стоксовскими длинами волн. Электрический диполь, который колеблется вследствие падающего излучения, создает вокруг себя колебательное электрическое поле. Поскольку колебательное электрическое поле падающего излучения создает колебательный электрический диполь, который создает вокруг него колебательное электрическое поле, то считается, что это колебательное электрическое поле может влиять на частоту колебаний или колебания электрического диполя, который его производит. Этот новый эффект изменит частоту (частоты) рассеянного излучения, что приведет к появлению линий Стокса и анти-Стокса с измененными частотами. Это теоретическое исследование и его значение можно объяснить следующим образом. Например, если есть две клетки или молекулы рядом, в которых одна является здоровой клеткой, а другая - раковой или два различных типов молекул, находящихся рядом, этот тип рассеяния должен быть в состоянии различить одну ситуацию от другой, поскольку линии Стокса и анти-Стокса от двух молекул не будут идентичными. Таким образом падающее излучение угловой частоты $\omega 1$ поляризует молекулу, на которую она падает, и это приводит к созданию колебательного диполя частоты $\omega 2$. Колебательный диполь создает колебательное электрическое поле, которое может создать дополнительную частоту колебательного диполя, который его создал, и пусть это будет $\omega D$. Тогда линии Рамана могут иметь частоты ($\omega 1+\omega 2+\omega D$), ($\omega 1+\omega 2-\omega D$), ($\omega 1-\omega 2+\omega D$) и ($\omega 1-\omega 2-\omega D$). В зависимости от относительных величин $\omega 2$ и $\omega D$, линии Рамана будут обозначаться как линии Стокса и анти-Стокса. Через закон сохранения энергии $\omega D$ будет меньше чем $\omega 2$, поскольку колебательный диполь не может создать поле частоты больше своей собственной частоты. Итак, частоты ($\omega 1-\omega 2+\omega D$) и ($\omega 1-\omega 2-\omega D$) соответствуют линиям Стокса и частотам. ($\omega 1+\omega 2+\omega D$) и ($\omega 1+\omega 2-\omega D$) будут соответствовать линиям анти-Стокса. Расчеты линий Стокса и анти-Стокса были сделаны для некоторых молекул: аммиака ($NH3$), оксида азота ($N_2O$), воды ($H_2O$), диоксида серы ($SO_2$), озона ($O_3$). Расчеты также были проведены для соединений, содержащих углерод, таких как дихлорметан ($CH_4Cl_2$), муравьиная кислота ($CH_2O_2$), метанола соединение ($CH_4O$), бензола ($C_6H_6$), пропана ($C_3H_8$) и карбонилхлорида ($Cl_2CO$). Разработанная теория предполагает новые явления для получения линий Стокса и анти-Стокса с измененной длиной волны, что не наблюдались экспериментально на сегодняшний день.
**КЛЮЧЕВЫЕ СЛОВА:** электрический диполь, линии Рамана, линии Стокса, анти-Стокса, колебательный электрический диполь

# THREE-STEP RESONANCE ENERGY TRANSFER IN INSULIN AMYLOID FIBRILS

Uliana Tarabara[1]*, Mykhailo Shchuka[1], Kateryna Vus[1], Olga Zhytniakivska[1], Valeriya Trusova[1], Galyna Gorbenko[1], Nikolai Gadjev[2], Todor Deligeorgiev[2]

*[1]Department of Medical Physics and Biomedical Nanotechnologies, V.N. Karazin Kharkiv National University*
*4 Svobody Sq., Kharkiv, 61022, Ukraine*
*[2]Faculty of Chemistry and Pharmacy, Sofia University, "St. Kliment Ohridski" 1,*
*blv. J. Bourchier, Sofia, 1164, Bulgaria*
*\*E-mail: uliana.tarabara@gmail.com*
Received 15 October 2019, revised November 6, 2019; accepted November 11, 2019

The applicability of the three-step Förster resonance energy transfer (FRET) to detection of insulin amyloid fibrils was evaluated, using the chromophore system, containing Thioflavin T (ThT), 4-dimethylaminochalcone (DMC), and two squaraine dyes, referred to here as SQ1 and SQ4. The mediator chromophore DMC was found to enhance the fluorescence intensity of the terminal acceptor, SQ1, excited at 440 nm (at the absorption maximum of the principal donor, ThT), in fibrillar insulin compared to the system without DMC, providing the evidence for the cascade energy transfer in the chain ThT→DMC→SQ4→SQ1. Furthermore, the resulting Stokes shift in the four-chromophore system was 240 nm, as compared to 45 nm for the fibril-bound ThT, suggesting that higher signal-to-noise ratio is the advantage of amyloid fibril detection by multistep FRET. The maximum efficiencies of energy transfer in the insulin fibrils estimated from the quenching of the donor fluorescence in the presence of acceptor for the donor-acceptor pairs ThT-DMC, DMC-SQ4 and SQ4-SQ1 were 40%, 60% and 30% respectively, while negligible FRET occurred in the non-fibrillized protein. The most pronounced differences between fibrillar and non-fibrillized insulin were observed in the 3D fluorescence spectra. Specifically, two intensive spots centered at the emission wavelengths ~ 650 nm (SQ4) and ~ 685 nm (SQ1) were revealed at the excitation wavelength ~ 440 nm in the 3D patterns of insulin amyloid aggregates. In contrast, in the case of the non-fibrillized protein, the barely noticeable spots centered at the same wavelengths, as well as higher fluorescence intensities at the excitation above 550 nm were observed, suggesting the predominant impact of the direct excitation of SQ1 and SQ4 on their fluorescence responses. The inter-chromophore distances calculated from the experimental values of the energy transfer efficiency assuming the isotropic rotation of the dyes, were found to be 2.4, 4.5 and 4.3 nm for the ThT-DMC, DMC-SQ4 and SQ4-SQ1 pairs, respectively, revealing the different fibril binding sites for the examined dyes. The quantum-chemical calculations and simple docking studies provided evidence for the SQ1, SQ4 and ThT, DMC binding to the wet and dry interface of the insulin amyloid protofilament, respectively. The dye-protein complexes are likely to be stabilized by the hydrophobic, van der Waals, aromatic and electrostatic interactions. In summary, the above technique based on the multistep FRET can be employed for the identification and characterization of amyloid fibrils in vitro along with the classical ThT assay, allowing the increase of the amyloid detection sensitivity and lowering the probability of the pseudo-positive result. The applicability of the multistep FRET for amyloid visualization in vivo can be also tested by the involvement of the near-infrared fluorescent dyes to the cascade.

**KEYWORDS**: cascade resonance energy transfer, 4-dimethylaminochalcone, fibrillar insulin, squaraine dyes, Thioflavin T.

During the past decade a phenomenon of the Förster resonance energy transfer (FRET) has emerged as an extremely useful tool for retrieving information about proximity relationships and structural dynamics of biological macromolecules and their assemblies [1-3]. Due to a strong dependence of the energy transfer efficiency on the donor-acceptor distance, FRET is particularly useful while determining the intra- and intermolecular distances on a nanometer scale [4,5]. Although most FRET studies involve analysing a conventional one-step energy transfer, a multistep FRET (msFRET) has been attracting much attention in recent years [6-10], inspired by the natural photosynthetic systems containing several light-harvesting complexes that efficiently transfer the absorbed energy between a number of chromophores [11,12]. The energy transfer within multiple chromophore systems usually follows a cascade route, moving from an initial donor chromophore through the intermediate donors/acceptors onto a final acceptor chromophore [6-10,13]. The multistep FRET offers several advantages over the one-step FRET: i) a higher efficiency of long-range transfer [14]; ii) a larger Stokes shift [13,15]; iii) the possibility to monitor inter- and intramolecular interactions beyond the range 1-10 nm [16]; and iv) an extended excitation wavelength range for fluorescence lifetime measurements [14]. As a result, the cascade, or multistep FRET appeared to be especially useful in developing molecular photonic wires and light harvesting systems [6-8, 17]. Most of such artificial systems are devised through synthesizing the arrays of covalently linked chromophores with a specific design to ensure large collection efficiencies, as well as fast and efficient energy migration. By analogy with the natural antenna, the majority of these systems are based on the porphyrin pigments [13,15,18,19]. Another application of msFRET involves the DNA photonic wires self-assembled around CdSe/ ZnS semiconductor quantum dots acting as a nanoscaffold and a FRET donor to a series of DNA-intercalating dyes [17]. More importantly, the msFRET systems are effectively used in biosensors for sensitive detection of multivalent complexation [20], protein labeling [15], genotyping of single nucleotide polymorphism [21], DNA sequencing [16], estimating the stoichiometry of protein complexes [22], determination of the tumor necrosis factor [23] and analysis of multiprotein interactions in living cells [24], to name only a few.

Remarkably, the multistep FRET have been successfully employed for the detection of a specific type of protein aggregates – amyloid fibrils, whose formation is associated with the pathogenesis of neurodegenerative diseases, type II diabetes, systemic amyloidosis, etc. [25]. More specifically, it was demonstrated that amyloid-sensing potential of the classical amyloid marker, Thioflavin T, can be reinforced by its implication as a primary donor in the two-step energy transfer process [25], creating a background for application of amyloid nanostructures as a molecular framework for controlled positioning of a multitude of chromophores communicating via the multi-step FRET in photonic devices. To the best of our knowledge, so far, the potential of amyloid-scaffolded msFRET remains poorly investigated. In view of this, the aim of the present study was to assess the insulin amyloid-sensing potential of the three-step Förster resonance energy transfer using the four-chromophore system containing a benzothiazole dye Thioflavin T, 4-dimethylaminochalcone and two squaraine dyes, SQ1 and SQ4.

## THEORY

Förster resonance energy transfer is a long-range electrodynamic interaction of two chromophores: the excited donor and the ground-state acceptor, as a result of which the energy of the excited donor is non-radiatively transferred to the acceptor [26]:

$$D^* + A \rightarrow D + A^* \tag{1}$$

The main prerequisites for FRET include i) the overlap between emission spectrum of a donor and absorption spectrum of an acceptor and ii) the donor-acceptor separation falling in the range 0-10 nm. Each donor-acceptor pair can be characterized by the three parameters: $k_t$, the energy transfer rate; $r$, the distance between chromophores; and $R_0$, the Förster radius, related by the equation [27]:

$$k_t(r) = \frac{1}{\tau_D}\left(\frac{R_0^6}{r}\right) \tag{2}$$

where $\tau_D$ is the donor fluorescence lifetime in the absence of acceptor. The energy transfer efficiency $E$, i.e. the probability that the excited donor will transfer energy to the ground-state acceptor, can be written as:

$$E = \frac{k_t}{k_t + \tau_D^{-1}} = \frac{R_0^6}{R_0^6 + r^6} \tag{3}$$

The Förster radius, i.e. the donor-acceptor distance at which the energy transfer efficiency equals 50%, is given by:

$$R_0 = 979\left(\kappa^2 n_r^{-4} Q_D J\right)^{1/6}, \quad J = \int_0^\infty F_D(\lambda)\varepsilon_A(\lambda)\lambda^4 d\lambda \Big/ \int_0^\infty F_D(\lambda)d\lambda \tag{4}$$

where $J$ is the overlap integral; $F_D(\lambda)$ is the donor fluorescence intensity, $\varepsilon_A(\lambda)$ is the acceptor molar absorbance at the wavelength $\lambda$, $n_r$ is the refractive index of the medium; $Q_D$ is the donor quantum yield; $\kappa^2$ is the orientation factor defined as:

$$\kappa^2 = \left((\overrightarrow{e_D}, \overrightarrow{e_A}) - 3(\overrightarrow{e_D}, \overrightarrow{e_{DA}})(\overrightarrow{e_{DA}}, \overrightarrow{e_A})\right)^2 \tag{5}$$

where $\overrightarrow{e_D}$, $\overrightarrow{e_A}$ are the unit transition vectors of the donor and acceptor respectively; $\overrightarrow{e_{DA}}$ is the unit vector drawn from the donor to the acceptor [28]. The orientation factor may take a value from 0 to 4, but usually $R_0$ is calculated with $\kappa^2 = 2/3$ (when the orientations of the donor emission and acceptor absorption transition dipoles randomize during the fluorescence lifetime). The uncertainty in $\kappa^2$ is the main limitation of the FRET technique resulting in the distance estimation error up to 35%) [28-30]. This problem can be partly circumvented through narrowing the $\kappa^2$ limits by measuring the anisotropy of donor and acceptor [28, 29, 31].
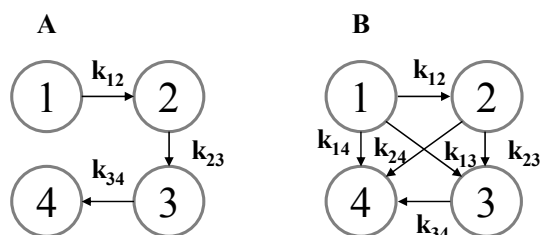


Fig. 1. A four-chromophore system for energy transfer: (A) three-step FRET (energy is transferred from chromophore 1 to 4 via 2 and 3), and (B) all possible pathways of the energy transfer.

In the present study, the FRET system consisting of four chromophores is considered. There are many scenarios for this system and the two most important of them are illustrated in Fig.1. Let us designate the chromophores 1, 2, 3, and 4 as D1, D2, D3, and A3, respectively.

In the case A (Fig. 1A), it is shown that the total three-step FRET efficiency ($E$) measured from the enhancement of the A3 emission is the product of efficiencies for each of FRET steps [33]:

$$E = E_{12}E_{23}E_{34} \tag{6}$$

where $E_{12}$, $E_{23}$ and $E_{34}$ are energy transfer efficiencies from D1 to D2, from D2 to D3 and from D3 to A3, respectively.

In the case B (Fig. 1B), the concentration of chromophores in the excited state can be described by the following differential equations:

$$\frac{d\left[D_1^*\right]}{dt} = -\left[D_1^*\right](k_{12} + k_{13} + k_{14} + \tau_{D1}^{-1}) \tag{7}$$

$$\frac{d\left[D_2^*\right]}{dt} = -\left[D_2^*\right](k_{23} + k_{24} + \tau_{D2}^{-1}) + \left[D_1^*\right]k_{12} \tag{8}$$

$$\frac{d\left[D_3^*\right]}{dt} = -\left[D_3^*\right](k_{34} + \tau_{D3}^{-1}) + \left[D_1^*\right]k_{13} + \left[D_2^*\right]k_{23} \tag{9}$$

$$\frac{d\left[A_3^*\right]}{dt} = -\left[A_3^*\right]\tau_{A3}^{-1} + \left[D_1^*\right]k_{14} + \left[D_2^*\right]k_{24} + \left[D_3^*\right]k_{34} \tag{10}$$

The energy transfer efficiency measured through monitoring the increase in acceptor fluorescence is given by [33]:

$$E = \frac{I_A}{\tau_A} \tag{11}$$

$$I_A = \frac{1}{n_0}\int_0^\infty \left[A_3^*\right](t)\,dt \tag{12}$$

where $n_0 = [D_1^*](t = 0)$, $\tau_A$ is the acceptor lifetime. Assuming that $\left[D_1^*\right](t = 0) = 1$, and $\left[D_2^*\right](t = 0) = \left[D_3^*\right](t = 0) = \left[A_3^*\right](t = 0) = 0$, from equations (10) and (12) one obtains:

$$I_3 = \frac{k_{12}\,k_{23}\,k_{34} + k_{13}\,k_{34}(k_{23} + k_{24} + \tau_{D2}^{-1}) + k_{12}\,k_{24}(k_{34} + \tau_{D3}^{-1}) + k_{14}(k_{23} + k_{24} + \tau_{D2}^{-1})(k_{34} + \tau_{D3}^{-1})}{(k_{12} + k_{13} + k_{14} + \tau_{D1}^{-1})(k_{23} + k_{24} + \tau_{D2}^{-1})(k_{34} + \tau_{D3}^{-1})\,\tau_{A3}^{-1}} \tag{13}$$

Using the formula for the energy transfer efficiency within one donor-acceptor pair (Eq. 11), the $E$ value in the three-step FRET can be written as follows:

$$E = E'_{12}\,E'_{23}\,E_{34} + E'_{13}\,E_{34} + E'_{12}\,E'_{24} + E'_{14} \tag{14}$$

where $E'_{ij}$ is the energy transfer efficiency from the donor $i$ to the acceptor $j$ in the presence of the parallel energy transfer from the donor $i$ to other acceptors.

## EXPERIMENTAL SECTION
### Materials
Bovine insulin, dimethyl sulfoxide (DMSO), Tris, thioflavin T (ThT) and phosphotungstic acid hydrate for electron microscopy were purchased from Sigma. 4-dimethylaminochalcone (DMC) was from Signe (Latvia). The squaraine dyes SQ1 and SQ4 were synthesized in the University of Sofia, Bulgaria. All other reagents were used without further purification.

### Preparation of working solutions
The insulin stock solution (10 mg/ml) was prepared in 10 mM glycine buffer (pH 2.0). The reaction of the protein fibrillization was conducted at 37 °C in the above buffer under constant agitation on the orbital shaker. The kinetics of amyloid formation was monitored using the Thioflavin T assay [34]. Hereafter, the fibrillar protein and its non-fibrillized counterpart (the insulin solution in glycine buffer that was not subjected to agitation) are denoted as InsF and InsN, respectively.

The dyes stock solutions were prepared in DMSO (SQ1 and SQ4) and ethanol (DMC), while ThT was dissolved in 10 mM Tris buffer (pH 7.4). The fluorimetric measurements were carried out in 10 mM Tris-HCl buffer (pH 7.4).

For the transmission electron microscopy assay, a 10 μl drop of the protein solution was applied to a carbon-coated grid and blotted after 1 min. A 10 μl drop of 1.5% (w/v) phosphotungstic acid solution was placed on the grid, blotted

after 30 s, and then washed 3 times by deionized water and air dried. Then the grids were viewed with the EM-125 electron microscope (Selmi, Ukraine).
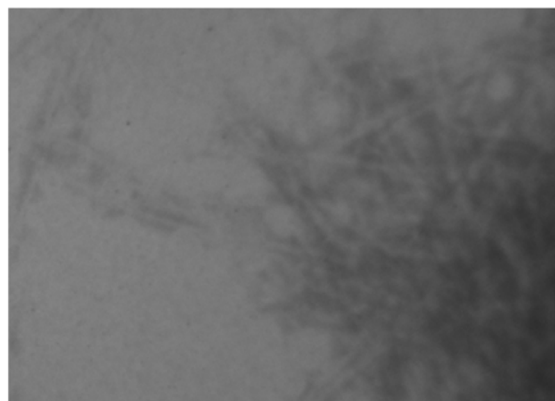


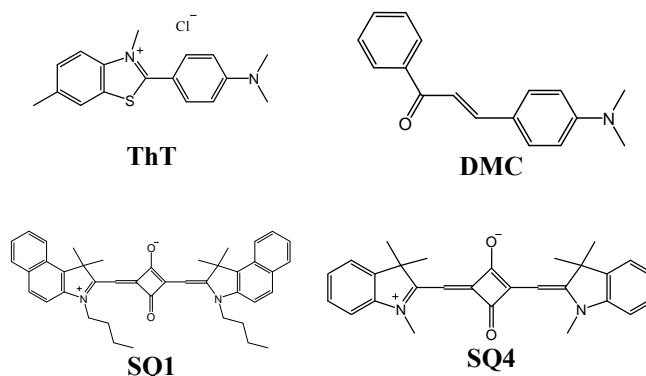Fig. 2. Transmission electron microscopy photograph of the insulin amyloid fibrils.



Fig. 3. Chemical structures of the employed donor and acceptor fluorophores.

## Spectroscopic measurements

The absorption spectra of the examined dyes were recorded with the spectrophotometer Shimadzu UV-2600 (Japan) at 25 ℃. The dye concentrations were determined spectrophotometrically using the extinction coefficients $\varepsilon_{418}^{Ethanol} = 3.46 \cdot 10^4$ M$^{-1}$cm$^{-1}$, $\varepsilon_{662}^{DMSO} = 2.3 \cdot 10^5$ M$^{-1}$cm$^{-1}$, $\varepsilon_{641}^{DMSO} = 4.21 \cdot 10^5$ M$^{-1}$cm$^{-1}$ and $\varepsilon_{412}^{water} = 3.6 \cdot 10^4$ M$^{-1}$cm$^{-1}$ for DMC, SQ1, SQ4 and ThT, respectively. Steady-state fluorescence spectra were recorded with RF6000 spectrofluorimeter (Shimadzu, Japan). Fluorescence measurements were performed at 25 °C using 10 mm pathlength quartz cuvettes. Fluorescence spectra were recorded within the range 460–820 nm with the excitation wavelength 440 nm. The excitation and emission slit widths were set at 10 nm.

The efficiency of energy transfer was determined from the quenching of the donor fluorescence in the presence of acceptor [29]:

$$E = 1 - \frac{I_{DA}}{I_D} \qquad (15)$$

where $I_D$, $I_{DA}$, are the donor fluorescence intensities in the absence and in presence of the acceptor, respectively. The donor fluorescence intensities measured in the presence of acceptor were corrected for inner filter effect using the following coefficients [29]:

$$k = 10^{(A_a^{ex} + A_a^{em})/2} \qquad (16)$$

where $A_a^{ex}$, $A_a^{em}$ are the acceptor optical densities at the donor excitation and emission wavelengths, respectively. The critical distance of energy transfer was calculated from eq. (4) using the Mathcad 15.0 software.

## Molecular docking study

The molecular docking was carried out to ascertain the putative sites for the dye binding to insulin fibrils. The model of fibrillar insulin was taken from http://people.mbi.ucla.edu/sawaya/jmol/fibrilmodels/ [35]. The structures of the dyes were optimized using the semiempirical method PM6 (MOPAC2016 version18.012L) [36]. The top 10 conformations obtained with the PatchDock algorithm were then refined by the FireDock software [37]. The docked complexes were visualized by the Visual Molecular Dynamics (VMD) software.

## Quantum-chemical calculations

Using the MOPAC2016 software, the geometry optimization of the dye conformations was performed, followed by the calculation of the quantum-chemical characteristics, such as: the solvent-accessible area ( $CA$ ); molecular volume ( $CV$ ); energy of the highest occupied ( $E_{HOMO}$ ) and lowest unoccupied ( $E_{LUMO}$ ) molecular orbitals; molecular length ( $L$ ), height ( $H$ ) and width ( $W$ ); ground state dipole moment ( $\mu_g$ ) and molecular weight ( $M.wt.$ ). The $LogP$ , a compound lipophilicity, was obtained using the ALOGPS 2.1 program (http://www.vcclab.org/lab/alogps/) [38]. All the calculated parameters are presented in Table 3.

## RESULTS AND DISCUSSION

The ensemble of four dyes including the classical amyloid marker ThT (donor D1), chalcone dye DMC (acceptor A1 for ThT and donor D2), squaraine dyes SQ4 (acceptor A2 for DMC and donor D3) and SQ1 (acceptor A3) were selected to study the msFRET applicability to amyloid detection based on our previous results [25].

At the first step of the study we addressed the question of how the fluorescence of the terminal acceptor (SQ1) is sensitized by the other donors/acceptors of the energy transfer chain. To this end, the fluorescence spectra of the SQ1-protein mixtures were measured with the excitation wavelength 440 nm (Fig. 4) that was chosen based on the spectral characteristics of the primary donor, ThT. The fluorescence intensity of SQ1 in the emission maximum (680 nm) did not exceed 1000 a.u. in the presence of fibrillar insulin (InsF). The addition of SQ4 (D3) into this system led to some decrease in SQ1 (A3) fluorescence, as well as to the appearance of the SQ4 fluorescence band. This implies that the expected enhancement of acceptor fluorescence does not occur at this stage, presumably because of relatively low fluorescence signal from SQ4 under the employed experimental conditions. At the same time, no SQ1 and SQ4 fluorescence was observed in the presence of the control protein (InsN). However, the subsequent addition of ThT resulted in the pronounced fluorescence increase in InsF, indicating that the energy is transferred from ThT to the squaraines. There are two possibilities by which such energy transfer may occur, the parallel pathway (ThT→SQ4 and ThT→SQ1) and the sequential one (ThT→SQ4→SQ1). Moreover, when the FRET chain was complemented by DMC serving as a bridge between ThT and SQ4, the squaraine fluorescence showed a further enhancement increasing with the elevation of DMC concentration (Fig. 4A,B). It is interesting to note that squaraine peaks emerging in the presence of DMC were observed also for InsN with SQ4 fluorescence signal being higher than that of SQ1, while in the absence of the mediator SQ1 and SQ4 fluorescence was negligibly small. The excitation spectra measured at the emission wavelength 720 nm at the highest DMC concentration also are indicative of the marked difference between the InsF and InsN (Fig. 4C). The squaraine peaks are clearly resolved in these spectra at 637 nm for SQ4, and 676 nm for SQ1, in the presence of the fibrillar insulin, while small hypsochromic shifts *ca.* 8 and 3 nm for SQ4 and SQ1, respectively, along with significantly lower fluorescence intensities were observed for the control non-fibrillized protein.
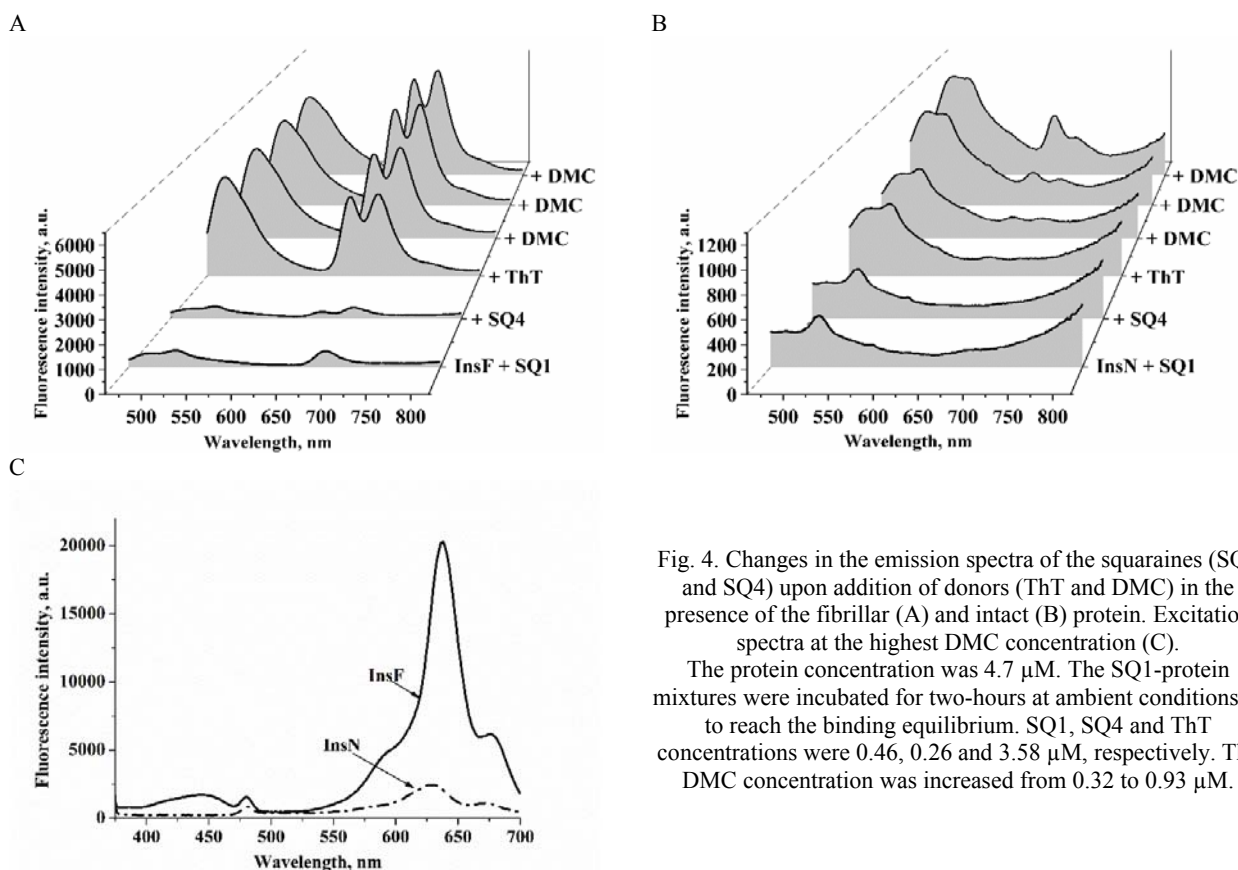
A



B

C

Fig. 4. Changes in the emission spectra of the squaraines (SQ1 and SQ4) upon addition of donors (ThT and DMC) in the presence of the fibrillar (A) and intact (B) protein. Excitation spectra at the highest DMC concentration (C).
The protein concentration was 4.7 μM. The SQ1-protein mixtures were incubated for two-hours at ambient conditions to to reach the binding equilibrium. SQ1, SQ4 and ThT concentrations were 0.46, 0.26 and 3.58 μM, respectively. The DMC concentration was increased from 0.32 to 0.93 μM.

To quantify the above effects, the enhancement in the fluorescence intensity was calculated as the ratio $I_i^{683} / I_{SQ1}^{683}$ for SQ1, and $I_i^{648} / I_{SQ4}^{648}$ for SQ4 at increasing DMC concentration (Fig. 5), where $I_i^{683}$ and $I_i^{648}$ are the fluorescence intensities at the *i*-th point of the sample titration with DMC; $I_{SQ1}^{683}$ and $I_{SQ4}^{648}$ are the initial fluorescence intensities of the squaraines. As seen in Fig.5, the addition of the donor D1 (ThT) resulted in the SQ1/SQ4 fluorescence enhancement by 6/12 times in the presence of fibrillar insulin and by 1.2/1.6 times in the presence the of the control protein, respectively. The mediator (DMC) led to a further enhancement of the squaraine fluorescence for both fibrillar and the non-fibrillized control protein with respect to that of the mediator-free systems.

The ratio of the signal amplification in the presence of the fibrillar protein to that in the control showed somewhat decrease with increasing the DMC concentration (Fig. 5C). However, at all mediator concentrations, the dye fluorescence enhancement was more than 3 times stronger in the presence of fibrillar insulin with respect to the control protein for both SQ1 and SQ4.
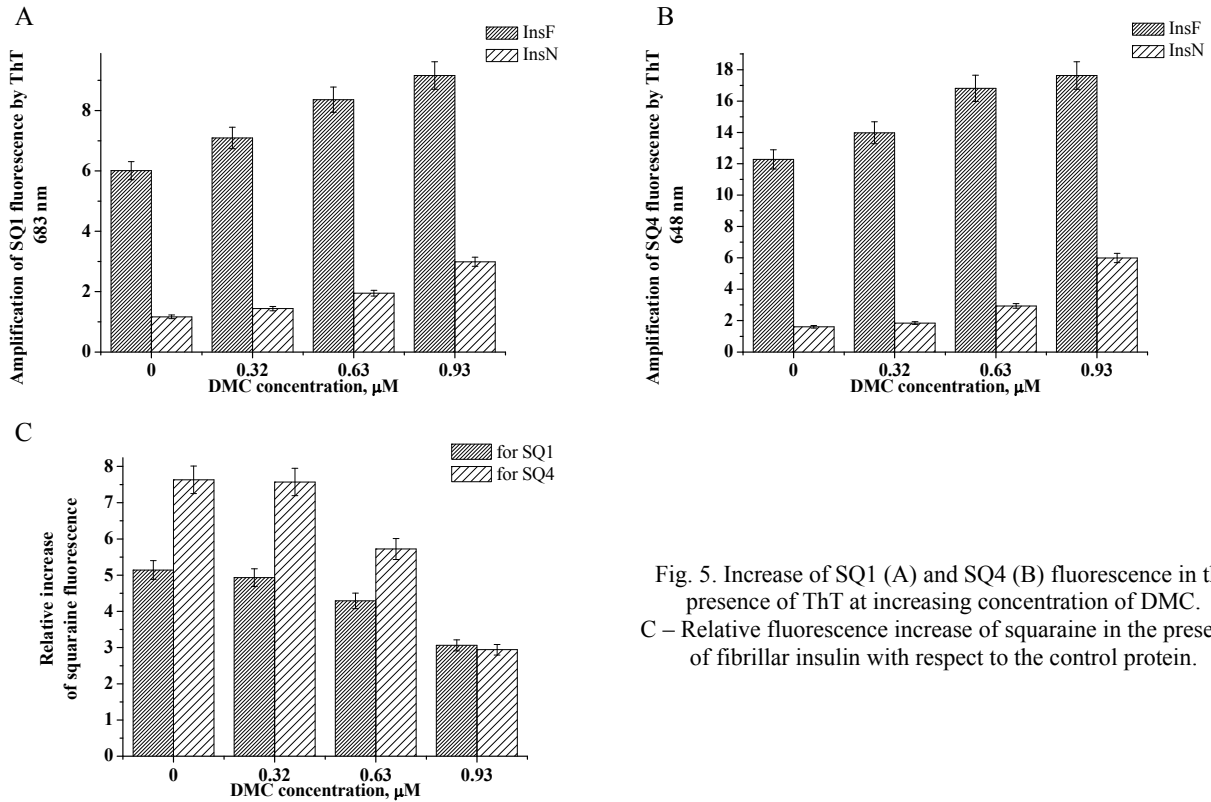


Fig. 5. Increase of SQ1 (A) and SQ4 (B) fluorescence in the presence of ThT at increasing concentration of DMC.
C – Relative fluorescence increase of squaraine in the presence of fibrillar insulin with respect to the control protein.
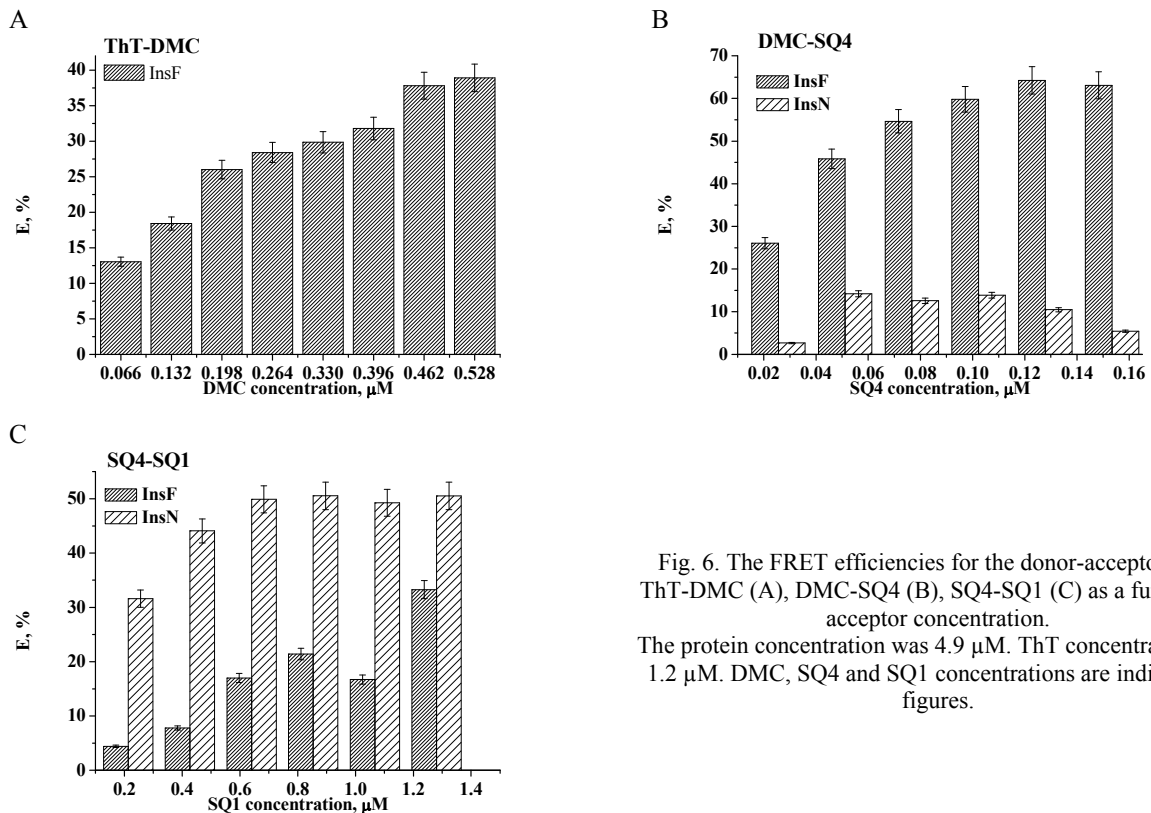


Fig. 6. The FRET efficiencies for the donor-acceptor pairs ThT-DMC (A), DMC-SQ4 (B), SQ4-SQ1 (C) as a function of acceptor concentration.
The protein concentration was 4.9 μM. ThT concentration was 1.2 μM. DMC, SQ4 and SQ1 concentrations are indicated in figures.

At the next step of the study, the ThT-protein mixtures were consecutively titrated with DMC, SQ4 and SQ1. The donor fluorescence gradually decreased with increasing acceptor concentration for each FRET step in the presence of both fibrillar and control protein, except for the ThT-DMC pair in InsN, where the donor and acceptor fluorescence increased simultaneously due to superposition of the DMC and ThT emission spectra (data not shown). The efficiencies of energy transfer for the three donor-acceptor pairs were calculated from the quenching of the donor fluorescence. As illustrated in Fig. 6, FRET efficiencies in the presence of fibrillar insulin increased with increasing acceptor concentrations by the factors of 3, 2.4 and 7.5 for the pairs ThT-DMC, DMC-SQ4 and SQ4-SQ1, respectively. The largest values of FRET efficiency were observed for the pair DMC-SQ4 (*E*> 60%). Remarkably, the energy transfer efficiencies in the presence of fibrillar insulin were ~ 12 times greater and ~1.5 times lower than those for the control protein for the pairs D2-A2 and D3-A3, respectively. A more pronounced FRET observed in the control protein for the pair SQ4-SQ1 as compared to InsF did not have a critical influence on the resulting transfer efficiency, since at the first step of cascade FRET the energy was not transferred in InsN and at the second step the efficiency was lower than that in InsF.

As seen from Eqs. (3) and (4), the efficiency of energy transfer depends on the distance between donor and acceptor and the Förster radius which, in turn, is determined by the overlap between the donor emission and acceptor absorption spectra, the donor quantum yield and the acceptor extinction coefficient, the refractive index of the medium and the orientation factor. The overlap integrals, the Förster radii and the donor-acceptor separations were calculated for the pairs ThT-DMC, DMC-SQ4 and SQ4-SQ1 taking the isotopic value of the orientation factor ($\kappa^2 = 2/3$).

The relative quantum yield of the donors (Table 1) was calculated as:

$$Q_d = Q_s \cdot \frac{(1-10^{A_s})S_d n_d^2}{(1-10^{A_d})S_s n_s^2} \qquad (17)$$

where $Q_s$ is the quantum yield of the standard, $A_d$ and $A_s$ are the optical densities at the donor excitation wavelength, $S_d$ and $S_s$ are the areas under the fluorescence bands, $n_d$ and $n_s$ are the refractive indexes of the medium for the donor and standard, respectively. Notably, the binding of ThT to fibrillar insulin resulted in the increase of the dye quantum yield by more than two orders of magnitude (Table 1).

Table 1

Donor quantum yields in the presence of fibrillar insulin

| Donor | $Q_d$ | Standard |
|---|---|---|
| ThT | 0.02 | ThT in buffer ($Q_s$=10⁻⁴) [39] |
| DMC | 0.18 | DMC in ethanol ($Q_s$=0.2) [40] |
| SQ4 | 0.014 | Nile Blue in water ($Q_s$=0.01) [41] |

The normalized emission and absorption spectra of the three donor-acceptor pairs are depicted in Fig. 7, while the overlap integral value (*J*) evaluated by the numerical integration are presented in Table 2. The pair SQ1-SQ4 demonstrated the greatest *J* value due to a small shift (~32 nm) between SQ4 fluorescence and SQ1 absorption maxima, and a high extinction coefficient of SQ1.
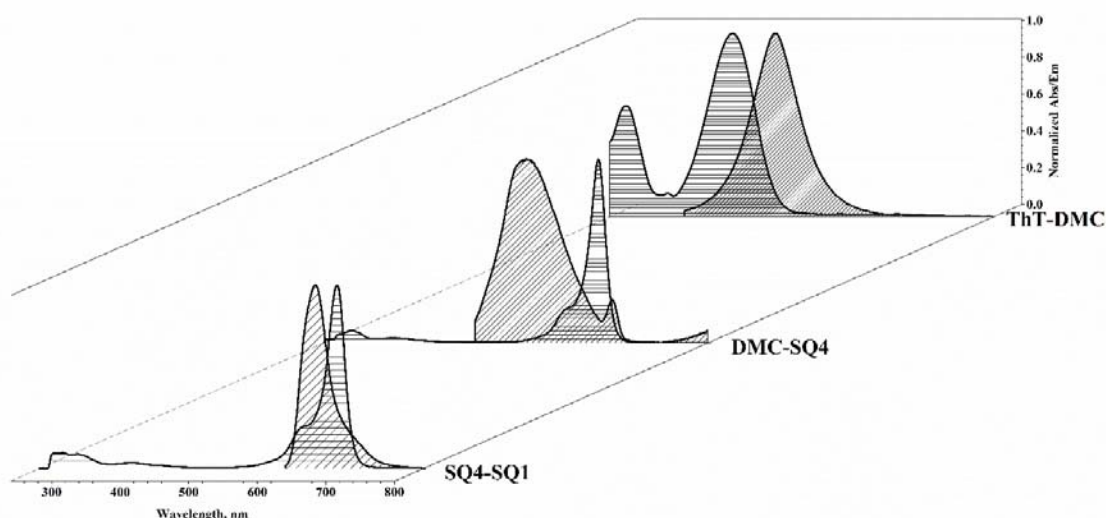


Fig. 7. Overlap of the normalized donor emission (slanting lines) and acceptor absorption (horizontal lines) spectra for the donor-acceptor pairs ThT-DMC ($\lambda_{max}^{fluor} = 483$ nm, $\lambda_{max}^{abs} = 421$ nm), DMC-SQ4 ($\lambda_{max}^{fluor} = 535$ nm, $\lambda_{max}^{abs} = 641$ nm) and SQ4-SQ1 ($\lambda_{max}^{fluor} = 644$ nm, $\lambda_{max}^{abs} = 676$ nm).

The Förster radius, a characteristic of each donor-acceptor pair, was calculated from equation (4). The largest value of the Förster radius (Table 2) was obtained for the pair DMC-SQ4 due to the greatest values of DMC relative quantum yield (0.18) and SQ4 extinction coefficient ($\varepsilon_{641}^{DMSO} = 4.21 \cdot 10^5$ M$^{-1}$cm$^{-1}$). The donor-acceptor distance $r$ was estimated based on the classical expression for the distance dependence of FRET efficiency (Eq. 3) using the $E$ values at the maximum acceptor concentrations.

Table 2

FRET parameters obtained under assumption of isotopic rotation of the fluorophores

| System | $J$, M$^{-1}$cm$^{-1}$nm$^4$ | $R_0$, nm | $r$, nm |
|---|---|---|---|
| ThT-DMC | $3.73 \cdot 10^{14}$ | 2.3 | 2.4 |
| DMC-SQ4 | $5.32 \cdot 10^{15}$ | 5.0 | 4.5 |
| SQ4-SQ1 | $1.52 \cdot 10^{16}$ | 3.9 | 4.3 |

The distinctions between the fibrillar and control proteins appeared to be the most pronounced in the 3D fluorescence spectra. As illustrated in Fig. 8A, in the system consisting of ThT, DMC and SQ4 bound to InsF, the strongest fluorescence centered around ~ 650 nm corresponds to SQ4; the spot located above the excitation wavelength 550 nm is related to the direct excitation of SQ4, while the bottom spot centered at $\lambda_{Ex}$ ~ 440 nm originates from the energy transfer ThT→DMC→SQ4. A residual ThT fluorescence is observed at $\lambda_{Ex}$ ~ 440 nm and $\lambda_{Em}$ ~ 580 nm. The addition of SQ1 into the above ternary system resulted in the appearance of a new spot centered at $\lambda_{Em}$ ~ 685 nm and $\lambda_{Ex}$ ~ 440 nm, and in the decrease of SQ4 signal (Fig. 8C), suggesting that the energy is transferred from ThT to SQ1 via SQ4. As seen in Figs. 8B and 8D, the intensity of the analogous patterns is substantially lower in InsN compared to InsF. The barely noticeable spots centered at the SQ4 (Fig. 8B) and SQ1 (Fig. 8D) emission maxima at $\lambda_{Ex}$ ~ 440 nm were observed, while the higher emission intensities observed at $\lambda_{Ex}$ > 550 nm are related to the direct excitation of the fluorophores.



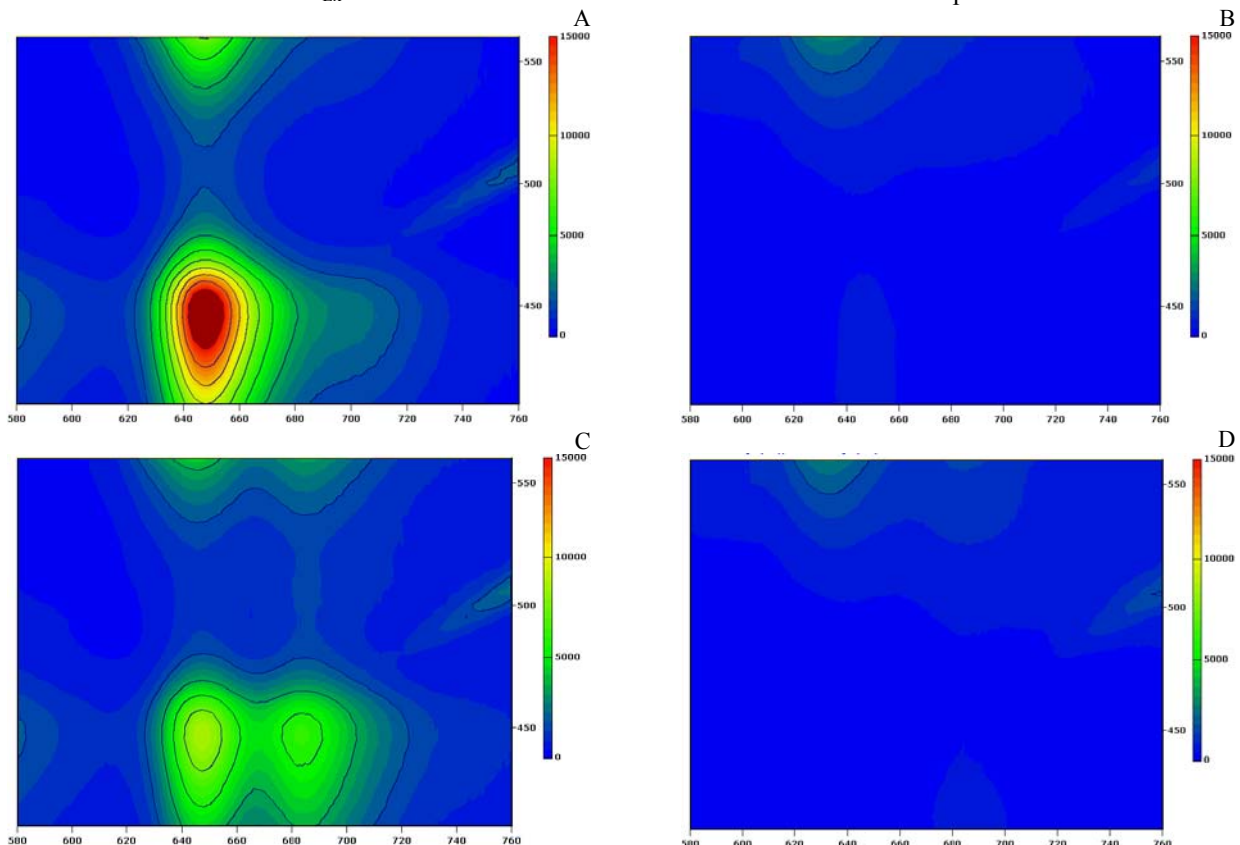Fig. 8. 3D fluorescence spectra recorded in the presence of DMC (0.53 μM) and SQ4 (0.16 μM) in the ThT– fibrillar (A) and control (B) protein mixtures, followed by the addition of SQ1 (1.4 μM) to the fibrillar (C) and control (D) insulin. The emission and excitation wavelengths were varied within the ranges 580-760 nm and 410-560 nm, respectively. The excitation and emission slit widths were set at 10 nm. The protein and ThT concentrations were 4.9 and 1.2 μM, respectively.

In the last step of our investigation, the simple docking studies were performed to provide additional structural characterization of the dye-fibril complexes. As seen in Fig. 9A, ThT, DMC and SQ4 tend to associate with the 4–5 residues of the L17 ladder of the insulin fibril protofilament located on the dry steric zipper interface, suggesting the predominant role of hydrophobic and van der Waals dye-protein interactions. A similar binding motif was previously proposed for ThT [42]. In turn, the bulky moieties of zwitterionic SQ1 seem to prevent its binding to the dry amyloid

surface, and thus, SQ1, being the most hydrophobic among the examined dyes (possessing the highest *LogP* value, Table 3) binds to the wet surface groove formed by the residues GLN15 and GLU17 of the insulin A-chain. In this case, the hydrophobic, aromatic and electrostatic forces may stabilize the dye-protein complex. Interestingly, the distance between fibril-bound SQ4 and SQ1 was about 3 nm, being close to the value *ca.* 3.9 nm obtained from the FRET efficiency (Table 2).

However, precise identification of the fibril binding sites for the dyes seem to be complicated because the rigid docking algorithms used here are based on the shape complementarity principles (PatchDock) and perform only the protein side-chain optimization (FireDock). In turn, the ligand structure remains fixed during the docking process that may lead to the appearance of the false protein binding sites if the optimized dye geometry used for calculations differs from the real geometry. Thus, the discrepancies between ThT-DMC, and DMC-SQ4 distances obtained experimentally (Table 2) and by the molecular docking (Fig. 9A) can be explained by the drawbacks of the docking technique. To

Table 3

Quantum-chemical characteristics of the dyes after geometry optimization (PM6, MOPAC)

| Dye | SQ1 | SQ4 | DMC | ThT |
|---|---|---|---|---|
| $CA$, Å$^2$ | 611 | 438 | 304 | 318 |
| $CV$, Å$^3$ | 767 | 519 | 320 | 350 |
| $E_{HOMO}$, eV | −6.9 | −6.8 | −8.3 | −11.0 |
| $E_{LUMO}$, eV | −2.0 | −1.9 | −0.7 | −4.4 |
| $L$, Å | 21.1 | 18.5 | 14.4 | 14.3 |
| $W$, Å | 10.7 | 6.4 | 5.7 | 5.7 |
| $H$, Å | 8.1 | 4.5 | 3.4 | 3.7 |
| $\mu_g$, D | 3.2 | 5.8 | 5.7 | 2.7 |
| $M.wt.$, g/M | 608.82 | 424.54 | 251.33 | 188.61 |
| $LogP$ | 9.81 | 1.59 | 3.84 | −0.14 |

correlate the FRET and docking results, one should assume that SQ4 and SQ1 are bound to the wet insulin protofilament surface (because of their similar structure), while DMC and ThT reside at the dry amyloid surface due to their small volumes and molecular weights (Table 3). If SQ4 and SQ1 are associated with the two opposite sides of the fibril surface, the intermolecular distance will be about 3 nm. In turn, if ThT and DMC are bound to the L17 ladders available on the first and second β-sheet of the insulin protofilament, respectively, the distance between the two fluorophores will be about 2.5 nm (Table 2).
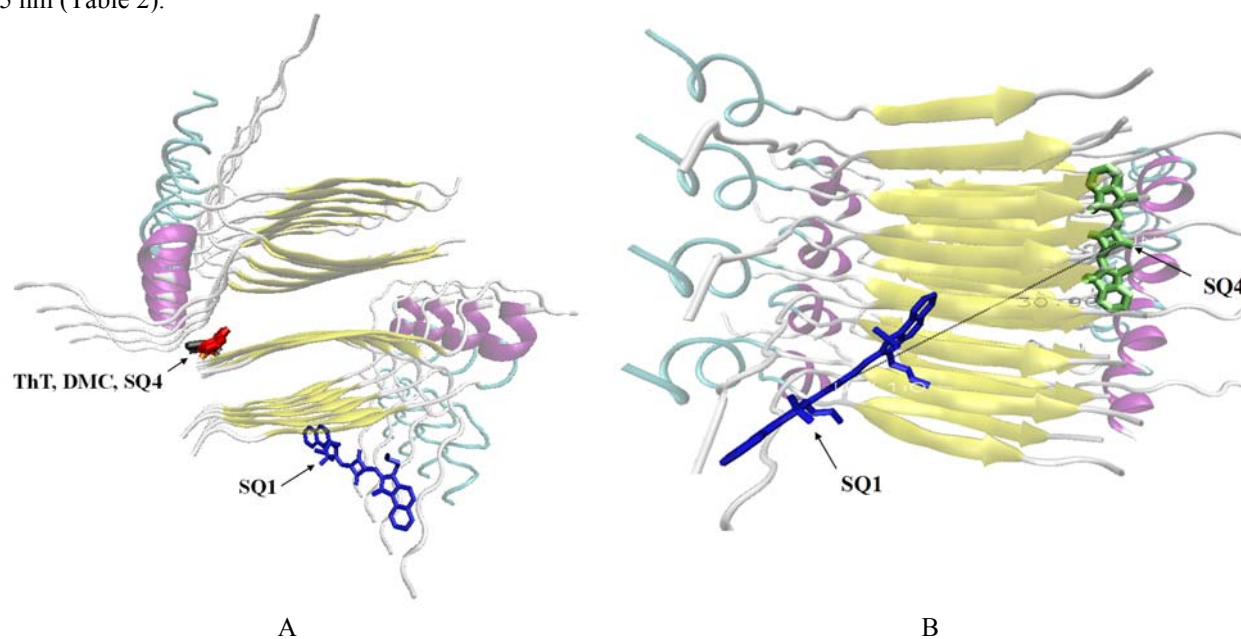


| A | B |
|---|---|

Fig. 9. Schematic representation of the energetically most favorable dye complexes with fibrillar insulin, obtained using PatchDock/ FireDock servers and visualized by VMD software.

The drawing method was set as Bonds and NewCartoon for the dyes and the protein, respectively. ThT, DMC, SQ4 are bound to the L17 ladder of the B chain, located at the dry steric zipper of the insulin fibril protofilament, while SQ1 is attached to the surface groove formed by the residues GLN15 and GLU17 of the A chain (A). The distance between SQ1 and SQ4 is about 3 nm (B).

## CONCLUSIONS

To summarize, we have successfully designed the dye ensemble suitable for the three-step sequential FRET in the insulin amyloid fibrils. The following chromophores were recruited as the components of the fibril-scaffolded FRET chain: i) a primary donor, Thioflavin T, transferring its energy to the mediator dye, DMC, upon excitation at 440 nm; ii) a novel squaraine dye SQ4 accepting the energy from DMC; and iii) squaraine fluorophore SQ1 accepting the energy from SQ4, followed by the emission enhancement at 680 nm. The above cascade showed notable increase in the SQ1 fluorescence compared to that devoid of DMC. Despite the parallel FRET between the dyes cannot be excluded, the donor-acceptor distances estimated for each pair assuming the isotopic chromophore rotation appeared to be consistent with the intergroove separations in the core of insulin fibrils. The recovered distances fall in the range 2.4 – 4.5 nm, suggesting different fibril binding sites for the dyes. The fact that no cascade FRET was observed in the non-fibrillized protein, highlights the importance of the dye association with the highly ordered amyloid structure for the energy transfer to occur in the chain ThT→DMC→SQ4→SQ1. These results may prove of importance in the development of the novel sensitive fluorescence approaches to amyloid detection and characterization, particularly, in vivo, by introducing the near-infrared fluorophores to the cascade.

### ORCID IDs

**Uliana Tarabara** https://orcid.org/0000-0002-7677-0779, **Kateryna Vus** https://orcid.org/0000-0003-4738-4016,
**Olga Zhytniakivska** https://orcid.org/0000-0001-9554-0090, **Valeriya Trusova** https://orcid.org/0000-0002-7087-071X,
**Galyna Gorbenko** https://orcid.org/0000-0002-0954-5053

### REFERENCES

[1]  P. Wu and L. Brand, Anal. Biochem. **218**, 1-13 (1994), https://doi.org/10.1006/abio.1994.1134.
[2]  P.R. Selvin, Nature Struct. Biol. **7**, 730-734 (2000), https://doi.org/10.1038/78948.
[3]  L.M. Loura and M. Prieto, Front. Physiol. **2**, 82 (2011), https://doi.org/10.3389/fphys.2011.00082.
[4]  G. Ramanoudjame, M. Du, K.A. Mankiewicz and V. Jayaraman, Proc. Natl. Acad. Sci. U.S.A. **103**, 10473-10478 (2006), https://doi.org/10.1073/pnas.0603225103.
[5]  A. Coskun and E.U. Akkaya, J. Am. Chem. Soc. **128**, 14474-14475 (2006), https://doi.org/10.1021/ja066144g.
[6]  P. Tinnefeld, M. Heilemann and M. Sauer, Chem. Phys. Chem **6**, 217-222 (2005), https://doi.org/10.1002/cphc.200400513.
[7]  B. Albinsson, J.K. Hannestad and K. Borjesson, Coordination Chemistry Reviews, **256**, 2399-2413 (2012), https://doi.org/10.1016/j.ccr.2012.02.024.
[8]  S. Buckhout-White, C.W. Brown III, D.A. Hastman Jr, M.G. Ancona, J.S. Melinger, E.R. Goldmana and I.L. Medintz, RSC Adv. **6**, 97587-97598 (2016), https://doi.org/10.1039/C6RA23079B.
[9]  A. Bodi, K.E. Borbas and J.I. Bruce, Dalton Trans. **2007**, 4352-4358 (2007), https://doi.org/10.1039/B708940F.
[10]  D. Navarathne, Y. Ner, J.G. Grote and G.A. Sotzing, Chemical Communications, **47**, 12125-12127 (2011), https://doi.org/10.1039/C1CC14416B.
[11]  G. McDermott, S.M. Prince, A.A. Freer, A.M. Hawthornthwaite-Lawless, M.Z. Papiz, R.J. Cogdell and N.W. Isaacs, Nature, **374**, 517-521 (1995), https://doi.org/10.1038/374517a0.
[12]  W. Kühlbrandt and D.N. Wang, Nature, **350**, 130-134 (1991), https://doi.org/10.1038/350130a0.
[13]  C. Goze, G. Ulrich and R. Ziessel, J. Org. Chem. **72**, 313-322 (2007), https://doi.org/10.1021/jo060984w.
[14]  J. Saha, D. Dey, A.D. Roy, P. Bhattacharjee and S.A. Hussain, J. Luminesc. **172**, 168-174 (2016), https://doi.org/10.1016/j.jlumin.2015.12.004.
[15]  G. Ulrich, C. Goze, M. Guardigli, A. Rodda and R. Ziessel, Angew. Chem. Int. Ed. **44**, 3694-3698 (2005), https://doi.org/10.1002/anie.200500808.
[16]  A. Aneja, N. Mathur, P.K. Bhatnagar and P.C. Mathur, J. Biol. Phys. **34**, 487-493 (2008), https://doi.org/10.1007/s10867-008-9107-y.
[17]  K. Boeneman, D.E. Prasuhn, J.B. Blanco-Canosa, P.E. Dawson, J.S. Melinger, M. Ancona, M.H. Stewart, K. Susumu, A. Huston and I.L. Medintz, Proc. of SPIE, **7909**, 1-7 (2011), https://doi.org/10.1117/12.879272.
[18]  R.W. Wagner and J.S. Lindsey, J. Am. Chem. Soc. **116**, 9759–9760 (1994), https://doi.org/10.1021/ja00100a055.
[19]  R.W. Wagner, J.S. Lindsey, J. Seth, V. Palaniappan and D.F. Bocian, J. Am. Chem. Soc. **118**, 3996–3997 (1996), https://doi.org/10.1021/ja9602657.
[20]  X. Song, J. Shi, J. Nolan and B. Swanson, Anal. Biochem. **291,** 133–141 (2001), https://doi.org/10.1006/abio.2001.5024.
[21]  X. Duan, S. Wang and Z. Li, Chem. Commun. **2008,** 1302–1304 (2008), https://doi.org/10.1039/B717300H.
[22]  V. Raicu, J. Biol. Phys. **33**, 109-127 (2007), https://doi.org/10.1007/s10867-007-9046-z.
[23]  L. He, X. Wu, J. Simone, D. Hewgill and P.E. Lipski, Nucleic Acid Res. **33**, 61–73 (2005), https://doi.org/10.1093/nar/gni057.
[24]  E. Galperin, V. V. Verkhusha and A. Sorkin, Nature Methods, **1**, 209–217 (2004), https://doi.org/10.1038/nmeth720.
[25]  G. Gorbenko, V. Trusova, T. Deligeorgiev, N. Gadjev, C. Mizuguchi and H. Saito, J. Mol. Liq. **294**, 111675 (2019), https://doi.org/10.1016/j.molliq.2019.111675.
[26]  M. Kuscu and O.B. Akan, IEEE Transactions on nanotechnology, **11**, 200-207 (2012), https://doi.org/10.1109/TNANO.2011.2170705.

[27] G. Bunt and F.S. Wouters, Biophys. Rev. **9**, 119-129 (2017), https://doi.org/10.1007/s12551-017-0252-z.

[28] B.W. Meer, D.M. Meer and S.S. Vogel, in: *FRET - Förster Resonance Energy Transfer: From Theory to Applications*, edited by I.L. Medintz and N. Hildebrandt (Wiley-VCH, Weinheim, 2014), pp. 63-104, https://doi.org/10.1002/9783527656028.ch04.

[29] J.R. Lakowicz, *Principles of fluorescence spectroscopy*, 3rd ed., (Springer, New York, 2006), pp. 445-453.

[30] L. Stryer, Annual review of biochemistry, **47**, 819-846 (1978), https://doi.org/10.1146/annurev.bi.47.070178.004131.

[31] Z. Gryczynski, I. Gryczynski and J.R. Lakowicz, in: *Molecular imaging: FRET microscopy and spectroscopy*, edited by A. Periasamy, R. Day (Qxford, New York, 2005), pp. 19-56.

[32] B. Valeur, *Molecular fluorescence: principles and applications*, (Wiley-VCH, Weinheim, 2001), pp. 247-272, https://doi.org/10.1002/3527600248.ch9.

[33] H.M. Watrob, C.P. Pan and M.D. Barkley, J. Am. Chem. Soc. **125**, 7336-7343 (2003), https://doi.org/10.1021/ja034564p.

[34] M. Groenning, J. Chem. Biol. **3**, 1-18 (2010), https://doi.org/10.1007/s12154-009-0027-5.

[35] M.I. Ivanova, S.A. Sievers, M.R. Sawaya, J.S. Wall and D. Eisenberg, Proc. Natl. Acad. Sci. USA. **106**, 18990-19995 (2009), https://dx.doi.org/10.1073%2Fpnas.0910080106.

[36] J.J. Stewart, J. Comput. Aided. Mol. Des. **4**, 1-105 (1990), https://doi.org/10.1007/BF00128336.

[37] D. Duhovny, R. Nussinov, H.J. Wolfson, Lect. Notes Comput. Sci. Eng. **2452**, 185-200 (2002), https://doi.org/10.1007/3-540-45784-4_14.

[38] I.V. Tetko and V.Y. Tanchuk, J. Chem. Inf. Comput. Sci. **42**, 1136-1145 (2002), https://doi.org/10.1021/ci025515j.

[39] A.I. Sulatskaya, A.A. Maskevich, I.M. Kuznetsova, V.N. Uversky and K.K. Turoverov, PLoS ONE, **5**, e15385 (2010), https://doi.org/10.1371/journal.pone.0015385.

[40] J.A. Vladimirov and G.E. Dobretsov, *Флуоресцентные зонды в исследовании биологических мембран [Fluorescent probes in study of biological membranes]*, (Nauka, Moscow, 1980), pp. 40. (in Russian)

[41] H.P. Oliveira, A.J. Camargo, L.G. Macedo, M.H. Gehlen and A.B. da Silva, Spectrochim. Acta A Mol. Biomol. Spectrosc. **58**, 3103–3111 (2002), https://doi.org/10.1016/S1386-1425(02)00119-1.

[42] K. Vus, M.Girych, V. Trusova, G. Gorbenko, A. Kurutos, A. Vasilev, N. Gadjev and T. Deligeorgiev, Journal of Molecular Liquids, **276**, 541-552 (2019), https://doi.org/10.1016/j.molliq.2018.11.149.

## ТРЬОХЕТАПНИЙ РЕЗОНАНСНИЙ ПЕРЕНОС ЕНЕРГІЇ В АМІЛОЇДНИХ ФІБРИЛАХ ІНСУЛІНУ

**У. Тарабара[1], М. Щука[1], К. Вус[1], О. Житняківська[1], В. Трусова[1], Г. Горбенко[1], Н. Гаджев[2], Т. Делігеоргієв[2]**

*[1]Кафедра медичної фізики та біомедичних нанотехнологій,*
*Харківський національний університет імені В.Н. Каразіна*
*пл. Свободи 4, Харків, 61022, Україна*
*[2]Факультет хімії і фармації, Софійський університет, Софія, 1164, Болгарія*

За допомогою системи хромофорів, що складалась із тіофлавіну Т (ThT), 4-диметиламінохалкону (ДМХ) і двох сквараїнових барвників, SQ1 і SQ4, проведено оцінку можливості використання трьохетапного індуктивно-резонансного переносу енергії (ІРПЕ) для детектування амілоїдних фібрил інсуліну. Виявлено, що медіаторний барвник ДМХ збільшує інтенсивність флуоресценції кінцевого акцептора SQ1, що збуджується на 440 нм (у максимумі поглинання основного донора, ThT), у фібрилярному інсуліні, у порівнянні з флуоресценцією у відсутності ДМХ, що свідчить про наявність каскадного переносу енергії вздовж ланцюга ThT→ДМХ→SQ4→SQ1. Окрім цього, Стоксовий зсув у системі з чотирма хромофорами складав 240 нм, у порівнянні з 45 нм для зв'язаного з амілоїдними фібрилами тіофлавіну Т, що свідчить про перевагу детектування амілоїдних фібрил за допомогою багатоетапного ІРПЕ завдяки вищому співвідношенню сигнал-шум. Максимальні значення ефективності переносу енергії в фібрилах інсуліну, визначені для кожної каскадної пари при вимірюванні гасіння флуоресценції донора в присутності акцептора, складали 40%, 60% і 30% для донорно-акцепторних пар ThT-ДМХ, ДМХ-SQ4 і SQ4-SQ1, відповідно, , тоді як у випадку нефібрилізованого білка перенос енергії був практично відсутній. Найбільш виражені відмінності між фібрилярним та нефібрилізованим білком спостерігались в 3D спектрах флуоресценції. Зокрема, у фібрилярних агрегатах інсуліну виявлено дві інтенсивні області з центрами на довжинах хвиль флуоресценції ~ 650 нм (SQ4) та ~ 685 нм (SQ1) при збудженні на довжині хвилі ~ 440 нм. Натомість, для нефібрилізованого білка, були наявні ледь помітні області на тих самих довжинах хвиль, а також, більш інтенсивні області при збудженні на довжині хвилі понад 550 нм, що свідчить про переважний вплив прямого збудження SQ1 та SQ4 на флуоресцентну відповідь зондів. Міжмолекулярні відстані, розраховані на основі експериментальних значень ефективності переносу енергії у припущенні ізотропного обертання хромофорів, становили 2.4, 4.5 і 3.2 нм для пар ThT-ДМХ, ДМХ-SQ4 і SQ4-SQ1, відповідно, що свідчить про різні сайти зв'язування барвників з фібрилами. Квантово-хімічні розрахунки і метод молекулярного докінгу дозволили припустити, що зв'язування SQ1, SQ4 і ThT, ДМХ відбувається з «вологою» і «сухою» поверхнями протофіламентів інсуліну, відповідно. Комплекси зонд-білок, вочевидь, стабілізуються гідрофобними, ван-дер-Ваальсовими, ароматичними та електростатичними взаємодіями. Таким чином, завдяки високій чутливості та нижчій вірогідності псевдо-позитивного результату, розроблений метод можна використовувати для детектування та характеризації амілоїдних фібрил in vitro паралельно з класичним тіофлавіновим методом. Перспективним також є використання багатоетапного ІРПЕ для візуалізації амілоїдів in vivo, за умови включення до каскаду зонду, що має смуги поглинання і флуоресценції у ближній інфрачервоній області.

**КЛЮЧОВІ СЛОВА:** каскадний резонансний перенос енергії, 4-диметиламінохалкон, фібрилярний інсулін, скварaїнові зонди, тіофлавін Т.

## ТРЕХЭТАПНЫЙ РЕЗОНАНСНЫЙ ПЕРЕНОС ЭНЕРГИИ В АМИЛОИДНЫХ ФИБРИЛЛАХ ИНСУЛИНА

**У. Тарабара[1], М. Щука[1], К. Вус[1], О. Житняковская[1], В. Трусова[1], Г. Горбенко[1], Н. Гаджев[2], Т. Делигеоргиев[2]**

*[1]Кафедра медицинской физики и биомедицинских нанотехнологий,*
*Харьковский национальный университет имени В.Н. Каразина*
*пл. Свободы 4, Харьков, 61022, Украина*
*[2]Факультет химии и фармации, Софийский университет, София, 1164, Болгария*

С помощью системы хромофоров, содержащей тиофлавин Т (ThT), 4-диметиламинохалкон (ДМХ) и два сквараиновых красителя, SQ1 и SQ4, проведена оценка возможности использования трехэтапного индуктивно-резонансного переноса энергии (ИРПЕ) для детектирования амилоидных фибрилл инсулина. Обнаружено, что медиаторный краситель ДМХ

увеличивает интенсивность флуоресценции конечного акцептора SQ1, возбуждаемого при 440 нм (в максимуме поглощения основного донора, ThT), в фибриллярном инсулине по сравнению с флуоресценцией в отсутствие ДМХ, что свидетельствует о наличии каскадного переноса энергии вдоль цепи ThT→ДМХ→SQ4→SQ1. Кроме того, Стоксов сдвиг в системе с четырьмя хромофорами составил 240 нм, по сравнению с 45 нм для тиофлавина Т, связанного с амилоидными фибриллами, что свидетельствует о преимуществе детектирования амилоидных агрегатов при помощи многоэтапного ИРПЕ благодаря более высокому отношению сигнал-шум. Максимальные значения эффективности переноса энергии в фибриллах инсулина, определенные для каждой каскадной пары при измерении тушения флуоресценции донора в присутствии акцептора, составили 40%, 60% і 30% для донорно-акцепторных пар ThT-ДМХ, ДМХ-SQ4 и SQ4-SQ1, соответственно, тогда как в случае нефибриллизованого белка перенос энергии практически отсутствовал. Наиболее выраженные различия между фибриллярным и нефибриллизованным белком наблюдались в 3D спектрах флуоресценции. В частности, в амилоидных агрегатах инсулина обнаружено две интенсивных области с центрами на длинах волн эмиссии ~ 650 нм (SQ4) и ~ 685 нм (SQ1) при возбуждении на длине волны ~ 440 нм. В свою очередь, для нефибриллизованного белка выявлены едва заметные области с центрами на тех же самых длинах волн, а также – области с более высокими интенсивностями при возбуждении выше 550 нм, что свидетельствует о преимущественном влиянии прямого возбуждения SQ1 и SQ4 на флуоресцентный ответ этих красителей. Межмолекулярные расстояния, рассчитанные на основе экспериментальных значений эффективности переноса энергии, составили 2.4, 4.5 и 3.2 нм для пар ThT-ДМХ, ДМХ-SQ4 и SQ4-SQ1, соответственно, указывая на различные сайты связывания красителей с фибриллами. Квантово-химические расчеты и метод молекулярного докинга позволили предположить, что связывание SQ1, SQ4 и ThT, ДМХ проходит с «влажной» и «сухой» поверхностями протофиламентов инсулина, соответственно. Комплексы зонд-белок, по-видимому, стабилизируются,гидрофобными, ван-дер-Ваальсовыми, ароматическими и электростатическими взаимодействиями. Таким образом, благодаря высокой чувствительности и более низкой вероятности псевдо-положительного результата, разработанный метод можно использовать для детектирования и характеризации амилоидных фибрилл in vitro параллельно с классическим тиофлавиновым методом. Перспективной является также оценка возможности использования многоэтапного ИРПЕ для визуализации амилоидов in vivo, при условии включения в каскад зонда, который имеет полосы поглощения и испускания в ближней инфракрасной области.

**КЛЮЧЕВЫЕ СЛОВА:** каскадный резонансный перенос энергии, 4-диметиламинохалкон, фибриллярный инсулин, скварраиновые зонды, тиофлавин Т.

# EFFECT OF THE TRANSATMOSPHERIC SUN ELECTROMAGNETIC RADIATION, SIMULATED LABORATORY, ON THE MECHANICAL PROPERTIES OF THE KAPTON H TYPE POLYIMIDE FILMS

Viktory A. Lototskaya[1]*, Leonid F. Yakovenko[1], Evgeniy N. Aleksenko[1],
Nikolay I. Velichko[1], Yuriy S. Doronin[1], Anna A. Tkachenko[1],
Ivan P. Zaritskiy[1], Vyacheslav V. Abraimov[2], Wen Zhu Shao[2]

*[1]B. Verkin Institute for Low Temperature Physics and Engineering of NAS of Ukraine*
*Prospect Nauky, 47, Kharkov, 61103, Ukraine*
*[2]Harbin Institute of Technology*
*Harbin, the People's Republic of China*
*\*E-mail: lototskaya@ilt.kharkov.ua*

Received August 27, 2019; revised September 17, 2019, accepted Ocober 21, 2019

The mechanical properties (limit of forced elasticity, fracture stress, total deformation to failure and its components) of a 75 µm-thick polyimide film of kapton H type under uniaxial tension conditions at 293 K after exposure to the outer space factors were studied. The electromagnetic radiation of the transatmospheric Sun in the wavelength range of 250-2500 nm (EMRS) for 100 hours and vacuum ultraviolet (VUV) and ultra soft x-ray (USX) radiation in the range of 1.24-170 nm – for 100 and 500 hours were simulated under laboratory conditions. The effect of separate exposure in each of the wavelength ranges was investigated. It was found that after irradiation in the both wavelength ranges the films remained in a forced-elastic state. The tension diagrams, like in the initial state, have two stages. The contributions of the elastic, irreversible and highly elastic (delayed and reversible at test temperature) components to the total deformation to failure were determined. It was found that the limit of forced elasticity increased after irradiation both with EMRS, and with VUV and USX radiation. In this case an increase in the limit of the forced elasticity under the influence of EMRS was caused by heating of the film in the course of irradiation, and under the influence of VUV and USX radiation – by radiation effects. The fracture stress and total deformation to failure change weakly and only under the influence of VUV and USX radiation. With changing the duration of exposure to VUV and USX radiation (100 or 500 hours), the fracture stress and the total deformation to failure change non-monotonously. The negative consequence of exposure to VUV and USX radiation is the contribution values redistribution of the individual components of the total deformation to failure. VUV and USX radiation within 500 hours leads to a halving of the contribution of elastic deformation, which is reversible at deformation temperature.

**KEY WORDS:** polyimides, space factors, limit of forced elasticity, fracture stress, deformation

For several decades polyimide with the monomeric unit $C_{22}H_{10}N_2O_5$ (of kapton H, PM-A type, etc.) has been the main ultra-lightweight radiation-resistant polymer, used as a heat insulator on the outer surface of spacecrafts (SC). During this period the researchers' attention, primarily, was paid to the influence of space factors on the polymer electrical and thermo-radiation properties. In the process of development and design of small-sized satellites with an increased "lifetime" in orbit, a great interest arose to the mechanical properties of the polymer. In the outer space a number of extraordinary factors act simultaneously and alternately on the materials and elements of the spacecrafts: high vacuum, electromagnetic radiation, charged particle fluxes, thermal cycling, etc. In our previous work [1] we considered the influence of protons and electrons of the Earth's radiation belts with a length free path, comparable with the thickness of the film, on its mechanical properties under uniaxial tension. The obtained results on changing the limits of the forced elasticity, fracture stress, and overall elongation are in good agreement with the results given in the review [2]. The data on redistribution of different contributions to the total deformation (contributions of highly elastic, reversible at test temperature, delayed highly elastic and irreversible deformation) are presented only in our work.

The object of this work is to study the patterns of deformation and strength of kapton H-type polyimide films after simulating the separate effects of electromagnetic radiation from the transatmospheric Sun in the ranges of 250–2500 nm and 1.24–170 nm.

## MATERIAL AND METHOD OF RESEARCH

The objects of study were samples of thermoplastic film of aromatic polyimide – poly-4,4'-diphenylene oxide pyromellitimide, manufactured by PRC (People's Republic of China), with the thickness of 75 µm. The mechanical properties of this film in its initial state and after its exposure to fluxes of corpuscular radiation were studied in [1, 3].

Samples for testing under uniaxial tension (Fig. 1) were obtained using a special die. The axis of tension coincided with the direction of the film drawing. The shape and dimensions of the sample are close to type 1 according to State Standard 11262, which is admitted for use in tensile tests of film polymer samples (State Standard 14236). The sample was fixed with special grippers. The gripper consists of a roller, around which the sample blade is bent, and two clamps that capture the roller with the blade.

The mechanical properties of the samples subjected to space factors (SF) were studied at room temperature in the open air (293 K) not later than 24 hours after irradiation. The samples deformation under uniaxial tension was

performed using FPZ-100/1 tensile testing machine with a low-temperature unit, created in the Institute for Low Temperature Physics and Engineering [4], with the active rod moving speed $V_{def.}$ = 0.85 mm/min and, correspondingly, with the deformation rate $\dot{\varepsilon}$ =7·10$^{-4}$s$^{-1}$ ( $\dot{\varepsilon}$ =$V_{def.}$/$L_o$, where $L_o$ is the initial working length of the sample).
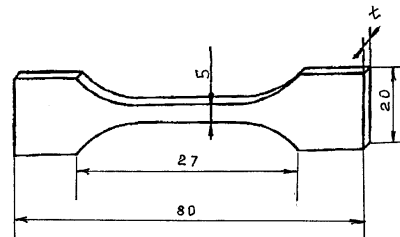


Fig. 1. The shape of the tensile test sample

In the process of deformation a tensile diagram was recorded in the coordinates "load P-elongation ΔL", from which the following mechanical characteristics were determined: the apparent limit of forced elasticity, corresponding to the stress, at which the highly elastic deformation is 1%, $\sigma_{forc.}$ = $P_{1\%}$/$S_o$; fracture stress of the sample $\sigma_{fr.}$ = $P_{fr.}$/$S_o$, where $S_o$ is the initial cross section of the sample; total elongation $\Delta L_{total}$, corresponding to the moment of the sample fracture; elongation $\Delta L_{elast.}$, corresponding to the elastic section of the curve. The other contributions to the total deformation $\Delta L_{total} = \Delta L_{elast.} + \Delta L_{high\ el.1} + \Delta L_{high\ el.2} + \Delta L_{irrevers.}$ were determined as in [3]. All these mechanical characteristics are presented below as average values according to the test results of six samples in each state.

The surface fractures of the samples were studied using MBS-9 optical microscope. In addition the surface fractures of the film samples, deformed in the initial state at 77 K, were analyzed. Mechanical properties of these samples are presented in [3].

The studied polyimide films were affected by SF (simulated in the laboratory) in a complex simulator of 8 space factors CSSF (Fig. 2), developed at the Institute for Low Temperature Physics and Engineering of NAS of Ukraine, which was described in detail in [5], and briefly – in [1].
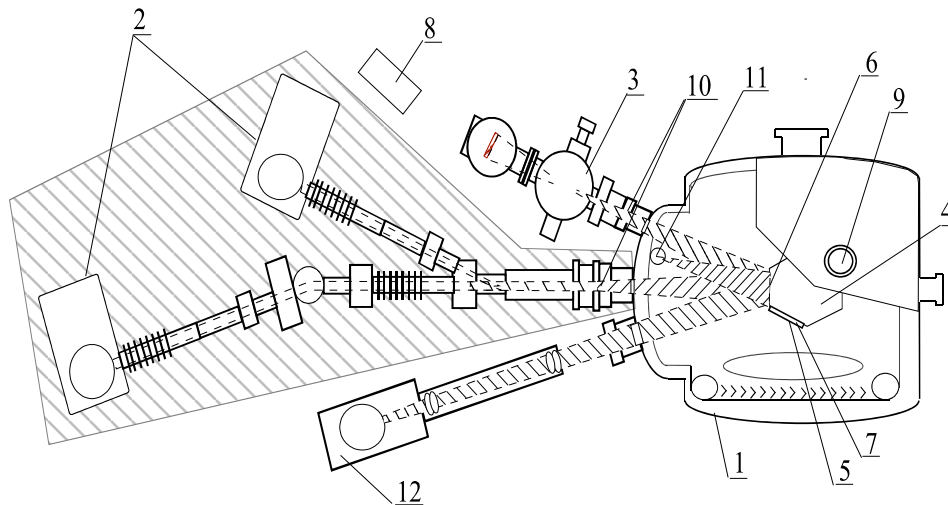


Fig. 2. Scheme of CSSF simulator

1 – cryogenic vacuum chamber; 2 – proton-electron accelerator on combined beams; 3 – gas-jet source of VUV and USX radiation; 4 – drum; 5 – zone for sample installation; 6 – zone of radiation factors effect on the sample; 7 – sample holder board; 8 – control system rack; 9 – electric vacuum connector; 10 – vacuum slide shutters; 11 – gas-discharge radiation source (GDRS); 12 – IS-160.

To simulate the electromagnetic radiation of the transatmospheric Sun (hereinafter EMRS) in the wavelength range λ = 200 - 2500 nm with the radiation intensity $J_S$ = 0.14 ÷ 0.28 W/cm$^2$ and the irradiation area S = 100 cm$^2$, a simulator of the transatmospheric Sun of CSSF type IS-160 is used (pos.12, Fig.2). In this investigation the samples were exposed to EMRS in the range of 250 - 2500 nm for 100 hours without cooling the chamber jacket with liquid nitrogen, what corresponded to 100 hours of solar irradiation on the near Earth orbit. The target temperature at irradiation under these conditions was 94° C. Heating in the process of irradiation was simulated separately on 6 samples, which were annealed in the open air in a muffle furnace at this temperature for 100 hours.

Simulation of the effect of vacuum ultraviolet (VUV) and ultra-soft X-ray (USX) radiation in the range of 1.24-170 nm was provided by a gas-jet source GJS (pos.3, Fig.2), developed at the Institute for Low Temperature Physics and Engineering [6,7]. The gas-jet method for generation of electromagnetic radiation is based on the excitation of the supersonic jet of a gas mixture in the vacuum by an electron beam. This method allows introducing VUV and USX radiation into the high-vacuum chamber of the CSSF simulator (10$^{-5}$ Pa) in a wide space angle without using

optical windows (Fig. 3). In this case the irradiation of the test object, located in the high-vacuum CSSF chamber at the distance of 70 cm from the axis of the jet, can vary from 2 to 10-fold excess of solar irradiation in the Earth orbit. The GJS source radiation spectrum is as close as possible to the solar radiation spectrum in the specified wavelength range [6].

To reduce the experiment time, the irradiated films were placed not on the CSSF target, but directly in the GJS source chamber, what allowed increasing the irradiancy on the samples to $2 \cdot 10^{-4}$ W/cm$^2$. Two doses of the samples irradiation with VUV and USX radiation, corresponding to 100 and 500 hours of solar irradiancy on the Earth orbit, were chosen.



a)                                                                                         b)
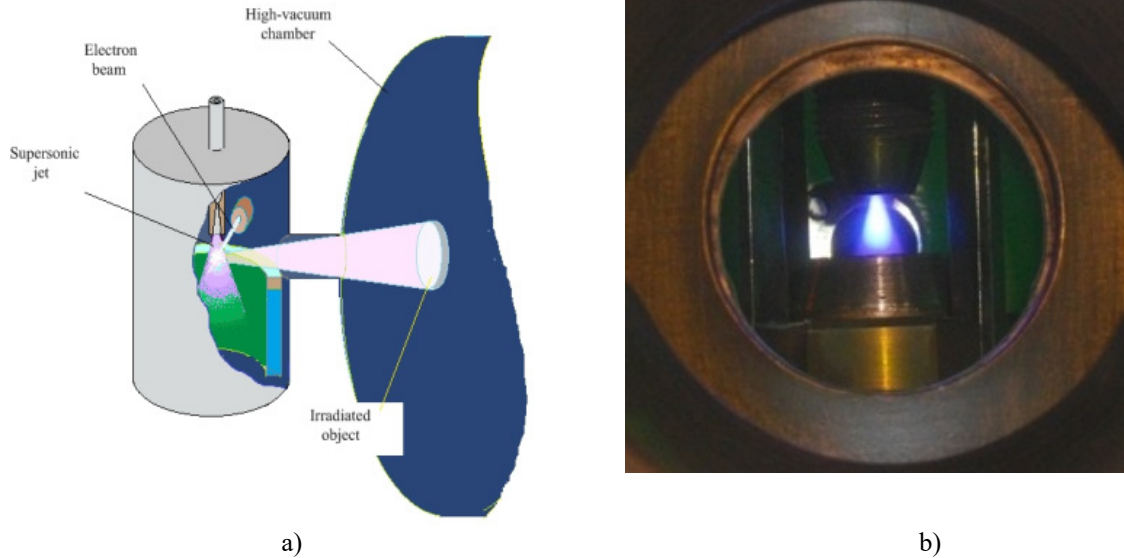
Fig. 3 GJS – gas-jet simulator of the Sun

a) schematic representation of the gas-jet method for generating electromagnetic radiation and introducing it into the high-vacuum chamber, b) semi-cryogenic version of the VUV and USX radiation simulator of the Sun as a part of the CSSF simulator.

### RESULTS OF EXPERIMENTS AND THEIR DISCUSSION

Fig. 4 shows typical curves "stress ($\sigma$)-deformation ($\varepsilon$)" of polyimide film samples in the states under study: (1) – initial, (2) – after EMRS irradiation, (3) – after heating in a muffle furnace, (4 and 5) – after irradiation with VUV and USX radiation during to 100 (4) and 500 (5) hours. The $\sigma$ - $\varepsilon$ curves of the samples, both in the initial state and after all types of exposure, have two stages – linear and nonlinear. At the linear stage, only elastic deformation $\varepsilon_{elast.}$ occurs and the $\sigma$-$\varepsilon$ diagram during loading and unloading is the same (Fig. 4). In the process of unloading, from the beginning of the second stage of deformation a hysteresis of the $\sigma(\varepsilon)$ curve trend is observed, and a part of the deformation is a reversible highly elastic one $\varepsilon_{high\ el.1}$. With further loading, the contributions of the delayed highly elastic $\varepsilon_{high\ el.2}$ and irreversible $\varepsilon_{irrevers.}$ deformation also occur (Fig. 5). The last mentioned contribution does not disappear at heating to the temperature $T < T_{soft.}$ in the range of the polymer softening temperature $T_{soft.}$.



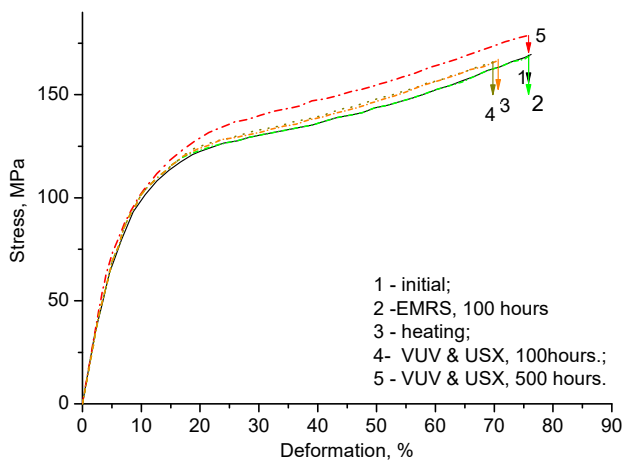Fig. 4. Typical curves "stress ($\sigma$) - deformation ($\varepsilon$)" of a polyimide film 75 microns thick
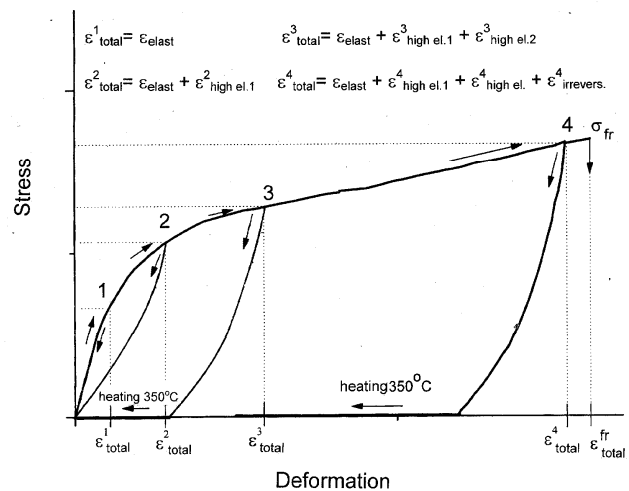


Fig. 5. The curve of deformation under loading and unloading of an irradiated film deformed to some loading values (1,2,3,4) at 293 K

The deformation curves σ-ε of the film after all types of exposure differ little (Fig. 4). Only σ-ε curves of the films, exposed to VUV and USX radiation for 500 hours, show higher stress values all over the curve. After the other types of exposure, the strengthening effect was found only at the limit of the forced elasticity $\sigma_{forc}$. Figure 6 presents histograms with average values of the limit of forced elasticity $\sigma_{forc}$, fracture stress $\sigma_{fr.}$, and the total deformation $\varepsilon_{total}$ of the initial and irradiated samples. The $\sigma_{forc.}$ limit increases after exposure to SF by an average of 14% (EMRS), and by 17% (VUV and USX). However, under exposure to EMRS, the heating of the target was observed, which was absent under exposure to VUV and USX radiation. Heating of the samples at the temperature corresponding to the target one (94°C) for the same 100 hours of exposure causes a similar increase in the value of $\sigma_{forc.}$, therefore we associate hardening when simulating the effect of EMRS only with heating of the sample on the target. The fracture stress $\sigma_{fr.}$ and total deformation $\varepsilon_{total}$ after exposure to EMRS remain at the same level as in the initial samples.

After exposure to VUV and USX radiation, the values of these characteristics ($\sigma_{fr.}$, $\varepsilon_{total}$) also change slightly, but ambiguously at different duration of irradiation. It was found that after 100 hours of irradiation, the average values of the both characteristics were slightly lower than the initial ones (by 7%), and after 500 hours of exposure the average values of the fracture stress became 5% higher than the initial ones, and the total elongation value was equal to that in the initial samples.
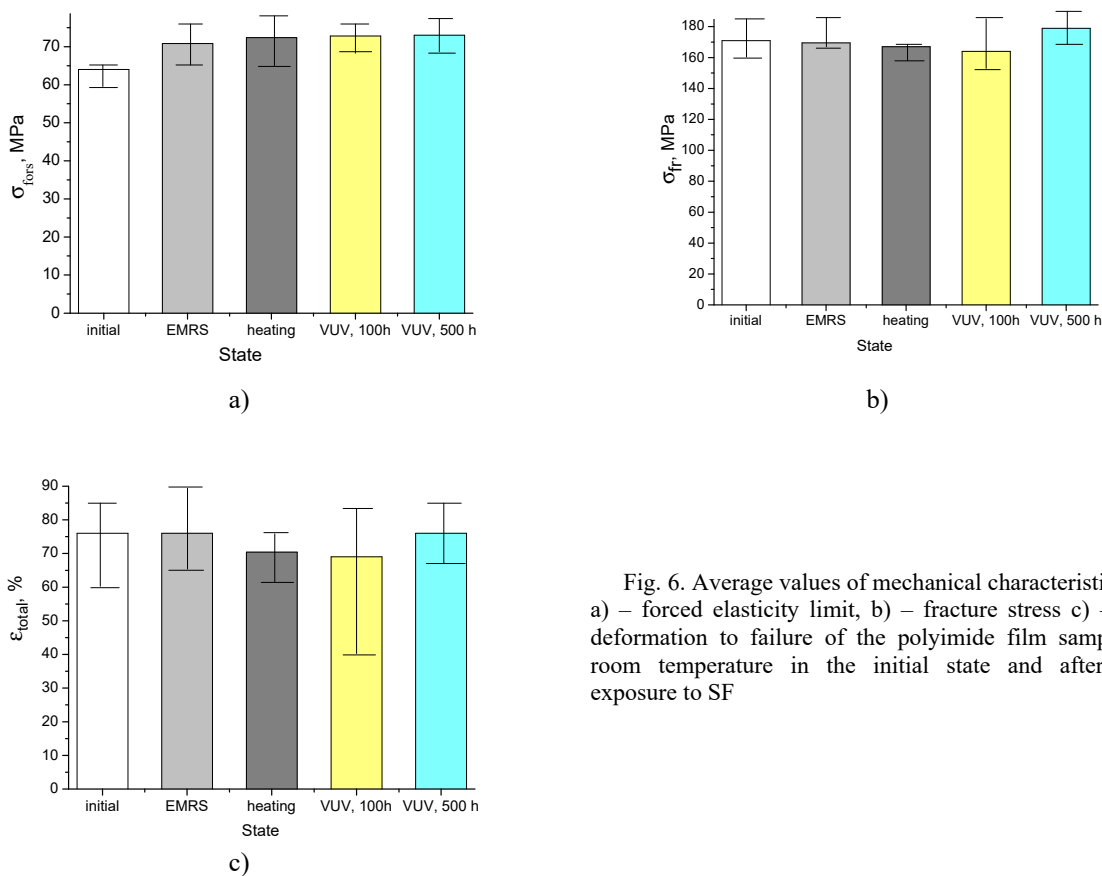


Fig. 6. Average values of mechanical characteristics: a) – forced elasticity limit, b) – fracture stress c) – total deformation to failure of the polyimide film samples at room temperature in the initial state and after their exposure to SF

The average values of total deformation $\varepsilon_{total}$ and its individual components (highly elastic deformation $\varepsilon_{high\ el.1}$, reversible at the test temperature, total forced highly elastic deformation: reversible $\varepsilon_{high\ el.1}$+ delayed $\varepsilon_{high\ el.2}$ and irreversible deformation $\varepsilon_{irrevers.}$) of the samples, tested in the initial state and after their exposure to SF, are given in Fig. 7. It is seen that EMRS effect does not cause any significant redistribution of the values of the total deformation components. 10%-decrease in the contribution of the irreversible deformation $\varepsilon_{irrevers.}$ after exposure to EMRS, as well as after annealing in a muffle furnace, can be due to heating of the target. Exposure to VUV and USX radiation leads to an unambiguous decrease in the contribution of the highly elastic deformation $\varepsilon_{high\ el.1}$, reversible at the test temperature, which reached 50% after 500 hours of irradiation. It should be also noted, that a large spread of $\varepsilon_{irrevers.}$ values in the samples exposed to irradiation for 100 hours can be observed.

In contrast to the samples, that were exposed to corpuscular radiation [1], no twisting was detected in the samples deformed to failure and, hence, no macrostresses in them. However, in the samples exposed to VUV and USX radiation, a change in the nature of the samples fracture was detected (Fig. 8).

The initial films destruction at 293 K (Fig.8a) arises due to tearing off transversely to the tensile axis of the sample with a slim neck. At the temperature of 77 K (Fig.8b) in the initial film fractures some zones of slight tear and tension bars are observed, what indicates to some embrittlement of the films. A similar picture is observed in the fractures of films exposed to VUV and USX irradiation.

Summarizing the results, we should note that our experiments confirm high radiation resistance of the polyimide films of kapton H type to the electromagnetic solar radiation. However, it should be emphasized, that despite the small content (10$^{-3}$%) of VUV and USX radiation with respect to the total energy of the Sun, its effect on the mechanical properties of polyimide is most evident. While the increase in the limit of the forced elasticity after exposure to EMRS in the range of 250-2500 nm is due only to heating, an increase in $\sigma_{forc.}$, as well as a decrease in the contribution of the reversible highly elastic deformation and embrittlement of the fractures after irradiation with VUV and USX radiation in the absence of heating, are associated only with radiation exposure. According to [2, 8] two competing processes, i.e. rupture of macrochains and intermolecular linking, can occur under irradiation. For a more detailed determination of the physical mechanisms of the processes, some spectroscopic studies are required.
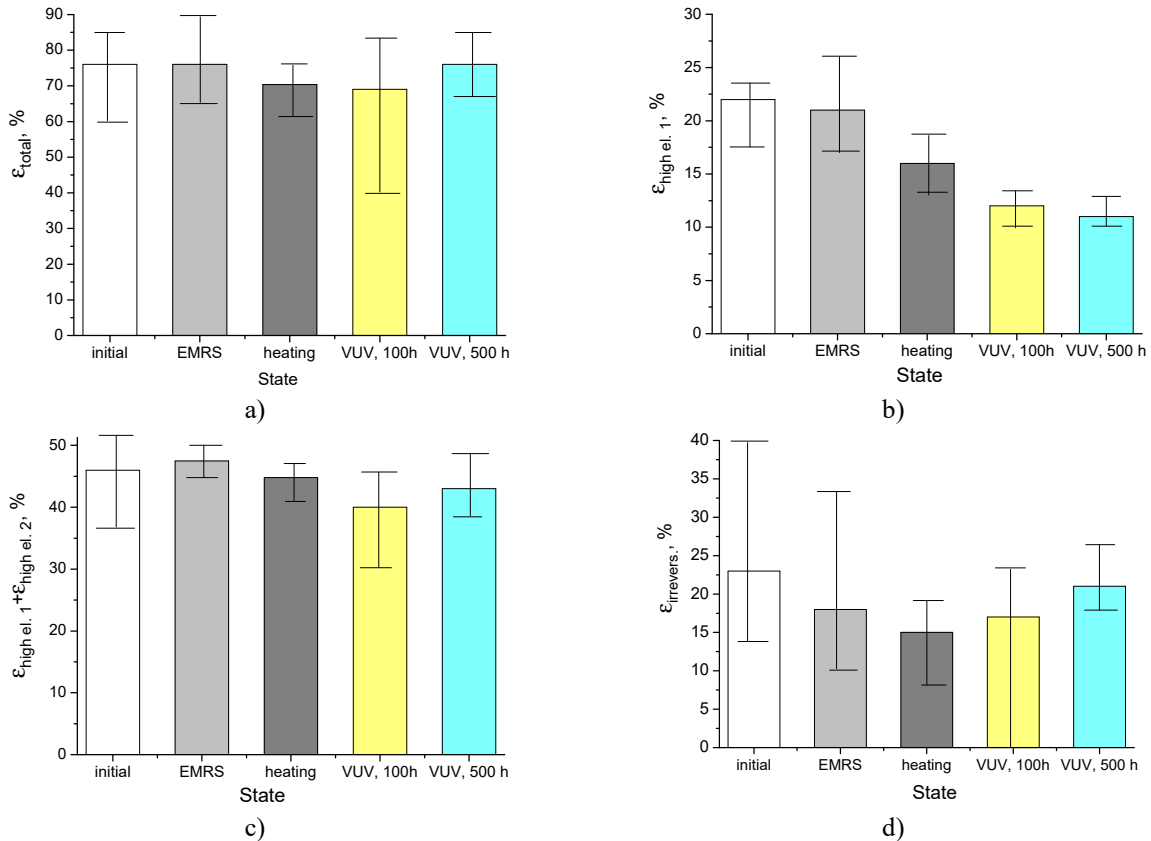


Fig. 7. Average values of the total deformation and its components for the polyimide film samples deformed at T = 293 K in the initial state and after exposure to SF.
a) – total deformation to failure of the samples $\varepsilon_{total}$, b) – highly elastic reversible deformation at the test temperature, $\varepsilon_{high\,el.1}$, c) – total forced highly elastic deformation ($\varepsilon_{high\,el..1} + \varepsilon_{high\,el.\,2}$), d) – irreversible deformation $\varepsilon_{irrevers.}$.
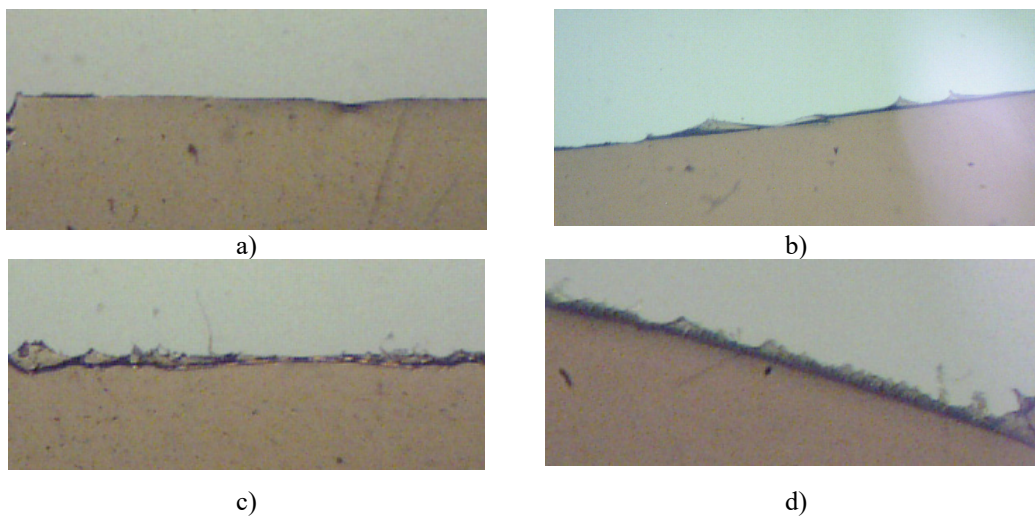


Fig. 8. Areas of destruction of the initial (a, b) and exposed to VUV and USX radiation for 100 hours (c), and for 500 hours (d) samples after deformation at the rate $\dot{\varepsilon} = 7 \cdot 10^{-4} s^{-1}$ at the temperature T = 293 K (a, c, d), and T = 77 K (b).

It should be also noted, that the increase in the forced elasticity limit after exposure to VUV and USX radiation for not more than 500 hours, corresponds to the level of increase in this characteristic after exposure to protons with the energy of 160 keV, when simulating a spacecraft flight for 100 years in the ISS orbit at H = 400 km, and a spacecraft flight on the geostationary orbit at H = 36000 km for 10 years. From the applied point of view, an increase in the level of the forced elasticity limit is of great importance. At the same time, a decrease in the level of reversible highly elasticity of films after exposure to VUV and USX radiation is a negative factor, especially under cyclic loading.

## CONCLUSION

1. It is shown, that kapton H-type polymer film under study is characterized by high radiation resistance to electromagnetic radiation from the transatmospheric Sun in the wavelength ranges of 250–2500 nm and 1.24–170 nm.

2. It is found, that an increase in the forced elasticity limit $\sigma_{forc.}$ by 14% after exposure to EMRS in the wavelength range of 250–2500 nm is due to the influence of film heating under irradiation.

3. An increase in the forced highly elasticity limit $\sigma_{forc.}$ by 17% was detected after exposure to VUV and USX electromagnetic radiation in the range of different time (100 and 500 hours), which did not relate to heating.

4. The fracture stress $\sigma_{fr.}$ and the total deformation to failure $\varepsilon_{total}$ after all types of exposure vary slightly, but non-monotonously after different time of exposure to VUV and USX radiation. After exposure for 100 hours, both characteristics are slightly reduced (by 7%), and after irradiation for 500 hours $\varepsilon_{total}$ returns to its almost original state, and $\sigma_{fr.}$ increases slightly (by 5%).

5. It is ascertained, that with a slight change in $\varepsilon_{total}$ after exposure to VUV and USX radiation, a significant redistribution of the values of its components occurs. The largest decrease (by 50%) is demonstrated by the contribution of highly elastic deformation $\varepsilon_{high\ el.1}$, reversible at the test temperature.

6. From the applied point of view, it is important to increase the level of the forced elasticity limit after exposure to electromagnetic radiation within all the wavelength range under study with a slight change in other macroscopic mechanical characteristics. A negative factor, especially under cyclic loading, is a decrease in the level of reversible elasticity of films after their exposure to VUV and USX radiation.

## ORCID IDs

Viktory A. Lototskaya https://orcid.org/0000-0001-8766-3154, Leonid F. Yakovenko https://orcid.org/0000-0003-0001-5571,
Evgeniy N. Aleksenko https://orcid.org/0000-0002-6505-0426, Ivan P. Zaritskiy https://orcid.org/0000-0003-2414-946X
Yuriy S. Doronin https://orcid.org/0000-0001-8860-7656, Anna A. Tkachenko https://orcid.org/0000-0002-1385-2857
Nikolay I. Velichko https://orcid.org/0000-0003-0021-9849

## REFERENCES

[1] V.A. Lototskaya, L.F. Yakovenko, E.N. Aleksenko, N.I. Velichko, I.P. Zaritskiy, V.V. Abraimov, Wen Zhu Shao and Liu Hai, East. Eur. J. Phys. **3**, 53-60 (2018), https://doi.org/10.26565/2312-4334-2018-3-06.

[2] E.A. Plis, D.P. Engelhart, R. Cooper, W.R. Johnston, D. Ferguson and R. Hoffman, Appl. Sci. **9**, 1999-2022 (2019), https://doi.org/10.3390/app9101999.

[3] V.A. Lototskaya, L.F. Yakovenko, E.N. Aleksenko, V.V. Abraimov and Wen Zhu Shao, East. Eur. J. Phys. **2**, 44-52 (2017), https://doi.org/10.26565/2312-4334-2017-2-06.

[4] L.M. Volikova and V.K. Chernetskiy, in: *Прикладне кріогенне і вакуумне матеріалознавство [Applied cryogenic and vacuum material science]* (Naukova dumka, Kyiv, 1991), pp. 137-143. (in Russian)

[5] V.V. Abraimov, A.A. Negoda, A.P. Zavalishin and L.K. Kolybaev, Space Science and Technology, **1**(2), 76-80 (1995), https://doi.org/10.15407/knit1995.02.076. (in Russian)

[6] E.A. Bondarenko, Yu.S. Doronin, E.T. Verkhovtseva, E.V. Gnatchenko and A.A. Tkachenko, in: *IVth Intern. Conf. on Laboratory Research for Planetary Atmospheres: Program of Invited Papers and Contributed Posters.* (Munich, 1992), pp. 26.

[7] E.T. Verkhovtseva, V.I. Yaremenko and V.D. Telepnev, Space Science and Technology, **4**(2), 102-109 (1998), https://doi.org/10.15407/knit1998.02.102 (in Russian)

[8] M.I. Bessonov, M.M. Koton, V.V. Kudryavtsev and L.A. Layus, *Полиимиды – класс термостойких полимеров [Polyimides – class of heat-resistant polymers]* (Nauka, Leningrad, 1984), pp. 328. (in Russian)

**ВПЛИВ ЕЛЕКТРОМАГНІТНОГО ВИПРОМІНЮВАННЯ ЗААТМОСФЕРНОГО СОНЦЯ, ЩО ІМІТОВАНО ЛАБОРАТОРНО, НА МЕХАНІЧНІ ВЛАСТИВОСТІ ПОЛІМІДНОЇ ПЛІВКИ ТИПУ КАРТОН Н**
**Вікторія О. Лотоцька[1], Леонід Ф. Яковенко[1], Євген М. Алексенко[1], Микола І. Величко[1], Юрій С. Доронін[1],**
**Ганна О. Ткаченко[1], Іван П. Заріцький[1], В'ячеслав В. Абраімов[2], Wen Zhu Shao[2]**
*[1]Фізико-технічний інститут низьких температур ім. Б.І. Вєркіна НАН України*
*пр. Науки, 47, м. Харків, 61103, Україна*
*[2] Харбінський Політехнічний інститут, м. Харбін, КНР*

Досліджено механічні властивості (границя вимушеної еластичності, напруга руйнування, загальна деформація до руйнування і її складові) поліімідної плівки типу kapton Н товщиною 75 мкм в умовах одновісного розтягування при температурі 293 К після впливу факторів космічного простору. Лабораторно імітували електромагнітне випромінювання заатмосферного Сонця в діапазоні довжин хвиль 250-2500 нм (ЕМВС) протягом 100 годин і вакуумне ультрафіолетове (ВУФ) і ультрам'яке рентгенівське (УМР) випромінювання в діапазоні 1,24-170 нм протягом 100 і 500 годин. Досліджували вплив роздільного опромінення в кожному з діапазонів довжин хвиль. Виявлено, що після опромінення в обох діапазонах

довжин хвиль плівки залишаються в вимушеноеластічному стані. Діаграми розтягування, як і в початковому стані, мають дві стадії. Визначено вклади пружної, незворотної і високоеластичної (затриманої і оборотної при температурі випробування) складових в загальну деформацію до руйнування. Виявлено, що границя вимушеної еластичності зростає, як після опромінення ЕМВС, так і ВУФ і УМР випромінюванням. При цьому підвищення границі вимушеної еластичності під дією ЕМВС викликано нагрівом плівки під час опромінення, а під впливом ВУФ- і УМР випромінювання - радіаційними ефектами. Напруга руйнування і загальна деформація до руйнування змінюються слабо і лише під дією ВУФ і УМР випромінювання. При зміні тривалості опромінення ВУФ і УМР випромінювання (100 або 500 годин) напруга руйнування і загальна деформація до руйнування змінюються немонотонно. Негативним наслідком впливу ВУФ і УМР випромінювання є перерозподіл величин вкладів окремих складових сумарної деформації. Випромінювання протягом 500 год. призводить до зниження в два рази вкладу еластичної деформації, оборотної при температурі деформації.

**КЛЮЧОВІ СЛОВА:** полііміди, фактори космічного простору, границя змушеної еластичності, напруга руйнування, деформація

**ВЛИЯНИЕ ЭЛЕКТРОМАГНИТНОГО ИЗЛУЧЕНИЯ ЗААТМОСФЕРНОГО СОЛНЦА, ИМИТИРУЕМОГО ЛАБОРАТОРНО, НА МЕХАНИЧЕСКИЕ СВОЙСТВА ПОЛИИМИДНОЙ ПЛЕНКИ ТИПА КАPTON H**
**Виктория А. Лотоцкая[1], Леонид Ф. Яковенко[1], Евгений Н. Алексенко[1], Николай И. Величко[1], Юрий С. Доронин[1], Анна А. Ткаченко[1], Иван П. Зарицкий[1], Вячеслав В. Абраимов[2], Wen Zhu Shao[2]**
*[1]Физико-технический институт низких температур им. Б.И.Веркина НАН Украины*
*пр. Науки, 47, г. Харьков, 61103, Украина*
*[2]Харбинский Политехнический институт, г. Харбин, КНР*

Исследованы механические свойства (предел вынужденной эластичности, напряжение разрушения, общая деформация до разрушения и ее составляющие) полиимидной пленки типа kapton H толщиной 75 мкм в условиях одноосного растяжения при температуре 293 K после воздействия факторов космического пространства. Лабораторно имитировали электромагнитное излучение заатмосферного Солнца в диапазоне длин волн 250-2500 нм (ЭМИС) в течение 100 часов и вакуумное ультрафиолетовое (ВУФ) и ультрамягкое рентгеновское (УМР) излучение в диапазоне 1,24-170 нм в течение 100 и 500 час. Исследовали влияние раздельного облучения в каждом из диапазонов длин волн. Обнаружено, что после облучения в обоих диапазонах длин волн пленки остаются в вынужденноэластическом состоянии. Диаграммы растяжения, как и в исходном состоянии, имеют две стадии. Определены вклады упругой, необратимой и высокоэластической (задержанной и обратимой при температуре испытания) составляющих в общую деформацию до разрушения. Обнаружено, что предел вынужденной эластичности возрастает, как после облучения ЭМИС, так и после воздействия ВУФ и УМР излучением. При этом повышение предела вынужденной эластичности под действием ЭМИС вызвано нагревом пленки в процессе облучения, а под воздействием ВУФ и УМР излучения - радиационными эффектами. Напряжение разрушения и общая деформация до разрушения изменяются слабо и только под действием ВУФ и УМР излучения. При изменении длительности облучения ВУФ и УМР излучения (100 или 500 час.) напряжение разрушения и общая деформация до разрушения изменяются немонотонно. Негативным последствием воздействия ВУФ и УМР излучения является перераспределение величин вкладов отдельных составляющих суммарной деформации. Облучение в течение 500 час. приводит к снижению в два раза вклада эластической деформации, обратимой при температуре деформации.

**КЛЮЧЕВЫЕ СЛОВА:** полиимиды, факторы космического пространства, предел вынужденной эластичности, напряжение разрушения, деформация

# DIGITAL TRIGGERING DEVICE AND GENERATOR OF STARTING PULSES FOR IGNITION OF SPARK GAPS OF REB ACCELERATOR "TEMP"

**Aleksey B. Batrakov\*, Eugeniy G. Glushko, Andrey A. Zinchenko, Yuriy F. Lonin, Anatoliy G. Ponomarev, Sergei I. Fedotov**

*National Science Center "KhPTI"*
*Str. Akademichna 1, Kharkov, Ukraine, 61108*
*\*E-mail: a.batrakov67@gmail.com*

To ensure the controllability and high noise immunity while measuring the characteristics of the accelerators of relativistic electron beams (REB) "TEMP", and parameters of the processes in them, triggering devices with galvanic isolation of input and output circuits, allowing to set up the pulse delays in the range from 1 μs to tens of milliseconds, have been developed. When they are used, the effect of loop currents, which flow in the common ground circuits and affect the operation of the measuring equipment, is eliminated. To synchronize the operation of the REB accelerator "TEMP" a triggering device was developed and assembled. It was assembled from blocks produced on the up-to-date elemental base and is a complete functional product. The triggering device comprises a trigger block and delay units. The trigger block is developed on the basis of an AND - NOT chip and a multivibrator. The delay units are built on single-shot vibrators K155AG1 and differ in the value of adjustable delays, which are determined by the external elements R and C, connected to the multivibrator. Unfortunately, in case the millisecond delays are set up, the pulse drop on the multivibrator is not stable. Therefore, a digital triggering device was developed. The digital triggering device is built on the basis of digital microcircuits and consists of the following blocks: binary-decimal counters, decoders, and one oscillator with quartz frequency stabilization, which is common to all four channels. It contains four identical channels with delay adjustment from one microsecond to one hundred milliseconds. Such a pattern of the circuit allows, if necessary, adding channels for starting other units. Pulse signals of the triggering device are fed to the ignitor unit of the spark-gaps. A pulse generator for igniting the spark-gaps of the REB accelerator "TEMP" has been developed. A generator, designed to control the spark gaps ignition in the High Voltage Pulse Generator (HVPG) and spark gaps ignition in the magnetic systems, which are used in switching systems of the capacitor banks with the energy of $60 \div 150$ kJ, has been described. The generator provides voltage pulses with the amplitude of up to 20 kV, at the current in the short circuit mode of 5 A, the pulse duration of the first half wave of 12 μs, and the pulse repetition frequency (PRF) of not more than 10 Hz.

**KEYWORDS:** accelerator, relativistic electron beam, spark-gap, digital triggering device.

The REB accelerator "TEMP" is designed to produce high-power pulses of REB and X-ray bremsstrahlung (XRBS) with the energy of up to 150 kJ. The devices allow obtaining a REB with the current of $2 \div 20$ kA and particle energy of $300 \div 800$ keV. In this case the maximum dose of X-ray bremsstrahlung per current pulse can be obtained ~ 9100 R without induced activity. The REB accelerator "TEMP" comprises the following major components: a high-voltage pulse generator (*HVPG*) with the circuits of charging, triggering and monitoring of the charging voltage; solenoids of magnetic systems intended to generate focusing and transporting REB of magnetic fields; a magnet; isolated vacuum diodes with diagnostic equipment, as well as vacuum pumping facilities, capable to maintain the working pressure in the diodes at the level of $1 \cdot 10^{-4}$ Pa. For the successful functioning of the Radiation Beam Complex (RBC) of "TEMP" a reliable operation of its numerous units is required. This is achieved by the stable triggering of its systems [1]. In the process of the REB "TEMP" accelerator operation some transient current and voltage steps occur, causing electromagnetic fields, which can produce loop currents flowing in common ground buses and in connecting cables. The currents flowing in the wires, connecting various units of the REB accelerator "TEMP", can reach considerable values, what causes uncontrolled starts of its devices or failure in its operation. A radical method of controlling the disturbances of this type is galvanic isolation of all the circuits, connecting the synchronization system with the pulse sources and registering apparatus.

Object of the work: for better controllability of the REB accelerator "TEMP" to develop a triggering device that would allow setting up the pulse delays in the range from 1 μs to tens of milliseconds. The digital triggering device should stably and accurately preset the start-up time of the REB accelerator "TEMP" units under the strong electromagnetic interference caused by its operation, and have a galvanic isolation for improving the noise immunity and low power consumption.

To develop a pulse generator for igniting spark-gaps of High-Voltage Pulse Generator (HVPG), which allows obtaining an ignitor pulse several times higher than that of similar devices. To develop a scheme of the ignitor pulse generator, which would reliably and stably control the accelerator spark gaps operation.

## TRIGGERING DEVICES

To synchronize the operation of the REB accelerator "TEMP" a triggering device was developed and assembled. A simple circuit, providing a galvanic isolation of the input and output circuits of the synchronization system, is proposed, what allows eliminating the occurrence of pulsed currents caused by operation of various accelerator units.

The triggering device was assembled from blocks, produced on the up-to-date elemental base, and is a complete functional product. The triggering device comprises a trigger block and delay units. The schemes of the input part and the delay channel of the triggering device are presented in Fig. 1 and Fig. 2, respectively.
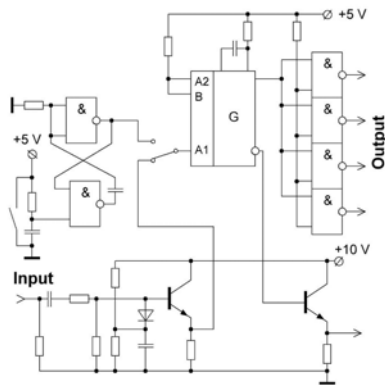


Fig. 1. Schematic diagram of the input part
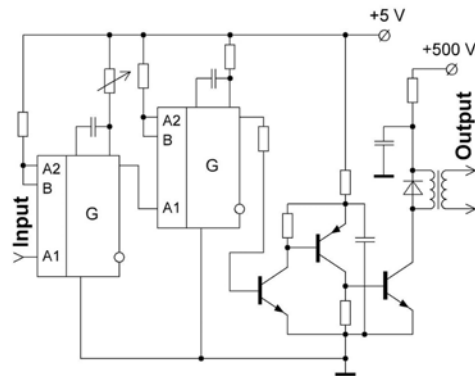of the triggering device

Fig. 2. Schematic diagram of the delay channel
of the triggering device.

The trigger block is built on the basis of an AND NOT chip and a multivibrator. It allows triggering both manually and by an external positive pulse with the amplitude of up to 50 V. The delay units are built on single-shot multivibrators K155AG1 and differ in the number of adjustable delays, which are determined by the external elements R and C, connected to the multivibrator. The output pulse shaper is based on a multivibrator and three transistors. The output positive pulse amplitude makes 500 V. Channel # 1 provides triggering of the cone-shaped solenoid of the first magnetic field without delay. Channel # 2 provides triggering of a cylindrical solenoid of the second magnetic field with the delay of 20 ms, which is adjustable with the time step-interval of 0.2 ms ÷ 20 ms. Channel # 3 is triggered from channel # 2 and provides the oscilloscope start with the delay of 5 ms and adjustment of 0.1 ms ÷ 10 ms. Channel # 4 is triggered from channel # 3 and provides the start of the high-voltage pulse generator (HVPG) with the delay of 100 μs and adjustment of 10 μs ÷ 100 μs. The delay setting accuracy is not worse than one percent at each range; time resolution is 0.001 of the range duration. All the channels of the delayed pulses of synchronization system have one common power source; the output cascades are galvanically isolated by optical couplers with the common synchronization system. The oscillogram of the control pulses and the total magnetic field distribution along the axis of the accelerating column, when two solenoids are triggered, is shown in Fig. 3.
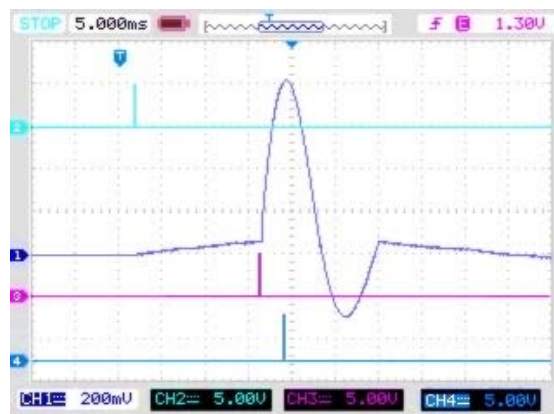


Fig. 3. Oscillogram of the control pulses and of the total magnetic field strength distribution along the axis of the accelerator column

In Fig. 3 beam 1 is the total magnetic field distribution along the axis of the accelerating column, beam 2 is the trigger pulse of the first solenoid, beam 3 is the trigger pulse of the second solenoid, beam 4 is the HVPG trigger pulse. Unfortunately, when the millisecond delays are set up, the pulse drop on the multivibrator is not stable. The errors at triggering of the first channel cause the failure of the entire device. Therefore, a new digital device of trigger pulses was developed and manufactured. To improve the noise immunity, the digital triggering device has a galvanic isolation of all the circuits, connecting the device to various units of the facilities. The galvanic isolation eliminates the flow of the pulsed currents caused by the operation of various units of the accelerators. The triggering device is based on digital chips [2] and consists of the following units: binary-decimal counters, decoders, and one generator with quartz frequency stabilization, which is common to all four channels. The triggering device contains four identical channels with adjustable delay, ranging from one microsecond to one hundred milliseconds. Such a construction of the scheme allows, if necessary, adding channels to trigger some other units. The delay adjustment is performed using decoders.

The triggering device works as follows: the input trigger (T) is started both manually and by an external positive pulse with the amplitude of up to 50 V, and allows pulses propagation from the crystal oscillator (G) to 5 binary-decimal counters (CT1-CT5) with decoders (DC1-DC5). The crystal oscillator frequency is 1 MHz. Each channel has its own decoder ($DC_{k1}$-$DC_{k4}$), which allows setting up the necessary delay of the trigger pulse. The delay is adjustable from 1 μs to 100 ms. After the counters are filled up the last pulse resets the input trigger and sets the counters to zero initial state. The device is ready for the next external start. The block diagram of the triggering device is presented in Fig. 4.
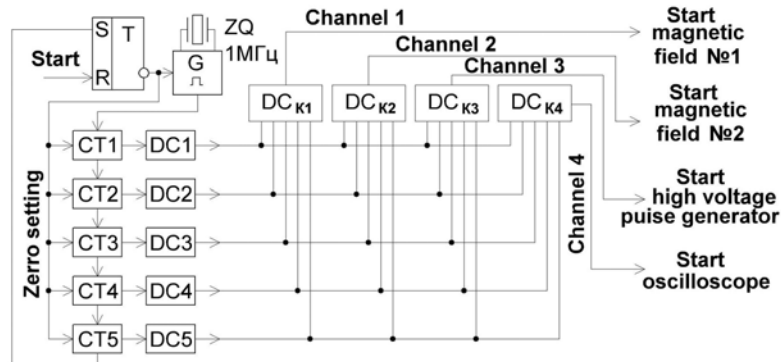


Fig. 4. Block diagram of the digital triggering device

The digital triggering device generates pulses for starting the dischargers of the conical and cylindrical solenoids [3]. They allow creating conditions for magnetic isolation and beam transport. The delay in start of the discharger of the cylindrical solenoid is about 15 ms. The magnetic field strength of the conical solenoid makes 4 kOe, and that of the cylindrical solenoid is 11.7 kOe. In case a digital triggering device is used, the high-voltage pulse generator is started at the moment of the highest intensity of the magnetic fields in the solenoids. A typical oscillogram of the REB current and voltage in the REB accelerator "TEMP", obtained using the developed digital triggering device, is shown in Fig. 5.
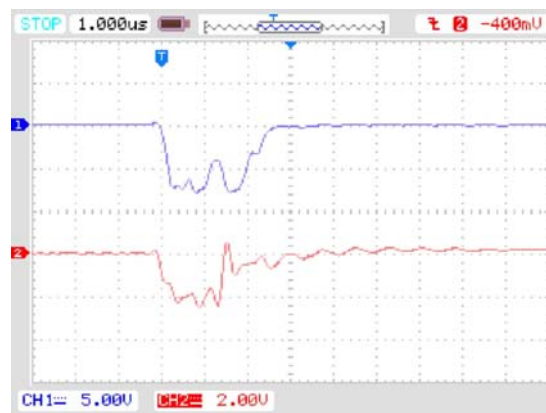


Fig. 5. Oscillogram of the REB current and voltage in the accelerator "TEMP-B"

In Fig. 5 the upper beam corresponds to the HVPG voltage of 750 kV, and the lower beam corresponds to the REB current of about 20 kA. The duration of the REB current pulse is about 1.5 μs. The developed digital triggering device allows the accelerator to work stably in the normal mode.

### GENERATOR OF STARTING PULSES FOR IGNITION OF SPARK GAPS

For galvanic isolation of the triggering device from the REB accelerator "TEMP" some pulse transformers and starting pulse receivers with low input resistance are used, what significantly reduces the interference influence in the connecting cables. Pulse signals of the triggering device are supplied to the spark gap ignition unit. A circuit based on a transistor high-voltage pulse shaper was developed. The generator provides voltage pulses with the amplitude of up to 20 kV, current in the short circuit mode of 5 A, pulse duration of the first half wave of 12 μs, and pulse repetition frequency of not more than 10 Hz.

Schematic diagram of the generator for spark gaps ignition in HVPG and for the ignition of the spark gaps in the magnetic systems is presented in Fig. 6.

The circuit comprises: an isolation transformer T1, a voltage doubler made on VD1, VD2, C1, C2, storage capacitors C3, C4, a switch based on a triac VD6, a step-up pulse transformer T3, from the secondary winding of which the signal is fed to the control electrode of the spark gap. As the switch, a BTA41-800B triac is used, which provides a discharge of the storage capacitors to the high-voltage transformer. The transformation coefficient of T3 transformer

is 35. The secondary high-voltage winding of the transformer consists of 4 sections and allows obtaining the ignitor pulse of about 20 kV. The developed pulse generator for ignition of spark gaps allows obtaining an ignition pulse several times higher than that in similar devices [4]. The oscillogram of the voltage pulse is shown in Fig. 7. Fig. 8 presents the current oscillogram, obtained in the short circuit mode.
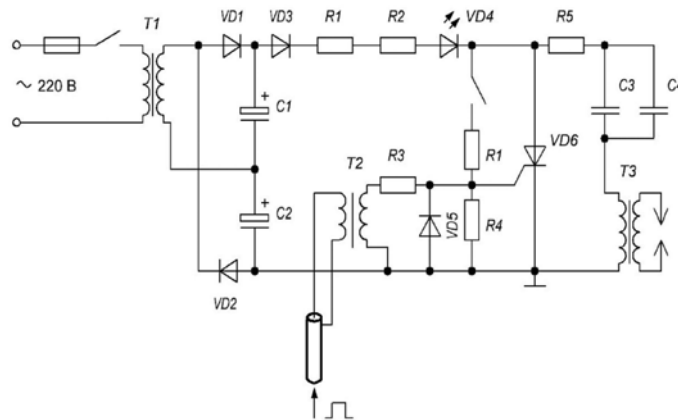


Fig. 6. Schematic diagram of spark gaps ignition circuit
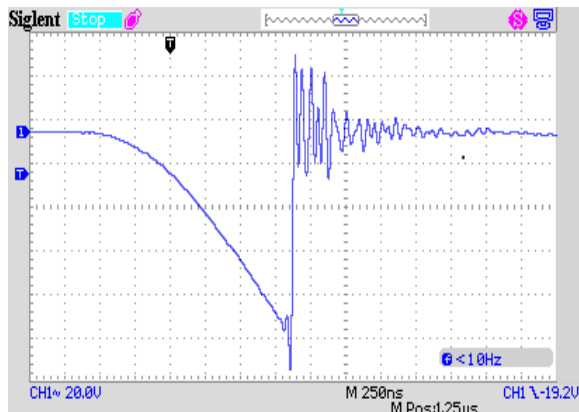


Fig. 7. Oscillogram) of the output voltage pulse in the idling mode
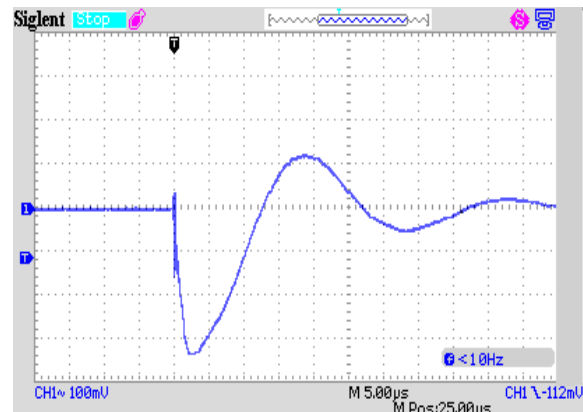
Fig. 8. Oscillogram of the ignition current pulse in the short circuit mode on the resistive load of 0.13 Ohms

The maximum value of the current that flows in the discharge circuit is determined by the inductance of the transformer primary winding and makes about 40 A.

The triac VD6 control pulse comes from the triggering device via the pulse isolating transformer T2 and the current-limiting resistor R3. The control pulse for starting the VD6 triac has a positive polarity with the amplitude of 15 V and the duration of 4 μs. Resistors R1, R2 are used to limit the charge current of storage capacitors C3, C4. Resistor R5 limits the discharge current of capacitors C3, C4 to 400 A. The indication of the ignition generator operation is performed using the light-emitting diode VD4.

The presented scheme of the ignition pulse generator allowed obtaining a stable triggering of the high-voltage spark gaps and can be utilized in the power systems of HVPGs and HCPGs (high-current pulse generators), used to solve various technological tasks, which are applied for changing the properties of the condensed matters and modification of the surfaces of polycomposite materials, [5].

## CONCLUSION

The digital triggering device allows to preset stably and accurately the start-up time of the REB accelerator "TEMP" units under the strong electromagnetic interference, resulting from its operation, it has a galvanic isolation for improving the noise immunity and low power consumption.

The developed pulse generator for ignition of spark gaps allows obtaining an ignitor pulse several times higher than that in similar devices. The developed circuit of the ignition pulse generator allows controlling reliably and stably the operation of the accelerator spark gaps.

**ORCID IDs**
**Aleksey B. Batrakov** https://orcid.org/0000-0001-6158-2129, **Eugeniy G. Glushko** https://orcid.org/0000-0001-8398-9915,
**Andrey A. Zinchenko** https://orcid.org/0000-0002-0534-1918, **Yuriy F. Lonin** https://orcid.org/0000-0003-2601-5035,
**Anatoliy G. Ponomarev** https://orcid.org/0000-0001-6914-6057, **Sergei I. Fedotov** https://orcid.org/0000-0002-7216-0615

## REFERENCES

[1] V.V. Zhiznevsky, A.A. Turchin and A.A. Turchin, Problems of Atomic Science and Technology, **4**, 376-380 (2010), in: https://vant.kipt.kharkov.ua. (in Russian)

[2] V.L. Shilo, *Популярные цифровые микросхемы* [*Popular digital microchip*], (Радио и связь, Moscow, 1987). (in Russian)

[3] A.B. Batrakov, E.G. Glushko, A.A. Zinchenko, Yu.F. Lonin, A.G. Ponomaryov, S.I. Fedotov, Problems of Atomic Science and Technology. Series: Plasma electronics and new methods of acceleration, **4**, 7-9 (2013), in: https://vant.kipt.kharkov.ua. (in Russian)

[4] E.G. Krastelyov, Instruments and experimental equipment, 6, 51-56 (2014);

[5] D.V. Vinnikov, K.V. Korytchenko, V.I. Tkachev, V.V. Egorenkov, D.V. Kudin and T.Yu. Mirnaya, Electrical Engineering & Electromechanics, **1**, 39-46 (2017), https://doi.org/10.20998/2074-272X.2017.1.07.

## ЦИФРОВИЙ ПРИСТРІЙ ЗАПУСКАЮЧИХ ІМПУЛЬСІВ ТА ГЕНЕРАТОР ЗАПУСКАЮЧИХ ІМПУЛЬСІВ ДЛЯ ПІДПАЛУ РОЗРЯДНИКІВ ПРИСКОРЮВАЧА РЕП «ТЕМП»

**О.Б. Батраков, Е.Г. Глушко, А.О. Зінченко, Ю.Ф. Лонін, А.Г. Пономарев, С.І. Федотов**

*Національний науковий центр «Харківський фізико-технічний інститут»*
*вул. Академічна 1, Харків, Україна, 61108*

Для забезпечення керованості та високої завадостійкості вимірювань характеристик і параметрів процесів для прискорювачів релятівістскіх електронних пучків (РЕП) «ТЕМП» були розроблені запускаючі пристрої з гальванічною розв'язкою вхідних і вихідних ланцюгів, які дозволяють встановлювати затримки імпульсів в діапазоні від 1 мкс до десятків мілісекунд. При їх використанні усувається вплив контурних струмів, які протікають в загальних колах заземлення і впливають на роботу вимірювальної апаратури. Для синхронізування роботи прискорювача РЕП «ТЕМП» було розроблено та зібрано запускаючий пристрій. Його було зібрано з блоків на сучасній елементній базі і він є закінченим функціональним виробом. Запускаючий пристрій складається з блоку запуску і блоків затримок. Блок запуску побудований на основі мікросхеми І НЕ і мультивібратора. Блоки затримок побудовані на одневібраторах К155АГ1 і відрізняються рівнем регульованих затримок, які визначаються зовнішніми елементами R і С, підключеними до мультивібратора. На жаль при установці мілісекундних затримок спад імпульсу на мультивібраторі не стабільний. Тому було розроблено цифровий запускаючий пристрій. Цифровий запускаючий пристрій виконано на цифрових мікросхемах і складається з блоків: двійковіх-десяткових лічильників, дешифраторів і одного загального на всі чотири канали генератора з кварцовою стабілізацією частоти. Воно містить чотири ідентичних канали з регулюванням затримки від однієї мікросекунди до ста мілісекунд. Така побудова схеми дозволяє в разі необхідності додати канали для запуску інших вузлів. Імпульсні сигнали запускаючого пристрою подаються на блок підпалу розрядників. Розроблено генератор імпульсів запалювання розрядників прискорювача РЕП «ТЕМП». Наведено опис генератора, розробленого для управління розрядниками підпалу ГІНа і розрядниками підпалу магнітних систем, що використовуються в системах комутації конденсаторних батарей з енергозапаси від 60 до 150 кДж. Генератор забезпечує отримання імпульсів напруги з амплітудою до 20 кВ, при струмі в режимі короткого замикання 5 А, тривалості імпульсу першої напівхвилі 12 мкс, частоті повторення імпульсів не більше 10 Гц.

**КЛЮЧОВІ СЛОВА:** прискорювач, релятивістський електронний пучок, розрядник, цифровий запускаючий пристрій.

## ЦИФРОВОЕ ЗАПУСКАЮЩЕЕ УСТРОЙСТВО И ГЕНЕРАТОР ЗАПУСКАЮЩИХ ИМПУЛЬСОВ ДЛЯ ПОДЖИГА РАЗРЯДНИКОВ УСКОРИТЕЛЯ РЭП «ТЕМП»

**А.Б. Батраков, Е.Г. Глушко, А.А. Зинченко, Ю.Ф. Лонин, А.Г. Пономарев, С.И. Федотов**

*Национальный научный центр «Харьковский физико-технический институт»*
*ул. Академическая 1, Харьков, Украина, 61108*

Для обеспечения управляемости и высокой помехоустойчивости измерений характеристик и параметров процессов для ускорителей релятивистских электронных пучков (РЭП) «ТЕМП» были разработаны запускающие устройства с гальванической развязкой входных и выходных цепей, которые позволяют устанавливать задержки импульсов в диапазоне от 1 мкс до десятков миллисекунд. При их использовании устраняется влияние контурных токов, которые протекают в общих цепях заземления и влияют на работу измерительной аппаратуры. Для синхронизации работы ускорителя РЭП «ТЕМП» было разработано и собрано запускающее устройство. Оно было собрано из блоков на современной элементной базе и представляет собой законченное функциональное изделие. Запускающее устройство состоит из блока запуска и блоков задержек. Блок запуска построен на основе микросхемы И НЕ и мультивибратора. Блоки задержек построены на одновибраторах К155АГ1 и отличаются величиной регулируемых задержек, которые определяются внешними элементами R и С, подключёнными к мультивибратору. К сожалению, при установке миллисекундных задержек спад импульса на мультивибраторе не стабилен. Поэтому было разработано цифровое запускающее устройство. Цифровое запускающее устройство выполнено на цифровых микросхемах и состоит из блоков: двоично-десятичных счетчиков, дешифраторов и одного общего на все четыре канала генератора с кварцевой стабилизацией частоты. Оно содержит четыре идентичных канала с регулировкой задержки от одной микросекунды до ста миллисекунд. Такое построение схемы позволяет в случае необходимости добавить каналы для запуска других узлов. Импульсные сигналы запускающего устройства подаются на блок поджига разрядников. Разработан генератор импульсов поджига разрядников ускорителя РЭП «ТЕМП». Приведено описание генератора, разработанного для управления разрядниками поджига Генератора импульсного напряжения (ГИНа) и разрядниками поджига магнитных систем, используемыми в системах коммутации конденсаторных батарей с энергозапасом от 60 до 150 кДж. Генератор обеспечивает получение импульсов напряжения с амплитудой до 20 кВ, при токе в режиме короткого замыкания 5 А, длительности импульса первой полуволны 12 мкс, частоте повторения импульсов не более 10 Гц.

**КЛЮЧЕВЫЕ СЛОВА:** ускоритель, релятивистский электронный пучок, разрядник, цифровое запускающее устройство

# SPATIAL RESOLUTION AND MEASUREMENT ACCURACY OF THE ULTRASOUND DIAGNOSTIC SYSTEM AT ACOUSTIC REMOTE PALPATION USING HIGH INTENSITY FOCUSING ULTRASOUND

**Evgen A. Barannik[1]\*, Viktor I. Pupchenko[2], Anatoliy I. Marusenko[2], Olexiy V. Knyazyev[2], Igor M. Tsybin[3], Aleksandr E. Berkovich[4]**

[1]*V.N. Karazin Kharkiv National University, Kharkiv, Ukraine*
[2]*Ultrasign, Ltd., Kharkiv, Ukraine*
[3]*JSC "NPF BIOSS", Moscow, Russia*
[4]*Peter the Great St. Petersburg Polytechnic University, St. Petersburg, Russia*
*\*E-mail: ebarannik@ukr.net*

In this work the spatial resolution and measurement accuracy of the ultrasound diagnostic system at acoustic remote palpation (ARP) using high-intensity focusing ultrasound (HIFU) are studied theoretically and experimentally. A physical model is proposed, which describes the specific features of ARP taking into account the remote nature of ultrasound Doppler probing of the soft tissues local movements, which are caused by the radiation pressure of HIFU pulse. Taking into account the accepted simplifying assumptions it is shown that the model conclusions are in a good agreement with the results of the experiments on measuring the value of displacements under the influence of HIFU. In particular, the nontrivial dependence of the value of displacements, measured by the Doppler method, on the probing depth and focusing degree of the incident and scattered wave beams, is proved. An experimental study was performed on the transverse resolution at ARP in the case of probing of the medium with Young's modulus irregularity, as well as on the influence of noise and interference on the measurement accuracy and resolution. It is concluded, that the transverse resolution at ARP is determined by the parameters of the local area of the movement, and can be significantly higher than the transverse intrinsic resolution of the ultrasound system at B-mode of diagnostics. The obtained results indicate that ARP is a promising method for monitoring the process of the soft tissues thermal ablation, when HIFU is used.
**KEY WORDS:** ARP, HIFU, ablation, Doppler probing, elastography, spatial resolution, measurement accuracy

Nowadays the techniques based on the high-intensity focusing ultrasound (HIFU) are widely used in medicine and are still intensively developed towards expanding the scope of medical applications. For example, it has been demonstrated *in vivo* and *in vitro*, that within a few minutes the short-pulse HIFU can mechanically crush the blood clots, caused by blood vessel thrombosis, due to the developing cavitation processes [1-4]. An important task here is providing safety of HIFU application in order to prevent the involvement of biological tissues outside the defined local area, what requires strong focusing of ultrasound waves.

At the same time, the most common and well-known technology is the ultrasound ablation of soft tissues [5-11] using HIFU through coagulation necrosis of malignant neoplasms and other soft tissue regions with pathological changes. Strong wave focusing and high radiation intensity in such traditional medical applications are necessary to achieve high temperature (about 80˚-90˚C) in the focal region resulting in thermal ablation of soft tissue. Nevertheless, the real-time monitoring of the thermal ablation process and the tissues state diagnostics remains one of the topical questions. Insufficient exposure can cause a relapse and even an accelerated growth of the neoplasms, while the excessive exposure can cause the involvement of the neighboring healthy tissues.

As it is known, the most common methods in diagnostics of the soft tissues and cardiovascular system are ultrasound methods. They are, in particular, ultrasound Doppler methods, including spectral Doppler studies, color Doppler mapping of blood flows and some others, whose physical properties are described, for example, in [12-15]. The Doppler methods are successfully applied and developed also for diagnostics of the soft tissue state [16-18]. At the same time, considering the intrinsic physical meaning of ultrasound methods [19], it is quite difficult to directly determine directly with their help the level of the biological tissue thermal destruction.

Recently, in ultrasonic medical diagnostics the methods of ultrasound elastography of soft tissues, such as acoustic radiation force impulse (ARFI) imaging [20-22] and shear wave elastography (SWE) [22-24], have been widely used. These methods are based on ultrasound registration of the soft tissue response to the radiation force of an ultrasound pulse, and in the both methods the same ultrasound transducer of the diagnostic system is used for both creation of the radiation pressure force and registration of the response [20]. The difference is in the fact, that in the ARFI method the value of the tissue displacement is measured directly at the region of the radiation force pulse impact, while at SWE the velocity of the shear wave, propagating in the tissues from the initial region of the force impact, is measured.

In [25] for monitoring the process of tissue thermal ablation it has been proposed to use a diagnostic system, which measures the value of the tissue displacement at the region of the radiation force impact, generated directly by the HIFU. It was shown experimentally [25], that under local heating up to the temperature of 43° C, the value of the maximum displacements in the muscle tissue of a cow *in vitro* changes, what indicates to a change in its viscoelastic properties. Earlier, a similar strong dependence of the value of displacements and the velocity of shear waves on the growth of temperature, caused by the HIFU exposure, was found in gelatinous phantoms of tissue [26].

The focal length of the real HIFU transducers, used for ablation of soft tissue, can reach a large value, of about 10 - 20 cm. This naturally requires solving the problem on the spatial resolution of the ultrasound Doppler diagnostic

system and on the accuracy of measuring the value of tissue displacement in the HIFU focal region at acoustic remote palpation (ARP), carried out using HIFU transducers.

## PHYSICAL MODEL

When describing the ultrasound response of soft tissues, the continual physical model of scattering by fluctuations in mass density and compressibility is generally accepted [27], which allows, in particular, to describe in detail the spectral characteristics of Doppler signals [13-15,28,29]. A distinctive feature of both ARFI and ARP is the fact, that the direction of tissue movement under the radiation force impact coincides with the direction of probing. If we neglect the geometrical and transit time spectral broadening [13.27] of the complex signal of ultrasound Doppler response, then in the plane-wave approximation it can be written in a simple form:

$$e(\varphi') = \int_S g(\vec{r})e^{i\varphi(\vec{r})}dS,$$ (1)

where $g(\vec{r}) = g_0(\vec{r})exp(i2kd)$ is the dimensional complex value, proportional to the diagnostic system sensitivity function, averaged over the sample volume in the direction of probing; $Ox$, $d$ is the probing depth along the probing direction; $k$ is the wave number; $\varphi(\vec{r}) = 2ku(\vec{r})$ is the phase of a local Doppler signal, depending on the local tissue displacement $u(\vec{r})$, and $\varphi'$ is the phase of the complex signal of the full Doppler response, having the in-phase and quadrature components. In expression (1) the integration is carried out over the cross-sectional area of the sample volume, therefore $\vec{r}$ is the coordinate of the area element $dS$ in the plane of section $(y, z)$, and the actual value $g_0(\vec{r})$ describes the spatial distribution of ultrasound fields in the plane of section and determines the transverse resolution of the ultrasound system in the usual B-mode. Note, that the real signal of the ultrasonic Doppler response is also proportional to the average level of the medium density and compressibility fluctuations.

The transverse dimensions of the area of the radiation force impact for the real HIFUs are of the order of 1–1.5 mm. Therefore, a specific feature of ARP, as compared to ARFI, is the fact, that the transverse dimensions of the local displacement region and, accordingly, its cross-sectional area $S_0$ at the probing depth, can be considered small: $S_0 \ll S$. In particular, the transverse resolution of the ultrasound diagnostic system depending on the probing depth, the degree of focusing, and the ultrasound frequency is of the order of 3–7 mm, what results in a large difference in the value of the areas. This allows to write down the contribution of the localized region of displacements under the influence of HIFU in (1) as a separate term

$$e(\varphi') = \int_{S-S_0} g(\vec{r})e^{i\varphi(\vec{r})}dS + g(\vec{R})S_0 e^{i\varphi},$$

where $\vec{R}$ is the coordinate of the center of the radiation force impact region in the sectional plane, $\varphi$ is Doppler phase of the signal from the region of the force impact and $g(\vec{R})S_0$ is the complex amplitude of the response from the region of the force impact. In the remaining integral $\varphi(\vec{r}) = 0$, as long as it describes the contribution of those areas of the measuring volume, where there is no movement. As a result, we have the equation:

$$e(\varphi') = \bar{g}(\vec{R})(S - S_0) + g(\vec{R})S_0 e^{i\varphi},$$ (2)

where $\bar{g}(\vec{R})$ is the average value of the response amplitude in the cross section of the measuring volume minus $S_0$ area. It is evident, that such an average value also depends on the position of the center of the radiation force impact.

The value of the displacement between two sequential probes can be determined using the Doppler phased tracking method [19,30]) by calculating the correlation function $C = e^*(\varphi')e(\varphi' + \Delta\varphi')$, where $\varphi'(\vec{R})$ is the phase of the observed Doppler signal at the first probing, which depends on the location of the displacement region, and $\Delta\varphi'(\vec{R})$ is the change in this phase. In accordance with the phased tracking method, the phase change of the Doppler signal is described by the formula:

$$tg\Delta\varphi'(\vec{R}) = \frac{ImC}{ReC}.$$ (3)

It is easy to show that, taking into account that the area $S_0$ is small, the greatest contribution to the real part of the correlation function is made by the term:

$$ReC = \bar{g}_0(\vec{R})^2(S - S_0)^2 \cong \bar{g}_0(\vec{R})^2 S^2.$$ (4)

When calculating the imaginary part, with the strict inequality $S_0 \ll S$ taken into account, we can neglect the quadratic $S_0$ terms. In this approximation we find:

$$ImC = \bar{g}_0(\vec{R})g_0(\vec{R})SS_0[sin\varphi(cos\Delta\varphi - 1) + cos\varphi sin\Delta\varphi].$$ (5)

where $\Delta\varphi = 2k\Delta u$ is the change in the phase of the Doppler response of the movement region, which is determined by the true tissue displacement $\Delta u$.

The phase increment between two sequential probes, virtually in all important cases, satisfies the strong inequality $\Delta\varphi \ll 1$, therefore the first term on the right-hand side of formula (5) can be neglected. As a result after substituting (4) and (5) into (3), we find:

$$tg\Delta\varphi'(\vec{R}) = \frac{g_0(\vec{R})s_0}{\bar{g}_0 S} cos\varphi sin\Delta\varphi \ll 1 . \qquad (6)$$

Taking into account that the phases $\Delta\varphi'(\vec{R})$ and $\Delta\varphi$ are small, it is easy to write down the relationship directly between the true and the measured displacements during the probing period as follows:

$$\Delta u'(\vec{R}) = \frac{g_0(\vec{R})s_0}{\bar{g}_0(\vec{R})S} cos(2ku)\Delta u . \qquad (7)$$

The total displacement in the process of observation is obtained by summing the displacements from the start of the movement to the value $u$ at any moment of the displacements registration. Taking into account, that the displacements are small, we can turn from summing small increments (7) to integrating, what results in the final equation for the observed displacement:

$$u'(\vec{R}) = \frac{g_0(\vec{R})s_0}{\bar{g}_0(\vec{R})S} \int_0^u cos(2ku)du = (2k)^{-1}\frac{g_0(\vec{R})s_0}{\bar{g}_0(\vec{R})S} sin(2ku) . \qquad (8)$$

Equation (8) determines the accuracy of the displacements measurement during ARP without taking into account the influence of noise and interference. Directly from (8) we also obtain the formulae:

$$\frac{u'(\vec{R})}{u'(0)} = \frac{g_0(\vec{R})}{g_0(0)}\frac{\bar{g}_0(0)}{\bar{g}_0(\vec{R})} . \qquad (9)$$

As it is known, the transverse spatial resolution of the ultrasound diagnostic system is determined by the width of the point spreading function. In the above discussion the role of the point source was played by a rather well-localized region of the tissue displacements, induced by the radiation force impact. In this sense, equation (9) describes the transverse resolution of the diagnostic system at ARP in the case, when the displacements are determined at different spatial positions of the probing transducer axis relative to the axis of HIFU and the region of tissue movement.

However, according to the meaning of the problem of monitoring the ablation process, the issue concerning the ability to distinguish the stiff (soft) Young's modulus irregularities on the homogeneous soft (stiff) background in the area under study is, obviously, more important. According to the physical meaning, in such a formulation of the experiment the resolution during the ARP is determined by the maximum distance, at which the movement in the soft (stiff) part of the inhomogeneous medium still experiences the braking (accelerating) effect of the adjacent stiff (soft) parts due to the arising internal viscoelastic stresses. At such a definition of the resolution, the axes of the HIFU transducer and of the probing transducer must coincide, what ensures the highest sensitivity and locality of determining the displacements in the tissue area with a given stiffness.

## MATERIALS AND METHODS

In our experiments we used a commercial ultrasound diagnostic scanner Angiodin-Sono/P (JSC "NPF BIOSS", Moscow, Russia) as an ultrasound diagnostic system, which is capable to perform measurement of tissue displacements at SWE and ARFI modes with the accuracy of not worse than 10%. The measurements were carried out in the ultrasonic phantom of soft tissue CIRS Model 049 (CIRS, Norfolk, VA, USA), which is used for elastographic and elastometric studies. The Young's modulus in the region of homogeneity of this phantom and in stiff heterogeneities of a spherical shape with diameter $D = 1$ cm was, respectively, 18 kPa and 67 kPa. The Doppler probing of the phantom points was carried out using commercial ultrasound transducers P2-4/20APX and P4-9/16 (Prosonic Co., Seoul, Korea) with the carrier frequency of 3.5 MHz (wavelength $\lambda = 0.42$ mm) and 6.5 MHz ($\lambda = 0.23$mm), respectively. Due to the developed specialized software, the Angiodin diagnostic scanner control system allowed to fine-adjust all the parameters, necessary for performing ARP, and to measure the displacements at the chosen point of phantom. Like in [23–26], the Doppler probing was synchronized with the HIFU pulses, whose parameters, for example pulse duration, could also vary.

As the HIFU emitter, the focusing ultrasound transducer H-148 (SONIC CONCEPTS, INC., Bothell, WA, USA) with the radiation aperture diameter of 64 mm and the radius of the radiating surface curvature of 64 mm was used. In these experiments, the HIFU pulses with the carrier frequency of 2.2 MHz had the duration of 900 μs at the voltage of the emitter power supply of 20 V. In the center of the HIFU transducer there was a hole (Fig. 1) with the diameter of 20 mm, through which the Doppler probing was performed. To superimpose the axes of the HIFU transducer and the ultrasound transducer of the diagnostic system, a positioning device was used, which allowed to position the probing transducer in the horizontal plane with the accuracy of 0.1 mm, and to change the distance between the probing transducer and the HIFU emitter in the vertical direction.

Figure 2 shows the general scheme of the experiments, from which it can be seen, that the focus of the HIFU emitter is always located at the distance $F_{HIFU}=71$ mm from the upper surface of the emitter holder. The probing depth $d$ was chosen so, that the cross section plane $(y, z)$ of the sample volume of the diagnostic system passed through the focal point of the HIFU. In the process of the measurements the acoustic phantom, the HIFU emitter, and the working surface of the probing transducer were located in a container with water.
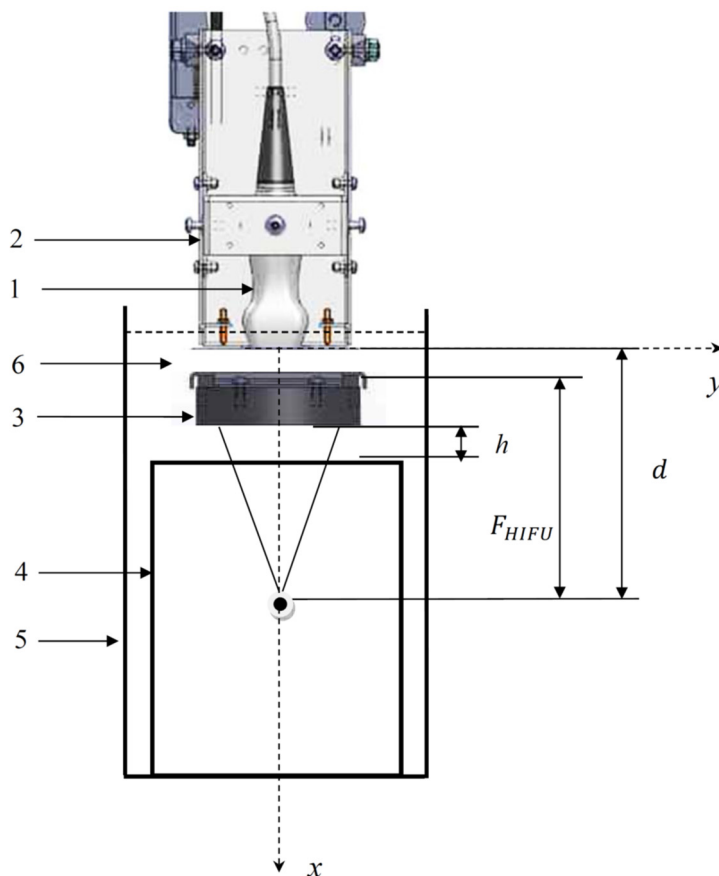
Fig. 1. HIFU Emitter



Fig. 2. General scheme of the experiments
1 – probing ultrasound transducer; 2 – ultrasound transducer holder; 3 – holder with the HIFU transducer; 4 – ultrasound soft tissue phantom; 5 – container with water; 6 – water.

## EXPERIMENTAL RESULTS AND DISCUSSION

From expression (8) it follows, that the displacements, measured at ARP, are always smaller than the true ones, and strongly depend on the ratio of the areas $S_0$ and $S$. With an increase in the area of the diagnostic system focal spot the value of the measured displacements decreases. This specific property of the measurements at ARP is illustrated by the Table data, which show the value of the measured maximum displacements, during their registration, in the region of phantom homogeneity at the probing depth $d = 78$ mm. The measurements were carried out under conditions, when the holder of the HIFU transducer was located directly on the phantom surface ($h = 0$). The largest displacement $u'(0) = 12.9$ μm in the HIFU focal region was found at electronic focusing by the P2-4/20APX transducer both of the transmitted and of the received beams of ultrasound waves with the focal length $F = d = 78$ mm. Switching-off at least one focusing (infinity focusing, $F = \infty$) caused a decrease in the value of the measured displacements due to an increase in the width of the sample volume, formed by the probing wave beams. When the electronic focusing of both the transmitted and received wave beams was switched off, the value of the measured displacements significantly decreased to the value $u'(0) = 3.3$ μm. In this case the probing transducer formed piston-like wave beams, which were similar to the plane waves in the Fresnel zone.

Table

The value of the maximum displacements, measured during their registration, at the probing depth $d = 78$ mm

| Transmitter: $F$, mm | Receiver: $F$, mm | Displacement, $u'(0)$, μm |
|---|---|---|
| 78 | 78 | 12.9 |
| $\infty$ | 78 | 11.7 |
| 78 | $\infty$ | 11.2 |
| $\infty$ | $\infty$ | 3.3 |

Note, that even in the absence of focusing in the probing plane $(x, y)$ the static focusing always takes place in the plane $(x, z)$, perpendicular to the probing plane, due to the own focusing lens of the probing transducer. For the ultrasound

transducer P2-4/20APX the corresponding focal length is about 70 mm. That is why the shape of the focal spot is close to a circle, strictly speaking, only if the electronic focusing of the transmitted and received waves with $F = 70$ mm is available.
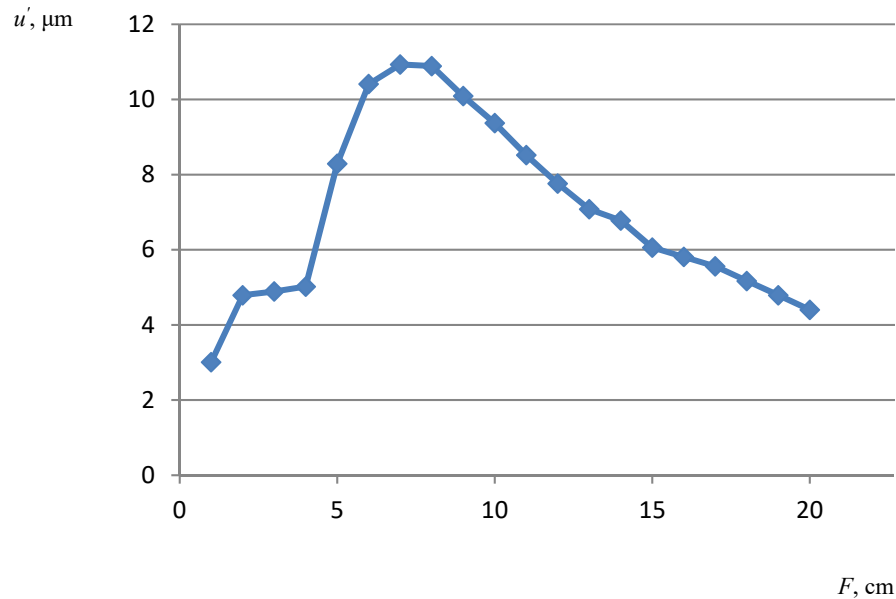


Fig. 3. Dependence of the measured value of displacement in the HIFU focal region on the focal distance of the probing transducer at the constant depth of probing = 78 mm

The results, obtained in the experiments with variable focal lengths (see Fig. 3.), have the same physical meaning as to the value of displacements.

In these experiments the probing depth remained unchanged and was in the focal region of the HIFU under the same experimental conditions and the focal length at transmitting was varied in a wide range (from 10 mm to 200 mm) in the absence of electronic focusing of the received wave beams.

From Fig. 3 it follows, that the measured value of the displacement has a sharp maximum in the HIFU focal region, and drops abruptly as the focus of the probing transducer moves away from it both with a decrease in the focal length and with its increase. In both cases this is due to an increase in the sample volume and its cross section for a defocused beam, both in front of and behind the focal region of the probing transducer. A more abrupt drop at strong focusing (small focal lengths) of the waves is caused by the considerable diffraction divergence of the wave beam behind the focus, and in particular, on the probing depth corresponding to the HIFU focus. At weak focusing of the incident converging wave the beam width changes substantially smaller in a prefocal region, and, as a result, the dependence of the beam width in the HIFU focal region on the focal length is weaker, what also affects the value of the measured displacements.

The ratio $g_0(\vec{R})/g_0(0)$ on the right-hand side of equation (9) describes the sensitivity distribution of the ultrasound system in the sectional plane of the sample volume and has a maximum at $\vec{R} = 0$. The width of this maximum at the given level determines the transverse spatial resolution of the system at B-mode of diagnostics. The second ratio $\bar{g}_0(0)/\bar{g}_0(\vec{R})$ also has a maximum at $\vec{R} = 0$, as long as the average value of the response amplitude, without the contribution of the area $S_0$, increases as its center moves away from the center of the sample volume cross section, where the sensitivity is maximal. As a result, the transverse resolution of the ultrasound diagnostic system, when registering a localized area of movement, can be even a bit higher, than at B-mode of diagnostics.

The experimental data on the transverse distribution of maximum displacements in the probing plane are presented in Fig. 4 for two probing depths $d = F = 78$ mm and $d = F = 108$ mm at electronic focusing of both transmitted and received wave beams. From these data it follows, that when registering the movement in localized region at the depth of 78 mm, the transverse resolution at the level of 6dB is about $4 \div 4.5$ mm, and at the depth of 108 mm it is about 5.5 mm. These values are, at least, not worse, than the transverse resolution at B-mode of ultrasound diagnostics, when using a transducer P2-4/20APX with the same frequency of 3.5 MHz.

Strictly speaking, with a greater probing depth of 108 mm, the value of the displacements, shown in Fig. 4, should be not higher, but lower than that in Fig. 3 due to the larger cross-sectional area of the sample volume. This result can be explained by the influence of noise and, in particular, speckle noise on the measurements accuracy. If the probing transducer is displaced along the probing line so that the sample volume does not completely coincide with the volume, which was set at a lesser depth, then the speckle noise level can change considerably. Another significant factor, affecting the measurements accuracy in these experiments, was the reverberation of ultrasound caused by the reflections from the upper surface of the HIFU transducer. A high level of noises and interferences is indicated, in particular, by the zigzag

curve in Fig. 4 for the depth of 108 mm. For the same reason, because of a high level of reverberation noise and interference in our experiments, we failed to obtain reliable results for the depths of more than 108 mm.
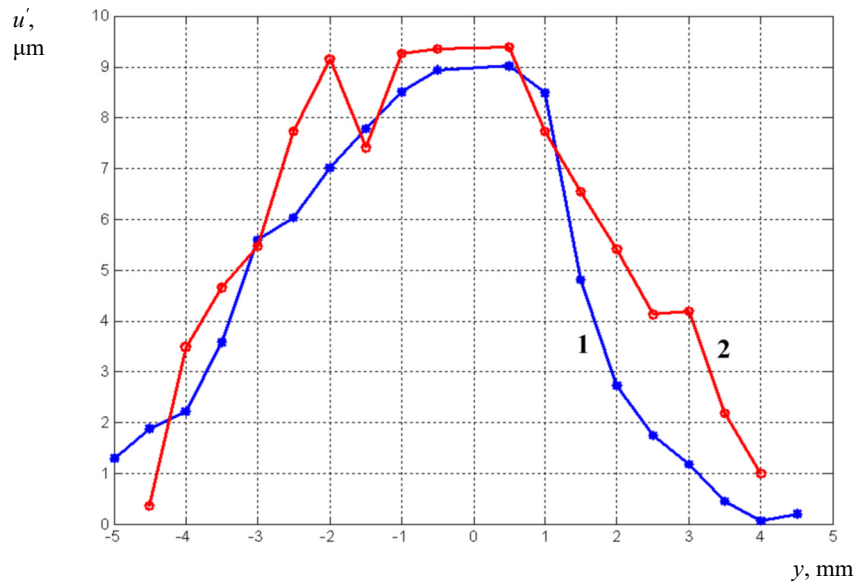


Fig. 4. Distribution of displacements along the direction $Oy$ in the probing plane at the depth $d = F = 78$ mm (1), and $d = F = 108$ mm (2) in the homogeneous part of the soft tissue phantom with localized region of displacements.

The distributions, whose example is shown in Fig. 4, were used to adjust the probing transducer for superimposing its axis with that of the HIFU transducer. To study the transverse resolution of the diagnostic system, when probing the inhomogeneities of shear stiffness in the medium, the probing and HIFU transducers were rigidly fixed relative to each other after aligning the axes, so that the working surface of the probing transducer was directly adjacent to the hole in the HIFU transducer. Such a schematic of the experiment allowed reducing considerably the reverberation noise. As Fig. 2 shows, in this case $d = F = F_{HIFU} = 71$ mm, and the distance between the lower edge of the holder of the HIFU transducer and the phantom surface was chosen equal to $h = 35$ mm, what ensured the positioning of the foci of HIFU and probing transducers at the same depth with the center of the stiff spherical inhomogeneity. To find the inhomogeneity in the plane $(y, z)$ we used a B-image of the inhomogeneity and a positioning device, which moved the rigidly connected HIFU and probing transducers.

In these experiments the distributions of the displacement of the phantom material under the influence of HIFU along the both transverse directions $Oy$ and $Oz$ were determined. To improve the accuracy of the results, the data for 10 depths of probing, spaced 0.4 mm apart was obtained, so that $d = 71$ mm represented the average value. The distributions, obtained using the ultrasonic transducers P2-4/20APX and P4-9/16, are shown in Fig. 5 and Fig. 6, respectively. The red curve in all the figures corresponds to the average value, with the data for all 10 depths of probing taken into account.

First of all, note, that according to the data in Fig. 5 and Fig. 6, the average value of the maximum displacements in the central part of the spherical stiff inhomogeneity is always approximately four times greater, than that in the soft environment, what indicates that ARP is the promising method for controlling the changes in the mechanical properties of the medium under study. On the other hand, this result is in a good agreement with the ratio of the Young's modules for these areas of the used phantom. The inversely proportional dependence of the displacements value on the Young's modulus indicates to the quasistatic nature of the resulting deformation, at which the displacement reaches the maximum value, corresponding to the given force of the radiation pressure due to the sufficiently long pressure pulses [31].

The distributions, shown in Fig. 5 and Fig. 6, as to their meaning, are one-dimensional images of a stiff spherical inhomogeneity inside the soft environment. If the boundary of inhomogeneity of this kind is defined, for example, from the coordinate of the point, at which the displacement corresponds to a certain average value in the soft environment region, then in this case the apparent diameter of the inhomogeneity is equal to $D = 12$–$13$ mm. Given the true size of the spherical inhomogeneity, we can conclude that the broadening of its boundary does not exceed 1.0–1.5 mm. An important feature of this result was, that it practically did not depend on the type of the used ultrasonic transducer, on the carrier frequency of the probing wave beams, and on the choice of the transverse direction, along which the distribution of the displacements value was build.

The latter circumstance gives a reason to assert, that the maximum distance, at which the movement, for example, in the soft part of the medium with Young's modulus irregularity can still experience the braking effect of the adjacent stiff inhomogeneity, in our experiments corresponds to the obtained value of $1.0 - 1.5$ mm. In physical terms, this means, that the region of the internal stresses, resulting from the effect of the radiation force, which cause the displacements, and, accordingly, the value of the displacements region itself in our experiments was 2.0–3.0 mm. As it was expected, this

value was larger than the diameter of the focal region of the HIFU transducer (see, for example, [26, 31]). On the other hand, this result means, that when probing the medium with Young's modulus irregularity using ARP, the resolution is determined by the transverse dimensions of the movement area, formed by a certain HIFU transducer, and therefore can be significantly better than the own spatial resolution of the ultrasound diagnostic system used for the tissue ablation monitoring.
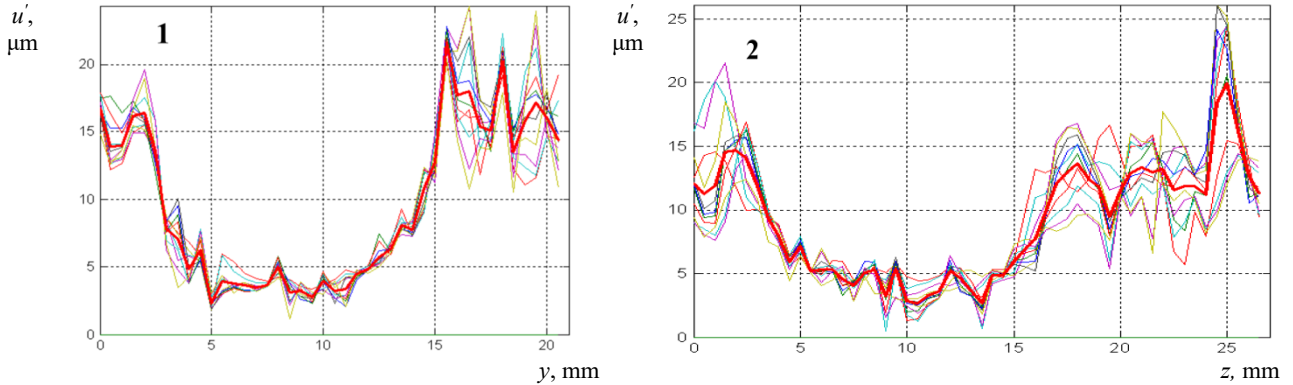


Fig. 5. Transverse distribution of displacements, obtained using a P2-4/20APX transducer, in the region of the inhomogeneity inside the soft tissue phantom at $F = F_{HIFU} = 71$ mm, and at ten values of the depth of probing, the average depth being $d = 71$ mm (red line corresponds to the average distribution): 1 – along the axis $Oy$; 2 – along the axis $Oz$.
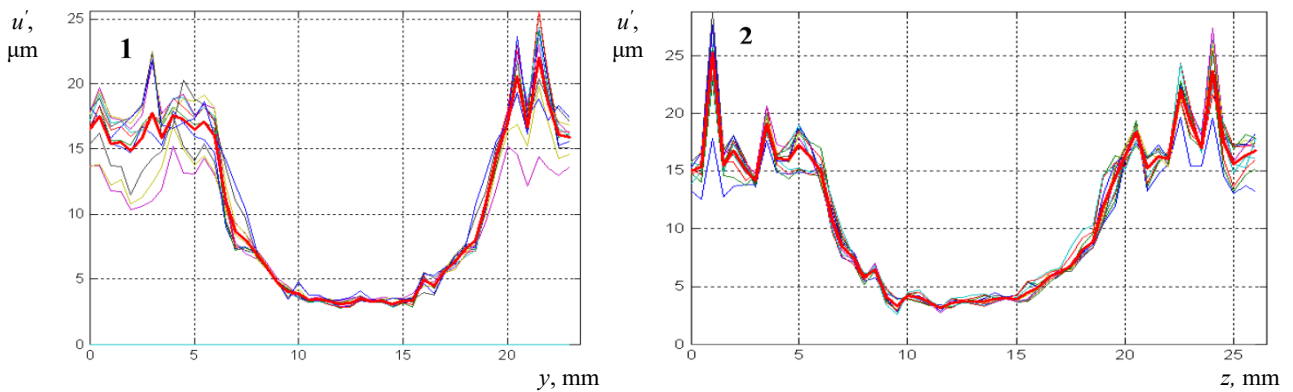


Fig. 6. Transverse distribution of maximum displacements, obtained using a P4-9/16 transducer, in the region of the inhomogeneity inside the soft tissue phantom at $F = F_{HIFU} = 71$ mm, and at ten values of the depth of probing, the average depth being $d = 71$ mm (red line corresponds to the average distribution): 1 – along the axis $Oy$; 2 – along the axis $Oz$.

In conclusion, we note, that in the focal region of the HIFU the dependence of the measured displacements (8) on the real ones remains monotonically increasing in a fairly wide range of displacements. Under the simplifying assumptions, which we made, the uniform dependence ends when $\varphi_c = 2ku_c = \pi/2$, what, for example, at the diagnostic system carrier frequency of 3.5 MHz corresponds to the real displacements of about 50 μm. With a further increase in the value of the real displacements under the radiation force impact, the determined displacement will decrease according to the sinusoidal law. In this case, when the medium moves back to the equilibrium state, an increase in the measured displacement should be observed until $u_c$ value is reached, and then the measured displacements decrease again.

In all our experiments the displacement value was measured for all the moments of time, from the start of the movement under the radiation force impact to the end of the relaxation movement to the equilibrium state, however, the movement of such a pseudo-oscillatory nature was not observed. This means, that the real displacements did not reach the critical value, what was due, in particular, to a sufficiently high stiffness of the used soft tissue phantom. Besides, the critical value of the phase $\varphi_c$ is always greater than that of $\pi/2$, obtained under accepted simplifying assumptions, and grows with the increase of the area $S_0$. From formula (2), for example, it follows, that in the limiting case of ARFI, when $S_0 = S$ and $\vec{R} = 0$, the equality $\varphi'(0) \equiv \varphi$ is always satisfied, i.e. the critical value is missing. The above results regarding the transverse dimensions of the movement region indicate, that in these experiments the phase value $\varphi_c$ was quite high.

## CONCLUSION

In conclusion, we note that in this work, the spatial resolution and measurement accuracy of the ultrasound diagnostic system at ARP are theoretically and experimentally investigated. A physical model is proposed, which describes the specific features of ARP, taking into account the remote nature of ultrasonic Doppler probing of the soft tissues local movements, which are caused by the radiation pressure of a high-intensity focused ultrasound pulse. Taking

into account the accepted simplifying assumptions, it is shown that the model conclusions are in a good agreement with the results of the experiments on measuring the value of displacements under the influence of HIFU.

In particular, the nontrivial dependence of the value of displacements, measured by the Doppler method, on the probing depth and the focusing degree of the incident and scattered wave beams, in the process of probing the localized region of the movement under the HIFU impact, is proved. An experimental study was performed on the transverse resolution at ARP in the case of probing the medium with Young's modulus irregularity, as well as on the influence of noise and interference on the measurement accuracy and resolution. On the basis of the carried out studies it was concluded, that the transverse resolution at ARP was determined by the transverse dimensions of the of soft tissues movement region, formed by the HIFU transducer, and could be significantly better than the own spatial resolution of the used ultrasound diagnostic system at the B-mode of diagnostics.

In the real commercial soft tissue ablation systems, which use HIFU, the diagnostic probing transducers are built directly into the hole of HIFU transducer, through which ultrasound probing is performed. This allows to avoid the problems with the interference, caused by the reverberation of ultrasound probing wave beams. Taking this circumstance into account, the results, obtained in this work, indicate that ARP is a promising method for monitoring the process of the tissues thermal ablation, when HIFU is used.

**ORCID IDs**
**Evgen A. Barannik** https://orcid.org/0000-0002-3962-9960
**Viktor I. Pupchenko** https://orcid.org/0000-0001-8074-4867
**Anatoliy I. Marusenko** https://orcid.org/0000-0001-8093-4732
**Oleksiy V. Knyazyev** https://orcid.org/0000-0001-8738-8033
**Aleksandr E. Berkovich** https://orcid.org/0000-0002-0459-274X

**REFERENCES**

[1]  A.D. Maxwell, G. Owens, H.S. Gurm, K. Ives, D.D. Myers and Z. Xu, Journal of vascular and interventional radiology, **22**(3), 369-377 (2011), https://doi.org/10.1016/j.jvir.2010.10.007.
[2]  W. Yang and Y Zhou, Ultrasonics Sonochemistry, 35(Part A), 152–160 (2017), https://doi.org/10.1016/j.ultsonch.2016.09.014.
[3]  D. Suo, S. Guo, W. Lin, X. Jiang and Y. Jing, Phys. Med. Biol. **60**, 7403–7418 (2015), https://doi.org/10.1088/0031-9155/60/18/7403.
[4]  B. Petit, E. Gaud, D. Colevret, M. Arditi, F. Yan, F. Tranquart and E. Allémann, Ultrasound Med. Biol. **38**(7), 1222–1233 (2012), https://doi.org/10.1016/j.ultrasmedbio.2012.02.023.
[5]  R. Chen, D.G. Paeng, K.H. Lam, Q. Zhou, K.K. Shung, N. Matsuoka and M.S. Humayun, Journ. Med. Biol. Eng. **33**(1), 103-110 (2013), https://www.ncbi.nlm.nih.gov/pmc/articles/PMC4209747/.
[6]  R.J.E. van den Bijgaart, D.C. Eikelenboom, M. Hoogenboom, J.J. Fütterer, M.H. den Brok, G.J. Adema, Cancer Immunol. Immunother. **66**(2), 247–258 (2017), https://doi.org/10.1007/s00262-016-1891-9.
[7]  R. Cirincione, F.M. Di Maggio, G.I. Forte, L. Minafra, V. Bravatà, L. Castiglia, V. Cavalieri, G. Borasi, G. Russo, D. Lio, C. Messa, M.C. Gilardi and F.P. Cammarata, Ultrasound Med. Biol. **43**(2), 398–411 (2017), https://doi.org/10.1016/j.ultrasmedbio.2016.09.020.
[8]  N.N. Petrishchev, D.Y. Semyonov, A.Y. Tsibin, A.E. Berkovich and A.A. Bursian, Application of HIFU technology in angiology. Grekov's Bulletin of Surgery, **176**(5), 101-105 (2017), https://doi.org/10.24884/0042-4625-2017-176-5-101-105. (In Russian).
[9]  Berkovich A.E., Bursian A.A., Senchik K.U., Petrishchev N.N., Tsibin A.U. and Yukina G.U. Biomedical Engineering, **50**(2), 96-99 (2016), https://doi.org/10.1007/s10527-016-9596-0.
[10] F. Wu, J. Acoust. Soc. Am. **134**(2), 1695–1701 (2013), https://doi.org/10.1121/1.4812893.
[11] M. Wang, Y. Lei and Y. Zhou, Ultrasonics, **91**(2), 134–149 (2019), https://doi.org/10.1016/j.ultras.2018.08.017.
[12] P.N.T. Wells, Eur. J. Ultrasound, **7**(1), 3–8 (1998), https://doi.org/10.1016/S0929-8266(98)00006-8.
[13] E.A. Barannik, Ultrasonics, **39**(2), 311–317 (2001), https://doi.org/10.1016/S0041-624X(01)00059-2.
[14] I.V. Skresanova and E.A. Barannik, Ultrasonics, **52**(5), 676–684 (2012), https://doi.org/10.1016/j.ultras.2012.01.014.
[15] O.S. Matchenko and E.A. Barannik, Acoust. Phys. **63**(5), 596–603 (2017), https://doi.org/10.1134/S1063771017050086.
[16] N. Pulkovski, P. Schenk, N.A. Maffiuletti and A.F. Mannion, Muscle Nerve, **37**(5), 638–649 (2008), https://doi.org/10.1002/mus.20996.
[17] E.A. Barannik, A.A. Kulibaba, S.A. Girnyk, D.A. Tolstoluzhskiy and I.V. Skresanova, J. Ultrasound Med. **31**(12), 1959–1972 (2012), https://doi.org/10.7863/jum.2012.31.12.1959.
[18] J. Ophir, S.K. Alam, B.S. Garra, F. Kallel, E. Konofagou, T.A. Krouscop, C.R.B. Merritt, R. Righetti, R. Souchon, S. Srinivasan and T. Varghese, J. Med. Ultrasonics, **29**(4), 155–171 (2003), https://doi.org/10.1007/BF02480847.
[19] C.R. Hill, J.C. Bamber and G.R. ter Haar, *Physical Principles of Medical Ultrasound,* (Chichester, John Wiley&Sons, 2004), https://doi.org/10.1002/0470093978.
[20] K. Nightingale, Curr. Med. Imaging Rev. **7**(4), 328–339 (2011), https://doi.org/10.2174/157340511798038657.
[21] K. Nightingale, M. Palmeri, R. Nightingale and G. Trahey, J. Acoust. Soc. Am. **110**(1), 625–634 (2001), https://doi.org/10.1121/1.1378344.
[22] R.M.S. Sigrist, J. Liau, A. El Kaffas, M.C. Chammas and J.K. Willmann, Theranostics. **7**(5), 1303–1329 (2017), https://doi.org/10.7150/thno.18650.
[23] E.A. Barannik, S.A. Girnyk, V.V. Tovstiak, A.I. Marusenko, S.Y. Emelianov and A.P. Sarvazyan, Ultrasonics, **40**(1-8), 849–853 (2002), https://doi.org/10.1016/S0041-624X(02)00243-3.

[24] E.A. Barannik, S.A. Girnyk, V.V. Tovstiak, A.I. Marusenko, V.A. Volokhov and A.P. Sarvazyan, J. Acoust. Soc. Am. **115**(5Pt 1), 2358–2364 (2004), https://doi.org/10.1121/1.1698796.

[25] S.A. Girnyk, A.E. Barannik,.V. TovstiakV, D.A. Tolstoluzhsky and E.A. Barannik, Ultrasound Med. Biol. **35**(5), 764–772 (2009), https://doi.org/10.1016/j.ultrasmedbio.2008.11.008.

[26] S. Girnyk, A. Barannik, E. Barannik, V. Tovstiak, A. Marusenko and V. Volokhov, Ultrasound Med. Biol. **32**(2), 2011–2019 (2006), https://doi.org/10.1016/j.ultrasmedbio.2005.11.015.

[27] P.J. Fish, in: *Physical Principles of Medical Ultrasonics*, edited by C.R. Hill (Ellis Horwood, Chichester, 1986), pp. 338–376.

[28] E.A. Barannik, The effect of ultrasound wave focusing on the mean-square width of the Doppler spectrum // Acoust. Phys. **40**(2), 188–190 (1994), http://www.akzh.ru/pdf/1994_2_212-214.pdf. (in Russian)

[29] E.A. Barannik, Optimum resolution of pulsed Doppler systems, Acoust. Phys. **43**(4), 387–390 (1997), http://www.akzh.ru/pdf/1997_4_453-457.pdf. (in Russian)

[30] H. Hasegawa, H. Kanai, Yo. Koiwa and J.P. Butler, Jpn. J. Appl. Phys. **42**(5B), 3255–3261 (2003), https://doi.org/10.1143/JJAP.42.3255.

[31] E.A. Barannik, in: *Proceedings of the 5th World Congress on Ultrasonics*, (Paris, France, 2003), pp. 397-400.

## ПРОСТОРОВА РОЗДІЛЬНА ЗДАТНІСТЬ ТА ТОЧНІСТЬ ВИМІРЮВАНЬ УЛЬТРАЗВУКОВОЇ ДІАГНОСТИЧНОЇ СИСТЕМИ ПРИ АКУСТИЧНІЙ ВІДДАЛЕНІЙ ПАЛЬПАЦІЇ ЗА ДОПОМОГОЮ СФОКУСОВАНОГО УЛЬТРАЗВУКУ ВИСОКОЇ ІНТЕНСИВНОСТІ

**Є.О. Баранник[1], В.І. Пупченко[2], А.І. Марусенко[2], О.В. Князєв[2], І.М. Цибін[3], О.Ю. Беркович[4]**
*[1]Харківський національний університет імені В.Н. Каразіна, Харків, Україна*
*[2]ТОВ «Ультрасайн», Харків, Україна*
*[3]АТ «НВФ БІОСС», Москва, Росія*
*[4]ФГАОУ ВО «Санкт-Петербурзький політехнічний університет Петра Великого», Санкт-Петербург, Росія*

В даній роботі теоретично та експериментально досліджені просторова роздільна здатність та точність вимірювань ультразвукової діагностичної системи при акустичній віддаленій пальпації (АВП) за допомогою сфокусованого ультразвуку високої інтенсивності (СУВІ). Запропонована фізична модель, яка описує особливості АВП з урахуванням віддаленого характеру ультразвукового допплерівського зондування локального руху м'яких тканин, що викликаний силою радіаційного тиску імпульсу СУВІ. Показано, що з урахуванням зроблених для спрощення припущень виводи моделі добре узгоджуються з результатами проведених експериментів щодо вимірювання величини переміщень під впливом СУВІ. Доведена, зокрема, нетривіальна залежність величини переміщень, що вимірюються допплерівським методом, від глибини зондування та ступені фокусування падаючого та відбитого пучків хвиль. Експериментально досліджена поперечна роздільна здатність при АВП у випадку зондування неоднорідного за модулем Юнга середовища, а також вплив шуму і перешкод на точність вимірювань та роздільну здатність. Зроблений висновок про те, що поперечна роздільна здатність при АВП визначається параметрами локальної області руху і може бути суттєво кращою, ніж власна роздільна здатність ультразвукової системи при В-режимі діагностики. Отримані результати свідчать про перспективність АВП для моніторингу процесу термічної абляції м'яких тканин за допомогою СУВІ.

**КЛЮЧОВІ СЛОВА:** АВП, СУВІ, абляція, допплерівське зондування, еластографія, просторова роздільна здатність, точність вимірювань.

## ПРОСТРАНСТВЕННАЯ РАЗРЕШАЮЩАЯ СПОСОБНОСТЬ И ТОЧНОСТЬ ИЗМЕРЕНИЙ УЛЬТРАЗВУКОВОЙ ДИАГНОСТИЧЕСКОЙ СИСТЕМЫ ПРИ АКУСТИЧЕСКОЙ УДАЛЕННОЙ ПАЛЬПАЦИИ С ПОМОЩЬЮ ФОКУСИРОВАННОГО УЛЬТРАЗВУКА ВЫСОКОЙ ИНТЕНСИВНОСТИ

**Е.А. Баранник[1]*, В.И. Пупченко[2], А.И. Марусенко[2], А.В. Князев[2], И.М. Цыбин[3], А.Е. Беркович[4]**
*[1]Харьковский национальный университет имени В.Н. Каразина, Харьков, Украина*
*[2]ООО «Ультрасайн», Харьков, Украина*
*[3]АО НПФ «БИОСС», Москва, Россия*
*[4]ФГАОУ ВО «Санкт-Петербургский политехнический университет Петра Великого», Санкт-Петербург, Россия*

В настоящей работе теоретически и экспериментально исследованы пространственная разрешающая способность и точность измерений ультразвуковой диагностической системы при акустической удаленной пальпации (АУП) с помощью фокусированного ультразвука высокой интенсивности (ФУВИ). Предложена физическая модель, которая описывает особенности АУП с учетом удаленного характера ультразвукового допплеровского зондирования локального движения мягких тканей, вызванного силой радиационного давления импульса ФУВИ. Показано, что с учетом сделанных упрощающих предположений выводы модели хорошо согласуются с результатами проведенных экспериментов по измерению величины перемещений под действием ФУВИ. Доказана, в частности, нетривиальная зависимость величины измеряемых допплеровским методом перемещений от глубины зондирования и степени фокусировки падающего и отраженного пучков волн. Экспериментально исследована поперечная разрешающая способность при АУП в случае зондирования неоднородной по модулю Юнга среды, а также влияние шумов и помех на точность измерений и разрешающую способность. Сделан вывод о том, что поперечная разрешающая способность при АУП определяется параметрами локальной области движения и может быть существенно лучше, чем собственная разрешающая способность ультразвуковой системы при В-режиме диагностики. Полученные результаты свидетельствуют о перспективности АУП для мониторинга процесса термической абляции мягких тканей с помощью ФУВИ.

**КЛЮЧЕВЫЕ СЛОВА:** АУП, ФУВИ, абляция, допплеровское зондирование, эластография, пространственное разрешение, точность измерений

# THE THRESHOLD OF DETECTION OF FISSION MATERIALS BY ZnWO₄ AND Bi₄Ge₃O₁₂ SCINTILLATION DETECTORS

 **Gennadiy M. Onyshchenko[1,2]\***,  **Volodymyr D. Ryzhikov[2]**,
 **Ivan I. Yakymenko [1]**,  **Oleksandr P. Shchus'[1]**

*[1]V.N. Karazin Kharkiv National University*
*4 Svobody Sq., Kharkiv, 61022, Ukraine;*
*[2] Institute for Scintillation Materials, STC "Institute for Single Crystals"*
*National Academy of Sciences of Ukraine, 60 Nauky Ave., 61001 Kharkiv, Ukraine*
*\*E-mail: gennadiy.m.onyshchenko@karazin.ua*
Received October 15, 2019; revised November 25, 2019; accepted December 3, 2019

In the present work we found the maximum discovery distance for $^{239}$Pu-Be source using the detectors based on ZWO (ZnWO₄) and BGO (Bi₄Ge₃O₁₂) oxide scintillators. Detection distance was defined by using the radiation monitoring system "PORTAL". This research gives us data for estimation of the contribution of low-energy cascade gamma quanta CGQ. The CGQ emitted by excited scintillator nuclei defined the effective discovery distance of the fast neutrons source. The maximum detection distance was obtained with PMT in a single-photon counting mode. The maximum discovery distance for a BGO scintillator of size Ø40×40 mm – 38 cm, ZWO scintillator of size Ø52×40 mm – 54 cm, with reliability about 0.001. The results of the experiment on the ZWO scintillator can be explained by the registration of additional gamma quanta from the inelastic scattering reaction and the CGQ arising from resonant neutron capture region. This two mechanisms further lead to increase the sensitivity of the detector and increase the detection distance of the monitoring system. The key features of the monitoring system are: ZWO oxide scintillator, wide band measuring path, utilize PMT in single photon mode. The obtained detection distance was about 1.4 times higher in comparison with the spectrometric recording mode and 1.9 times higher in values of efficiency. Our results demonstrate the advantages of the ZWO scintillator compared to the BGO and demonstrate the possibility of using the resonant capture mechanism by ZWO detector nuclei to increase the fast neutrons sensitivity. The resonance capture mechanism increase sensitivity and maximum detection distance of the monitoring system. The low-energy gamma-quanta, which discharge of compound nuclei, are substantially suppressed in comparison with the classic spectrometric recording mode.

**KEY WORDS:** detector, fast neutrons, excited states, countable efficiency, density of nuclear levels

The compact gamma-neutron radiation detectors based on the oxide scintillators allow the creation of compact, highly sensitive systems for monitoring the unauthorized movement of fissile and radioactive materials. The response of detectors during neutron moderation in oxide scintillators is primarily formed by instantaneous gamma quanta of the inelastic scattering reaction and delayed cascade of gamma quanta from the radiation capture reaction in the resonance region emitted by excited states of the scintillator compound nuclei [1, 2]. Both of these reactions can be realized when neutrons are thermalized in some oxide scintillators of a few centimeters in thick.

Earlier [3-5], the signals of oxide scintillation detectors in order to suppress CGQ were amplified in the spectrometric mode, while the time of formation of the signal from the PMT in this mode was in the range 1 – 10 microseconds. Also, the physical efficiency (impulse×s$^{-1}$×cm$^{-2}$/neutr$^{-1}$×cm$^{-2}$) in spectrometric mode does not exceed 1. In [6,7] the first results of counting efficiency studies with ZWO scintillators and BGO. When using the mode of counting single photons in the ZWO scintillator, an increased (up to 60 pulse×s$^{-1}$×cm$^{-2}$/neutron×s$^{-1}$×cm$^{-2}$) was detected, compared to the BGO scintillator (2.5 pulse×s$^{-1}$×cm$^{-2}$/neutron×s$^{-1}$×cm$^{-2}$), which was explained by the registration of cascade quanta arising in the scintillator nuclei.

The aim of this work is a comparative assessment of the maximum neutron detection distance of a $^{239}$Pu-Be source by a monitoring system using ZWO, BGO detectors in two significantly different modes - spectrometric and single photon counting mode. It was the use of the single photon counting mode in the monitoring system with the highly sensitive wideband preamplifier that made it possible to estimate the contribution of low energy CGQ generated in the compound nuclei of the oxide scintillator to the maximum detection distance.

Since the energy of CGQ emitted by excited states of compound nuclei is small due to the high-level density, a preamplifier with a high gain and baseline low noise level was used. Due to the fact, that the CGQ emitted by the compound nuclei can be superimposed in the measuring path, it was possible to register them separately by using a broadband preamplifier with a differentiating delay line. To ensure the highest possible counting efficiency of cascade gamma-quanta, a single photon counting mode was applied in the PMT, which made it possible to isolate signals of extremely low energies and durations about nanoseconds.

Earlier [6] the obtained data indicated the absence of a noticeable generation of CGQ in the BGO scintillator with size of Ø40×40 mm. The measurement results by using the monitoring system confirm the previous results, since the measured maximum detection distances for the case of counting single photons and the spectrometric mode for the BGO scintillator are practically the same.

## RESEARCH & METHODS

The counting efficiency of neutron detection by oxide scintillators in units of impulse$\times$s$^{-1}\times$cm$^{-2}$/neutron$\times$s$^{-1}\times$cm$^{-2}$ was previously estimated according to the procedure described in [6]. For effective coupling of scintillator with monitoring system in current work, we use parameter "maximum distance of discovery". This parameter is defined by monitoring system threshold and can be obtained by using equation

$$x_{tr}=x_{avg}+k\times(1/(n-1)\times\Sigma(x_i-x_{avg})^2),$$

where $k = 3.5$, $x_{tr}$ – threshold level, $x_{avg}$ – average value, $x_i$ – enumeration of all values. The dispersion of the count rate was achieved by using standard deviation low for each data point. It was also found that the background fluctuation is not depend on Poisson distribution. The data reliability of the maximum detection distance was set at 0.001% (error rate), otherwise, no more than 1 false pulse per 1000 pulses. The sensitivity measurements of a radiation monitor system based on ZWO, BGO single crystal detectors under fast neutron irradiation were carried out in a spherical geometry [8]. We use $^{239}$Pu-Be with flux $0.95\times10^5$ neutron$\times$s$^{-1}$, $\emptyset20\times30$ mm and 52 grams. The source is placed inside a lead ball $\emptyset100$ mm with a well $\emptyset20$ mm. The lead ball simultaneously attenuates the accompanying gamma radiation from the $^{239}$Pu-Be source [6, 7]. We add an additional lead shield – 5 mm to protect the detector from background gamma radiation. The principle diagram of the monitoring system Fig. 1.
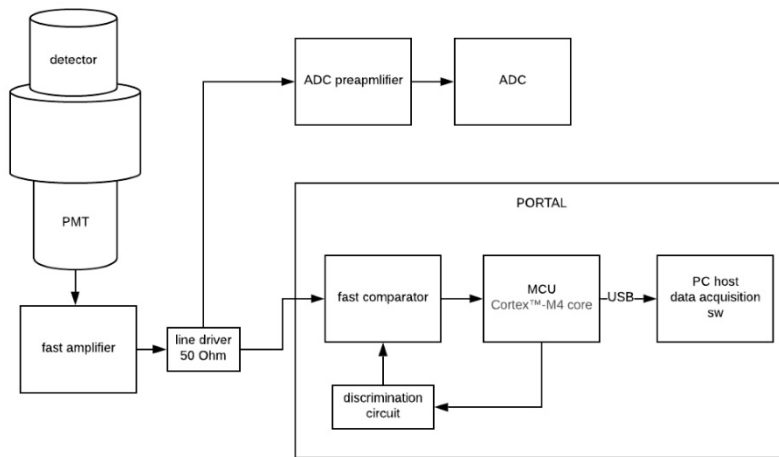


Fig. 1. The principle diagram of the monitoring system

The minimum pulse width of the input signals is $\sim 4$ ns. The signal accumulation time was defined by software and can be set from 10 ms and more.

In experiment of determination the maximum discovery distance the pulse accumulation time was about 1000 seconds, number of iterations – 1000, time of one sample accumulation 1 sec. Data was obtained in two mode with neutron source and without. Counting rate in single photon counting mode for ZWO $\emptyset52\times40$ mm$^3$ was $\sim 3000$ sec$^{-1}$, in spectrometric mode $\sim 40$ sec$^{-1}$. Principle of data accumulation was shown on Fig. 2. Where red line is calculated threshold, data below the red line is background fluctuation without source and data above threshold from $^{235}$Pu-Be.
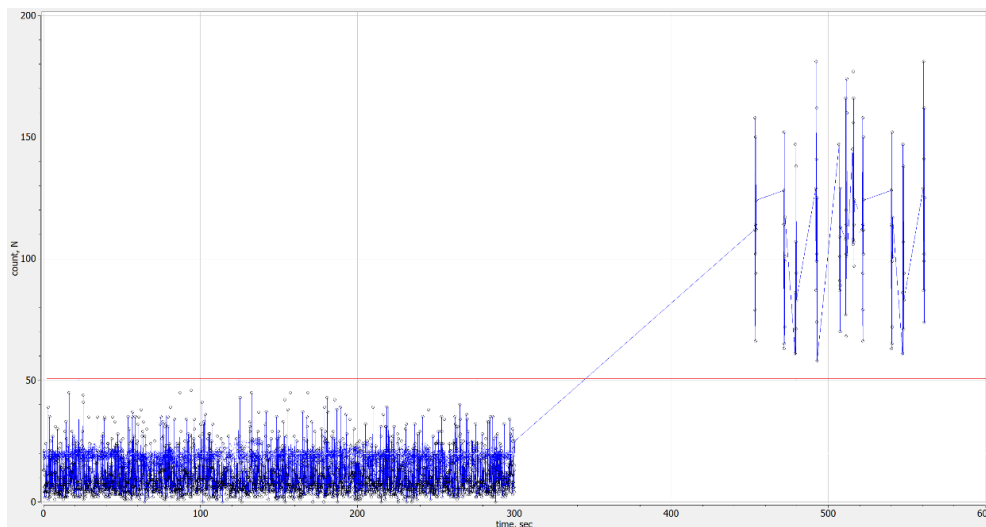


Fig. 2. The data accumulation by using portal software (source $^{239}$Pu-Be). Red line is threshold

Structure diagram of measurement setup contain PMT R1307 Hamamatsu, ultra-low noise amplifier and was discussed previously [6] in our works. The signals from PMT (baseline noise fluctuation + electronic noise ~ 10 mV) was amplified by 6x stage preamplifier (band ~ 200 МГц, 60 dBm, output current on 50 Ohm 80 mA). In addition, output signal was trimmed by shorted delay line of 2 m length. The PMT voltage in single photon mode was 1250 – 1350 V, in spectrometric mode – from 650 V to 850 V. Signal slew rate in spectrometric mode was 1 us, in "PORTAL" path ~ 2 ns.

## RESULTS

In this work, we obtained the experimental values of the maximum detection distance "source-detector". The counting speed of the recorded signals did not exceed the predefined threshold $x_{tr} = x_{avg} + k \times ((n-1)^{-1} \times \Sigma (x_i - x_{avg})^2)$). The reliability of the measurements is about 1 false alarm per 1000 pulses for ZWO detectors and BGO. The measurements were carried out in two modes – in the spectrometric mode and the mode of counting single photons. The Table shows the results of measurements of the maximum detection distance R (cm) for ZWO, BGO scintillators in the monitor, K1 coefficients — increase in the maximum detection distance, K2 – increase in sensitivity in the monitoring system, K3 – increase in the effective area of the detector compared to the spectrometric mode.

The sensitivity increment and the effective area of the detector were estimated according to the law of inverse squares.

Table.

Discovery distance R (cm) for ZWO, BGO

| scintillator | R, cm (τ ~ 2 ns) | R, cm (τ = 1 us) | K1 (increase in detection distance) | K2 (increase in detection efficiency) | K3 (increase in detector window) |
|---|---|---|---|---|---|
| ZWO | 54 | 39 | 1.4 | 1.9 | 1.9 |
| BGO | 38 | 38 | 1 | 1 | 1 |

## DISCUSSIONS AND CONCLUSIONS

The obtained values of the maximum detection distance of the "detector – radiation monitor" system during the registration of fast neutrons of a [239]Pu-Be source for a ZWO single crystal detector can be explained as follows.

In the ZWO scintillator [6, 7] arise the additional CGQ which associated with the primary gamma quantum from the inelastic scattering reaction, which results in the case of their efficient isolation and registration (single photon counting mode) to increase the statistics of signals related to one input particle and, as a result, to increase the sensitivity of the system. At the same time, measurements carried out in the spectrometric mode on a ZWO scintillator did not give an increase in sensitivity, since CGQ (with low energies ~ 0.2-1 keV) are suppressed in this mode. CGQ registration is require high amplifier gain ( ~60 dBm) and single photon counting mode for PMT.

In the BGO scintillator of the indicated sizes [6, 7, 9, 10], CGQ are practically not observed, which is confirmed by the results of measuring the maximum detection distance of the monitor in different modes — photon counting and spectrometric. Thus, for BGO-type scintillators, an increase in statistics (photon counting mode) practically does not lead to an increase in sensitivity, since the conditions for the extraction of CGQ are not realized in BGO. It should be noted that in monitoring systems, in addition to signal statistics, the dispersion of the signal from neutrons plays an important role, which depends on the mechanism of neutron energy conversion in the scintillator, i.e. on the type of scintillator and reaction.

Thus, the use of the ZWO scintillator as part of a monitor recording signals in the photon-counting mode makes it possible efficiently using of a CGQ from the resonance capture of fast neutrons. That leads to increase the sensitivity of the monitoring system compared to the spectrometric mode by about 1.9 times and increasing the maximum detection distance by about 1.4 times.

### ORCID IDs

**Gennadiy M. Onyshchenko** https://orcid.org/0000-0001-6945-8413

**Volodymyr D. Ryzhikov** https://orcid.org/0000-0002-2833-2774

**Ivan I.Yakymenko** https://orcid.org/0000-0002-0194-8376

**Oleksandr P. Shchus'** https://orcid.org/0000-0001-6063-197X

### REFERENCES

[1] M. Anellia, G. Battistoni, S. Bertolucci, C. Bini, P. Branchini, C. Curceanu, G. De Zorzi et al., Nucl. Inst. Meth. Phys. Res. A, **580**, 368-372 (2007), https://doi.org/10.1016/j.nima.2007.08.005.

[2] L.L. Nagornaya, V.D. Ryzhikov, B.V. Grinyov, L.A. Piven', G.M. Onyshchenko and E.K. Lysetska, in: *Abstracts IEEE Nuclear Science Symposium*, (Drezden, Germany, 2008), pp. 714-719. https://doi.org/10.1109/NSSMIC.2008.4775229.

[3] B. Grynyov, V. Ryzhikov, L. Nagornaya, G. Onishcenko, L. Piven'. US Patent No. 8058624 (15 November 2011), http://patft.uspto.gov/netacgi/nph-Parser?Sect1=PTO2&Sect2=HITOFF&p=1&u=%2Fnetahtml%2FPTO%2Fsearch-adv.htm&r=1&f=G&l=50&d=PTXT&S1=(%228058624%22.PN.)&OS=PN/.

[4] V.D. Ryzhikov, B.V. Grinyov, G.M. Onyshchenko, L.A. Piven, O.K. Lysetska, O.D. Opolonin, S.A. Kostioukevitch and C.F. Smith, in: *XVI SPIE Optical Engineering Proceedings, "Hard X-Ray, Gamma-Ray, and Neutron Detector Physics"*, (IEEE, San Diego, 2014), https://doi.org/110.1117/12.2058185.

[5] V.D. Ryzhikov, S.V. Naydenov, G.M. Onyshchenko, L.A. Piven, T. Pochet and C.F. Smith, Nucl. Inst. Meth. Phys. Res. A, **903**, 287–296 (2018), https://doi.org/10.1016/j.nima.2018.06.074.

[6] V. Ryzhikov, G. Onyshchenko, I. Yakymenko, S. Naydenov, A. Opolonin and S. Makhota, East Eur. J. Phys. **2**, 11-18 (2019), https://doi.org/10.26565/2312-4334-2019-2-02.

[7] G. Onyshchenko, V. Ryzhikov, I. Yakymenko, V. Khodusov, S. Naydenov, A. Opolonin and S. Makhota, East Eur. J. Phys. **3**, 54-62 (2019), https://doi.org/10.26565/2312-4334-2019-3-07.

[8] O. Kazachkovskij, Atomic Energy, **83**(1), 509-515 (1997), https://doi.org/10.1007/BF02418976.

[9] A. Voronov, S. Naydenov, I. Pritula, G. Onyshchenko, A. Shchus' and I. Yakymenko, East Eur. J. Phys. **5**(3), 45-52 (2018). https://doi.org/10.26565/2312-4334-2018-3-05.

[10] V.D. Ryzhikov, G.M. Onishenko, I.I. Yakymenko, S.V. Najdenov, A.D. Opolonin and S.V. Mahota. *XVII конференция по физике высоких энергий и ядерной физи*ке [*XVII Conference on High Energy Physics and Nuclear Physi*cs], (NSC "KIPT", Kharkiv, 2019), pp. 96, https://www.kipt.kharkov.ua/conferences/ihepnp/2019/collection_of_theses_%D0%A5VII_hepnp.pdf. (in Russian)

## ПОРІГ ВИЯВЛЕННЯ МАТЕРІАЛІВ ПОДІЛУ СЦИНТИЛЯЦІЙНИМИ ДЕТЕКТОРАМИ ZnWO₄ ТА Bi₄Ge₃O₁₂

**Г.М. Оніщенко[1,2], В.Д. Рижіков[2], І.І. Якіменко[1], О.П. Щусь[1]**

*[1]Харьковскій Національний Університет імені В. Н. Каразіна, 61022, Харків, Україна*
*[2]Інститут сцинтиляційних матеріалів, НТЦ "Інститут монокристалів", НАН України, 61001, Харків, Україна*

У даній роботі виміряна максимальна відстань виявлення $^{239}$Pu-Be джерела швидких нейтронів детекторами на основі оксидних сцинтиляторів ZWO (ZnWO₄) і BGO (Bi₄Ge₃O₁₂). Виміри відстані виявлення проводилися з використанням розробленої системи радіаційного моніторингу. Це дозволило оцінити величину вкладу низькоенергетичних каскадних гамма-квантів (КГК), що випускаються збудженими ядрами сцинтилятора в відстань виявлення швидких нейтронів. Значення максимальної відстані виявлення детекторів отримані в режимі рахунку одиничних фотонів і склали 38 см для сцинтилятора BGO розміром Ø40×40 мм, для сцинтилятора ZWO розміром Ø52×40 мм – 54 см з надійністю не гірше 0.001. Результати експерименту для сцинтилятора ZWO можуть бути пояснені реєстрацією, крім гамма-квантів з реакції непружного розсіювання, також КГК, що виникають при резонансному захопленні нейтронів, що призводить до зростання чутливості детектора і збільшенню відстані виявлення системи моніторингу. Низькоенергетичні КГК реєструвалися в режимі рахунку одиничних фотонів. Отже, застосування в системі моніторингу оксидного сцинтилятора ZWO, в складі якого містяться ядра, що випускають КГК з реакцій резонансного захоплення, і широкосмугового вимірювального тракту, що працює в режимі рахунку одиничних фотонів дозволяє збільшити ефективну чутливість детектора приблизно в 1.9 рази, що призводить до збільшення відстані виявлення джерела нейтронів детектором ZWO приблизно в 1.4 рази в порівнянні зі спектральним режимом реєстрації. Отримані результати демонструють переваги сцинтилятора ZWO в порівнянні з BGO і вказують на можливість використання механізму резонансного захоплення нейтронів ядрами детектора ZWO для збільшення чутливості детектора до швидких нейтронах. Використання механізму резонансного захоплення призводить до підвищення чутливості і збільшення максимальної відстані виявлення системи моніторингу в порівнянні зі спектрометричним режимом реєстрації, в якому низькоенергетичні гамма-кванти розрядки компаунд ядер, що утворюються в результаті резонансного захоплення, істотно пригнічені.

**КЛЮЧОВІ СЛОВА:** детектор, швидкі нейтрони, збуджені стани, лічильна ефективність, щільність ядерних рівнів

## ПОРОГ ОБНАРУЖЕНИЯ МАТЕРИАЛОВ ДЕЛЕНИЯ СЦИНТИЛЛЯЦИОННЫМИ ДЕТЕКТОРАМИ ZnWO₄ И Bi₄Ge₃O₁₂

**Г.М. Онищенко[1,2], В.Д. Рыжиков[2], И.И. Якименко[1], А.Ф. Щусь[1]**

*[1]Харьковский Национальный Университет имени В.Н. Каразина, 61022, Харьков, Украина*
*[2]Институт Сцинтилляционных Материалов, НТЦ "Институт Монокристаллов", НАНУ, 61001, Харьков, Украина*

В настоящей работе измерено максимальное расстояние обнаружения $^{239}$Pu-Be источника быстрых нейтронов детекторами на основе оксидных сцинтилляторов ZWO (ZnWO₄) и BGO (Bi₄Ge₃O₁₂). Измерение расстояния обнаружения проводились с использованием разработанной системы радиационного мониторинга. Это позволило оценить величину вклада низкоэнергетичных каскадных гамма-квантов (КГК), испускаемых возбужденными ядрами сцинтиллятора в расстояние обнаружения быстрых нейтронов. Значения максимального расстояния обнаружения детекторов получены в режиме счета единичных фотонов и составили 38 см для сцинтиллятора BGO размером Ø40×40 мм, для сцинтиллятора ZWO размером Ø52×40 мм – 54 см с надежностью не хуже 0.001. Результаты эксперимента на сцинтилляторе ZWO могут быть объяснены регистрацией, кроме гамма-квантов из реакции неупругого рассеяния, также КГК, возникающих при резонансном захвате нейтронов, что приводит к росту чувствительности детектора и увеличению расстояния обнаружения системы мониторинга. Низкоэнергетичные КГК регистрировались в режиме счета единичных фотонов. Таким образом, применение в системе мониторинга оксидного сцинтиллятора ZWO, в составе которого содержатся ядра, испускающие КГК из реакций резонансного захвата, и широкополосного измерительного тракта, работающего в режиме счета единичных фотонов позволяет увеличить эффективную чувствительность детектора примерно в 1.9 раза, что приводит к увеличению расстояния обнаружения источника нейтронов детектором ZWO примерно в 1.4 раза по сравнению со спектрометрическим режимом регистрации. Полученные результаты демонстрируют преимущества сцинтиллятора ZWO по сравнению с BGO и указывают на возможность использования механизма резонансного захвата нейтронов ядрами детектора ZWO для увеличения чувствительности детектора к быстрым нейтронам. Использование механизма резонансного захвата приводит к повышению чувствительности и увеличению максимального расстояния обнаружения системы мониторинга по сравнению со спектрометрическим режимом регистрации, в котором низкоэнергетичные гамма-кванты разрядки компаунд ядер, образующихся в результате резонансного захвата, существенно подавлены.

**КЛЮЧЕВЫЕ СЛОВА:** детектор, быстрые нейтроны, возбужденные состояния, счетная эффективность, плотность ядерных уровней

### Алла Таньшина[i]

*До 90-річниці фундації лабораторії низьких температур Українського (Харківського) фізико-технічного інституту*

За своїм технічним обладнанням ХФТІ є першим фізичним інститутом у СРСР.
*За резолюцією комісії ВФМН АН СРСР од 12-18 травня 1939 р.*

## «ТРЕБА ПАМ'ЯТАТИ, ЩО ДО ПОЯВИ ПЕТРА КАПИЦІ НАША ЛАБОРАТОРІЯ БУЛА ПЕРШОЮ І ЄДИНОЮ В СРСР…»[ii]

Якщо б мені запропонували
оголосити прізвища тільки двох фізиків,
котрі найбільш уславили українську науку,
то я  назвав би теоретика Л. Д. Ландау
та експериментатора Л. В. Шубнікова.
*Академік НАН України О. І. Ахієзер*

### Фундатори.
### *Лев Васильович Шубніков*

Лев Васильович Шубніков народився 1901 року в Санкт-Петербурзі. Його батько, Василь Васильович, працював бухгалтером, а мама – Любов Сергіївна – була домогосподаркою.

1911 року Лева зарахували до одного з найкращих  навчальних закладів міста – гімназії Марії Андріївни Лентовської. Навчався Лев, як свідчать архівні документи гімназії, добре. В табелі (за останній, 8 клас) у графі «фізика» є запис: «зацікавлення предметом завелике». Тож-бо, обираючи майбутній фах, він не кидався в крайнощі, бо вже усвідомив, що його покликання – фізика.

1918 року Шубніков вступає до Петроградського університету. Натомість спочатку йому довелося слухати лекції з тими, хто був на курс старшим, бо  він був єдиним студентом-фізиком набору 1918 року.

Ілюстрацією студентського життя за тих часів є спогади тодішньої студентки Ольги Миколівни Трапезнікової, доктора фізико-математичних наук: *«1919 року я вступила на фізичне відділення Петроградського університету. В університеті зустрілася з Левом  Васильовичем…*

*Життя було заважким. Після лекцій Лев Васильович складав список присутніх, лектор підписував, й всім видавали по тоненькому шматочку хліба з повидлом – ми називали це чайним постачанням…*

*У 1919 р. вже існував Оптичний інститут, і Д. С. Рождественський улаштував туди всіх старшокурсників лаборантами… Всі лаборанти одержували так званий "атомний пайок", і це їх дуже підтримувало. Такий самий пайок отримували й викладачі»* [2, С. 257-258].

Лев Васильович захоплювався вітрильним спортом. Однак це хобі зіграло у його житті фатальну роль. За словами його дружини О. М. Трапезнікової, *«найбільшою розвагою для нас була яхта, яку Фізичний інститут орендував у колишньому імператорському яхт-клубі…*

*Усім господарством яхт-клубу завідував якийсь Рябов. Одного разу університетська компанія хіміків звернулася до нього з проханням підібрати матросів задля походу вздовж Фінської  затоки… Рябов запропонував Левові  Васильовичу піти в цей похід матросом, і він із задоволенням погодився. Час минав, але він не повертався. Рябов висловив припущення, що сталася катастрофа.*

*Насправді ця компанія викрала в університеті приладову платину і вирішила втекти за кордон. Яхту прибило до Фінляндії, де їх усіх за незаконний перетин кордону ув'язнили. Їм запропонували покинути Фінляндію. Але повертатися назад аніхто, крім Лева Васильовича, не погодився.  Тож  їх вислали до Німеччини…*

*Л. В. Шубніков працював там фотографом, згодом – на кварцовому заводі. Зрештою він звернувся до нашого консульства з проханням щодо повернення. Саме  цього часу в Німеччині в службових справах перебував викладач М. М. Глаголєв, який приїхав задля закупівлі трансформаторів. Він підказав Левові Васильовичу до кого звернутися, і дозвіл повернутися було отримано»* [2, С. 258-2589].

Понад рік Шубніков перебував за  кордоном; повернувшись 1922 року, він не поновився в Петроградському університеті, а перевівся на 3-й курс фізико-механічного факультету Політехнічного інституту.

Лев Васильович успішно поєднував навчання з підробітком в лабораторії Івана Васильовича Обреїмова в Ленінградському фізико-технічному інституті (надалі – ЛФТІ). Й по закінченні інституту (1926 р.) Шубніков мав дві наукові праці за співавторства з Обреїмовим: перша – щодо нового і простого способу вирощування

---

[i] Ювілейний нарис підготовлено за дисертаційними матеріалами (науковий керівник – академік НАН України Віктор Григорович Бар'яхтар)

[ii] Цитування за мемуарними спогадами директора-організатора Українського фізико-технічного інституту (УФТІ) академіка Івана Васильовича Обреїмова [1, С. 22.]

великих досконалих металевих монокристалів заданої форми (метод Обреїмова-Шубнікова), інша – з оптичного методу спостереження деформацій в кам'яній солі.

Восени 1926 року директор ЛФТІ Абрам Федорович Йоффе направляє талановитого молодого співробітника до Лейденського університету, на стажування в лабораторію низьких температур.

**Історична довідка**

Лейденський університет зорганізовано 1575 року принцем Вільгельмом I Оранським  на вшанування героїчної оборони міста від іспанських військ.

1894 року Гейке Камерлінг-Оннес (*Heike Kamerlingh Onnes,* 1853-1926) в університеті облаштував першу в світі кріогенну лабораторію, що згодом стала світовим центром низьких температур. Саме Камерлінг-Оннес уперше досяг температур, близьких до абсолютного нуля.

1908 року він перший в світі одержав рідкий гелій, а 1911 року відкрив явище надпровідності.

1923 року Гейке Камерлінг-Оннес пішов з посади директора (1923); керівниками (співдиректорами) кріогенної лабораторії стали його учні Вандер-Йоханес де Гааз (*Wander Johannes de Haas,* 1878-1960)  й Віллем-Хедрік Кеєзом *(Willem Hendrik Keesom,* 1876-1956*).*

Гасло Лейденської кріогенної лабораторії: «Door meten – tot weten».

Лев Васильович Шубніков проходив стажування у відділі В.-Й. де Гааза. Задля наочності послугуємося мемуарними нотатками О. М. Трапезнікової: *«ставлення В.-Й. де Гааза до Лева Васильовича було винятково доброзичливим, сповненим довіри, поваги й приязні. Співробітники лабораторії та обслуговуючий персонал ставилися до Лева Васильовича дуже уважно, він припав їм до душі своїм спокійним, доброзичливим і рішучим характером. Однак він був неговіркий і важко зближувався з людьми, та й росіян там не було. Тож тривалий час почував себе самотньо…*

*У вихідні дні він іноді їздив на велосипеді, подорожуючи до прилеглих міст,  де оглядав музеї, собори; докладно мені писав, що бачив, що сподобалося. На жаль, ці листи не збереглися – всі вони зникли за час арешту Лева Васильовича.*

*1927 року я одержала запрошення від В.-Й. де Гааза приїхати… Кріогенна лабораторія, або, як її офіційно називали, "Фізична лабораторія Лейденського університету, зорганізована Камерлінг-Оннесом", справила на мене велике враження.*

*У Лейдені була спеціальна кімната задля вимірів («Meet Kamer»). Численні хлопчики-помічники, працівники майстерень робили для науковців усе, що запотрібно. Панувала така атмосфера, в якій наукових співробітників високо поціновували, була повага до наукової праці. За укладом лабораторії – виміри мають бути дуже точними, міряти необхідно на чистих зразках…*

*У Ленінградському університеті, та й у Фізтесі кількісним вимірам такої точності не надавали значення. Окрім того, ми не мали таких приладів.  Я вперше побачила, як потрібно міряти»* [2, С. 262-263].

За пропозиції В.-Й. де Гааза Шубніков почав вивчати властивості вісмуту в магнітному полі за низьких температур. Варто зауважити, що, незважаючи на інтенсивні дослідження тогочасних учених, поведінка вісмуту залишалася нерозгаданою: не вдавалося пояснити істотні розбіжності  в експериментальних результатах.

В.-Й. де Гааз і Л.В. Шубніков припустили, що розгадка прихована в монокристалічних зразках вісмуту, а саме – в наявності дефектів й вмісті домішок.  Найпершим завданням у дослідженні вісмуту стало одержання достатньо чистих зразків.

Упродовж першого року перебування в Лейдені Шубніков займався хімічним очищенням і перекристалізацією вісмуту. Отримавши кристали вісмуту винятково високої якості з малим вмістом домішок і дефектів, він розпочав вивчати поведінку цих зразків у магнітному полі за азотних і водневих температур. Цикл досліджень тривав чотири роки.

Результатом експериментів було відкриття нового явища – низькотемпературних осциляцій опору зі зміною магнітного поля. Це відкриття одержало назву «ефект Шубнікова - де Гааза».

У наукових статтях, присвячених  ефекту, В.-Й. де Гааз завжди ставив, порушуючи алфавітну чергу, прізвище Шубнікова поперед власного – підкреслюючи вирішальну роль Лева Васильовича в цьому відкритті.

1930 року Л. В. Шубніков радо припав на добру пораду директора-організатора Українського фізико-технічного інституту Івана Васильовича Обреїмова – продовжити наукову діяльність в Харкові; а від 1931 року на нього вже покладено обов'язки  керманича кріогенної лабораторії інституту.

Й нині принагідна згадка: саме Лейденська лабораторія надала найбільш питому допомогу кріогенній лабораторії УФТІ. Як зауважує О. М. Трапезнікова, *«дуже велику допомогу лабораторії надавав Е. Вірсма. Він щороку, аж до 1935, приїздив до Харкова і привозив купу всіляких речей, без яких ми не мали можливості працювати. Перебуваючи в Лейдені, він довідався про нову гелієву машину, сконструйовану Ф. Саймоном, і негайно надіслав нам ескізи машини, випередивши П. Еренфеста, який мав на думці зробити теж саме.*

*Ми не мали чим вимірювати занизькі температури, задля цього необхідні були спеціальні платинові термометри. Щоб їх виготовити, треба було намотати платиновий дріт на порцеляновий циліндр, випалити все це за високих температур і відкалібрувати. Ми не мали платини потрібного ступеня чистоти; брудною була порцеляна, з якої при випалюванні випаровувалися різні домішки, що забруднювали платину. Щоправда, для калібрування був у нас платиновий термометр Pt-38, подарований В. Кеєзомом. Е. Вірсма привозив нам із*

It Should Be Remembered Before Peter Kapitsa Our Laboratory Was the First...

97

EEJP. 4 (2019)

Лейдена чистий платиновий дріт і спеціальні порцелянові циліндри, щоб ми самотужки мали змогу виготовити термометри.

Задля збереження рідин потрібні були дьюари. Металеві дьюари паяли оловом. За низьких температур наше олово тріскалося, і дьюари виходили з ладу. Е. Вірсма постачав у великій кількості спеціальну припайку, що витримувала занизькі температури.

Він привозив усе, чого ми в Союзі не мали можливості дістати. Привозив лічильник обертів для намотування трансформаторів. У нас були погані важки для аналітичних ваг – він привіз важки. Лейкопластиру не було – він і лейкопластиром забезпечив. Усе, що він міг придбати і чого в нас не було, він привозив. Зрозуміло, все це він привозив зі схвалення В.-Й. де Гааза...

Е. Вірсма дуже допоміг кріогенній лабораторії, хоча мало хто знає» [2, С. 280-281].

Так само щиро Е. Вірсма бажав за потреби піти до армії замість Лева Шубнікова. До того ж мав на меті переїхати до Харкова: навіть продав усе своє майно, але візу так і не одержав.

Від самого початку робота лабораторії низьких температур УФТІ була скерована на освоєння кріогенної техніки й одержання фундаментальних результатів, як-от: рідкий азот було отримано вже 1930 року, рідкий водень (вперше в СРСР!) – 23 березня 1931 року, а рідкий гелій – 1932 року.

Як сповіщає академік Микола Євгенович Алексєєвський, тодішній співробітник лабораторії Л. В. Шубнікова: «Лев Васильович був справжнім лідером, й всі роботи, що велися в лабораторії, зазвичай пропонувалися саме за його думкою. Він був надзвичайно фаховим експериментатором, як підтвердження – ефекти, що пов'язані з його ім'ям: ефект Шубнікова-де Гааза, виміри магнітного моменту протона, які він виконав за співпраці з Б. Г. Лазарєвим, антиферомагнетизм і роботи надпровідних сплавів.

Лев Васильович дуже добре "відчував" фізику, й це давало йому можливість майже безпрограшно визначати необхідні умови експерименту. Багато праць він обговорював з Л. Д Ландау, з яким був у дружніх взаєминах.

Напевне, Лев Васильович мав тоді ще й велике адміністративне навантаження, але нам, молодим його співробітникам, здавалося, що все робиться самотужки...

А головне – винятково товариська атмосфера лабораторії, сприятлива для наукової співпраці...

У лабораторії діяв цікавий семінар за обраною Левом Васильовичем тематикою. Це давало можливість відстежувати усі цікаві роботи за фізикою низьких температур» [2, С. 308-309].

Понад те, слушно наголосити, що саме за сприяння Л. В. Шубнікова було зорганізовано – вперше на теренах СРСР! – студентський кріогенний практикум у Харківському університеті.

Либонь, й академік Олександр Ілліч Ахієзер на своїх мемуарних сторінках немарно окреслив той факт, що «із великим задоволенням він [Ландау. – А. Т.] обговорював результати експериментальних досліджень, що проводилися в УФТІ. Часто-густо опівночі він бував у кріогенній лабораторії Л. В. Шубнікова, обговорюючи з ним результати його дослідів, що призвели до важливих відкриттів.

З-поміж них, перши за все, доведення неможливості проникнення магнітного поля у надпровідник. Це явище одержало назву ефекту Мейснера, хоча незалежно було відкрито Шубніковим, який вперше довів, що магнітна індукція в надпровіднику дорівнює нулю.

Шубнікову належить також відкриття проміжного стану надпровідників, теорія якого була побудована Ландау.

Дотепер старожили згадують, як запізно надвечір дружина Л. В. Шубнікова О. М. Трапезнікова приносила до лабораторії чоловіка вечерю для обох Левів» [3, С. 46-47].

До слова: одне з найулюбленіших тогочасних висловлювань Лева Васильовича – «Творчість розпочинається там, де закінчується копіювання».

У червні 1935 року в УФТІ гостювали французькі колеги – професор теоретичної фізики Франсіс Перрен й дійсний член Французької та Української академій наук Жан Перрен. Процитуємо їхній відгук (мовою першоджерела): «Ми занадто щасливі, що можемо розповісти про те сильне враження, яке викликало в нас відвідання Українського фізико-технічного інституту в Харкові.

Проблеми, що вивчаються в ньому, обіймають найважливіші теми чистої фізики й опрацьовуються з найсучаснішої точки зору...

Особливо відзначимо установки, що відносяться до низьких температур (надпровідність, явище магнето-калорійного ефекту, адсорбція), і установки, що відносяться до ядерної фізики (установки для зруйнування атомів).

Але ще більше, ніж апарати для дослідів, ми були щасливі бачити всіх молодих співробітників, бадьорих і життєрадісних, які віддають свою працю туди, де теоретики і експериментатори об'єднують свої зусилля, тому що коли важливо мати апарати, то занадто важливіше, а це буває рідко, мати голови, які уміють користуватися ними.

З найкращими побажаннями від французьких фізиків харківським товаришам» [4].

Отож-бо й своє перше виїзне засідання фізична група АН СРСР недарма провела саме на підґрунті УФТІ (23-24 січня 1937 р., м. Харків). Зокрема, за повідомленням «Журнала технической физики», «на порядку денному засідання розглядалися питання низьких температур та звіт акад. УРСР О. І. Лейпунського про роботу УФТІ.

На засіданні була присутня велика кількість вчених, які приїхали з Москви, Ленінграда, Свердловська, Києва, Одеси і Дніпропетровська…

Центральна проблема фізики низьких температур – надпровідність – була окреслена роботами Л. В. Шубнікова й теоретичними дослідженнями Л. Д. Ландау…

Л. В. Шубніков оприлюднив також цікаві результати експериментів стосовно руйнування надпровідності в магнітному полі як щодо чистих металів, так і сплавів…

Доречно виокремити в цих ґрунтовних роботах кріогенної лабораторії плідне співробітництво теорії та експерименту, доведене до високого щабля досконалості» [5, C. 884-885].

УФТІ не оминуло й лихоліття: наприкінці 30-х років розпочалися репресії. Послугуємося мемуарами тодішнього іноземного співробітника УФТІ О. Вайсберга: *«Наш інститут – один із найзначніших у Європі. Можливо навіть, що в Європі немає інституту так добре обладнаного і з такою великою кількістю різноманітних лабораторій, як наш.*

*Уряд не шкодував грошей. Провідні вчені частково отримали освіту за кордоном. Тривалий час їх посилали за державний кошт до найвідоміших фізиків світу для продовження освіти. В нашому інституті 8 відділів, на чолі яких стояло 8 наукових керівників. Який це має вигляд зараз?*

*Лабораторія кристалів…Керманич  Обреїмов – арештований.*

*1 кріогенна лабораторія… Керманич Шубніков – арештований.*

*2 кріогенна лабораторія… Керманич Руеманн – відворений з країни.*

*Ядерна лабораторія… Керманич Лейпунський – арештований.*

*Рентгенівський відділ… Керманич Горський – арештований.*

*Відділ теоретичної фізики… Керманич Ландау – арештований.*

*Дослідна станція глибокого охолодження… Керманич Вайсберг – арештований.*

*Лабораторія ультракоротких хвиль… Керманич Слуцкін – ще працює.*

*Серед заарештованих: професор Обреїмов, засновник і перший директор інституту; професор Лейпунський, академік Академії наук і директор інституту; професор Лев Давидович Ландау, найбільш відомий в країні фізик-теоретик і один із найбільш талановитих учених світу. Ще раніше через напади НКВС Ландау був змушений полишити інститут і переїхати до Москви, до професора Капиці.*

*Я побудував дослідну станцію низьких температур. Якраз напередодні її пуску був арештований. Моїм наступником став Комаров. Його так само арештували. То хто ж працюватиме?»* [6, C. 277]…

### Борис Георгійович Лазарєв

Харківський фізико-технічний інститут буде центральним для СРСР…
інститутом низьких температур й науково-технічною базою промисловості.
*Академік А. Ф. Йоффе,*
*співфундатор УФТІ*

Борис Георгійович Лазарєв, десятий з одинадцяти дітей парафіяльного священика,  народився 6 серпня 1906 року в селі Миропілля (нині Сумської обл.).

1916 року, після дворічного навчання в церковнопарафіяльній школі батька, Борис Лазарєв був зарахований до Білгородської класичної гімназії. Але лихоліття суспільних катаклізмів – революційні події 1917 року та руйнація соціальних підвалин – примусили його на певний час відмовитись від навчання і, щоб вижити, шукати заробітків.

Працював він й помічником пасічника (1920 р.), й розсильним на металургійному заводі (1921-1922 рр.), й учнем лаборанта (1923 р.), й конторником, й рахівником (1924-1926 рр.). Однак перші суворі іспити життя не зрекли бажання вчитися: Борис закінчив вечірню семирічну школу (1920-1923 рр.), а згодом й фабрично-заводське училище (*ФЗУ*, 1924-1926 рр.).

*«Про гімназію і ФЗУ Борис Георгійович відгукувався дуже схвально. Це стосувалося як складу викладачів, так і методу та програми викладання… У бібліотеці ФЗУ, до слова,  Борис Георгійович уперше дізнався, що таке занизькі температури…*

*Живили душу за цих часів астрономія (у нього була непогана підзорна труба) і ботаніка (гербарії, покажчики рослин). Слушно зауважити, що й чимало десятиліть потому Борис Георгійович вражав обізнаністю зоряного неба та знаннями з ботаніки»* [7, C. 843].

1926 року Борис Лазарєв вступив до Ленінградського політехнічного інституту, на фізико-механічний факультет. Ще студентом почав працювати в Ленінградському фізико-технічному інституті (зокрема, переймався установками з досліджень субміліметрових хвиль).

По закінченні інституту (1930 р.) Бориса Георгійовича Лазарєва запрошують на постійну роботу до Ленінградського фізико-технічного інституту. Працюючи в магнітній лабораторії Я. Г. Дорфмана, він зацікавився новою галуззю науки – фізикою низьких температур. І вже на початку 30-х років були оприлюднені його перші наукові праці з розробки критерію надпровідності.

1932 року Борису Георгійовичу довелося вирушити до Свердловська: він бере участь в розбудові Уральського фізико-технічного інституту, як-от зорганізує кріогенну лабораторію.

1934 року його відряджають – задля набуття досвіду досліджень з техніки та фізики занизьких температур – до Українського фізико-технічного інституту (УФТІ, Харків), бо лабораторія Лева Васильовича Шубнікова до 1935 року була першою і єдиною кріогенною лабораторією на теренах СРСР.

Й варто згадки, що *«1935 року за участі Бориса Георгійовича було створено баки з рідким метаном і вперше в світі метан використали як моторне паливо; рідкий кисень – задля зварювання і різання металів, та життєзабезпечення екіпажів літаків…*

*З рідким киснем літали екіпажі Громова, Даниліна, Юмашева (1937 р.), Гризодубової та Расковою. За роки війни ці системи забезпечували висотні польоти нашої бомбардувальної авіації на Берлін»* [7, С. 844].

Принагідна й інша згадка: на конкурсі молодих учених АН УРСР Борис Георгійович та Любов Самійлівна Кан-Лазарєва одержали премію за простий метод одержання і використання зависоких тисків за низьких температур. Методика отримала широке застосування за назвою «льодова бомба».

1936 року на Б. Г. Лазарєва покладено обов'язки керманича кріогенної лабораторії Уральського фізико-технічного інституту, а 1938 року – очильника лабораторії низьких температур Українського фізико-технічного інституту.

За мемуарними нотатками Бориса Георгійовича, *«у 1937-1941 роках УФТІ, а разом з ним і кріогенна лабораторія (та й уся країна) пережили трагічні події – через безправ'я тієї епохи була репресована група співробітників: директор УФТІ академік АН УРСР Олександр Ілліч Лейпунський, засновник інституту член-кореспондент АН СРСР Іван Васильович Обреїмов, керівник кріогенної лабораторії Лев Васильович Шубніков. Олександр Ілліч та Іван Васильович повернулися з "того світу", Лев Васильович залишився там…*

*У серпні 1937 року мене викликали до Наркомважпрому (УралФТІ й ХФТІ – були за його підпорядкування); і в секторі науки його начальник А. А. Арманд сказав, що мені виписано призначення до Харкова. За цих часів я був дуже сором'язливою людиною, одначе тут відчайдушно, але марно чинив опір. Власне кажучи, мене безцеремонно наказом перевели з УралФТІ до ХФТІ.*

*Щоправда, за всієї безцеремонності процесу виявлялася стурбованість долею кріогенної лабораторії УФТІ. На моє зауваження: "Адже Ви знаєте, що я займаюся організацією кріогенної лабораторії в Свердловську" – почув відповідь: "В Свердловську Ви розпочинаєте, а в Харкові створене може розвалитися…".*

*1938 року мене призначили керівником кріогенної лабораторії УФТІ. В УралФТІ організація кріогенної лабораторії (все ж завершена за сприяння УФТІ) затрималася до 1957 року»* [8, С. 8-9].

1941 рік… УФТІ евакуйовано до Казахстану…

У квітні 1944 року інститут рееевакуйовано до Харкова. Як на переконання Бориса Георгійовича, то *«зашвидке відновлення інституту (навзаєм з ним і кріогенної лабораторії) зумовлювалося тим, що УФТІ був… максимально завантажений великою курчатівською програмою з уранової проблеми…*

*Робота за програмою І. В. Курчатова з її обов'язковістю і темпом завеликою мірою посприяла швидкому відновленню "форми", розширенню приладової бази, розмаїттю кріогенної техніки; і стала блискучим трампліном для подальших успіхів»* [8, С. 17].

Бориса Георгійовича Лазарєва було обрано членом-кореспондентом у віці 42 років, а в 45 – дійсним членом АН УРСР.

За спогадами його учня академіка НАН України Ігоря Михайловича Дмитренка, *«велика роль в науковому житті відділу належала семінару. Семінар – справа свята: науковий співробітник мав брати активну участь в семінарах, що регулярно проводилися в кабінеті Бориса Георгійовича, або в залі адміністративного корпусу.*

*Семінари Б. Г. Лазарєва були справжньою науковою школою. Сам він пам'ятав практично усі публікації минулих років з фізики низьких температур, включав їх до обговорення доповідей, стежив, щоб автори дотримувалися добропорядності за посиланнями на попередників.*

*Майже на всіх семінарах були І. М. Ліфшиць ("Ільмех"), М. І. Каганов ("Мусік"), часто приїздили Л. Д. Ландау ("Дау"), А. Ф. Приходько та багато інших фізиків. Бував і Петро Леонідович Капиця, до якого Б. Г. ставився з високим пієтетом і сам користувався великим авторитетом й повагою Петра Леонідовича[iii]\*.*

*Борис Георгійович був душею і володарем семінарів. Вимагав од доповідачів зрозумілого і чіткого викладу фізичного підґрунтя перш аніж переходити до написання формул і рівнянь. До його зауважень і критики уважно ставилися і експериментатори, і теоретики…»* [7, С. 846].

Доленосні факти виокремлено й ученим секретарем інституту Володимиром Соломоновичем Коганом: *«Борис Георгійович не тільки виховав цілу плеяду талановитих науковців, а й за його допомогою в нашій країні та за кордоном була створена мережа нових кріогенних лабораторій, оснащених зріджувальними машинами, розробленими в очолюваній ним кріогенній лабораторії УФТІ.*

*Він докладав чимало зусиль з організації кріогенних лабораторій в Ленінграді, Свердловську, Києві, Сухумі, Махачкалі. Не кажучи вже про нову лабораторію в Харківському університеті (її очолив його друг, майбутній ректор ХДУ Володимир Гнатович Хоткевич) і в Інституті радіоелектроніки АН УРСР.*

---

[iii] Як наочний приклад – листівка, що датована 1974 роком: *«Дорогий Борисе Георгійовичу! Вельми дякую за Ваші вітання. Мені особливо було приємно одержати їх від Вас, оскільки наші інститути й учні були міцно пов'язані з-поміж собою по роботі, і в мене родинні почуття до Харкова і до харківських інститутів. Вітання та найкращі побажання. Щиро Ваш, П. Л. Капиця»*

*У кріогенній лабораторії УФТІ проходили стажування, а згодом створили за її допомогою і в себе кріогенні лабораторії вчені з Польщі, Чехословаччини, Угорщини, Китаю».*

Спливали роки… Але попри те, як розповідає його учень академік НАН України Юрій Михайлович Мацевитий, *«до останніх років свого життя Борис Георгійович був фізично міцним, тримав себе у формі, мав молодечий вигляд. Ніхто ніколи не давав йому його років, він ніби був поза віком, належав до тієї рідкісної категорії людей, стосовно до яких аж ніяк не можна вживати слів "старість", "похилий вік" тощо. Цьому значною мірою сприяли його характер, цілеспрямованість, улюблена робота, захопленість, заняття альпінізмом, контакти з цікавими і близькими йому за духом людьми…».*

Дійсний член Національної академії наук України Борис Георгійович Лазарєв пішов зі земної юдолі 20 січня 2001 року.

## REFERENCES

[1]  I.V. Obreimov, Історія природничо-наукової думки за півстоліття [History of natural thought for half a centur], Вісник Академії наук Української РСР [Bulletin of the Academy of Sciences of the Ukrainian SSR], **10**, 10-25 1971. (in Ukrainian)

[2]  L.V. Shubnikov, *Избранные труды. Воспоминания.* [*Selected Works. Memories*], (Naukova Dumka, Kyiv, 1990), pp. 351. (in Russian)

[3]  I.M. Khalatnikov, editor, *Воспоминания о Л.Д. Ландау: Сборник*, [*Memoirs of L.D. Landau: Collection*], (Nauka, Moscow, 1988). pp. 352. (in Russian)

[4]  A.Ya. Usikov, *Мгновения жизни* [*Moments of life*], (Mystetstvo, Kyiv, 1990), pp. 62. (in Russian)

[5]  M. Divilkovskii, ZhTP, **7**(8), 884-885 1937. (in Russian)

[6]  A.I. Leipunskii, *Избранные труды. Воспоминания.* [*Selected Works. Memoriesю*], (Naukova Dumka, Kyiv, 1990), pp. 280. (in Russian)

[7]  I.M. Dmitrenko, К 90-летнему юбилею Бориса Георгиевича Лазарева [On the 90th anniversary of Boris Georgievich Lazarev], Fizika Nizkikh Temperatur, **22**, 1996. (in Russian)

[8]  B.G. Lazarev, К истории криогенной лаборатории УФТИ–ННЦ «ХФТИ» [To the history of the cryogenic laboratory UFTI – NSC "KIPT"], Fizika Nizkikh Temperatur, **26**, 2000. (in Russian)

# INSTRUCTIONS FOR PREPARING MANUSCRIPT IN EAST EUROPEAN JOURNAL OF PHYSICS

**[1]N.N. Author\*, [2]N.N. Co-author(s)**
*[1]Affiliation of first author*
*[2]Affiliation of second author (if different from first Authors)*
*\*E-mail: corresponding_authors@mail.com, [1]ORCID ID*
*E-mail: co_authors@mail.com, [2]ORCID ID*
Received October 25, 2019; revised November 25, 2019 accepted December 5, 2019

Each paper must begin with an abstract. The abstract should be typed in the same manner as the body text (see below). Please note that these Instructions are typed just like the manuscripts should be. The abstract must have at least 1800 phonetic symbols, supplying general information about the achievements, and objectives of the paper, experimental technique, methods applied, significant results and conclusions. Page layout: the text should be printed on the paper A4 format, at least 5 pages, with margins of: Top - 3, Bottom, Left and Right - 2 cm. The abstract should be presented in English (only for foreign authors), Ukraine and Russian.
**KEYWORDS:** there, must, be, at least, 5 keywords

This is introduction section. This paper contains instructions for preparing the manuscripts. The text should be prepared in .doc format (using MS Word).

## INSTRUCTIONS

The text should be typed as follows:
• **title**: Times New Roman, 12 pt, ALL CAPS, bold, 1 spacing, centred;
• **authors**: name, initials and family names; Times New Roman, 12 pt, bold, 1 spacing, centred;
• **affiliation(s)**: Times New Roman, 9 pt, italic, 1 spacing, centred;
• **abstract**: Times New Roman, 9 pt, 1 spacing, justified;
• **body text**: Times New Roman, 10 pt, 1 spacing, justified; paragraphs in sections should be indented right (tabulated) for 0.75 cm;
• **section titles**: Times New Roman, 10 pt, bold, 1 spacing, centred, without numbering, one line should be left, blank above section title;
• **subsection titles**: Times New Roman, 10 pt, bold, 1 spacing, centred, without numbering in accordance to the section (see below), one line should be left blank above subsection title;
• **figure captions**: width of the figure should be 85 or 170 mm, figures should be numbered (Fig. 1) and titled below figures using sentence format, Times New Roman, 9 pt, 1 spacing, centred (if one line) or justified (if more than one line); one line should be left blank below figure captions;
• **table captions**: width of the table should be 85 or 170 mm, tables should be numbered (Table 1.) and titled above tables using sentence format, Times New Roman, 10 pt, 1 spacing, centred (if one line) or justified (if more than one line), tables should be formatted with a single-line box around the outside border and single ruling lines between rows and columns; one line should be left blank below tables;
• **equations**: place equations centred, numbered in Arabic (1), flush right, equations should be specially prepared in MathType; one line should be left blank below and above equation.

## Additional instructions

Numerated figures and tables should be embedded in your text and placed after they are cited. Only black and white drawings and sharp photographs are acceptable. Letters in the figures should be 3 mm high. The figures should be presented in one of the following graphic formats: jpg, gif, pcx, bmp, tif.

## REFERENCES

Cite references in AIP style (https://guides.lib.monash.edu/citing-referencing/aip). Numbering in the order of referring in the text, e.g. [1], [2-5], etc. References should be listed in numerical order of citation in the text at the end of the paper (justified), Times New Roman, 9 pt, 1 spacing.

**Journal Articles**
[1] T. Mikolajick, C. Dehm, W. Hartner, I. Kasko, M. J. Kastner, N. Nagel, M. Moert and C. Mazure, Microelectron. Reliab. **41**, 947 (2001).
[2] S. Bushkova, B.K. Ostafiychuk and O.V. Copaiev, Physics and Chemistry of Solid State. **15**(1), 182-185 (2014), http://page.if.ua/uploads/pcss/vol15/!1501-27.pdf. (in Ukrainian)
[3] M. Yoshimura, E. Nakai, K. Tomioka and T. Fukui, Appl. Phys. Lett. **103**, 243111 (2013), http://dx.doi.org/10.7567/APEX.6.052301.

**E-print resourses with collaboration research**
[4] M. Aaboud et al. (ATLAS Collaboration), Eur. Phys. J. C, **77**, 531 (2017), http://dx.doi.org/10.1140/epjc/s10052-017-5061-9
[5] Sjöstrand et al., *Comput. Phys. Commun.* **191,** 159-177 (2015), e-print http://arxiv.org/abs/1410.3012.
[6] Boudreau, C. Escobar, J. Mueller, K. Sapp, and J. Su, (2013), e-print http://arxiv.org/abs/1304.5639.

**Books**
[7] S. Inoue and K.R. Spring, *Video Microscopy*: *The fundamentals*, 2nd ed. (Plenum, New York, 1997), pp. 19-24.
[8] I. Gonsky, T.P. Maksymchuk and M.I. Kalinsky, *Біохімія Людини [Biochemistry of Man],* (Ukrmedknyga, Ternopil, 2002), p. 16. (in Ukrainian)
[9] V.V. Mal'tsev, *Металлография промышленных цветных металлов и сплавов [Metallography of industrial nonferrous metals and alloys],* (Moscow, Metallurgiya, 1970), p. 364. (in Russian)
[10]M. Garkusha, *Основи Фізики Напівпровідників [Fundamentals of Semiconductor Physics]* (Vysshaja shkola, Moscow, 1982), retrieved from http://gagago.ru/g20-osnovi-fiziki-napivprovidnikiv-pidruchnik-dlya-tehniku.html.

**Book Chapters**
[11]M. Gonzalez-Leal, P. Krecmer, J. Prokop and S.R. Elliot, in: *Photo-Induced Metastability in Amorphous Semiconductors*, edited by A.V. Kolobov (Wiley-VCH, Weinheim, 2003), pp. 338-340.
[12]A. Kochelap and S.I. Pekar, in: *Теория Спонтанной и Стимулированной Хемилюминесценции Газов [Theory of Spontaneous and Stimulated Gas Chemiluminescence]* (Naukova dumka, Kyiv, 1986), pp. 16-29. (in Russian)
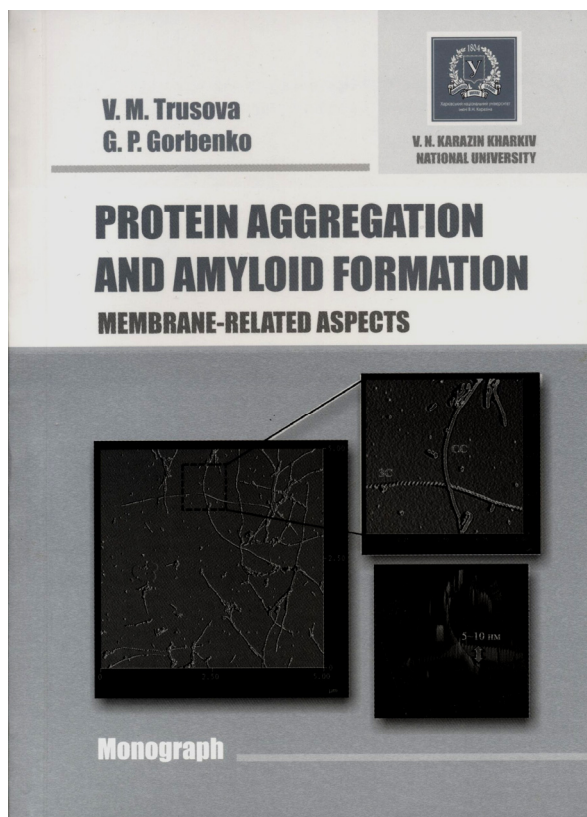
**Conference or symposium proceedings**
[13]C. Yaakov and R.Huque, in: *Second International Telecommunications Energy Symposium Proceedings*, edited by E. Yow (IEEE, New York, 1996), pp. 17-27.
[14]V. Nikolsky, A.K. Sandler and M.S. Stetsenko, in: *Автоматика-2004: Матеріали 11 Міжнародної Конференції по Автоматичному Управлінню [Automation-2004: Materials of the 11th International Conference on Automated Management]* (NUHT, Kyiv, 2004), pp. 46-48. (in Ukrainian)

**Patent**
[15]I.M. Vikulin, V.I. Irha and M.I. Panfilov, Patent Ukraine No. 26020 (27 August 2007). (in Ukrainian)

**Special Notes**
1. Use International System of Units (SI system). 2. It is undesirable to use acronyms in the titles. Please define the acronym on its first use in the paper. 3. Refer to isotopes as $^{14}$C, $^{3}$H, $^{60}$Co, etc.

**V. M. Trusova**
**G. P. Gorbenko**

V. N. KARAZIN KHARKIV NATIONAL UNIVERSITY

**PROTEIN AGGREGATION AND AMYLOID FORMATION**
**MEMBRANE-RELATED ASPECTS**

**Monograph**

Trusova V. M. G.P. Gorbenko.

Protein aggregation and amyloid formation: membrane-related aspects: monograph. – Kharkiv, V.N. Karazin Kharkiv National University, 2018. – 152 p.
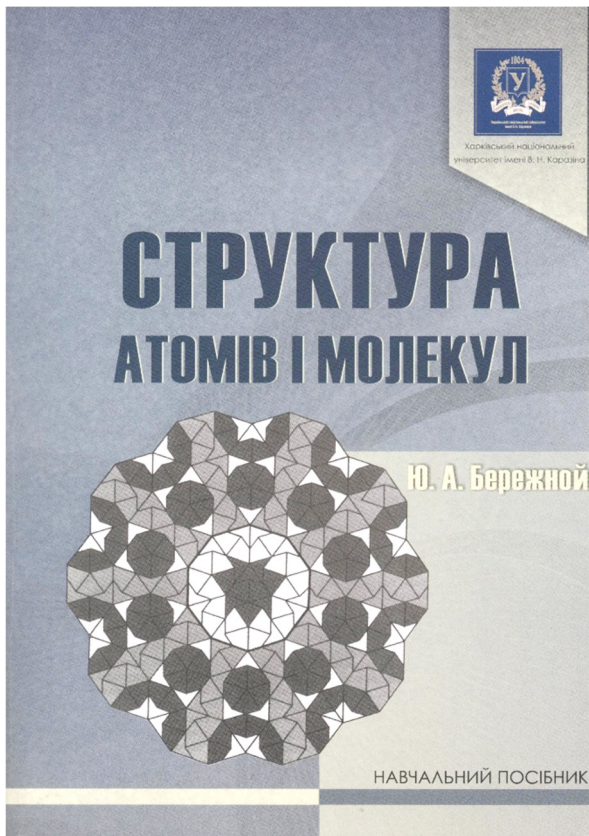
The monograph highlights the key aspects of the protein aggregating and amyloidogenic behavior in a membrane environment. The questions concerning the molecular architecture and structural polymorphism of amyloid aggregates, their physicochemical properties and membrane-modifying action are addressed. For students and researchers in biological and medical physics.

\*\*\*

**БЕРЕЖНОЙ ЮРІЙ АНАТОЛІЙОВИЧ**

Доктор фізико-математичних наук, професор, заслужений діяч науки і техніки України, заслужений професор Харківського національного університету імені В. Н. Каразіна, лауреат премій імені О. С. Давидова і К. Д. Синельникова НАН України, автор 16 підручників і монографій та понад 270 наукових робіт в галузях ядерної фізики, історії та філософії науки.

Викладено нерелятивістську та релятивістську теорії структури атомів і молекул. Розглянуто випромінення чорного тіла, квантування електромагнітного поля, рівняння Дірака та його квазірелятивістське наближення, тонку та надтонку структуру атомних рівнів енергії в електричному та магнітному полях, лембівський зсув атомних рівнів енергії, теорію Гайтлера-Лондона гомеополярного зв'язку, синглетні та мультиплетні терми двохатомних молекул. Призначається студентам, аспірантам, викладачам і науковцям фізичних спеціальностей вищих навчальних закладів для поглибленого вивчення квантової структури атомів і молекул.

\*\*\*

Наукове видання

# СХІДНО-ЄВРОПЕЙСЬКИЙ ФІЗИЧНИЙ ЖУРНАЛ
## Номер 4, 2019

# EAST EUROPEAN JOURNAL OF PHYSICS
## No 4, 2019

Збірник наукових праць
англійською, українською, російською мовами